HYBRID ADDITIVE MANUFACTURING PLATFORM FOR THE PRODUCTION OF COMPOSITE WIND TURBINE BLADE MOULDS

By

Timothy Benjamin Momsen

Submitted in fulfilment/partial fulfilment of the requirements for the degree of Master of Engineering in Mechatronics to be awarded at the Nelson Mandela Metropolitan University

April 2017

Supervisor: Prof. Russell Phillips
Co-Supervisor: Prof. Theo Van Niekerk

DECLARATION

I, Timothy Benjamin Momsen, s209033034, hereby declare that the dissertation for M.Eng Mechatronics to be awarded is my own work and that it has not previously been submitted for assessment or completion of any postgraduate qualification to another University or another qualification.

_____

Timothy Benjamin Momsen

Copyright Statement

Abstract

This dissertation discusses the application of additive manufacturing technologies for production of a large-scale rapid prototyping machine, which will be used to produce moulds for prototype composite turbine blades for the emerging renewables energy industry within the Eastern Cape region in South Africa. The conceptualization and design of three complete printer builds resulted in the amalgamation of a final system, following stringent theoretical design, simulation, and feasibility analysis. Following the initial product design cycle stage, construction and performance testing of a large-scale additive manufacturing platform were performed. In-depth statistical analysis of the mechatronic system was undertaken, particularly related to print-head locational accuracy, repeatability, and effects of parameter variation on printer performance. The machine was analysed to assess feasibility for use in the mould-making industry with accuracy and repeatability metrics of 0.121 *mm* and 0.156 *mm* rivalling those produced by some of the more accurate fused deposition modellers commercially available. The research data gathered serves to confirm that rapid prototyping is a good alternative manufacturing method for wind turbine blade plug and mould production.

Acknowledgements

First and foremost, I would like to thank the eNTSA engineering team at Nelson Mandela Metropolitan University, including, but not limited to: Mr Andrew Young and Prof. Danie Hattingh, for their numerous contributions, both in engineering expertise and experience, but also the financial assistance given to undertake the project. Their slogan “Innovation through Engineering” is definitely true of this group of intelligent individuals. Additionally, I would like to thank my master’s program mentors Prof. Theo Van Niekerk and Prof. Russell Phillips, for the wealth of engineering advice and knowledge, and guidance throughout the thesis writing and project build process. Special mention and thanks to Mr Sean Poole, who provided invaluable advice and ideas regarding 3D printer design. This has been an awesome and interesting learning endeavour.

Contents

List of Tables

List of Figures

Nomenclature

Symbols

Symbol	***Unit***	***Meaning***
$a_{x/y/z\text{-}dir}$	$[m/s^2]$	3D printer head linear acceleration
$\omega_{1,2}$	$[rad.s^{-1}]$	pulley angular velocity
$n_{1,2}$	$[rev/min]$	pulley rotational speed
M_1	$[N.m.]$	driving pulley torque
M_2	$[N.m.]$	torque at driven pulley
$\omega_{1,2}$	$[rad.s^{-1}]$	pulley angular velocities
$d_{1,2}$	$[m]$	pulley pitch diameters
P_2	$[W]$	driven pulley power requirement
η	$[const.]$	belt efficiency
F_a	$[N]$	slider acceleration force
F_f	$[N]$	slider bearing frictional force
F_w	$[N]$	slider weight component
F_{ab}	$[N]$	belt inertial acceleration force
F_{ai}	$[N]$	idler pulley inertial force
m_s	$[kg]$	slider mass
a	$[m.s^{-2}]$	slider block linear acceleration
μ_r	$[const.]$	slider dynamic frictional coefficient
g	$[9.81m/s^2]$	gravitational acceleration constant
F_{fi}	$[N]$	bearing/grease/preload friction
β	$[^O]$	slider incline angle

L	$[m]$	belt length
b	$[m]$	belt width
w_b	$[kg/m^3]$	belt specific weight
m_i	$[kg]$	idler pulley mass
d	$[m]$	idler pulley diameter
d_b	$[m]$	idler bore diameter
T_1	$[N]$	belt tight side tension
T_2	$[N]$	belt slack side tension
T_e	$[N]$	effective belt tension
d	$[m]$	pulley pitch diameter
m	$[kg]$	mass to be moved
v	$[m/s]$	speed
t_b	$[s]$	acceleration time
μ	$[const.]$	dynamic frictional coefficient
K_A	$[const.]$	load factor
f_n	$[const.]$	life-Time factor
S_B	$[const.]$	safety coefficient
L_{KHB}	$[const.]$	linear Load Distribution Factor
T_R	$[N.m.]$	lead-screw lifting torque
F	$[N]$	lead-screw lifting force
d_m	$[m]$	lead-screw mean diameter
l	$[m]$	lead-screw lead
f	$[const.]$	lead-screw frictional coefficient
d_m	$[m]$	lead-screw mean diameter
λ	$[^O]$	lead-screw lead angle
τ	$[MPa]$	torsional shear stress

T	$[N.m.]$	applied torque
d	$[m]$	lead-screw diameter
S_y	$[MPa]$	yield strength
S_{sy}	$[MPa]$	shear yield strength
F	$[N]$	applied force
A	$[m^2]$	surface area
p	$[m]$	lead-screw pitch
n_t	$[i]$	number of engaged threads
V	$[F]$	shear force
M	$[N.m.]$	moment at cross-section
I	$[m^4]$	moment of inertia
c	$[m]$	cross-section width
T_O	$[^OC]$	reference temperature
T	$[^OC]$	current temperature
R	$[\Omega]$	resistance at current temperature
R_O	$[\Omega]$	resistance at reference temperature
B	$[const.]$	characteristic temperature constant
Q	$[J/s]$	port heat flow
K_d	$[const.]$	dissipation factor
T_c	$[const.]$	thermal time constant
dT/dt	$[const.]$	temperature rate change
P_{motor}	$[W]$	motor output power
V	$[V]$	rated dc terminal voltage
$I_{supplied}$	$[A]$	supplied current from driver board
$Feedrate_{filament}$	$[mm/s]$	filament linear speed
n_{motor}	$[rev/min]$	current motor shaft speed

$r_{drive\text{-}gear}$	$[mm]$	knurled extruder gear radius
$T_{motor,required}$	$[N.m.]$	motor torque required for extruding
$F_{extrusion}$	$[N]$	material extrusion force
$r_{drive\text{-}gear}$	$[mm]$	knurled extruder gear radius
f'_w	$[const.]$	wall static friction coefficient
p	$[N/m^2]$	pressure at hopper base
p_o	$[N/m^2]$	pressure at height H in section
W	$[m]$	hopper width
ρ_{bulk}	$[kg/m^3]$	average pellet density
D^*	$[const.]$	distribution factor
δ	$[^O]$	effective friction angle
α	$[^O]$	hopper wall angle
p_O	$[N/m^2]$	feed hopper base pressure
z_b	$[m]$	down-channel distance
f_b	$[const.]$	dynamic frictional coefficient barrel
f_s	$[const.]$	dynamic frictional coefficient screw
H	$[m]$	screw channel depth
W_b, W_s	$[m]$	channel widths, screw ends
Θ_b, Θ_s	$[^O]$	helix angles, screw ends
D_b, D_s	$[m]$	barrel/screw diameters
W_a, D_a, θ_a	$[m,m,^O]$	average channel parameters
X	$[m]$	width of solid bed
v_{bx}	$[m/s]$	cross-channel barrel velocity
T_{bulk}	$[K]$	temperature of melt film
T_{melt}	$[K]$	melting temperature of polymer
T_{sol}	$[K]$	temperature of solid pellet bed

ρ_m	$[g/m^3]$	melted material density
Cp_m, Cp_s	$[J/g]$	specific heat of polymer melt/solid
K_m	$[W/m.K]$	melt thermal conductivity
λ	$[J/g]$	polymer heat of fusion
Q/W	$[kg/s]$	mass flow-rate
v_z	$[m/s]$	down-channel velocity of material
d_{pinion}	$[m]$	timing pulley pitch diameter
r_{pinion}	$[m]$	timing pulley pitch radius
T_{motor}	$[N.m.]$	motor torque
W_{hold}	$[kg]$	holding weight

Glossary

CAD: Computer-Aided Design - the implementation of computing technologies to assist with the creation, implementation, planning, analyses, and testing of a concept. (Narayan, K.:2008, p.3)

CNC: 'Computer Numerical Control' machines controlled via a number of coordinate position commands and milling commands to machine components via subtractive processes. (Lynch, M.: 1997)

G-Code (RS-274): Most widely used programming language used to control Numerical Control machines for machining or components. (Lynch, M.:1997)

Glass Transition Temperature: The correctable changeover in unstructured materials, or within semi-crystalline materials, from a rigid into a gel-like state. (ISO 11357-2: 1999)

Micro-controller: An integrated computer or 'SOC' (System-on-Chip), containing a processor core, memory, and programmable input and output peripherals. (Augarten, S.: 1983)

Polymer: A sizeable macromolecule comprised of recurring molecular subunits, which form long chains, with high relative molecular mass, and versatile physical properties. (Painter, C., Coleman, M.: 1997)

Print-bed: Flat plane made of glass or plastic, usually heated, upon which 3D printed model is built up. (Rep-Rap Glossary: Dec 2015)

.STL File (Stereo-lithography file format): File format created for rapid prototyping and computer-aided manufacturing, describes only the surface geometry of the modelled object. (Grimm, T., 2004)

Thermoplastic: A plastic polymer substance which transitions to a gel form above a specific temperature, and returns to a solid configuration upon cooling. (Baeurle S., Hotta A., Gusev A.: 2006)

Thermosetting Composites: A pre-polymer plastic material with embedded strands which, upon curing produces a solid structure which cannot be reheated and re-moulded thereafter. (The Open University: 2000)

Chapter 1

Introduction

The Collaborative Fibre Composites Research, Development and Innovation Programme (CFCP), through the Composite Innovation Centre (CIC) has identified an opportunity to enhance tooling, mould making, and manufacturing techniques required to develop lightweight turbine blades for the renewable energy industry. A multi-stage project will evaluate the potential in using additive manufacturing techniques for the development of composite moulds, and provide familiarisation with the rapid prototyping industry. The moulds produced will be used for the composite layup and production of prototype wind turbine blades, which upon completion, will be thoroughly tested and implemented in the wind energy sector.

As the research aims to develop new blade manufacturing technologies for the emerging wind-energy industry within southern Africa, which have, as yet, not been fully exploited, the work-plan is to be divided into four distinct project phases. Initially, a prototype horizontal wind turbine blade of 5 meters length is to be designed, which conforms to the IEC61400 structural standards [1]. Finite element analysis is to be used to determine composite layup with proposed weight and deflection restrictions for the blade. Following blade design, an automated blade mould manufacturing platform is to be designed and built, thereby resulting in the blade moulds being manufactured by said machine. Finally, the blades are to be manufactured via composite layup and traditional production methods using the newly-produced moulds, and the strength and deflection testing of the blades performed in due course.

This dissertation shall focus on the conceptualisation, development, and complete testing of a large-scale Additive Manufacturing machine, and the performance testing of said machine specifically looking into issues such as locational and printing performance. As a mechatronic [2] system, the resulting research output will focus on Additive Manufacturing, which has, as yet, not been applied to the turbine blade mould production process on such a large scale. This presents unique learning opportunities for the development of new engineering outputs in the moulding industry.

---

[1] – IEC 61400: A set of design configurations sanctioned to make sure that wind turbines are suitably engineered against damage from hazards within the product duty cycle (M. Woebbeking: 2008).

[2] – Mechatronic system: a multidisciplinary engineering field encompassing a combination of systems, mechanical, electrical, telecommunications, control, and computer engineering (L.J. Kamm: 1996).

1.1. What is additive manufacturing?

In order to fully understand the purpose for the research hypothesis statement, it is necessary to first define additive manufacturing, and various forms of the chosen research field. In a broad sense, the terms 'Additive Manufacturing' and 'Rapid Prototyping' refer to the family of manufacturing procedures which produce parts by slow deposition or building-up, layer upon layer, of solid material (Kruth, J.P., Leu, M.C., & Nakagawa, T: 1998, p.525). Over the years, said terms have evolved into a single commercially-coined phrase, '*3D printing*'. The contrast from subtractive manufacturing machines is that the tool head performs a material-depositing, binding, or melting operation instead of a grinding, polishing, or routing operation. Furthermore, additive manufacturing can be broken down into variations of the above parent concept, with print methods including '*Selective Laser Sintering*' (SLS), '*Selective Laser Melting*' (SLM), '*Selective Heat Sintering*' (SHS), '*Direct Metal Laser Sintering*' (DMLS), '*Fused Deposition Modelling*' (FDM), '*Fused Filament Fabrication*' (FFF), '*Direct Ink Writing*' (DIW), '*Stereolithography*' (SLA), '*Laminated Object Manufacturing'* (LOM), and '*Electron Beam Freeform Fabrication*' (EBF^3). (Grimm, T.: 2004)

1.2. Aim

The research project encompasses the design, construction, and performance testing of a large-scale additive manufacturing platform for the production of a finished plug used to manufacture composite 5 *m* long prototype blade moulds for a horizontal axis wind turbine.

1.3. Motivation

Significant growth of the renewable energy industry, and in particular the wind energy sector in the past two decades, presents unique opportunities for development of new turbine blade manufacturing technologies and methods.

This significant bias in favour of wind technologies and their development is due to several factors. Wind farms can be set up in any location globally, both onshore and offshore in the oceans, and are able to operate 97 to 98 % of the day (Trewby, J: 2014 p.13). Additionally, the cost of electricity generation per unit kilowatt-hour is lowest for onshore wind electricity generation compared to other avenues with levelled costs for energy generation being as follows: Gas-burning turbine at ZAR 1110 to ZAR 1859, coal at ZAR 1952 to ZAR 2602, nuclear at ZAR 1301 to ZAR 1952 per *MW/h* respectively. Onshore wind electricity generation sets the economic benchmark at ZAR 1301 to ZAR 2323 per *MW/h*, rivalling non-clean generation techniques such as gas and nuclear generation strategies (Trewby, J: p.48). Further push factors include the carbon emissions reduction performance of wind farms versus coal and gas generation methods. According to tests undertaken by the National Renewable Energy Laboratory, the median carbon footprint of wind energy is 11grams of carbon dioxide per *kWh* generation within a range of 5 units, when compared to coal at 970 to 1190 gCO_2/kWh, and open cycle gas turbine plants at 550 to 650 gCO_2/kWh (White, D: 2004).

Additionally, the myriad of benefits accrued by wind energy offset any challenges associated with the technology's initial expensive start-up investment costs. Firstly, turbines do not require water to operate, as conventional power stations do. The estimated water savings accrued in 2013 was in the region of 138.15 billion litres due to wind farm installations (American Wind Energy Association: 2014). The invention of this new energy source has created a sustainable highly-skilled workforce in the form of transportation, logistics, marketing, and legal services, manufacturing, maintenance, and operations jobs. According to the American Wind Energy Association (AWEA), the U.S. Market logged 50'500 full-time employees in 2013, with that number growing by 33 % annually (American Wind Energy Association: 2014). Benefits to land owners and farmers exist in the form of remote electricity access to single farms and villages, use in auxiliary applications such as phone sites, water and fuel pumps, and is an illimitable and generally-reliable power source.

Finally, the introduction of additive manufacturing as a means of producing moulds could have various benefits over the conventional alternative, that is, CNC machining. These benefits include development of a new manufacturing standard for mould production, eradication of environmentally-unfriendly CNC cutting fluids, material efficiency, part flexibility, and recyclability of AM residue (Faludi, J.: 2014 p.8). Furthermore, international competition, market internationalisation, and reduction of manufacturing costs affiliated with stringent product quality requirements mandate that moulds production component and prototype development be sped up. According to P.D. Hilton and P.F. Jacobs (2000), "*the application of Rapid Prototyping to the product development cycle has shown a 60 % decrease in lead time over traditional means.*" Finally, rapid prototyping of moulds has the ability to reduce product development cycle times and costs by up to 50 %, due to the rapid response of market demands ensured by the AM process compared to traditional casting and machining mould processes (Y. Ding, H. Lan, J. Hong, D. Wu: p.282). These facts alone are the driving force for further investigation into the development of rapid prototyping for the wind turbine blade mould industry.

1.4. Objectives

The technical performance metrics that the large-scale additive manufacturing platform should achieve or surpass in order to be considered successful include:

1. The additive manufacturing platform should have a total print area totalling an approximate work volume of 7 m^3.

2. The platform should make use of the commercially-suitable fused-deposition modelling print method, whereby parts are manufactured via the deposition of a melted thermoplastic filament material such as ABS, PLA, PET, nylon, or PC.

3. The platform should be able to print a 5 *m* long wind turbine blade plug without interruption, that is, an interruptible power supply should be integrated to prevent system power loss during unexpected municipal power failures.

4. The area on which parts are to be printed, called the print-bed, should be moveable, allowing the printed object to be transported away on the print bed after job completion.

5. The system should consist of a rigid gantry system with 3 axes of motion, allowing the FDM print-head movement in the x, y, and z directions, with print-head positioning accuracy of 0.1 *mm*, and repeatability of 0.1 *mm*.

6. The system should be designed so as to allow a maximum print speed of 150 *mm/s* without oscillation or deflection of the system above 0.1 *mm*.

7. The manufacturing platform should produce parts suitable for blade plug production, that is, its dimensional and surface finish quality should be at least 0.1 *mm* and 50 μm.

1.5. Hypothesis statement

The additive manufacturing platform, after being conceptualised, designed, and constructed, will be performance tested to ascertain whether or not additive manufacturing is a new acceptable manufacturing method for the production of horizontal-axis wind turbine blade plugs with respect to performance metrics specified for production of said blade moulds.

1.6. Delimitation

The following restraints are imposed on the research:

1. Printer performance shall be tested via the printing of smaller-scale objects such as cubes and not the full 5 *m* blade, so as to reduce material wastage and assess printer dimensional accuracy and other metrics more objectively, vizier, it is impossible to measure printer dimensional accuracy via the analysis of complex blade surfaces.

2. The material extruder, or print-head, shall be tested only with PLA material, so as to limit the scope of investigation to overall performance of a mechatronic system instead of materials performance.

1.7. Schedule and research timeframe

The master's research project, which encompasses conceptualisation, design, construction, simulation, real-life testing, and reporting elements, is to be scheduled in the following way. The entire work is expected to take one year, with completion and a final research output being produced by December 2016. Figure 1.1 illustrates the planned research timeframe.

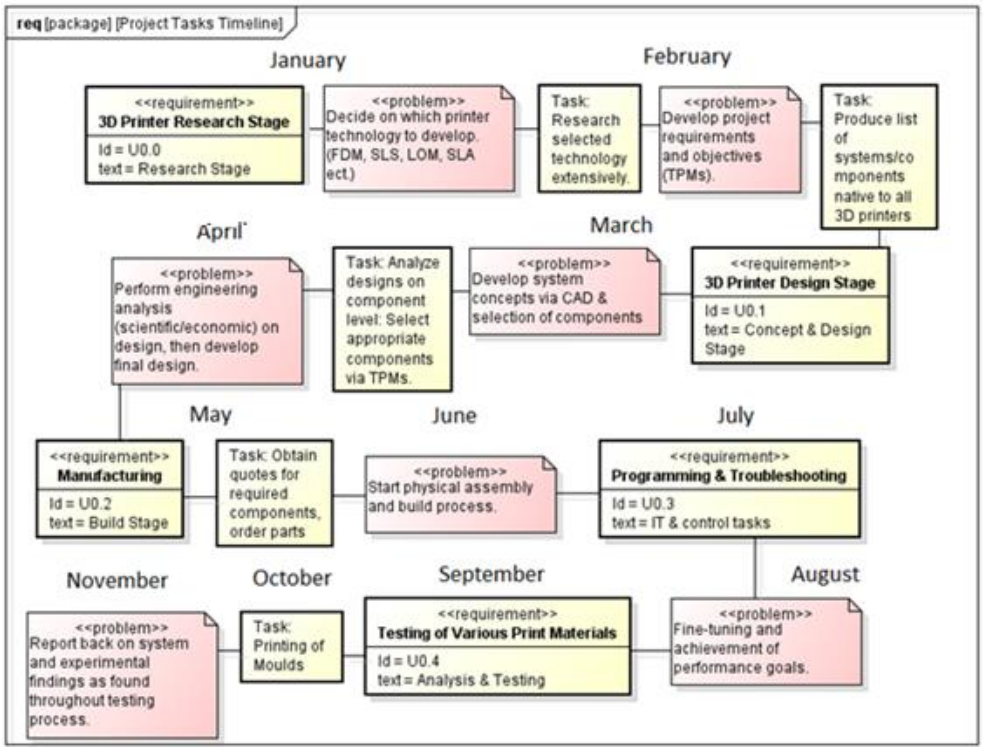

Figure 1.1: Research Project Proposed Timeline

1.8. Dissertation outline

This dissertation is structured in the manner described as follows. Chapter 1 introduces the topical research area of interest, and provides motivation for why the identified field requires further study and work. Chapter 2 functions as a theoretical background for the two Engineering fields that make up the project, namely, additive manufacturing and 3D printers, and give the reader a good general knowledge about the subject matter of the research question. Chapter 3 will look into the development of various additive manufacturing platforms, specifically the gantry, frame, and drive systems thereof, and provide a framework for further development in later chapters.

Thereafter, in Chapter 4, the concepts are scrutinised and a final design amalgamated, with pre-construction analyses being performed on the various subsystems, in addition to the development of a few print-heads for possible manufacture. Chapter 5 presents technical real-life analysis of the manufactured printer, with tests being performed, recorded, and presented, and these results compared and contrasted with the simulated results and with those of current CNC subtractive manufacturing processes. Finally, in chapter 6, the preceding data, analyses, and discussions make it possible to objectively answer the hypothesis question posed, vizier, “is additive manufacturing a suitable method of manufacture for the production of turbine blade plugs, as an alternative to other manufacturing processes?”, and if the objectives posed were met. The chapter also ends off with recommendations for future research and work.

1.9. Chapter conclusion

This chapter serves as an introduction to the research work which is to be investigated surrounding additive manufacturing and 3D printers, and discusses the aim, objectives, motivation, hypothesis statement, and expected timeframe for the master's dissertation. The following chapter will present a background on current turbine blade mould production, as well as the proposed additive manufacturing technique fused deposition modelling.

Chapter 2

Preliminary Theory and Literature Review

The literature review shall touch on the main topics of interest, namely a history of turbine blade production, an introduction to additive manufacturing, in particular fused deposition modelling, and the respective printers currently available in industry.

2.1. Background of current turbine blade mould production

At present, the vast majority of wind turbine mould manufacturers, such as Gurit, Dencam, and MFG Wind, employ 5-axis CNC milling for the production of blade profiles within large composite mould-beds. Moulds with a 20 meter diameter or smaller are constructed using an EPS foam base, whereby the desired blade profile is CNC-routed in the foam, and an epoxy resin or vinyl-ester layer applied to the routing. This layer is again CNC machined with high accuracy; in the region of +-0.1 *mm*. Additional post-processing of the moulds includes gel coats for the routed surface, and waterproofing for the exposed exterior surfaces. Variations exist regarding material selection, including using metals, composites, various resins, and polymers to produce moulds. The major setback with the use of 3D milling is the wastage of material that ensues following the subtractive manufacturing process (Gurit: 2015).

Figure 2.1: Current Turbine Moulding Process via CNC Machining and Manual Finishing

2.2. An Overview of extrusion-based additive manufacturing

In years gone by, the ability to produce or manufacture any kind of mechanical part, tool, machine, or apparatus, was hinged on the physical amenities available such as factories, assembly lines, moulds, dies, and forges. However, with the invention of the first additive manufacturing machine by Charles Hull in 1986 in the form of the stereo-lithographic 3D printer, (Srinivasan, V., Bassan, J.: 2012) and with others pioneering more accessible machines such as the fused deposition modeller, the world of manufacturing opened up to other sectors once restricted to industry. The accessibility of rapid prototyping technology to the general public, lower initial cost outlay, and ease of use, serves as a driving force towards implementation of 3D-printers in the business, academic, and private spheres for the manufacture of custom designed parts. A number of additive manufacturing methods have been pioneered since the 1980's, with the most common and viable printing method available being fused deposition modelling.

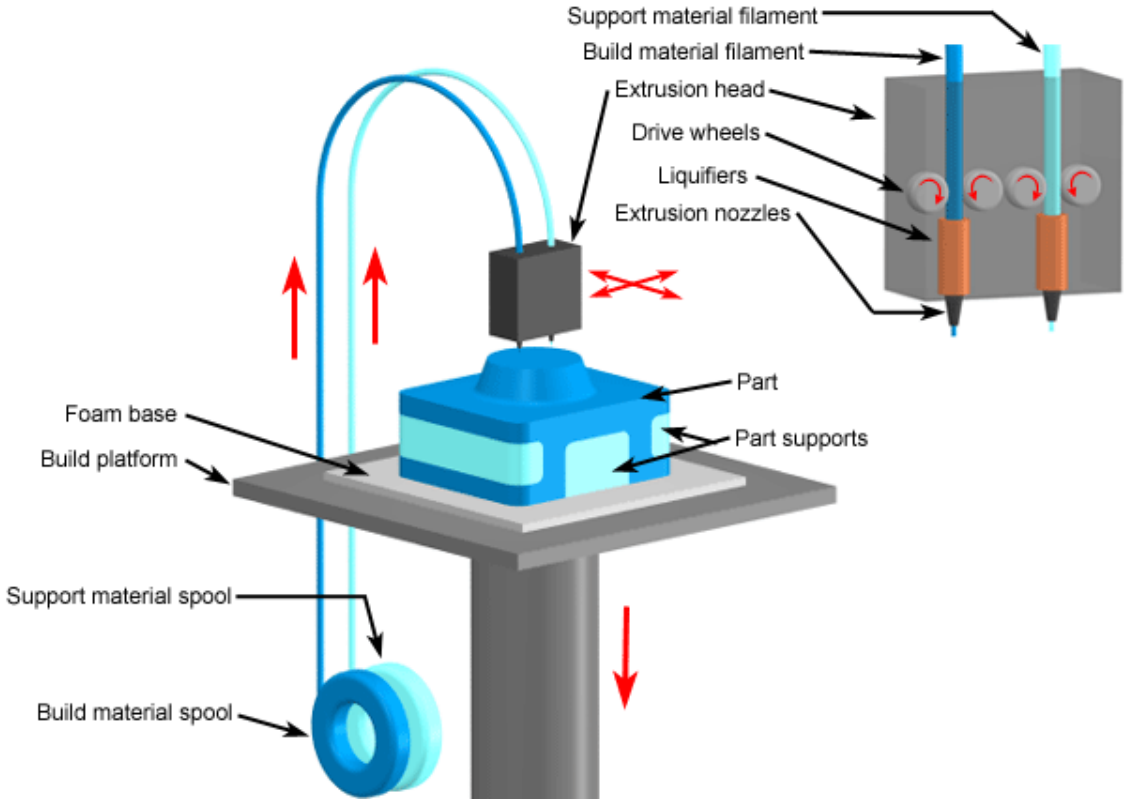

Figure 2.2: Fused Deposition Modelling Additive Manufacturing Process

Extrusion-based additive manufacturing is based on the concept of a material being heated, changing into a liquid form, and pressed out of a jet or nozzle into the desired shape. Materials employed as the substrate include thermoplastics, eutectic metals, metal clays, plasticine, rubbers, edible materials, ceramic materials, and composites. Fused deposition modelling (FDM) is the most widely-used additive manufacturing technology employed at the home, small business, and retail level (E. Pallermo: 2013).

FDM was first introduced in the United States by Stratus in 1992, subsequently becoming the most widely used 3D-printing method. According to Pallermo, "FDM 3D printing is quickly becoming the fastest, most affordable way to create custom consumer goods..." (E.Pallermo: 2013). Additionally, the technology is popular in the automotive and food industries for parts manufacturing, rapid prototyping, and manufacturing processes. The FDM process begins with a .STL format CAD model of the desired design being generated. The .STL file is imported into a G-Code converter software package, such as MatterSlice, Skeinforge, Slic3r, amongst others. (Bowyer, A.: 2016) These G-Code converters subdivide the .STL model into cross-sections of equal thickness approximately 0.172 *mm* to 0.356 *mm* thick, (Chee KC; Kah FL, & Chu SL: 2003 p.129) then produces a series of coordinate points at each layer which the print head, or extruder, will follow. The tool paths, in the form of G-Code, are then downloaded to the 3D printer's micro-controller memory. Following the instruction set download to hardware, the printing operation may commence. The fabrication material, generally a thermoplastic material such as polystyrene, poly-amide, or polycarbonate, amongst others, is pulled into the printer's extrusion head, heated until semi-molten by the thermistor-controlled heater tip, and deposited as plastic traces on the print-bed. The print bed then drops by a user-defined height between 0.250 *mm* and 0.965 *mm*, (Chee KC; Kah FL, & Chu SL: 2003 p.129) and then next thermoplastic layer is subsequently deposited.

2.3. Fused deposition modeller development thus far

With the expiry of the FDM patent held by Stratasys in 2012, a large surge in the design and production of Mechatronic machines which employ the Fused Deposition Modelling printing process has occurred. The vast majority of designs feature a three axis motion system driven via timing belt or lead screw drives in concert with stepper motors. The printer head, which heats and extrudes the material is attached to the three-axis sliding gantry system, and is controlled via a centralized integrated controller board. Delta printers, which employ three linear actuators to position the print-head, are far less common. Well-known machines commercially available include the Makegear M2, DeltaWASP, and Ultimaker 2 as shown:

Figure 2.3: Popular Fused Deposition Modellers (from left: DeltaWASP, Ultimaker 2, Makergear M2)

2.4. Chapter conclusion

This chapter introduced the three topical areas of interest related to the research work to be performed and presented later on. These included current turbine blade mould production techniques, fused deposition modelling, and some currently-available printer solutions. The subjects presented provide a clearer understanding of the engineering fields to be investigated, particularly those relating to fused deposition modelling in the next chapter.

CHAPTER 3

Fused Deposition Modellers: A Technical Analysis

Chapter 3 provides a framework for amalgamation of a final design on a detailed component-level basis.

3.1. System organisation and interaction of components

A fused deposition modeller is by nature a mechatronic system containing both a physical mechanical integration of components, and an electrical network which actuates the mechanical elements. The platform generically contains mechanical elements such as the extruder which ejects the printing material, a flat surface known as a print-bed upon which this material is deposited, a linear motion system which allows the print-head to move in three directions, and a sturdy chassis which supports and houses all components. Furthermore, the electrical system will always be comprised of a logical control board with centralized processor, motors to drive motion of the print-head, a display unit such as an LCD screen to allow control of the system, and peripheral control boards, known as driver breakout boards, to supply current to the motors. Mechanical and electrical subsystems are all controlled via Arduino-based cross-compiling, splicing, and G-code generating software. Figure 3.1 demonstrates the system:

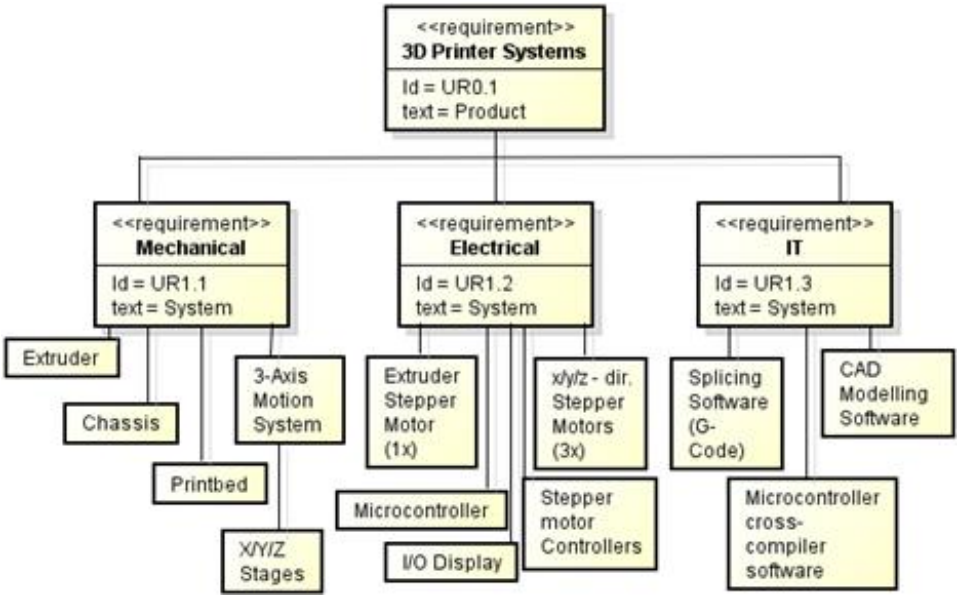

Figure 3.1: Fused Deposition Modelling Printer System Configuration

3.2. Control system

A control system is by definition a mechanical, optical, or electronic system that is used to conserve a certain pre-programmed output command (American Heritage Dictionary: 2016). Control systems are termed as either being "open-loop" or "closed-loop", with closed-loop systems containing feedback sensors to actively monitor system parameters in real-time, and the former containing no feedback sensors whatsoever. The system as a whole is both closed-loop and open-loop. The following components exist in an FDM printer:

- 1 logical Controller Board – controls the entire system including peripherals.
- 3 stepper Motors and driver boards – controls the movement of the 'x', 'y', 'z' axes.
- 2 limit switches per axis to signal end of printer axes range.
- 1 stepper Motor and driver board – controls the print material extrusion.
- 1 resistive heating cartridge and 1x 100K NPC thermistor for temperature feedback sensing.
- 1 PWM fan for cooling of the print head and material during operation if need be.

The system exhibits a dual nature as shown in Figure 3.2, where it can be noted that process parameters such as print-head temperature are actively monitored with a closed feedback loop, but the electrical drive system which consists of stepper motors and driver boards, remain under open-loop control.

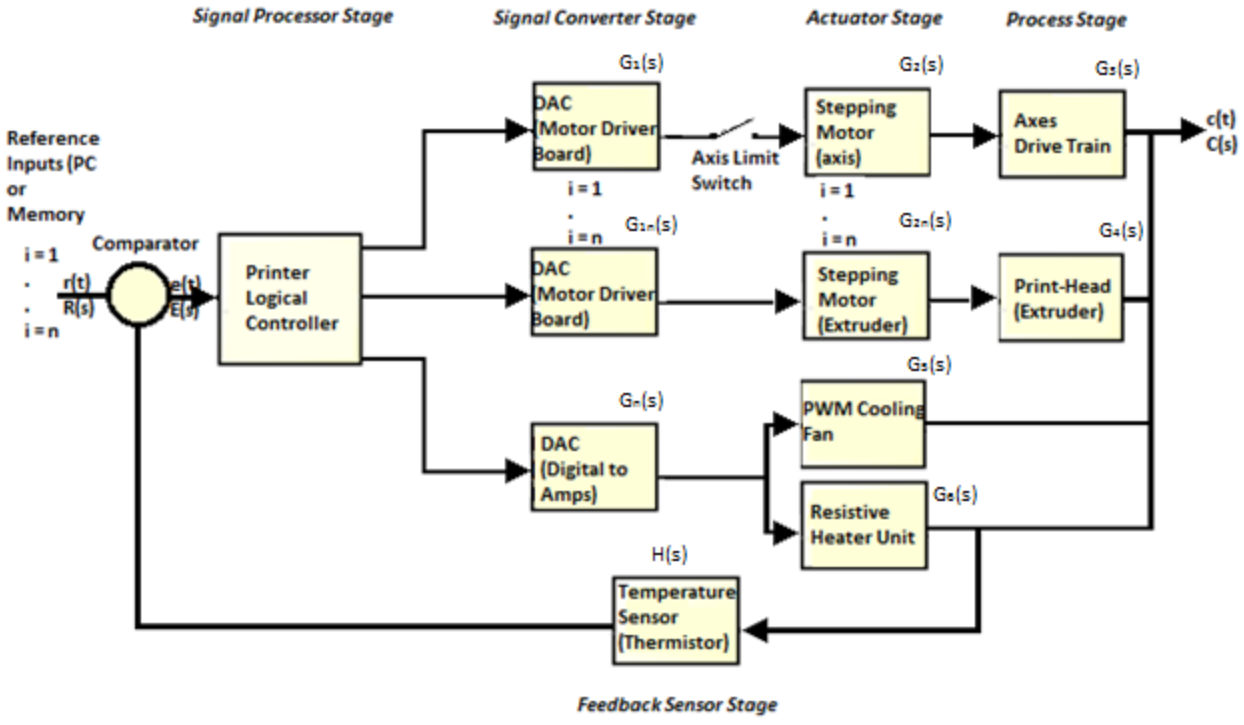

Figure 3.2: Fused Deposition Modeller Control System

The physical electrical layout of an FDM control system, including componentry, is shown in Figure 3.3. As highlighted in the figure, the motor driver boards and stepper motors control motion of the three axes and extrusion rate of material from the print-head, thermistors and heaters control melting of the extruded material, and fans are speed-controlled to regulate extruder and motor driver board temperatures during operation.

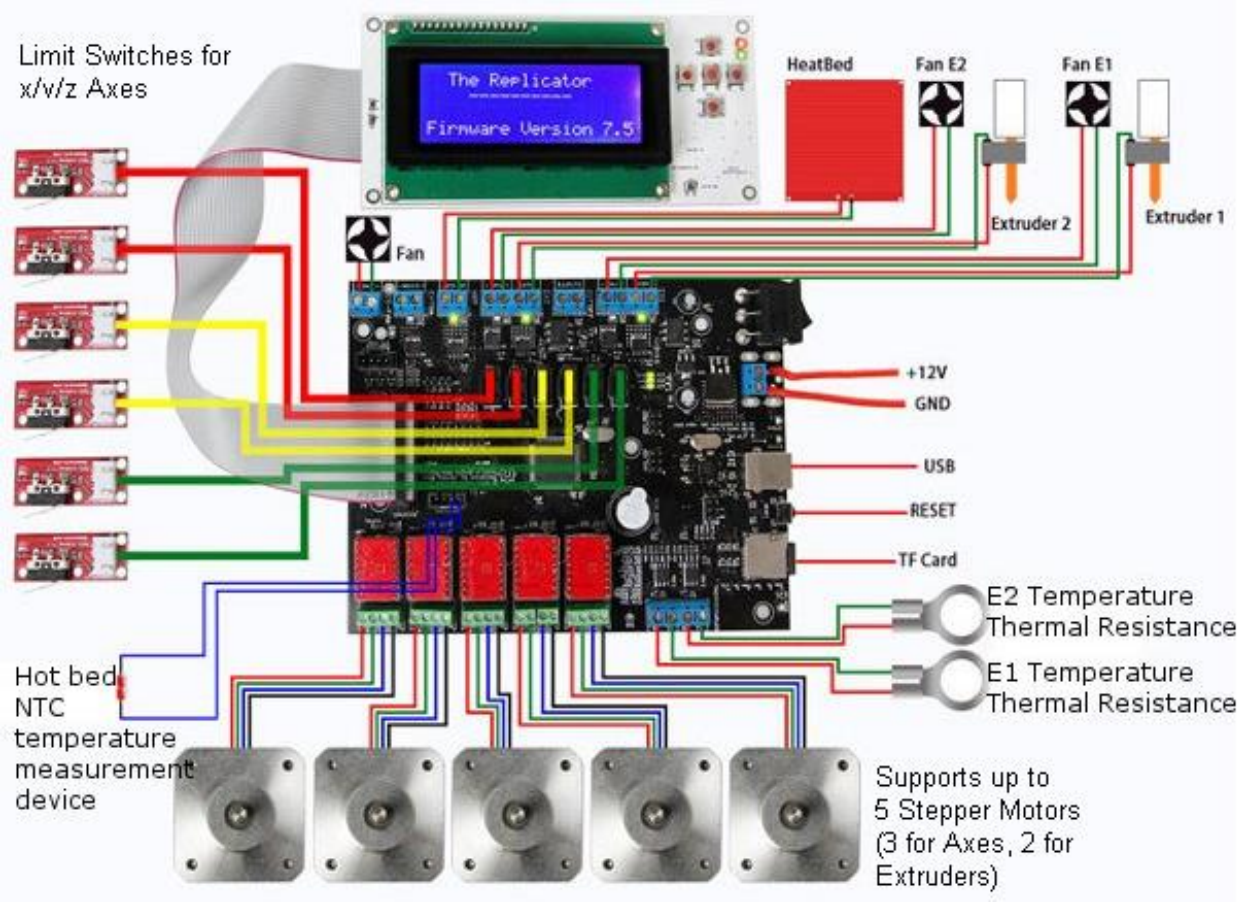

Figure 3.3: Fused Deposition Modeller Generic Electrical Layout

A crucial initial step in the development of an additive manufacturing solution is in the mathematical description and modelling of the system. The purpose thereof is that it permits the reader to gain concise and clear knowledge of the machine in terms of cause and effect relationships which exist between various system peripherals. As illustrated in Figure 3.2, control systems are generally illustrated in the form of a block diagram, with each system component or process represented by a transfer function, and link via signal control paths. According to Kuo, (Automatic Control Systems: 1993, p.21) a transfer function is a linear mathematical approximation of the relationship between a signal input and output for systems such as single-input single-output filters and controllers within communications and control machines. Since 3D printer technologies operate with voltages and currents in linear time, it can be

assumed that the control system is of a continuous nature, that is, the system values can be monitored at near infinite sample rates. Therefore, for a fused deposition modelling application, each system component can be represented by taking the Laplace Transform[4] of the input and output signals to the device. Then a general transfer function for each device is:

$$H(s) = \frac{Y(s)}{X(s)} = \frac{L\{y(t)\}}{L\{x(t)\}} \tag{3.1}$$

Where

$$X(s) = L\{x(t)\} = \int_{-\infty}^{\infty} x(t)e^{-st}dt$$

$$Y(s) = L\{y(t)\} = \int_{-\infty}^{\infty} y(t)e^{-st}dt$$

Full understanding of the system requires that each transfer function be fully expanded upon. The digital-to-analogue signal converters, in the form of stepper motor driver boards, convert a digital binary command signal into a corresponding analogue current at a nominal voltage, which is pulsed to the stepper drives. Typically, a DAC can be envisioned as a digitally-controlled potentiometer whose output is a percentage of the full-scale analogue voltage determined by the digital input code (Understanding Data Converters: 1999, p.3). The DAC transfer function has a ramp characteristic; therefore the signal converter stage transfer function is defined as:

$$G_{1i..n}(s) = \frac{1}{s^2} \tag{3.2}$$

The stepper motor transfer function at the end of a step, with initial load torque of zero, as derived in Appendix A.5., is given by:

$$G_{2i..n}(s) = \theta(s) = \frac{(\frac{-1}{J})\Delta T_L(s)(N_{RT})}{s^2 + \frac{D}{Js} + \frac{\sqrt{2K_T I N_{RT}}}{J}} \tag{3.3}$$

Transfer functions $G_3(s)$ and $G_4(s)$ for the drive train and print-head are as yet undecided and are analysed at a later stage. However, for a dc-powered fan with varying amperage and constant voltage, the transfer function is:

$$G_5(s) = \frac{V_o(s)}{V_i(s)} = \frac{1}{s*R_{fan}} \tag{3.4}$$

Similarly, for the dc-powered resistive heater unit of the print-head, the transfer function $G_6(s)$ is:

$$G_6(s) = \frac{V_o(s)}{V_i(s)} = \frac{1}{s*R_{heater}} \tag{3.5}$$

[4] – Laplace Transform: a function f(t) which is integrable over domain[0,∞), has the Laplace transform $F(s) = \int_0^{inf} e^{-st} f(t)dt$, where $s = \sigma + i\omega$ is the complex number frequency parameter (Kuo: 210, p.18).

Thereafter, the feedback transfer function H(s), is derived for NPC thermistor in Appendix A.6. as:

$$H(s) = R(s) = -\frac{R_o}{s}\left[\frac{1}{s-\frac{B}{T(s)-T_o}}\right] \tag{3.6}$$

Generally, a closed-loop system transfer function is given by:

$$M(s) = \frac{G(s)}{1+G(s)H(s)} \tag{3.7}$$

Where G(s) is the forward path transfer function and H(s) is the feedback path transfer function. For the 3D-printer system illustrated in Figure 3.2, the control system should be separated into two independent systems, namely a motor control system, and a print-head control system. The transfer functions of each are:

$$M(s)_{printhead} = \frac{G(s)}{1+G(s)H(s)} = \frac{G_n(s)[G_5(s)+G_6(s)]}{1+\{G_n(s)[G_5(s)+G_6(s)]\}H(s)} \tag{3.8}$$

$$M(s)_{axis\ control} = G_{1i}(s)G_{2i}(s)G_{3i}(s) \tag{3.9}$$

for all axes of motion I = 1…n. The overall transfer function of the system is then:

$$M_{sys}(s) = M(s)_{axis\ control} + M(s)_{printhead} \tag{3.10}$$

$$= G_{1i}(s)G_{2i}(s)G_{3i}(s) + \frac{G_n(s)[G_5(s)+G_6(s)]}{1+\{G_n(s)[G_5(s)+G_6(s)]\}H(s)}$$

$$= \left(\frac{1}{s^2}\right)\left(\frac{\left(\frac{-1}{J}\right)\Delta T_L(s)(N_{RT})}{s^2+\frac{D}{Js}+\frac{\sqrt{2K_T I N_{RT}}}{J}}\right)(G_{3i}(s)) + \frac{\left(\frac{1}{s^2}\right)\left[\frac{1}{s}\left(R_{fan}+R_{heater}\right)\right]}{1+\left\{\frac{1}{s^2}\left[\frac{1}{s}\left(R_{fan}+R_{heater}\right)\right]\right\}\left\{-\frac{R_o}{s}\left[\frac{1}{s-\frac{B}{T(s)-T_o}}\right]\right\}}$$

3.3. Drive system

Currently there are three methodologies used to produce motion of the print head. These are rack and pinion, timing belt and pulley, and power-screw systems. It is necessary to investigate all means of gantry movement in the ‘x’, ‘y’, and ‘z’ directions so as to better apply this knowledge to the development of the final design. Historically, a drive system is a combination of components which convert energy, whether it be electrical, chemical, or potential, or heat, into kinetic energy. When related particularly to FDM additive manufacturing platforms, it is comprised of a number of motors of the stepper or servo variety, and a drive system to convert rotational movement of the motor shafts, into a linear movement. The drive system components are generally duplicated three fold on the machine, so as to provide independent

perpendicular triaxial [5] motion. The machine print-head is assembled with the three axes of motion such that independent travel in each direction can be achieved simultaneously.

3.3.1. Drive options

Timing belt and pulley drives

Timing belt is toothed belting generically used in industrial and automotive power transmission applications, with a repeating square, trapezoidal, or round teeth profile on the underside of the belt. These provide accurate positional and velocity figures if tensioned correctly, and are typically constructed of reinforced polyurethane, with nylon, Kevlar, aramid, and carbon embedded fibre reinforcement. Furthermore, the belts are mated to aluminium or plastic timing pulleys with corresponding teeth profiles, and connected to motors for use on current 3D printers as a cost effective solution. This drive methodology has been implemented extensively on lower-cost printing machines in GT2 6 *mm* wide format in conjunction with linear stainless steel rod, bushings, and a linear position slider due to the low implementation costs and simplicity of design. Figure 3.4 illustrates such a 3D printer drive mechanism:

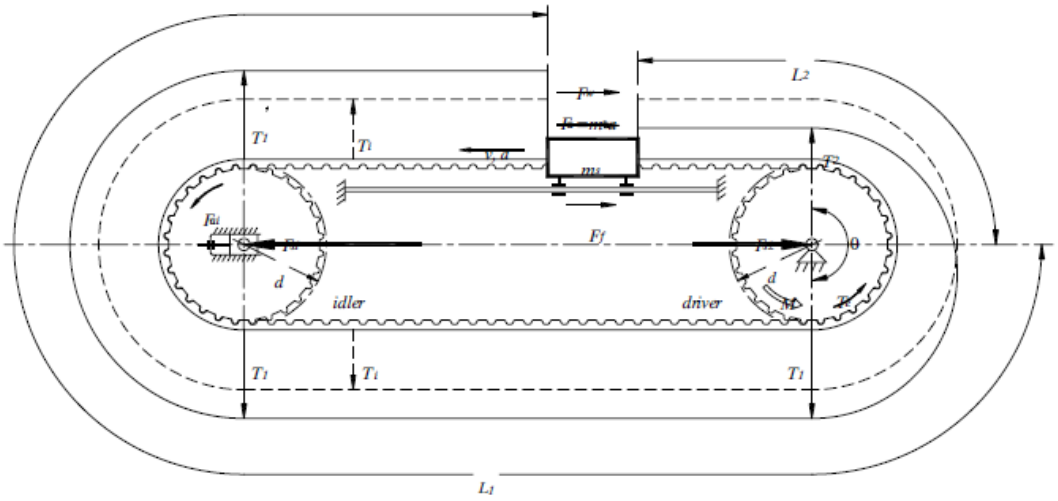

Figure 3.4: Timing Belt and Linear Bearing Slide Used On 3D Printers

[5] – Triaxial: three independent directions, vizier, ‘x’, ‘y’, and ‘z’ directions. (Merriam-Webster: 2016)

Suitability for the 3D-printing application from a power requirements standpoint can be assessed and calculated using the following pre-conceived timing belt and pulley specifications, as detailed in Appendix A.2. Employing 16-tooth T2.5 16 *mm* diameter aluminium pulleys with 6 *mm*-wide T2.5 timing belt and NEMA17 48 *mm* 0.471 *N.m.* stepper motors the required motor pulley torque is:

$$M = 0.09348\ N.m.$$

And since the stepper motors produce a maximum torque of 0.471 *N.m.*, the design factor is:

$$n = 5.0400$$

Leading to the conclusion that a timing belt and pulley drive system is a viable solution.

Rack and pinion drives

Conventionally employed almost entirely in the railway, stair-lift, and heavy industrial sectors, rack and pinion drives can be implemented in additive manufacturing for the conversion of rotational into linear movement. A rack and pinion system comprises a pair of gears, whereby a circular pinion engages a tooth rail, which, upon circular rotation, forces the rack system to move linearly in one direction, or vice-versa. Typically the system is made of steel in varying pitches and modules, and provides excellent repeatability and accuracy of up to 2 x 10^{-4} *mm* and 9.4x10^{-5} *mm/m* respectively (Entwistle, J.: 2011). The system does however have the drawback of having the motors attached to the moving pinion, which requires additional electrical cable management. Other concerns are backlash due to improper mounting and locating of pinions, which can be negated by employing a dual pinion configuration on each rail. Another advantage is the unlimited travel length possible achieved by the splicing of rack lengths. Figure 3.5 demonstrates a rack and pinion drive.

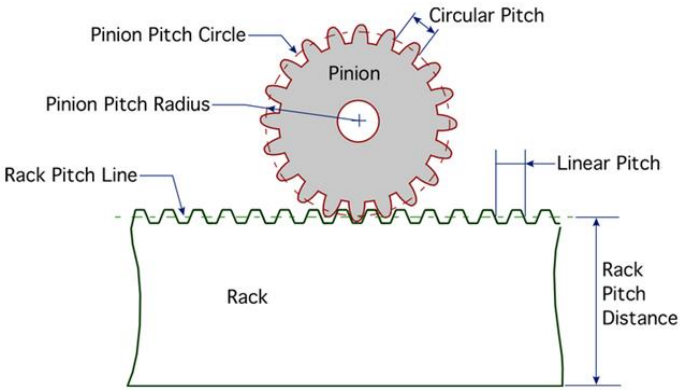

Figure 3.5: Rack and Pinion Drive Mechanism

Viability of rack and pinion systems are investigated from a mechanical standpoint, specifically relating to the forces, stresses, and power requirements needed for the 3d printer application. The system should be able to accelerate a 10 *kg* load up to 300 *mm/s* in the 'x' and 'y' linear directions with acceleration of $1 m/s^2$. Referring to the calculations performed in Appendix A.3., and selecting a generic module 3 C45 hardened indium rack with 16MnCr5 20 tooth pinion, the maximum allowable tangential force is:

$$F_{u\ zul,per.} = 4.05\ kN$$

With a safety factor for rack strength as:

$$n = 204.44$$

Additionally, the minimum system torque requirement may be derived from the tangential force, F_u, produced as:

$$T_{req.} = 0.1981\ N.m.$$

The torque design factor is given as:

$$n_m = 2.377$$

Power-screw and bearing drives

A power screw, also coined a lead-screw, is a cylindrical shaft with spiralled thread running along its longitudinal axis in a screw-like manner. The power-screw is conventionally attached at one end with a motor drive, which converts the rotational motion of the screw, into translational movement of the nut [6]. Three thread types, namely buttress, round and square profiles are available, with 90, 29, and 45 degree tooth angles respectively. Power screws are manufactured from low and high carbon steels, stainless steels, and aluminium alloys, with the threads being cold-rolled for higher accuracy than conventional cutting methods (Roton: 2009). Historically, lead-screws have been used predominantly in CNC and lathe applications due to their high repeatability and accuracy, but suffer with low overall acceleration values due to collar inertia. Additionally, due to the mating of threads between rod and collar, large frictional forces are present, resulting in a self-locking characteristic when not being rotated, unless of the screw is of the ball-screw variety, which contains ball bearings which rotate inside the collar threads, reducing the frictional coefficient and removing the self-locking property of the drive.

[6] – Leadscrew Nut: a collar with inside thread which screws onto a male power-screw; generally used to provide linear motion of objects attached to the collar.

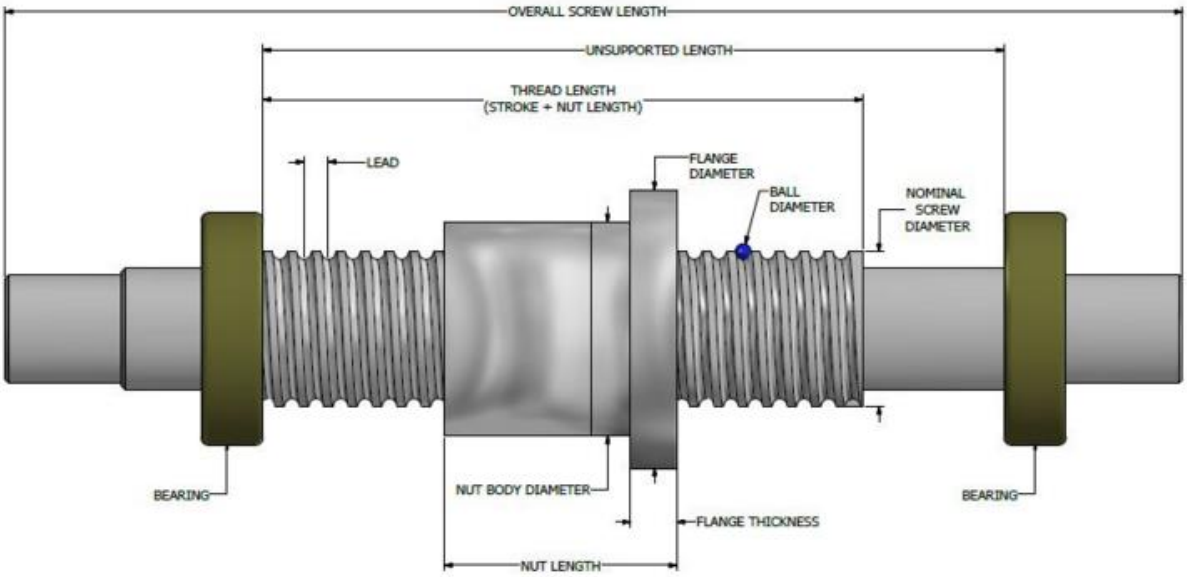

Figure 3.6: Power-Screw and Collar (Nut) General Layout

Referring to Appendix A.4, the viability of using a lead screw-nut combination is investigated thoroughly. Assuming that a TR8x82P2 lead screw and two NEMA17 60 *mm* stepper motors with 0.62 *N.m.* of torque are selected to drive each axis, the maximum weight that can be lifted was calculated as:

$$F_{lifting} \approx 38.36\,kg$$

Additionally, it was found that the maximum stress in the screw, namely the bearing stress is:

$$\sigma_b = 71.78\,MPa$$

This is significantly less than the yield strength of high carbon steel at approximately 470 *MPa.* Therefore from a physical analysis standpoint, the power-screw could be driven using the specified motors.

3.3.2. Comparison and selection of drive system

Careful analysis and scrutiny of the three drive methodologies needs to be undertaken in order for the design conceptualization process to commence. Particular selection bias is emphasized towards the accuracy and repeatability of the gantry assembly, as positioning performance of the print-head is essential to producing prints that are dimensionally accurate. Maximum travel of the drive system and cost are also of paramount importance since the required print volume is large at 12 m^3. Auxiliary performance metrics such maintenance, efficiency, and axial loading were given less weighting since the duty cycle, vizier, the operation schedule and durations thereof are sporadic and the loading scenario of the subassembly assumed to be under-stressed. The performance characteristics of each drive are summarized in Table 3.1.

Table 3.1: Order of Merits Table for Various 3D Printer Drive Train Options

Characteristic	**Weight (/1)**	**Drive Option Score (/5)**					
		Rack & Pinion		Power Screw & Rod		Timing Belt & Pulley	
Maximum Travel	**0.9**	unlimited spliced	**(4)**	3 *m*	**(1)**	unlimited	**(5)**
Accuracy	**1.0**	0.94 *mm/m*	**(3)**	0.2916 *mm/m*	**(4)**	1.04 *mm/m*	**(2)**
Repeatability	**1.0**	$2x10^{-4}$ *mm*	**(4)**	0.127 *mm*	**(3)**	0.508 *mm*	**(2)**
Linear Velocity	**0.5**	<7.3 *m/s*	**(5)**	<0.4 *m/s*	**(1)**	<5 *m/s*	**(5)**
Efficiency	**0.5**	98.5 %	**(5)**	45-90 %	**(2)**	<=95 %	**(5)**
Maintenance	**0.5**	Low (Gear Lubrication)	**(4)**	Medium (Thread & Bearing Wear)	**(3)**	Medium (Belt Tensioning/Replace	**(3)**
Axial Loading Capability	**0.3**	Very High (>4400 *kN*)	**(5)**	High (<3660 *N*)	**(4)**	Low (<440 *N*)	**(2)**
Price	**1.0**	+-ZAR 500	**(2)**	+-ZAR 3000/*m*	**(1)**	+-ZAR 60/*m*	**(5)**
Total:	(/27)		20		14		20.6
Rating (Out of 100):			74.07		51.85		**76.30**

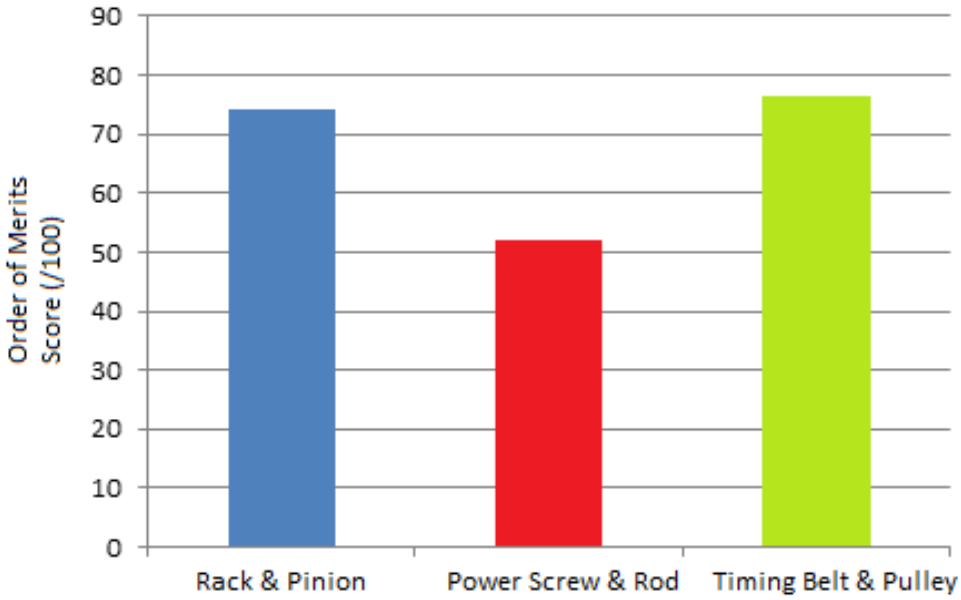

Figure 3.7: Order of Merits Graph for Selection of Printer Drive Train

Comparing the various attributes of each drive methodology, it can be noted from Table 3.1 that the accuracy level of solid machined mechanical assemblies, that is, the rack-pinion and power-screw drives, is very high at 0.94 *mm/m* and 0.2916 *mm/m* when compared with flexible timing belt at 1.04 *mm/m*. The higher accuracy levels nets these drives a higher merit score of 3 and 4 compared with 2 for timing belt. When analysing maximum travel lengths, it should be noted that power-screw rod is only available in lengths up to 3 *m*, critically restricting its application for axes with travel requirements surpassing this figure. The rack-pinion and timing belt may be spliced, or joined end-to-end, derestricting axis travel length, therefore these methods were allocated a score of 5 and the power-screw a score of 1. A critical limitation inherently imposed upon ball-screws and lead-screws is the phenomena of "screw-whip". Screw whip is defined as vibrations which develop at the critical rotational speed of the screw, that is, at the natural harmonic frequency of the solid, which is dependent on screw diameter and length (S. Mraz: May 6 2009). This phenomena, as well as the inherent inertial load of the rotating nut, limits power-screw linear velocity to less than 0.4 *m/s*, whereas rack-pinion and timing belt systems can tolerate much higher values up to 7.3 *m/s* (Wittenstein: 2016). These facts bias favour towards the timing belt and rack-pinion solutions, netting these options merit scores of 5. Furthermore, exorbitant prices of precision ball-screw and rack-pinion in the region of ZAR 3000/*m*, (Cncdirect: 2016) which is ultimately determined by machining costs, leads to the conclusion that timing belt is the best cost-effective drive solution, as evidenced by the highest merit rating or 76.30, albeit with a slight reduction in accuracy.

3.4. Print head

Two variations of FDM print heads exist which are each differentiated by the material being utilized, and the physical configuration thereof, whether filament reel or pellets. The first group of FDM extruders pulls a thin polymer wire into a heated Bowden tube via a gearing system, and melts the material for deposition on a flat surface, thereby building up an object layer by layer. The second group of extruder heads makes use of pellet, or pebble-like polymer beads which are fed into a screw-like assembly called an auger, which subsequently melts the material upon contact with a temperature controlled heated barrel subassembly. Both printing systems will be investigated thoroughly.

3.4.1. Filament extruding print head

The print head is a mechanical subassembly on a fused deposition modeller which performs the function of melting and ejecting material in a continuous stream. All extruders consist of the following critical components:

- Stepper motor & knurled gear – Attached to the motor shaft which catches the filament material and pushes it downwards towards the "hot end" subassembly.
- Hot end – An aluminium or brass funnel-nozzle system which melts and directs filament material downwards for deposition.
- 100 *K* thermistor – Attached to the hot end; used to measure temperature in degrees Celsius for hot end temperature control.
- Resistive heater – 40 *W* 12 *V* resistor cartridge which supplies heat up to 300 ^{O}C to the hot end.

Figure 3.8 details a generic filament extruder with all critical components.

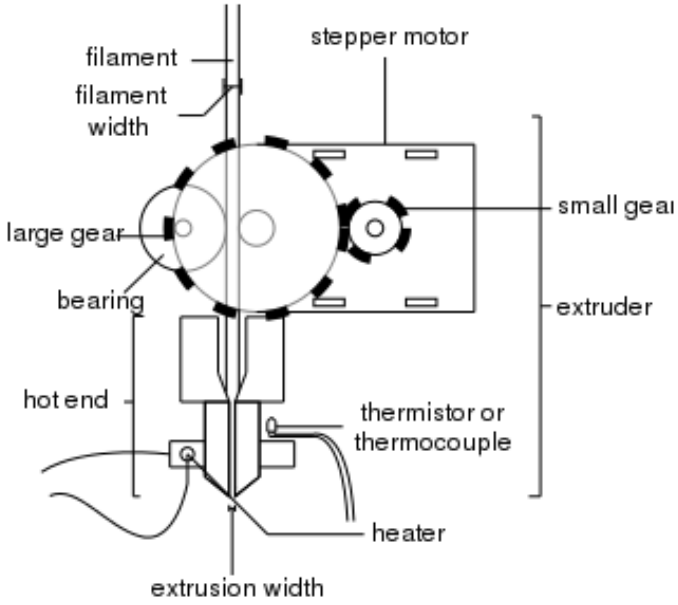

Figure 3.8: FDM Extruder Mechanical Sub-assembly

The rotation of the motor shaft with angular velocity ω rad.s^{-1} produces a linear movement of filament down into the heated section of the extruder. The linear velocity of filament, also known as the feed-rate, can be expressed as a function of the stepper motor speed as:

$$Feedrate_{Filament} = \frac{2\pi n_{motor}}{60} * r_{drive-gear} \tag{A7.2}$$

$$\approx 45\ mm/sec$$

Polylactic acid thermoplastic, commonly abbreviated as PLA, is selected as the printing material of choice over commonly-used Acrylonitrile Butadiene Styrene due its biodegradability being derived from starches, lower melting point of 180 ^{O}C compared to 210 ^{O}C, and does not warp or dimensionally-deform at the print-bed surface, compared with ABS (Chilson, L. 2013). Therefore, the required hot end temperature range is:

$$180^{O}C < T_{hot-end} < 200^{O}C$$

Additionally, it is known that the force required to push 1.75 *mm* thermoplastic filament through a hot-end heated to 190 ^{O}C is given by manufacturers, then the required stepper motor torque required to extrude various filaments is obtained via:

$$T_{motor,required} = F_{extrusion} r_{drive-gear} \tag{A7.3}$$

$$\approx 0.4\ N.m.$$

3.4.2. Pellet extruding print head

The second form of solid-liquid heated print-heads currently employed, particularly in large scale plastic processing, is the '*single-screw plasticising extruder*'. These extruders employ a feed hopper, auger screw drive, thermocouples, and heat channel, to facilitate the transport, melting, and extrusion of polymer granular pellets. These extruders consist of the following features:

- Feed hopper – Funnel shaped storage container which houses the plastic pellets prior to processing; pellets travel down into heating channel via gravitational action.
- Auger screw drive subassembly – A motor with auger screw characterised by a large thread pitch which facilitates transport of material between the screw threads.
- Melt conveying zone – The long cylindrical channel containing heating elements and thermocouples for temperature feedback and control; pellets are transported and melted in this region via the auger.
- Die exit – The end attachment unit or nozzle governing the thickness and shape of plastic extrudate [7].

Figure 3.9 illustrates a generic single-screw plasticising extruder upon which pellet print heads are based:

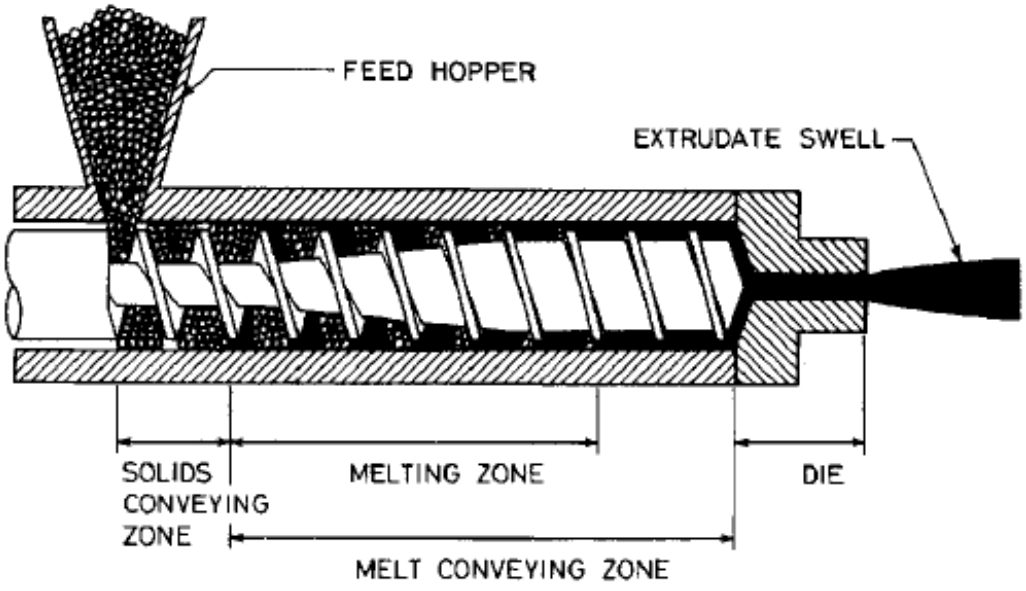

Figure 3.9: General Layout of Single Screw Plasticising Pellet Extruder

[7] – extrudate: material that has been extruded through a die. (https://en.wiktionary.org/wiki/extrudate)

The first four zones are mathematically modelled and explained in detail in Appendix A.8 with the relations for feed-hopper base distribution pressure, extruder barrel inter-particular pressure distribution, and the rate of polymer pellet melt at the hot end being given by:

$$p = p_o e^{\left(-\frac{4BDH}{W}\right)} + \frac{\rho_{bulk} g W}{4BD^*}\left[1 - e^{\left(-\frac{4BDH}{W}\right)}\right] \quad \text{(A8.1)}$$

$$p = \left(\frac{h_o}{H_o}\right)^{\psi} p_o + \frac{p_{bulk} g h_o}{\psi - 1} + \left[1 - \left(\frac{h_o}{H_o}\right)^{\psi - 1}\right] \quad \text{(A8.2)}$$

$$p = p_o e^{-\lambda z b} \quad \text{(A8.3)}$$

$$\omega = \Phi\left(\frac{dT}{dy}\right)_{y=0} X \quad \text{(A8.4)}$$

The above equations may prove useful for further testing and parameter verification in the Appendices.

3.4.3. Selection and development of print head

It was decided to commence with development of both a filament, as well as a pellet print-head assembly. The printer would first be calibrated and tested with the filament unit, and then the pellet extruder built and tested on the existing platform. The motivation therefore is that pellet material is 80 % more cost-effective than the filament option (M.McCracken: 2013). Additionally, pellet extruders have as yet, not been fully explored and integrated into 3D printer applications, which could produce useful research outputs and applications for future work. Lastly, the use of recycled plastics serves as an environmentally-friendly alternative to filament, reducing the carbon footprint.

3.5. Comparison and selection of electronic components

Having introduced the control and drive systems for a fused deposition modeller, it is required to analyse the control and electrical system on a component level, contrasting and comparing each peripheral so as to select components which will produce a machine with the desired performance characteristics.

3.5.1. Printer controller motherboard

Selection of the printer controller board is done first since all system peripherals are controlled by this component, and as such, need to be appropriately selected based upon the specifications of the motherboard. The controller board needs to at a minimum support the functions highlighted in the bulleted list in Section 3.2. Due to the emergence of the large open source RepRap DIY 3D printer community, a number of manufacturer's have started producing integrated 3d printer controller boards with capabilities such as 3-axis motion control, stepper motor interfacing and control, peripheral temperature control, and interfacing via universal serial bus and memory cards. Three controller board solutions are presented and their features and relative merit scores listed in Figure 3.10 and Table 3.2.

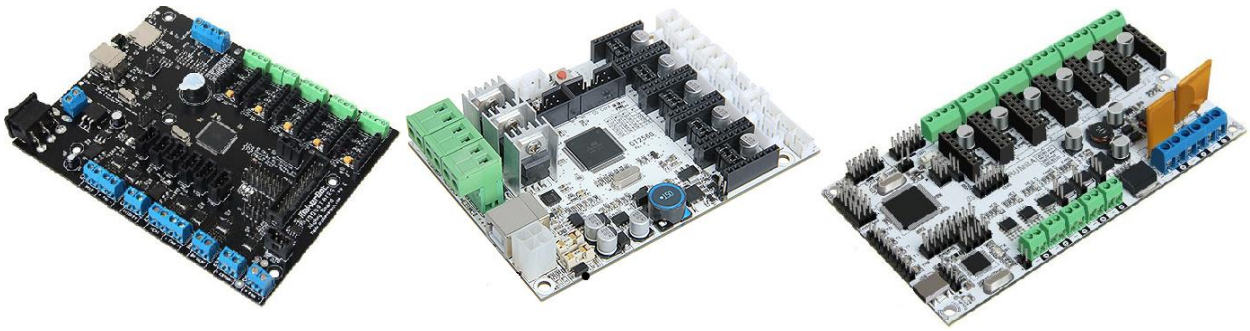

Figure 3.10: FDM System Motherboards (from left: MakerBot MightyBoard, GeeTech GT2560, and GeeTech Rumba

Table 3.2: Order of Merits Table for Various 3D Printer Controller Boards

Characteristic	**Weight (/1)**	**Controller Board Score (/5)**					
		MakerBot MightyBoard		GeeTech GT2560		GeeTech Rumba	
Power Input	**0.5**	12 – 24 *VDC*	**(3.5)**	12 – 24 *VDC*	**(3.5)**	12 – 35 *VDC*	**(5)**
Processor	**0.7**	Atmega 1280	**(2.5)**	Atmega 2560	**(2.5)**	Atmega 2560	**(5)**
Temp. Sensors	**0.7**	3x	**(3)**	3x	**(3)**	5x	**(5)**
Reset Button	**0.3**	Yes	**(5)**	Yes	**(5)**	No	**(2.5)**
Motor Driver Slots	**1.0**	5x	**(4)**	5x	**(4)**	6x	**(5)**
TF Card Slot	**0.5**	Yes	**(5)**	No, Exp.	**(3)**	No, Exp.	**(3)**
On/Off Switch	**0.3**	Yes	**(5)**	No	**(2.5)**	No	**(2.5)**
Display	**0.5**	LCD2004	**(2.5)**	LCD2004, LCD12864	**(5)**	LCD2004, LCD12864	**(5)**
Price	**0.8**	+-ZAR 2639	**(1.5)**	+-ZAR 1123	**(5)**	+-ZAR 1385	**(4.5)**
Total:	(/26.5)		17.55		19.85		23.6
Rating (Out of 100):			66.23		74.90		**89.05**

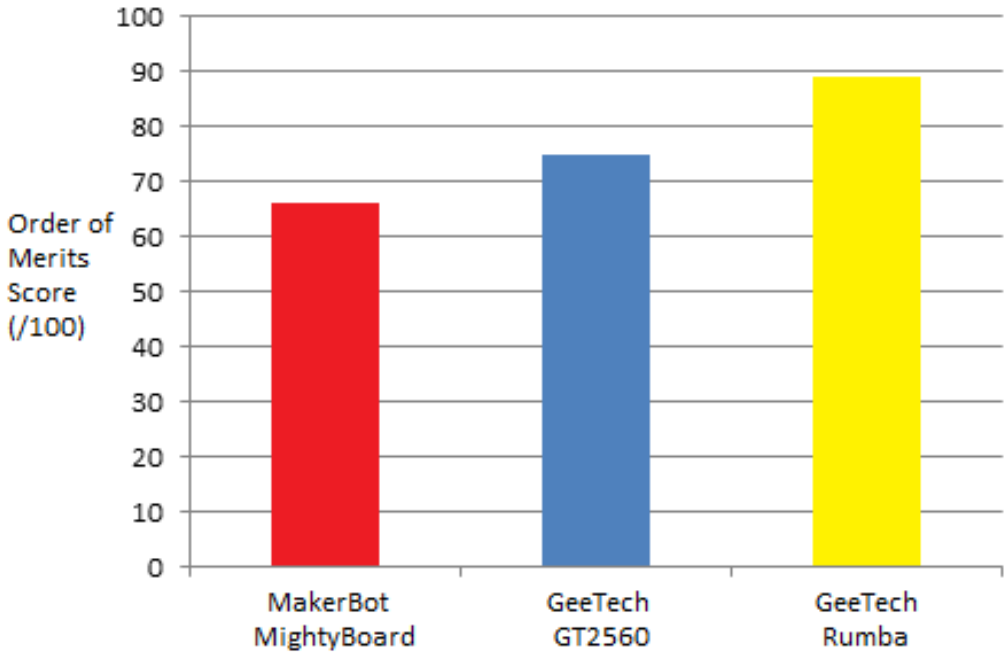

Figure 3.11: Order of Merits Graph for Selection of Printer Controller IC Board

Selection criterion for the controller board is based upon the need for a central processing unit which is able to adequately handle and process print G-code, as well as a board with as many motor driver outputs as possible. The reason thereof is so that should the need for extra axes drive motors arise, there are adequate outputs to facilitate such a design implementation. Other board features, namely the on/off switches and card slot are not of great importance, achieving a weighting of 0.3 and 0.5 respectively, since these features do not affect machine print performance. Due to the MakerBot Mightyboard's high cost of approximately ZAR 2639, the lower number of stepper drivers, and out-dated Atmega 1280 processor with only 128 *kB* of CPU cache, this product was considered underpowered for the application, evidently reflected in the final merit score of 66.23. The GeeeTech GT2560 and Rumba were evenly matched with regards to the price-point, but the Rumba is selected for further system development over the GT2560 due to the impressive number of stepper drivers, temperature measurement slots, and broader 12 *V* to 35 *V* input operating range.

3.5.2. Motor driver breakout board

As indicated in Figure 3.3, each stepper motor requires a motor driver board in order to operate. The reasons for the addition of these peripheral boards on the main controller board are three-fold. Firstly the board brings functionality via stepping up the supply voltage from 2.5 to 5.25 *V* on the motherboard side, to a maximum of 45 *V* at the stepper motor terminals. The driver board essentially acts as a power amplifier and transformer, by converting a high amperage low voltage supply current into a high voltage low amperage motor supply. Secondly, the board provides micro-stepping capability, whereby variation of current-sensing resistor values alters pole energisation, which results in minute movements, up to 1/32th of a step, of the motor shaft (Pololu.com: 2016). Thirdly, the driver board allows for direction and speed change of the motor, via varying the input current to the rotor coils from 0 *A* up to a maximum

value as specified and direction change via pole energisation manipulation. Three compatible driver boards were analysed and contrasted for the printer application in Table 3.3.

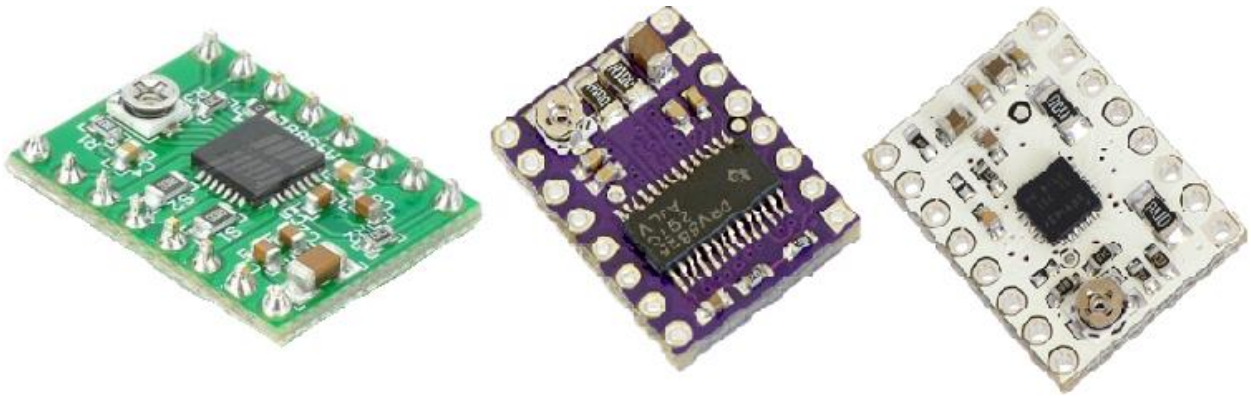

Figure 3.12: Stepper Motor Controllers (from left: Pololu A4988, DRV8825 and DRV8834)

Table 3.3: Order of Merits Table for Various 3D Printer Stepper Motor Driver Boards

Characteristic	**Weight (/1)**	**Driver Board Score (/5)**					
		Pololu A4988		Pololu DRV8825		Pololu DRV8834	
Output Voltage	**0.5**	3 – 5.5 *V*	**(3.5)**	2.5 - 5.25 *V*	**(4)**	2.5 – 5.5 *V*	**(4.5)**
Step Resolution	**0.7**	1/16 Step	**(3)**	1/32 Step	**(5)**	1/32 Step	**(5)**
Peak Amp Output	**0.9**	2 *A*	**(3)**	2.2 *A*	**(4)**	2 *A*	**(3)**
Input Voltage	**0.5**	8 V – 35 *V*	**(3.5)**	8.2 *V* – 45 *V*	**(5)**	2.5 *V* – 10.8 *V*	**(2.5)**
Continuous Current	**1.0**	1 *A*	**(3.5)**	1.5 *A*	**(4)**	1.5 *A*	**(4)**
Price	**0.8**	+-ZAR 89	**(5)**	+-ZAR 120	**(4)**	+-ZAR 140	**(3)**
Total:	(/22)		15.80		18.80		16.10
Rating (Out of 100):			71.81		**85.45**		73.18

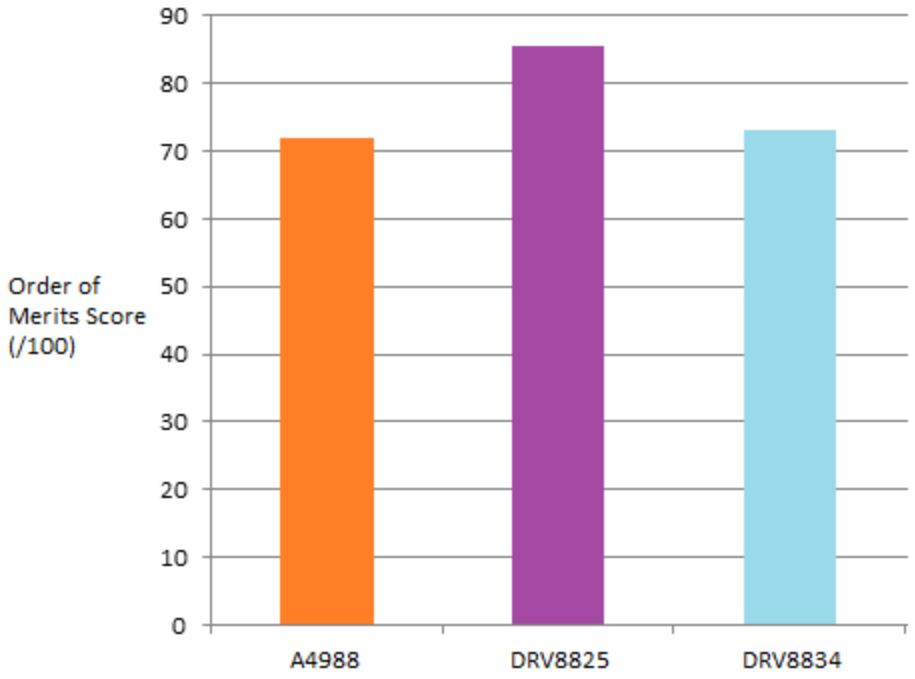

Figure 3.13: Order of Merits Graph for Selection of Printer Motor Driver Board

The main criterion of driver board selection was that the board has to be able to supply a large current to the motors over a wide voltage range, thereby resulting in a high torque being produced in the motors. A high load-moving capacity results in quicker acceleration of the print-head during operation, therefore "*peak amp output*" and "*continuous current*" were weighted at 0.9 and 1.0 respectively. Operating voltages are less important due to the large voltage range of roughly 30 *V* which all the boards operate over. As demonstrated in Table 3.3, the DRV8825 achieved the highest merit score as a result of its high 1/32 step resolution, high continuous current rating of 1.5 *A*, and the largest input voltage range of 36.8 *V* nominal. The Pololu DRV8825 was therefore selected for further product development.

3.5.3. End stops

Three-axis gantry-format machines, that is, machines which are able move a centralized work-head in three directions, require a home position to reference their movements from. This home position, also known as a datum, is achieved via the implementation of end-stops in the system. End stops, referred to as limit switches, are sensors or switches which stop the gantry work-head from moving out of the intended workspace of the machine, which could result in damage to the assembly. Three end stop variations are investigated and contrasted, namely, mechanical, optical, and Hall Effect sensors. Mechanical end-stops are 2-terminal on/off switches whereby if the switch is triggered by making physical contact a moving printer axis, the state of the signal changes, signalling the software to stop movement of the gantry. Optical sensors consist of a transmitter LED and receiver which sense the level of UV light in the immediate area. Should the moving axis in question move adequately close to the sensor, the emitted UV light is reflected off the axis surface and back into the sensor's UV receiver, thereby signalling the printer to cease motion. Finally, magnetic Hall-effect sensors employ a transducer which converts a magnetic field into a proportional voltage in the circuitry. In 3-axis assemblies, a magnet

is attached to the moving axis, which when appropriately close to the sensor, signals the controller to cease motion of the system. Having explained the operation of each, they are contrasted:

Figure 3.14: End-Stop Variations (from left: mechanical, optical, and magnetic)

Table 3.4: Order of Merits Table for Various Limit Switches

Characteristic	**Weight (/1)**	**Limit Switch Score (/5)**					
		Mechanical		Optical		Magnetic	
Electrical Damage Risk	**0.7**	None	**(5)**	Medium	**(3)**	Medium	**(3)**
Programming Complexity	**0.9**	None	**(5)**	Medium	**(3)**	High	**(1)**
UV Interference	**0.7**	None	**(5)**	High	**(1)**	None	**(5)**
Magnetic Interference	**0.7**	None	**(5)**	None	**(5)**	High	**(1)**
Mechanical Damage	**0.5**	Yes, possible.	**(2)**	None	**(5)**	None	**(5)**
Electrical Interference	**0.7**	None	**(5)**	Medium	**(2.5)**	Medium	**(2.5)**
Reliability	**0.5**	18’000 switches	**(2.5)**	50’000 sw.	**(3)**	100’000 sw.	**(5)**
Repeatability	**0.8**	100 %	**(5)**	<0.04 *mm*	**(4)**	>0.05 *mm*	**(4)**
Price	**0.3**	+-ZAR 26	**(5)**	+-ZAR 80	**(4)**	+-ZAR120	**(3)**
Total:	(/29)		26.25		19.15		18.05
Rating (Out of 100):			**90.52**		66.03		62.24

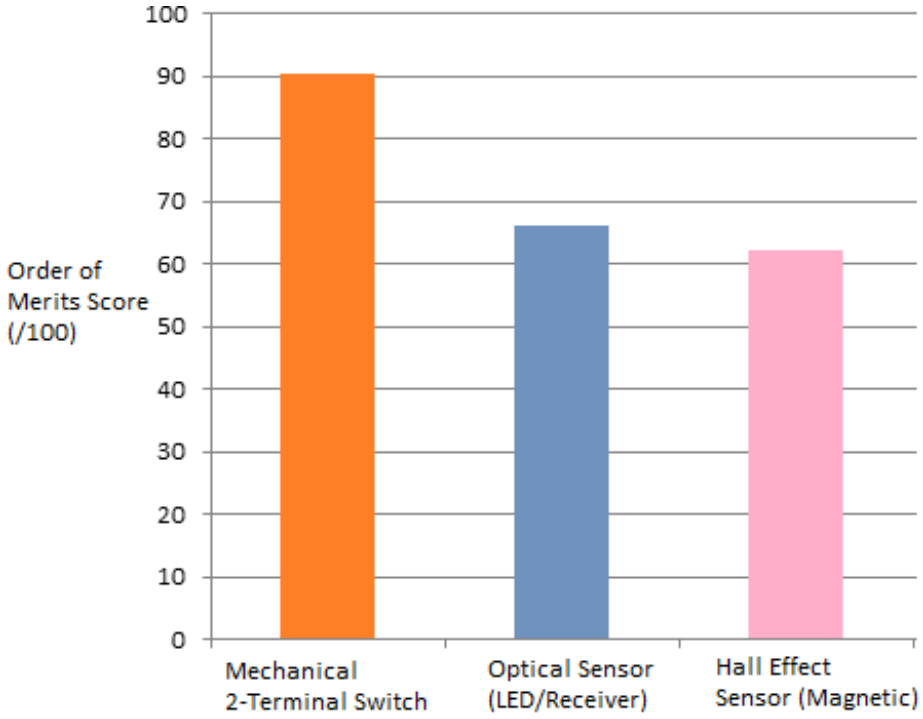

Figure 3.15: Order of Merits Graph for Selection of Printer End-Stops

Both optical and Hall Effect end-stops are susceptible to significant electrical, UV, and magnetic disturbance. This which may affect proximity sensing, resulting in misreads of the axes endpoints, whereas mechanical limit switches are simple on-off devices, with a 100 % possibility of endpoint detection. The uncertainty of operation accuracy surrounding the optical and magnetic sensor garnered lower scores of 1 in the "Interference" attributes. With regards to price, mechanical units are significantly cheaper due to reduced complexity, at approximately ZAR 26 compared to ZAR 80 to 120 for the latter, resulting in a score of 5 for price for the mechanical switch, and 4/3 respectively for the latter. Additionally, it should be noted that since the mechanical switches are being physically contacted, deformation of the metal read switch does occur over time, limiting the lifetime of the sensor to roughly 18'000 contacts, whereas with optical and magnetic sensors, lifetime is much improved to due non-contact, but is limited by system overvoltage and power spikes. Noting the above advantages and drawbacks, the mechanical switch netted the highest score of 90.52 due to the anti-interference properties, simple operation, no need for programming, and low cost, and is therefore selected for further system development.

3.5.4. Stepper motors

Following selection of the motor driver board in section, it becomes necessary to select motors based upon the electrical specifications of said Pololu DRV8825 driver board. A stepper motor is by definition a brushless direct current electric motor with multiple electromagnets distributed on the inner surface of the motor frame (B.G. Liptak: 2005, p. 2462). The electromagnets are individually energized by the Pololu driver board, causing an attraction and subsequent rotation of the inner iron rotor mechanism, thereby turning the motor shaft. The basic motor requirements according to the driver board are as follows:

- Motor format: bipolar DC stepper motor with 1/16 or 1/32 micro-stepping.
- Stepper motor operating voltage: 2.5 *V* – 5.25 *V* DC.
- Peak motor amperage per coil: 2.2 *A* maximum.
- Continuous motor amperage per coil: 1.5 *A* maximum.

A typical stepper motor is illustrated in Figure 3.16, with more detail available in Appendix D.

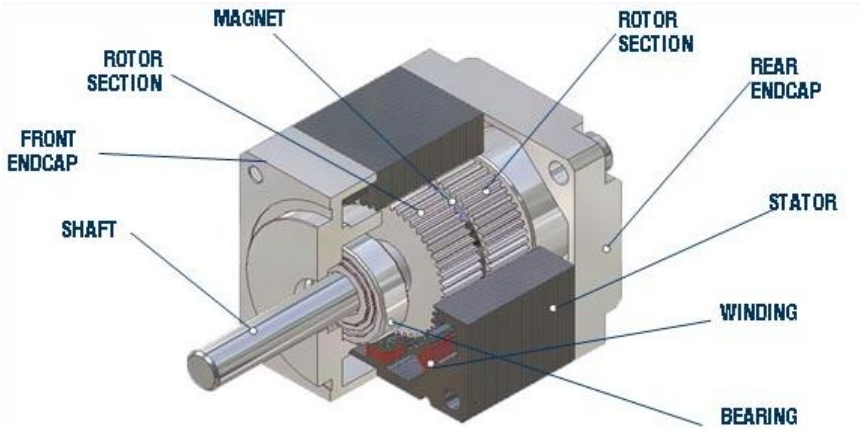

Figure 3.16: NEMA17 Bipolar Stepper Motor

The following motors as illustrated in Table 3.5 are suitable for the application:

Table 3.5: Suitable Stepper Motors for FDM Printer Design Application

Characteristic	**NEMA 17-34 *mm*/2.1**	**NEMA 17-48 *mm*/4.2**	**NEMA 17-48 *mm*/4.8**
Step Angle (^{O})	1.8	0.9	0.9
Motor Length (*mm*)	34	48	48
Rated Voltage (*V*)	12	2.7	2.4
Rated Current (*A*)	0.4	1.68	2.4
Phase Resistance (Ω)	30	1.6	1.0
Phase Inductance (*mH*)	37	3.5	1.8
Holding Torque (*N.m.*)	0.255	0.41	0.47
Rotor Inertia (g/cm^3)	34	68	68
Detent Torque (*N.m.*)	0.02	0.025	0.025
Weight (*kg*)	0.2	0.36	0.36
Price (ZAR)	≈ 242	≈ 265	≈ 320

3.6. Software

Additive manufacturing platforms, being practically identical from a control and physical standpoint when compared with CNC-based platforms, similarly make use of G-code as a software control language medium. G-code is a computer programming language and command system most commonly used in applications where the control of 3 to 6-axis tool-paths, as well as auxiliary machinery is desired (Lynch, M.: 2010). G-code may perform a host of system functions, but in the 3D printer context, controls the movement of the 3-axis gantry and operation of the printer head subsystem. The printer operation and software integration begins with the design of a CAD model in CATIA V6, which will eventually be printed. The CAD model is saved as a .STL file which describes only the surface geometry of the part to be printed (Stereolithography Interface Specification, 3D Systems Inc.: July 1988). Thereafter, the file is inputted into the slicer software Skeinforge, which dissects the model into a number of horizontal cross-sections roughly 0.5 *mm* in thickness. The G-code path for printing is produced, and subsequently edited and fine-tuned with a number other commands to ensure smooth operation of the printer. Finally, the G-code is uploaded on an SD card, and placed in the GeeeTech LCD card reader, and the printing operation started. The software and information flow diagram for the printer is shown.

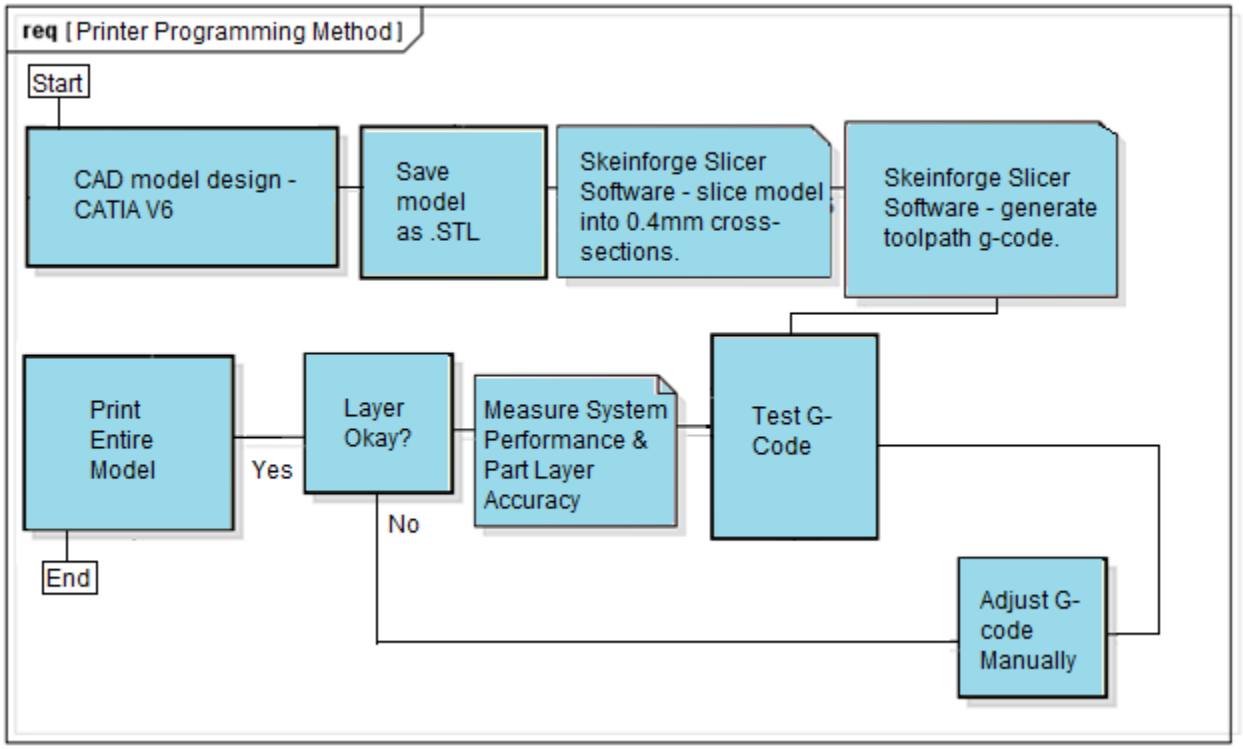

Figure 3.17: Software Process Flow Diagram

G-code is presented in single command lines with bold letter and double number types. For instance, first setting the printer gantry speed, or federate to 1700 *mm/min*, then moving the printer x-axis to the 60.7 *mm* location, y-axis to 6.7 *mm* location, while extruding 30.1 *mm* of filament, the G-code representation may be expressed as:

$$G1\ F1700$$

$$G1\ X60.7\ Y6.7\ E30.1$$

A basic explanation of all possible G-code commands and their functions are given in the Table 3.6.

Table 3.6: 3D Printer G-Code Syntax Explanations

Command Type	**Description**	**Example**
Dxxx	Filament diameter setting	D3: 3 *mm* Filament selected
Exxx	Length of filament available on reel	E10: Extrude 10 *mm* material
Fxxx	Print-head velocity (millimetre per minute)	F1200: Feed-rate 1200 *mm/m*
Gxxx	Standard movement command	G0/G1: Rapid linear move
Hxxx	Heater temperature setting (PID controlled)	H60: Heater bed at 60 ^{O}C
Ixxx	Gantry x-offset value, PID K_i constant setting	I20: Tool home position +20 *mm*
Jxxx	Gantry y-offset value	J20: Tool home position +20 *mm*
Mxxx	Electrical peripheral on/off command	M0: Machine E-stop
Nxxx	Line number for command/code	N21: 21st line of code
Pxxx	Set time parameter, PID K_P constant setting	P1: Tool number 1
Rxxx	extruder hot end standby temperature	R120: standby temp at 120 ^{O}C
Sxxx	extruder hot end temperature setting	S230: active temp at 230 ^{O}C
Txxx	Select tool and nozzle command	T1: Select first tool saved settings
Xxxx	Move to x-coordinate	X50: Move x = 50 *mm* position
Yxxx	Move to y-coordinate	Y20: Move y = 20 *mm* position
Zxxx	Move to z-coordinate	Z20: Move to z = 20 *mm* position
*xxx	Check for communication error	*10: Check line 10 for errors.

3.7. Chapter conclusion

This chapter presented the initial framework for development of the selected full printer system concept, by analysing a fused deposition modeller on the component level. This was achieved by first modelling the control system and system component hierarchy, and amalgamating FDM components such as motors, controller boards, limit sensors, and the like. Each component was investigated, all possible options for said component compared and contrasted, and the best options selected. The components are to be implemented into working printer designs in Chapter 4.

CHAPTER 4

Design Generation and Selection

This chapter shall detail the conceptualization, design, and feasibility analysis of three additive manufacturing platform solutions. The concepts will be scrutinized in detail, particularly with regards to operational function, printing process actualisation, feasibility, cost, as well as finite elemental analyses of the concepts, and a printer configuration will be selected for further analysis and product development.

4.1. Multiple zoned filament-based printer

The first additive manufacturing platform solution is a horizontal flat-bed printer with multiple printing zones. The operation, physical attributes, and print-head are described below.

4.1.1. Operation

Process cycle time optimization is the main goal of this concept. Five 1 *m* by 2 *m* print zones are allocated, with each zone printing a unique cross-section of the chosen part to be produced. The design incorporates five identical gantry systems as highlighted in Figure 4.1, which allow movement of each print-head in three directions. Additionally the system is to be controlled via five sets of identical controllers and electronics, whereby the desired part to be produced is cut into five sections, and G-Code produced for each controller. The data is then loaded into each controller, and the part is built up, reducing product cycle time five-fold.

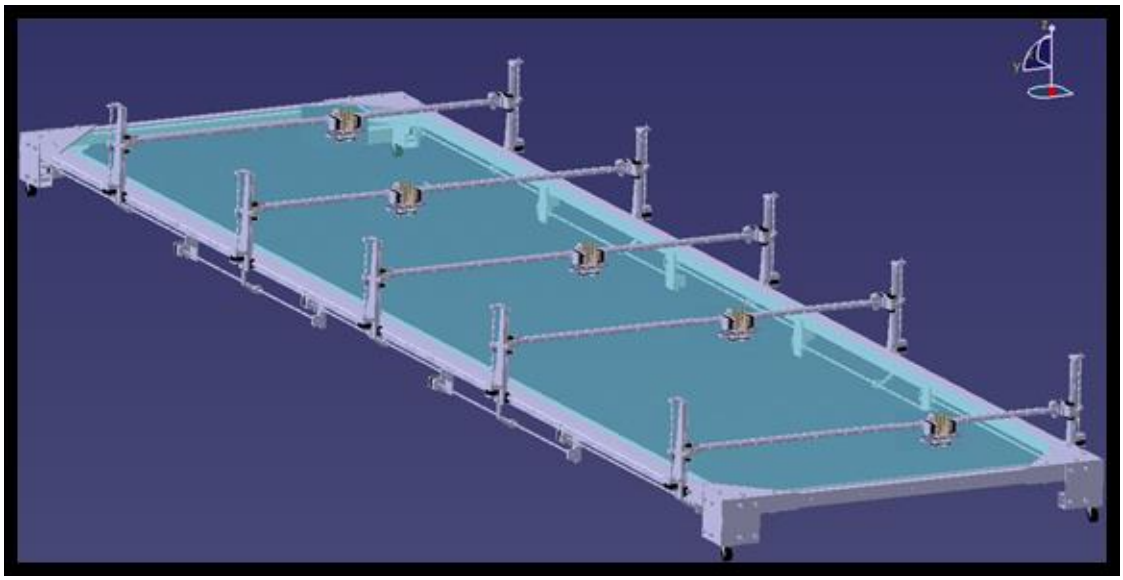

Figure 4.1: Multiple-Zoned Filament 3D Printer Concept: Isometric View

4.1.2. Physical layout

The physical layout of the system consists of a 5.3 *m* by 2 *m* rectangular frame constructed of 60 mm^2 aluminium extrusions, with five 2 *m* by 1 *m* plain untreated glass panes making up the print-bed surface. The frame is squared, oriented, and fastened using 6mm thick aluminium gusset plating and anodized M10 cap-screw fasteners. An innovative feature of the design, as indicated in Figure 4.2, is the incorporation of overlapping y-axis print zones, allowing for more robust printing capabilities. Axes are driven using a combination of 12 *mm* SKF ball-screw, NEMA17 stepper motors, and linear guide railing assemblies, giving the printer an effective print envelope of 10 m^2.

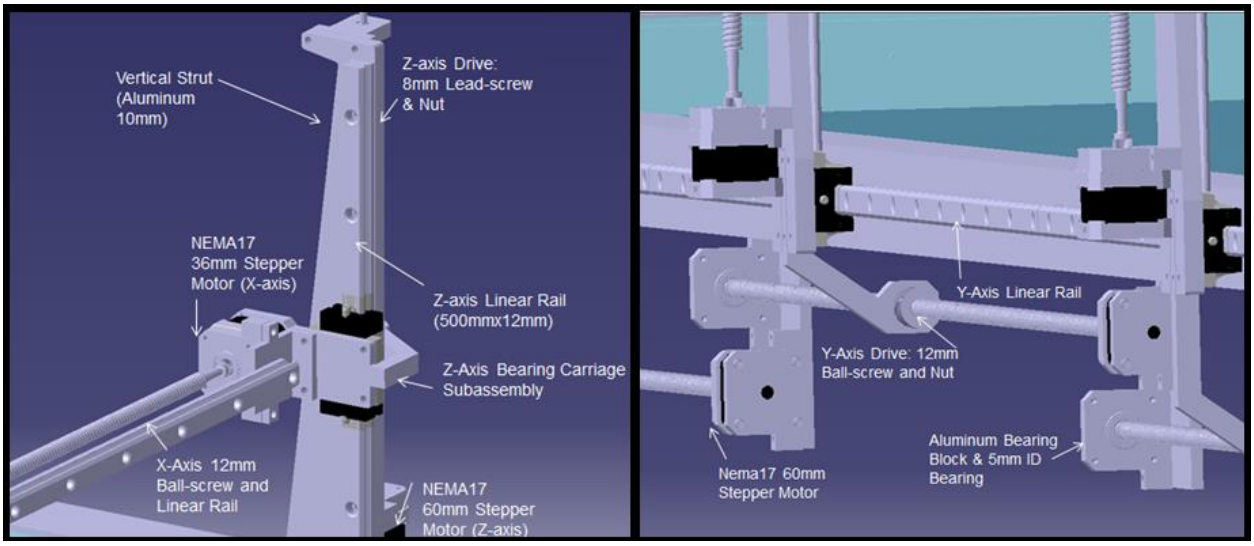

Figure 4.2: Multiple-Zoned Filament 3D Printer Concept: X and Z Axes

The initial specifications for the printer as given in Table 4.1:

Table 4.1: Multiple-Zone Filament Printer Attributes

Characteristic	**Value**	**Description**
Dimensions	6 *m* x 2 *m* x 1 *m*	Length x width x height.
Weight	+-200 *kg*	Total assembly weight.
Motors	Stepper Motors	NEMA17 48 *mm* 0.5 *N.m.* bipolar DC.
Drive	Ball-screw & Nut	SKF SH12 Mini Screw & 12 *mm* rod.
Axes	Linear Guide & Carriage	Hiwin MG12 rails/carriages.
Print Material Type	Filament	1.75 *mm* PLA thermoplastic filament.
Frame Material	Aluminium Extrusions	Bosch Rexroth Profile ALU. Series
Fasteners	Bolts, Nuts, T-Nuts	Black anodized Allen head caps crews.

4.1.3. Print head

The first print-head design makes use of two stepper motors, filament extruder cold ends, and heated material 'hot-ends' and associated mounting brackets and material cooling fans as illustrated in Figure 4.3. 1.75 *mm* thermoplastic filament material, usually PLA or ABS, is pulled into the cold end via a knurled gear attached to the rotating stepper motor shaft. The filament enters the hot-end top feeder hole, and is pushed down into the heater block region, where it is melted by a 12 *V* 40 *W* resistive cartridge heater element. Hot end temperature is maintained in the region of 190 to 240 ^{O}C, with feedback being sent to the 12 *V* DC cooling fans to solidify the extrudate (O. Martin, L. Averous.:2001, p.14).

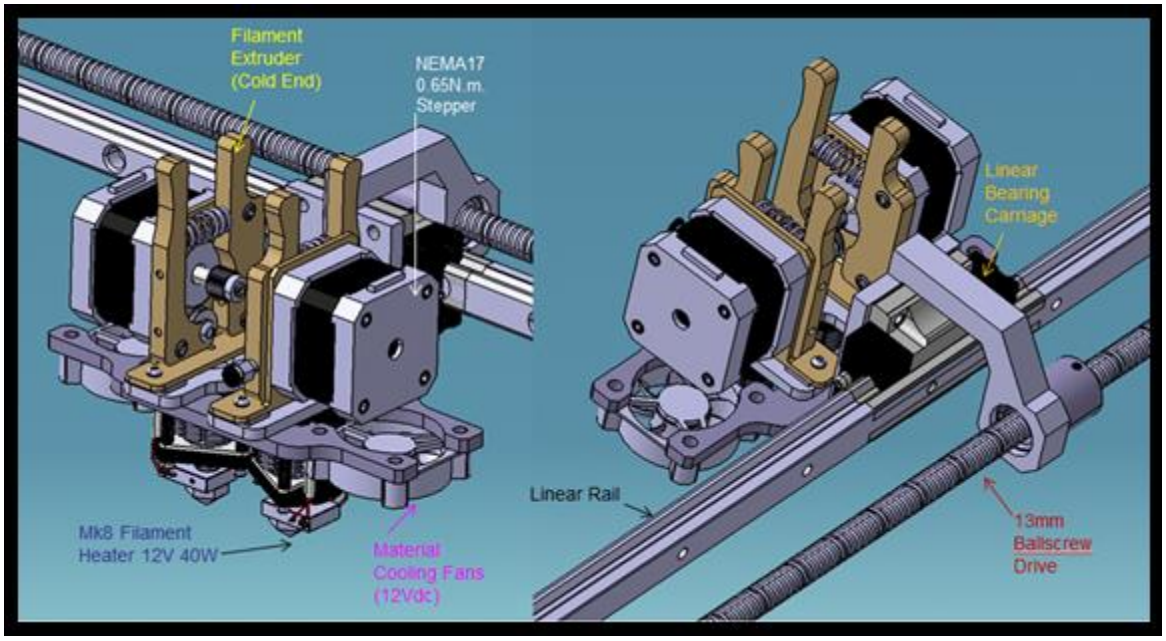

Figure 4.3: Multiple-Zoned 3D Printer Concept: Print Head

The perceived initial advantages and drawbacks for Design I are as follows:

Table 4.2: Expected Advantages and Disadvantages for Multi-Zone Filament 3D Printer

Expected Advantage	Expected Disadvantage
Print time increased five-fold due to five print-heads and zones working simultaneously.	Cost for the gantry (x,z) axis increases five-fold due to five sets of print assemblies.
Fast print-head and gantry dynamical response due to low inertia of gantry.	Possible loss of accuracy along z-axis (long axis) – increase in sum of errors over distance.
Filament extrusion methods are proven technology; relatively easy to calibrate print-head.	Synchronization of multiple print-heads is difficult with separate controllers for each print-zone: possible gantry collisions.

4.2. Pellet-based vertical 3D printer

The second additive manufacturing platform concept is based on a vertical design which prints upwards.

4.2.1. Operation

This second printer concept prints the object by laying down material of each cross-section layer by layer, producing the blade plug in an upright position. In most printing scenarios, the print head makes a number of start-stop operations, decelerating and accelerating the gantry when reaching object vertices and profile perimeters. Printing the plug vertically could reduce print time since the print-head motion is able to follow a circular print-path, due to the blade's naturally oval profile, reducing stop-start movements due to constant arcing circular motions of the gantry.

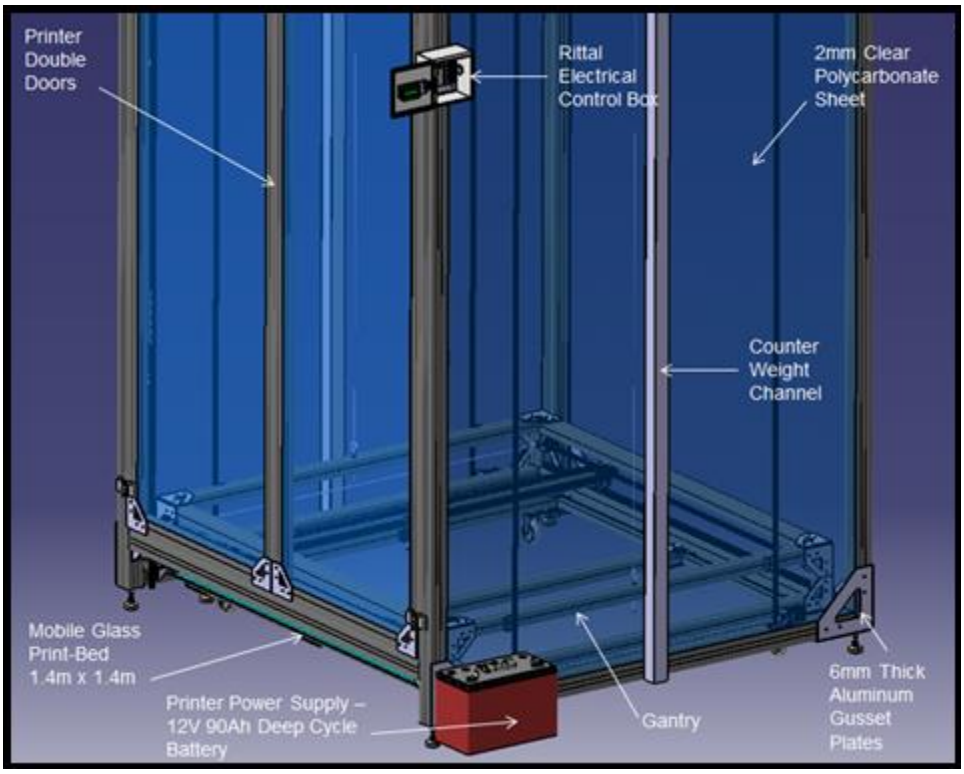

Figure 4.4: Vertical Pellet-Based 3D Printer Platform: Isometric View

4.2.2. Physical layout

Regarding the physical configuration and attributes of the concept, the printer is set up as a three-axis gantry system with a 1.5 *m* by 1.5 *m* by 5 *m* print envelope. The frame is constructed of 60 by 60 *mm* aluminium extrusions for rigidity and transportability due to lower weight than steel. Additionally, the outer frame is braced with 25 by 25 *mm* hollow extrusions in the form of crossbeams, which increase frame stiffness, and assist in the correct squaring of the frame, that is, ascertaining that the outer cross-members are perfectly perpendicular. Referring to Figure 4.6, it can be noted that the square gantry system runs on four 16 *mm* stainless steel round tubing and 16 *mm*

round profile aluminium slides on each corner. Furthermore, the 'x' and 'y' directions are driven by T2.5 6 *mm* steel-embedded polyurethane timing belts, 16-tooth T2.5 aluminium pulleys, and NEMA17 48 *mm* 0.5 *N.m.* stepper motors, and are axially located and run along 12mm stainless steel square-profile linear guides and carriages. The print-bed is a 1.4 m^2 5 *mm* thick plain untreated glass pane, supported by an aluminium square frame, which is removable from the printer assembly once the print is completed, while cable management is achieved using plastic drag-chain and aluminium channels. Relative positioning and locating of the axes and print-head are achieved via the use of 2-terminal micro-switches and spring-bracket end-stops, which define printer work area limits.

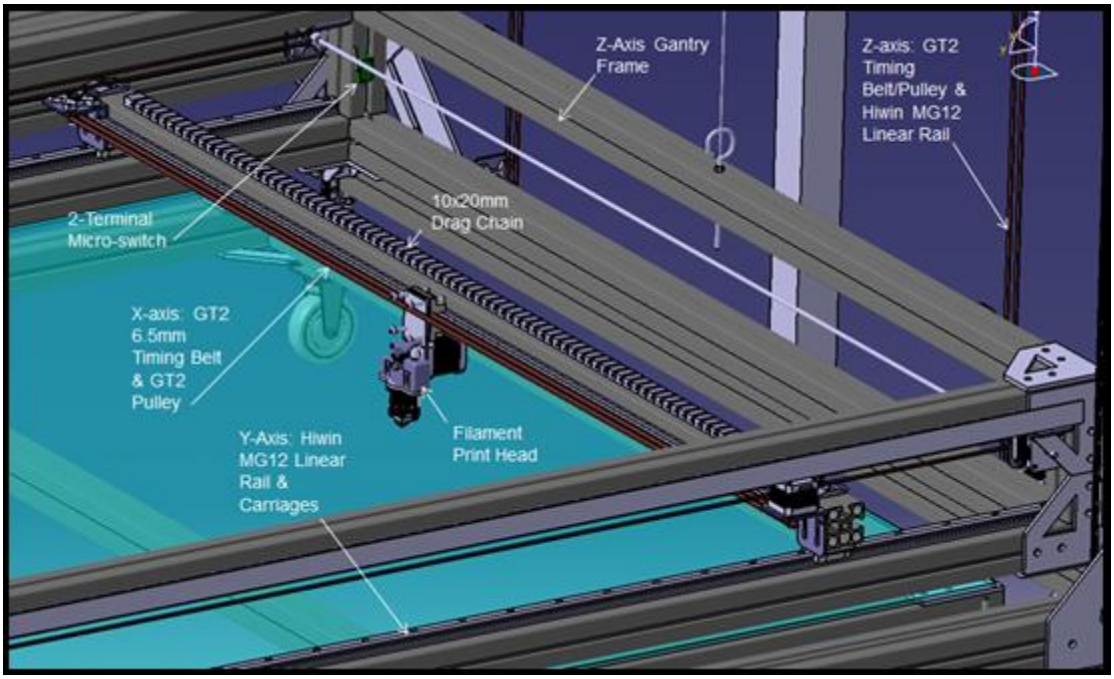

Figure 4.5: Vertical Pellet-Based 3D Printer Platform: Gantry View

Table 4.3: Vertical Pellet Extruder Printer Attributes

Characteristic	Value	Description
Height	5.3 *m* x 1.6 *m* x 1.6 *m*	Height x length x width.
Weight	+-250 *kg*	Total assembly weight.
Motors	Stepper Motors	NEMA17 48 *mm* 0.5 *N.m.* Bipolar DC
Drive	Timing Belt & Pulley	Alum. T2.5 16T Pulley, T2.5 6 *mm* Belt
Axes	Linear Guide & Carriage	Hiwin MG12 and MG12R rails/carriages
Print Material Type	Pellet	2 *mm* PLA thermoplastic recycled pellet
Frame Material	Aluminium Extrusions	Bosch Rexroth Profile ALU. Series
Fasteners	Bolts, Nuts, T-Nuts	Black anodized Allen head cap screws.

4.2.3. Print head

The second concept incorporates a print-head designed specifically to extrude, melt and print pellet-like thermoplastic material. Initially, the pellets are fed through the M22 feeder tube via gravity, as illustrated in Figure 4.6. The pellets are housed in a polycarbonate chamber, which are subsequently pulled down into the aluminium hot end channel by the rotating auger bit. The auger bit is rotated using a timing belt pulley torque increasing system attached to a powerful 60 *mm* NEMA17 stepper motor as shown. As the pellets are pushed down the aluminium channel via the rotational frictional action of the bit, the material is melted at the aluminium heater block interface via a 40 *W* 12 *V* resistive cartridge heater seated in the block. The temperature is maintained at a nominal 210 ^{O}C via a NTC 100K thermistor monitoring the block temperature. Should the temperature exceed or fall below the set point, resistive current is increased, or the 12 *V DC* fan is activated and speed controlled via PWM [3].

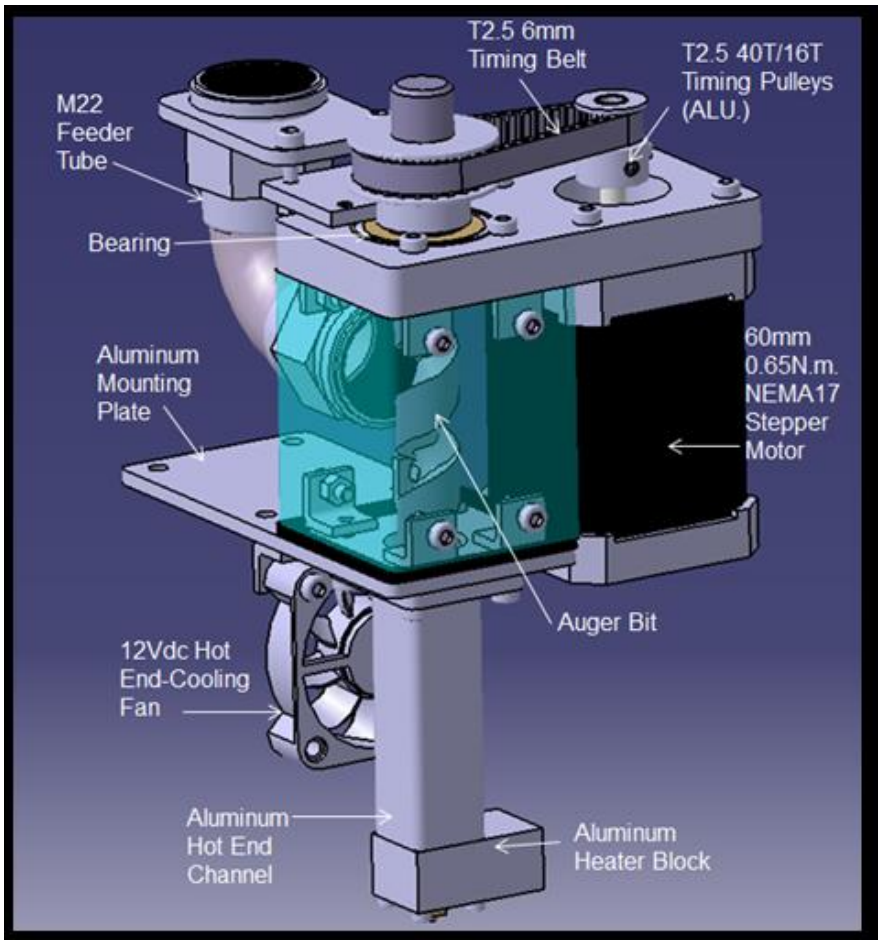

Figure 4.6: Vertical Pellet-Based 3D Printer Platform: Print Head

[3] pulse width modulation – a pulsing technique use to control amount of power sent to device. (A Schonung, H. Stemmler: 1964)

Table 4.4: Expected Advantages and Disadvantages for Vertical Pellet-Based 3D Printer

Expected Advantage	Expected Disadvantage
Printing material cost savings up to 70%	New extruder technology, testing and fine-tuning development stages extensive.
Decreased plug print time due to circular printing path taken. Improve cycle time.	Stability issues when gantry at the highest Position during printing. Possible oscillation. Possible belt stretch or misalignment of gantry in z-direction due to long belt length.

4.3. Horizontal CNC-FDM hybrid 3D printer

The final printer concept exhibits a print-head with both routing as well as printing capabilities, and makes use of the flat print-bed surface configuration similar to that of Concept I.

4.3.1. Operation

Concept III operates as a dual purpose hybrid 3-axis routing and finishing machine. A polystyrene, resin, or plastic rectangular block is placed on the print-bed. Thereafter, the CNC-chuck is activated, rotating at high rpm figures up to 3000 *rev/min*. A tool path is programmed into the controller, and the machine goes about routing out the profile of the turbine blade plug within the mould. Thereafter, another set of G-code is inputted into the controller, and a thermoplastic or composite molten fluid extruded onto the surface of the newly-routed profile.

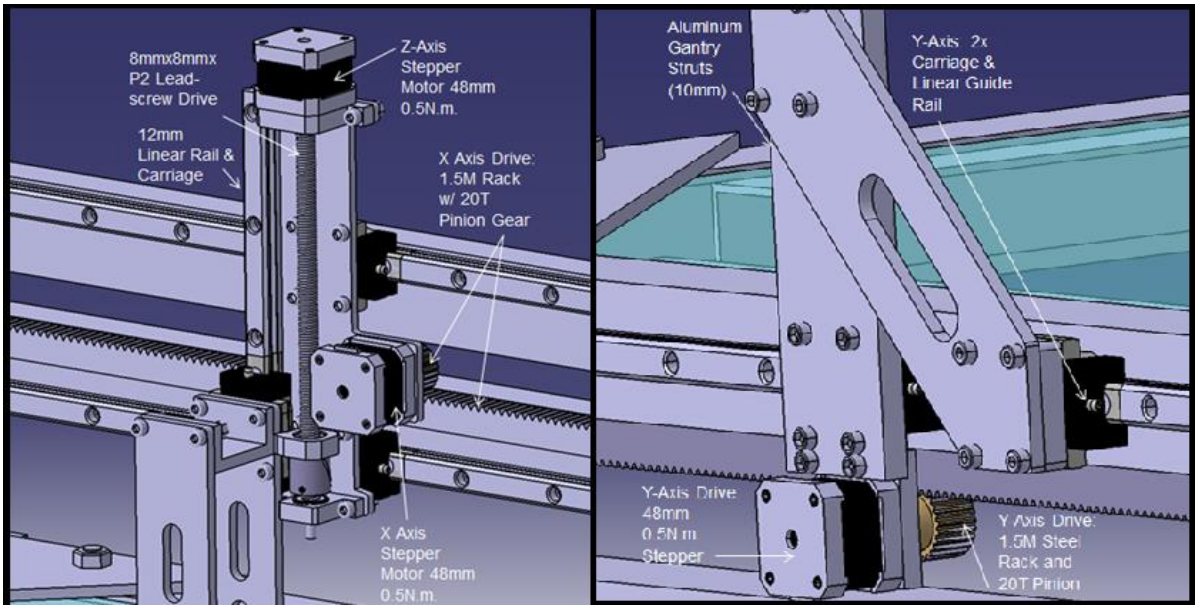

Figure 4.7: CNC/FDM Hybrid 3D Printer Concept: Isometric View

4.3.2. Physical layout

The physical layout of the system is similar to that of concept I, the multi-head filament printer, with the exception that the CNC-FDM printer contains a single gantry system which is heavily braced and reinforced to support the cutting forces induced on the spindle. The gantry contains a dual linear rail and carriage system for the 'x' direction, as well as single linear guides for the 'z' and 'y' directions. Furthermore, the axes are driven using Mod 1.5 hardened steel rack and pinion drive with NEMA17 48 *mm* 0.5 *N.m*. stepper motors. Additionally, the movement of the tool-head vertically, that is, in the z-direction, is achieved using a 8 *mm* x 8 *mm* x P2 lead-screw which is self-locking under static conditions. Table 4.5 details the general specifications for printer concept III.

Table 4.5: Horizontal CNC-FDM Hybrid 3D Printer Attributes

Characteristic	**Value**	**Description**
Height	1 *m*	Height from floor to top of gantry.
Width	2 *m*	Total frame width.
Length	5.3 *m*	Total frame length.
Weight	+-160 *kg*	Total assembly weight.
Motors	Stepper Motors	NEMA17 48 *mm* 0.5 *N.m*. Bipolar DC
Drive	Rack and pinion	Mod 1.5 15 *mm* Rail & 20T Pinion
Axes	Linear Guide & Carriage	Hiwin MG12 and MG12R rails/carriages
Print Material Type	Filament	1.75 *mm* PLA/ABS filament
Frame Material	Aluminium Extrusions	Bosch Rexroth Profile ALU. Series
Fasteners	Bolts, Nuts, T-Nuts	Black anodized Allen head cap screws.

4.3.3. Print head

The last conceptual print-head is based upon the idea that both printing and finishing of thermoplastic materials can be achieved with a single tool-head. The design incorporates a swivelling tool-head whereby the tool centre point, or location where the process is being performed, is at the exact same position whether in 'print mode', or in 'machining mode'. The concept incorporates a stainless steel CNC collet chuck and round-profile CNC drill bit, as well as a filament extruder head. Selection of the tool to be used is done manually, with securement via four locating pins. Additionally, extra tool height adjustment is achieved via the NEMA17 stepper motor and lead-screw combination. These features are illustrated in Figure 4.8

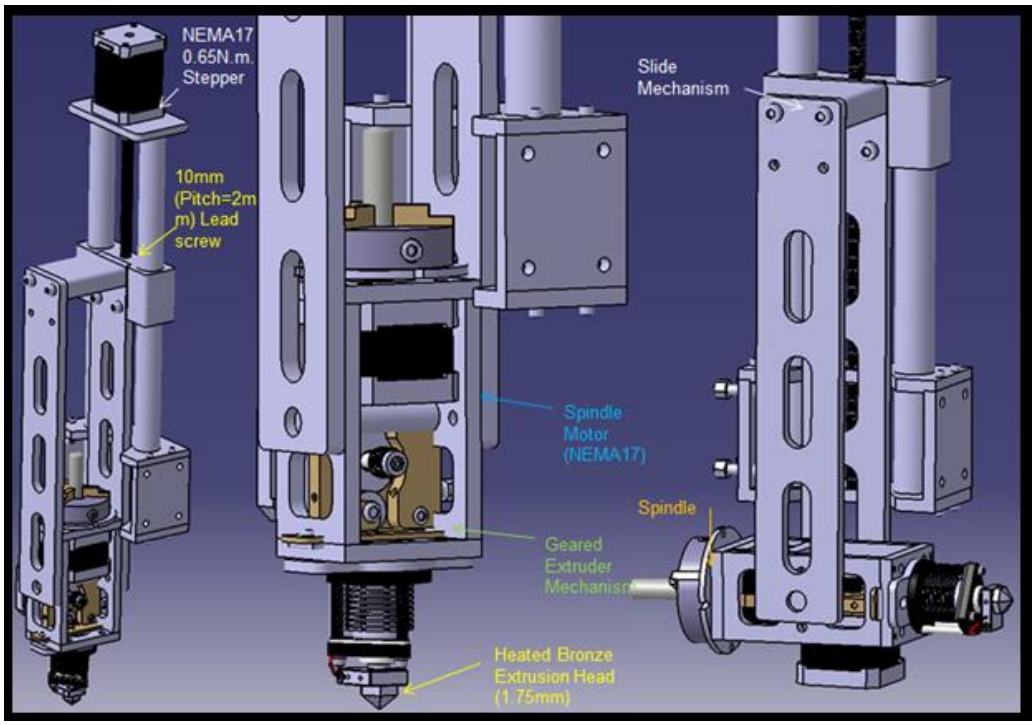

Figure 4.8: CNC/FDM Hybrid 3D Printer Concept: Print Head

Initial impressions and assumptions regarding design feasibility are tabulated below.

Table 4.6: Expected Advantages and Disadvantages for Horizontal CNC-FDM Hybrid 3D Printer

Expected Advantage	Expected Disadvantage
High finishing accuracy and smooth surface finish.	Extremely rigid gantry required. Expensive.
High machine versatility, usable for NC and	Possible deflection of tool-head under load.
machining of metal/wood/composite components.	Part finish errors, dimensional errors.
	Possible not enough torque from stepper
	Motor for routing operation required.

4.4. Cost analysis

Costing analyses was performed for each printer design, to assess the viability of each option from an economic standpoint. Each concept is subdivided into five costing sections based upon function, namely, the printer outer frame, gantry system including 'x', 'y', and 'z' axes, the print-head subassembly, electronics, and fasteners. It should be noted that the electronics and fasteners are common to all concepts. The full cost breakdown is observable in Appendix D.

Table 4.7: Costing Summary for Horizontal Multiple-Zoned Filament 3D Printer

Concept I: Horizontal Multi-Zoned Filament 3D Printer

Component	**Subtotal**	
Frame	ZAR 13377.89	
X,Y,Z Axes	ZAR 87523.50	
Extruder Subassembly	ZAR 1380.00	
Electronics	ZAR 6945.71	Total Cost: ZAR 129'476.68

Table 4.8: Costing Summary for Horizontal Multiple-Zoned Filament Printer

Concept II: Pellet-Based Vertical 3D Printer

Component	**Subtotal**	
Frame	ZAR 59375.54	
X,Y,Z Axes	ZAR 42103.30	
Extruder Subassembly	ZAR 809.70	
Electronics	ZAR 6945.71	Total Cost: ZAR 109'514.11

Table 4.9: Costing Summary for Horizontal FDM-CNC Hybrid 3D Printer

Concept III: Horizontal FDM-CNC Hybrid 3D Printer

Component	**Subtotal**	
Frame	ZAR 21958.86	
X,Y,Z Axes	ZAR 30703.01	
Extruder Subassembly	ZAR 31076.00	
Electronics	ZAR 6945.71	Total Cost: ZAR 91'474.95

4.5. Risk and feasibility analysis

Feasibility and the analysis thereof is the process of assessing how practical or beneficial the development of a system, process, or product will be to an organization, but generally ascertains the general success obtained by a project according to certain pre-defined metrics, or standards. Each design risk is categorized into eight sectors, namely technology, interfaces, safety, funding, schedule, quality requirements, contractor capabilities, and complexity of pollution. Furthermore, each risk factor is ranked from low to high, with an allocated sliding scale score between 1 and 5. Furthermore, a justification for each score is tabulated with possible prevention strategies for each possible problem.

Table 4.10: Risk Assessment Matrix for 3D Printer Designs

Risk Factor	Printer Concept	Risk Score	Risk Contributors	Mitigation/Contingencies
Technology	Filament Printer (I)	Low/Med **(2)**	Part deformation	Perform calibration
			Print errors/artefacts	Tighten/anchor assembly
	Pellet Printer (II)	Low/Med **(2)**	Extruder jamming	Powerful extruder motors
			Material handling	Hopper/piping assembly
	CNC/FDM Hybrid (III)	High **(5)**	Frame vibration	Reinforce/secure frame
			Routing tool deflection	Reinforce gantry/tool head
Interfaces	Filament Printer (I)	Low **(1)**	No dependency on other project timelines, therefore minimal 'Interfaces' risk involved.	
	Pellet Printer (II)	Low **(1)**		
	CNC/FDM Hybrid (III)	Low **(1)**		
Safety	Filament Printer (I)	Low **(1)**	No perceived health or safety risks.	No mitigation necessary.
	Pellet Printer (II)	Low **(1)**	No perceived health or safety risks.	No mitigation necessary.
	CNC/FDM Hybrid (III)	Medium **(3)**	High velocity routing tool; contact injuries.	Install protection barrier/windows.
Funding	Filament Printer (I)	Low **(1)**	Less than one year project duration.	No mitigation necessary.
	Pellet Printer (II)	Low **(1)**	Detailed estimated	No mitigation

			costs acquired.	necessary.
	CNC/FDM Hybrid (III)	Med/High **(4)**	NC tooling expensive, conceptual estimate.	Resort to more cost-effective design.
Time/Schedule	Filament Printer (I)	Low/Med **(2)**	Comfortable timeframe for project completion.	Project management plan implemented.
	Pellet Printer (II)	Low/Med **(2)**	Possible to complete within timeframe	Project management plan implemented.
	CNC/FDM Hybrid (III)	Med/High **(4)**	Difficult to reproduce under time constraints.	Requires task team implementation.
Quality Requirements	Filament Printer (I)	Medium **(3)**	50 μm surface roughness,	Accurate machine calibration.
	Pellet Printer (II)	Medium **(3)**	Dimensional accuracy +-0.1 *mm*	Print-head parameter fine-tuning.
	CNC/FDM Hybrid (III)	High **(5)**	5 μm Sur. Rough. dim. Acc. +-0.05 *mm*	Reinforced structure for accurate routing.
Contractor Capabilities	Filament Printer (I)	Low **(1)**	Proven track record and resources	No mitigation necessary.
	Pellet Printer (II)	Low **(1)**	available immediately.	
	CNC/FDM Hybrid (III)	Med/High **(4)**	Ltd. experience, Mod. resource capability.	External consultation required.
Complexity of Pollution	Filament Printer (I)	Low/Med **(2)**	ABS carcinogenic gases upon melting.	Well-ventilated print workspace, Sealed printer configuration advised.
	Pellet Printer (II)	Low/Med **(2)**	ABS carcinogenic gases upon melting.	
	CNC/FDM Hybrid (III)	Medium **(3)**	Polluting cutting fluid, Routed waste material	Manual clean method waste disposal.
Risk Score:	Filament Printer (I): 13/40		Pellet Printer (II): 13/40	CNC/FDM Hybrid: 29/40
	= 32.5%		**= 32.5%**	**= 72.5%**

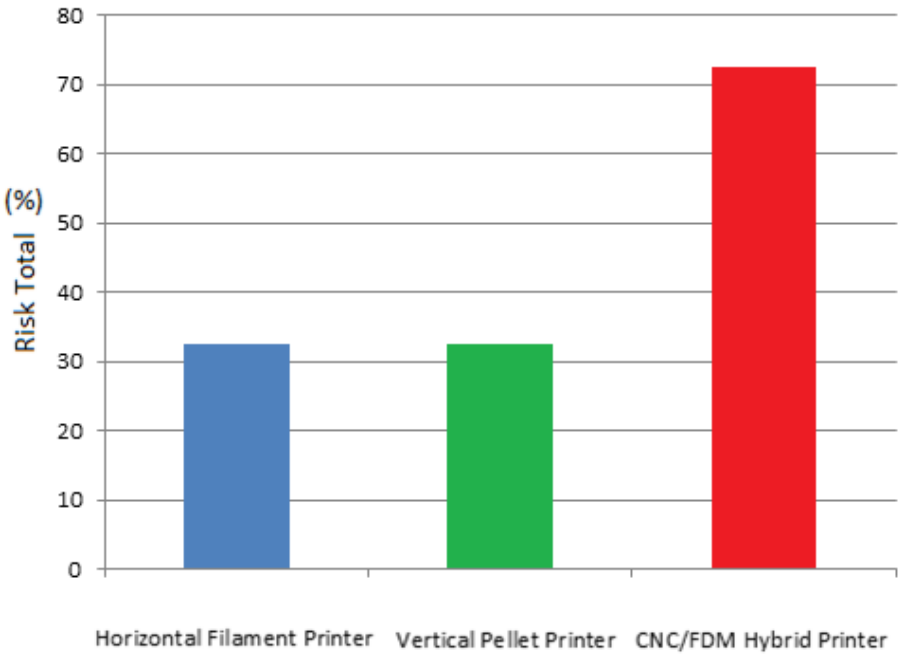

Figure 4.9: 3D Printer Conceptual Risk Analysis

From Figure 4.11 it should be noted that concepts I and II offer a much lower project risk of 32.5 % failure rate as opposed to 72.5 % for the CNC-FDM hybrid machine. The majority of the risk accumulated with the CNC printer hybrid lies in the machining complexities and difficulties which arise when developing a subtractive manufacturing process. Additionally, the accuracy of such a machine is dependent on structural rigidity, which is difficult to attain within a low budget threshold. This outcome will influence the selection of a final design in forthcoming sections.

4.6. Dynamic simulation of printers

Full simulation and stress testing of a product prior to manufacture is essential to ascertain whether or not the product is robust and strong enough to handle the stress placed upon it without undue physical deformation, in the form of elemental displacement, or in the extreme case, product failure. It is often extremely time-consuming and difficult to estimate the stresses induced in an assembly via simple analytic and mathematical principles; therefore finite elemental analysis will be used to test the robustness of each conceptual design. Finite element method, abbreviated FEM is a mathematical technique for finding approximate solutions for stress, deflections, displacements, and forces within a body. FEA is engineering application of the finite elemental method, whereby a large object with initial conditions is subdivided into a meshed object with nodes, and the stresses at each node computed (J.N. Reddy: 2006).

4.6.1. Environment setup and results

The printing operation will be simulated for each conceptual design in a FEA software package. During a conventional 3D printing operation, the print-head reaches gantry acceleration values of (Reprap: 2016):

$$a_{x-dir} = 1\ m.s^{-2}$$

$$a_{y-dir} = 1\ m.s^{-2}$$

$$a_{z-dir} = negligible$$

Acceleration values ranging from 0 m/s^2 to 1 m/s^2 are applied to the linear slides of each concept in CAD/CAM finite elemental analysis models, and the Von Mises stress, deformation, and induced moments tabulated. The printer base is clamped representing a bolting of the assembly to the floor. The simulation setup with red vectors representing gantry linear accelerations $a_{x\text{-}dir}$ and $a_{y\text{-}dir}$ are shown in Figure 3.12, in addition to the displacement vector representation of the deformation observed in the structures once the applied accelerations are simulated for Concepts I and II.

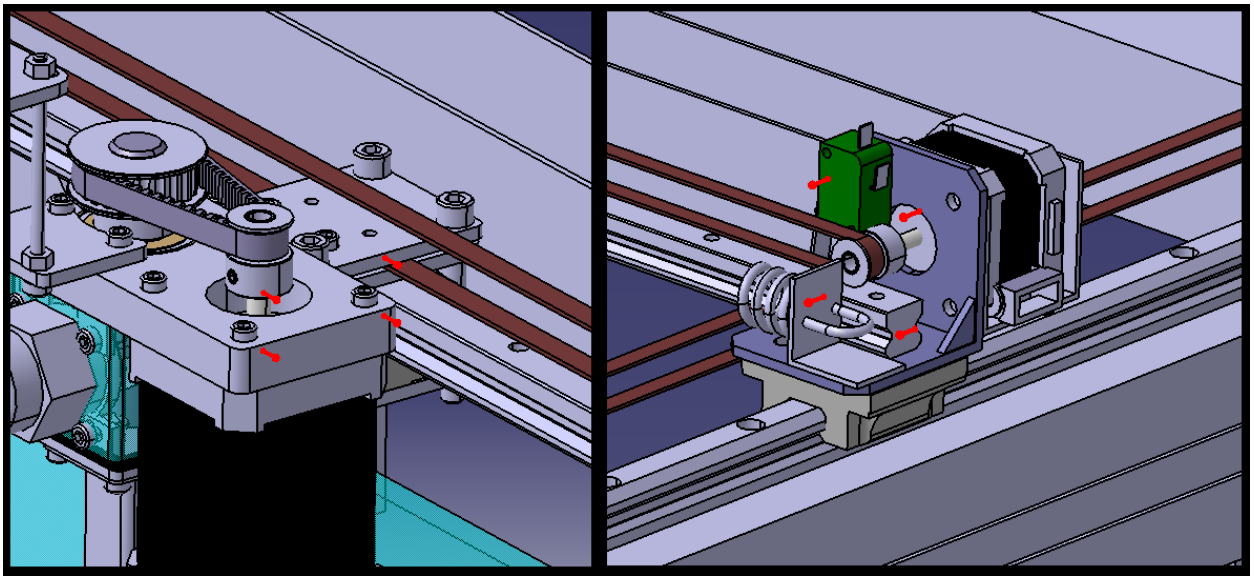

Figure 4.10: Print Head & Gantry Axes Acceleration Simulation Setup

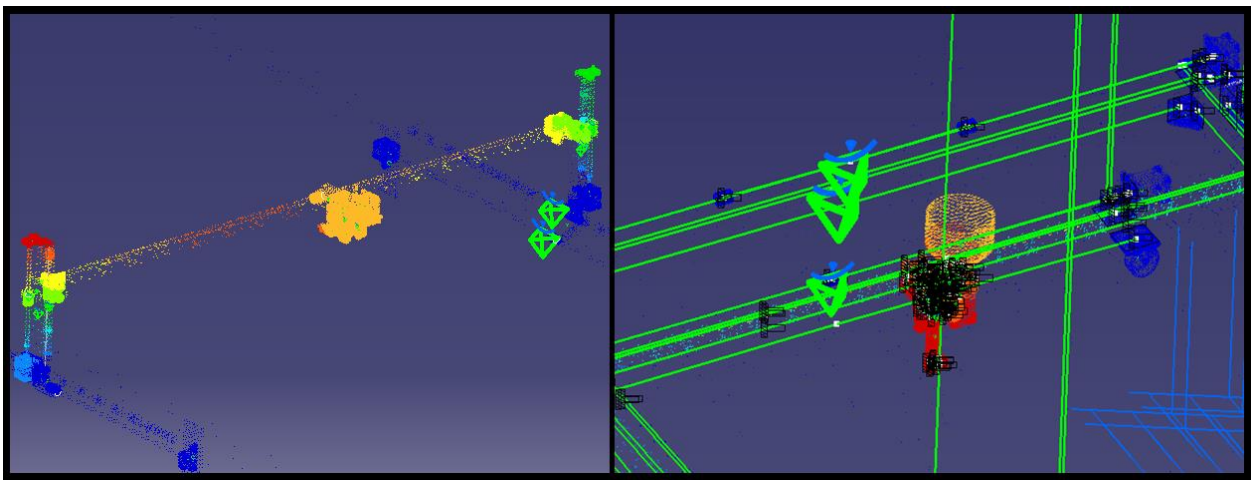

Figure 4.11: FEA Mesh Deformation Using Vector Representation

The simulated Concept I FEA results, including induced structural stresses, body stretch, torques, and strain are tabulated and represented graphically below for gantry acceleration values ranging from 0 to 1.0 m/s^2.

Table 4.11: Concept I FEA Results

Print Head	**Von Mises Stress**	**Structure Stretch**	**Resultant Moments**	**Strain Energy**
Accel, m/s^2	*MPa*	*mm*	*N.m.*	*J*
0.2	0.0109	0.000046	0.0178	$5.479x10^{-10}$
0.4	0.0219	0.000092	0.0527	$2.192x10^{-9}$
0.6	0.0328	0.000138	0.0885	$4.931x10^{-9}$
0.8	0.0437	0.000185	0.1305	$8.767x10^{-9}$
1.0	0.0547	0.000231	0.1780	$1.37x10^{-8}$

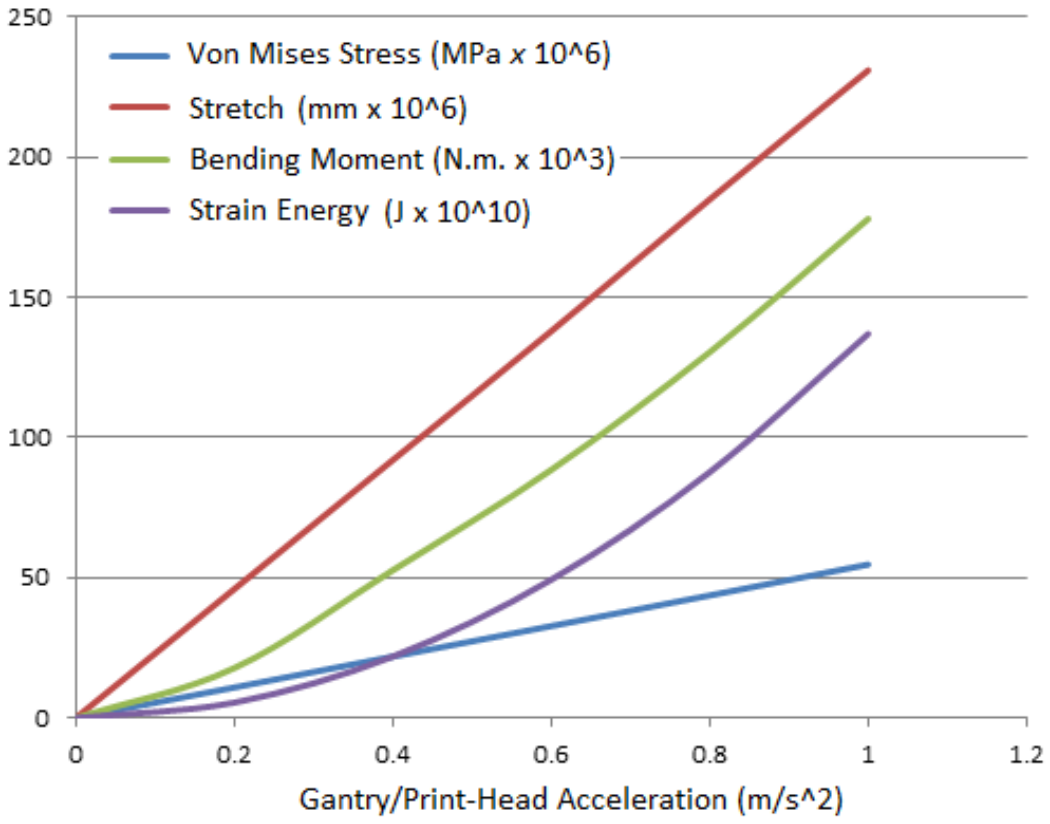

Figure 4.12: Concept I FEA Results

Similarly for concept II:

Table 4.12: Concept II FEA Results

Print Head	**Von Mises Stress**	**Structure Stretch**	**Resultant Moments**	**Strain Energy**
Accel. m/s^2	*MPa*	*mm*	*N.m.*	*J*
0.2	0.0255	0.0000401	0.1098	$7.295x10^{-10}$
0.4	0.0510	0.0000801	0.2195	$2.918x10^{-9}$
0.6	0.0765	0.00012	0.3269	$6.565x10^{-9}$
0.8	0.1020	0.00016	0.4384	$1.167x10^{-8}$
1.0	0.1270	0.00020	0.5470	$1.824x10^{-8}$

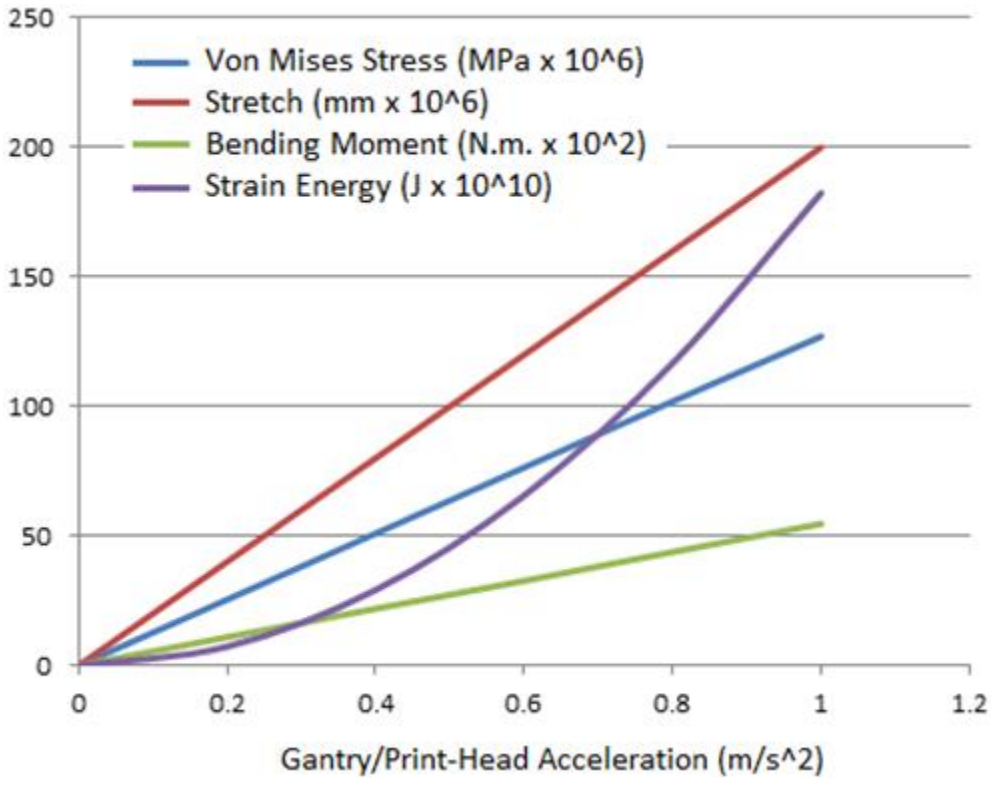

Figure 4.13: Concept II FEA Results

Regarding the third printer concept, which utilizes a CNC routing spindle during operation, a different simulation environment must be instantiated. It is known 3-axis CNC milling induces various stresses and loads on the routing tool, which is transferred to the machine gantry and frame. The force produced at the routing tool face is a three-dimensional one, and varies with rotation of the spindle from 0 to 360 ^{O}. The derived voxel simulation model of a CNC cutting tool, (O Yousefian, J.A. Tarbutton: 2015), as found in Appendix A.9 which estimates the tangential, radial, and axial forces acting on the cutting tool are:

$$\begin{bmatrix} F_t \\ F_r \\ F_a \end{bmatrix} = \begin{bmatrix} \cos(\theta) & \sin(\theta)\sin(\kappa) & \sin(\theta)\cos(\kappa) \\ \sin(\theta) & \cos(\theta)\sin(\kappa) & \cos(\theta)\cos(\kappa) \\ 0 & \cos(\kappa) & \sin(\kappa) \end{bmatrix} \begin{bmatrix} F_X \\ F_Y \\ F_Z \end{bmatrix} \quad \text{(A9.4)}$$

θ	local angle with respect to tool origin	degrees, ^{O}
κ	axial immersion angle	degrees, ^{O}

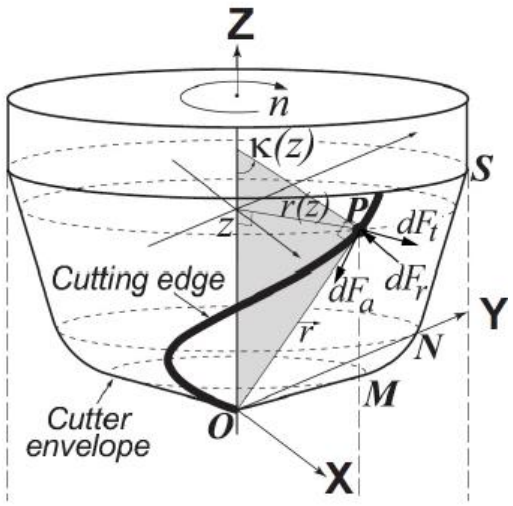

Figure 4.14: CNC Tool Cutting Forces Diagram

For a 1.2 *mm* depth cut at 1500 RPM spindle speed, with 762 *mm/min* feed-rate, the induced cutting tool forces when machining thermoplastic material are:

Table 4.13: Induced Cutting Forces on CNC Routing Tool for Concept III

Rotation Angle Cutting Tool, θ	**Cutting Force** F_t, *N*	**Cutting Force** F_r , *N*	**Cutting Force** F_a , *N*	**Resultant Force** F, *N*
0	-30	+80	+10	86.023
60	+0	-25	+60	65.000
120	-20	+75	+40	87.321
180	-30	+80	+20	87.75
240	+5	-25	+60	65.192
300	-13	+65	+55	86.134
360	-30	+60	+10	67.823

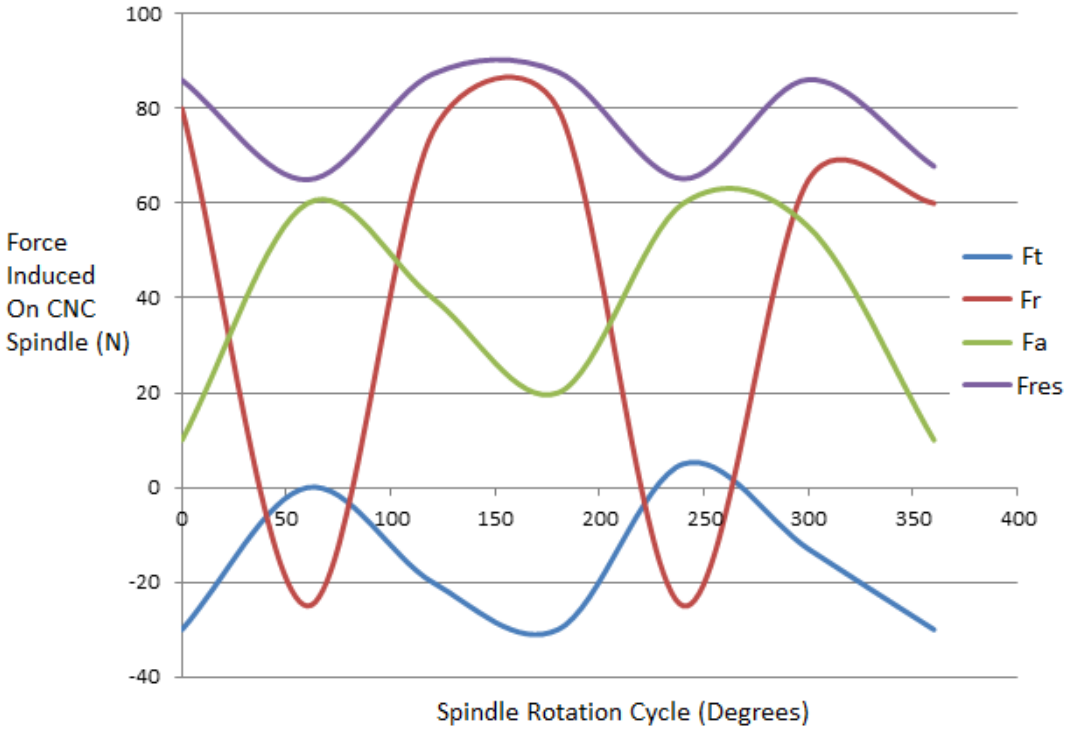

Figure 4.15: Induced Cutting Forces on CNC Routing Tool for Concept III

The above cyclical induced spindle cutting forces are transferred from the tooling bit to the third concept's frame. The tangential, axial, and radial forces, when applied to the FEA simulation, yield the following Von Mises stresses and body deformation in the printer, as given in Table 4.14 and Figure 4.16.

Table 4.14: Concept III FEA Results

Rotation ∡ Tool, θ	**Von Mises Stress** *MPa*	**Structure Stretch** *mm*	**Resultant Moments** *N.m.*	**Strain Energy** *J*
0	17.5	0.136	12.23	3.327×10^{-3}
60	8.97	0.0519	14.08	5.873×10^{-4}
120	21.7	0.142	18.55	4.362×10^{-3}
180	22.9	0.161	17.18	5.129×10^{-3}
240	7.24	0.039	13.79	4.780×10^{-4}
300	19.2	0.123	18.99	3.413×10^{-3}
360	17.5	0.136	12.23	3.327×10^{-3}

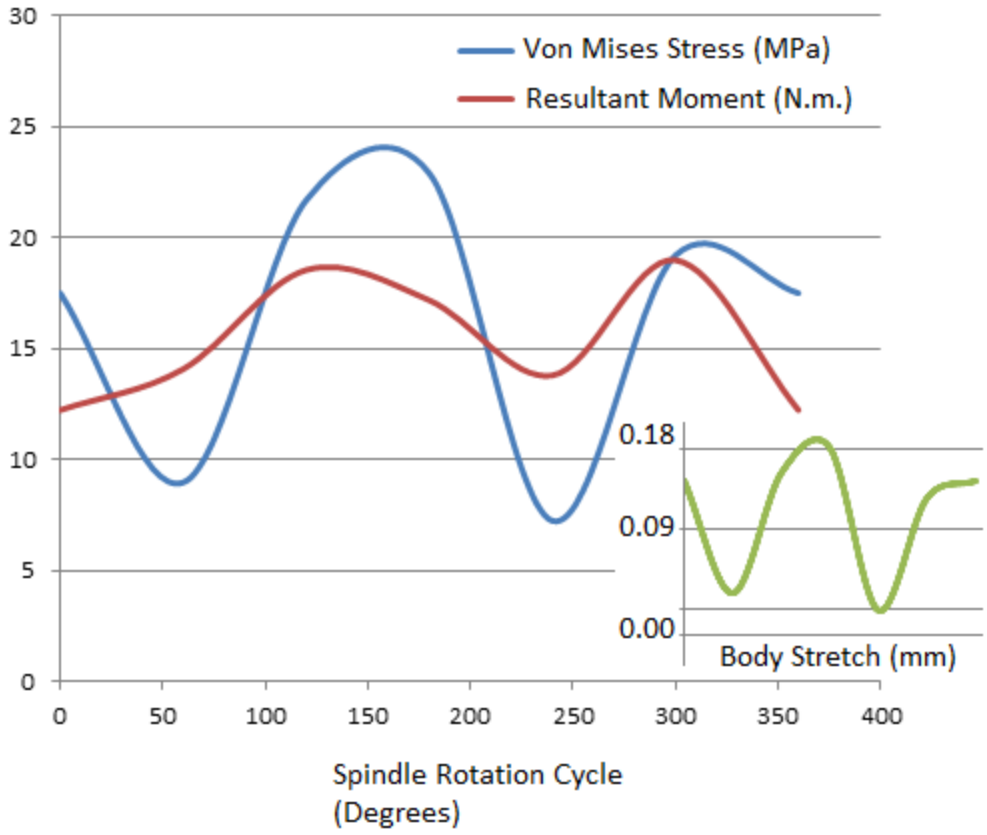

Figure 4.16: Concept III FEA Results

4.6.2. Discussion of FEA results

A linear increase in the lateral acceleration of the gantry was induced for each printer concept from 0.2 m/s^2 up to 1 m/s^2, and the FEA simulation model produced with associated results. These included maximum localized stress within the structure, known formally as Von Mises stress, the maximum body displacement observed, bending moments, as well as strain energy which gives an indication of the overall stretch of the systems. A linear relationship was noted between the applied input, that is, the gantry acceleration, and the measured outputs, where, as the acceleration was increased, the output stresses, displacements, and moments increased proportionally from 0.0109 *MPa* and 4.6×10^{-5} *mm* to 0.0547 *MPa* and 2.31×10^{-4} *mm* respectively at 1 m/s^2 acceleration, as evidenced in Table 4.11. The same trend was observed in Concepts I and II. However, comparing the induced stresses and body displacements, it may be observed that Concepts I and II exhibit almost identical body deformation figures at 2.31×10^{-4} *mm* and 2.00×10^{-4} *mm* respectively at 1 m/s^2 gantry acceleration. These results ascertain that the structure is suitably rigid for operation. Induced Von Mises stress is much higher for the vertical printer concept at 0.1270 *MPa* when contrasted with 0.0547 *MPa* for the horizontal flatbed printer, predominantly due to structural configuration. These figures are however well below the minimum yield strength value of 160 *MPa* for aluminium which is satisfactory for design purposes.

When observing trends for forces induced on Concept III, vizier, CNC machining forces on the machining spindle and to a lesser degree the gantry, it can be seen from Figures 4.15 and 4.16 that the maximum induced cutting force is 87.75 *N* when the spindle is at 180 ^{O} rotation phase. Subsequently, the maximum Von Mises stress and gantry displacement also occurs at this phase, with values of 22.9 *MPa* and 0.161 *mm* respectively. It should be noted that the stresses and body displacement induced in Concept III are much higher than those of I and II. The cyclic displacement of 0.18 *mm* during machining, as evidenced by the sinusoidal output in Figure 4.16, is much higher than associated displacement figures of $2.31x10^{-4}$ *mm* and $2x10^{-4}$ *mm* for Concepts I and II, deterring the selection of Concept III as a viable printer solution, from a structural-analysis standpoint.

4.7. Final printer design selection

Having analysed each design with regards to practicality, risk and design feasibility, costing, and structural integrity through FEA analysis, the combined results of the analyses performed in this chapter are presented in Table 4.15.

Table 4.15: Order of Merits Table for Selection of Final 3D Printer Configuration

Characteristic	**Weight (/1)**	**Score (/5)**		
		Concept I	Concept II	Concept III
Print Material Cost	**0.5**	ZAR 380/*kg* **(1)**	ZAR 100/*kg* **(4)**	ZAR 380/*kg* **(1)**
Printer Build Cost	**0.8**	ZAR 129’476.68 **(3)**	ZAR 109’514.11 **(4)**	ZAR 91’474.95 **(5)**
FEA Results	**1.0**	σ_m = 0.0547 *MPa* **(5)**	σ_m = 0.1270 *MPa* **(4)**	σ_m = 22.90 *MPa* **(1)**
		E = $2.31x10^{-4}$ *mm*	E = $2x10^{-4}$ *mm*	E = 0.1610 *mm*
Risk Analysis Results	**0.9**	Risk = 32.5 % **(4)**	Risk = 32.5 % **(4)**	Risk = 72.5 % **(2)**
Total:	(/16)	11.50	12.80	7.30
Rating (Out of 100):		71.875 %	**80.00 %**	45.625 %

Referring to Table 4.15, it is observed that filament printing material utilized in Concept I and II are nearly four times the cost of recycled pellets used in Concept II’s pellet extruder print-head, netting lower merit scores of ‘1’ versus ‘4’ (J. Lefebvre: 2015). Build costs for all concepts are similar, as evidenced in Appendix D, but significant bias of scores occurs in the ‘FEA Results” section with the more structurally-sound Concepts I and II receiving scores of ‘5’ and ‘4’ versus ‘1’ for the hybrid CNC-FDM design. It was also noted that increased project risk was present with the CNC design, as the field of study is currently un-researched and presents a plethora of additional engineering complexities. Accumulating a total merit percentage score of 80.00 %, the vertical 3D printer configuration is selected for manufacture and testing. The complete manufactured unit is displayed.

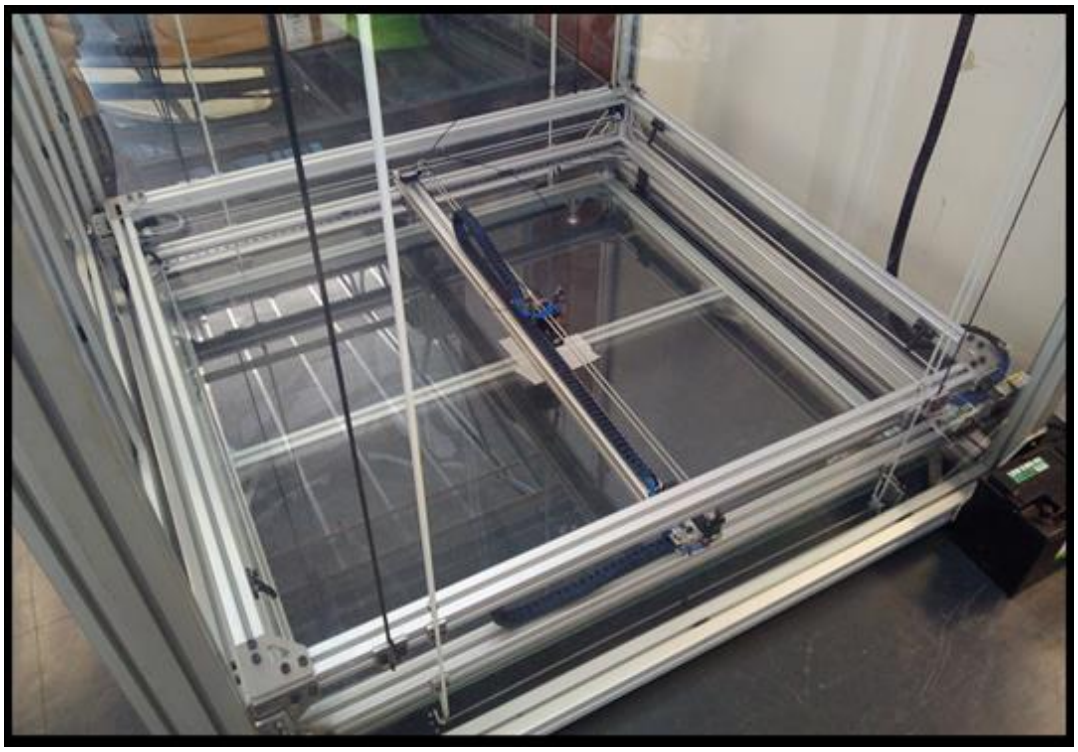

Figure 4.17: Printer X/Y/Z Axes – Gantry Subassembly View

Figure 4.18: Controller Box & 12V Battery Supply (left), Counterweight System (right)

Figure 4.19: Gantry ‘x’ Axis and Print-Head Subassembly

Figure 4.20: Top View of Printer – Printing Material Reel System

Figure 4.21: Full Isometric View of Large-Scale Additive Manufacturing Platform

4.8. Chapter conclusion

This chapter presented three additive manufacturing platform solutions, and analysed the feasibility of each from a practical, risk, structural, and cost point of view. In-depth comparisons for each attribute were performed using order of merit tables, and the ‘vertical pellet-based 3d printer’ concept finally selected for further design development and manufacture.

CHAPTER 5

Experimental Setup, Testing, and Results

This chapter presents the calibration and performance testing of the physical additive manufacturing platform. Initially, the expected precision and design uncertainty of the printer are estimated using statistical formulae. The calibration procedure is to be explained in detail, giving the reader an understanding of the machine setup and fine-tuning of system parameters. Thereafter, a variety of physical tests focusing on the performance of the gantry, which includes the frame and X/Y/Z axes, as well as the extruder printing capabilities are performed. The analysis performed in this chapter provides a strong foundation for later discussion and answering of the hypothesis statement.

5.1. Theoretical system performance

Theoretical statistical analysis is performed on both physical and electrical systems prior to performing physical calibration on selected equipment so as to provide an estimate of overall system accuracy while printing. The data utilized for obtaining the uncertainty threshold values are component statistical performance parameters such as instrument resolution, accuracy, range, and the like. By definition, the accuracy of a component attribute or instrument reading is how close the produced reading is to the actual value, whereas precision, or repeatability, is the range over which the measured value varies when measured under identical conditions (J.R. Taylor: 1999). This concept is detailed in Figure 5.1.

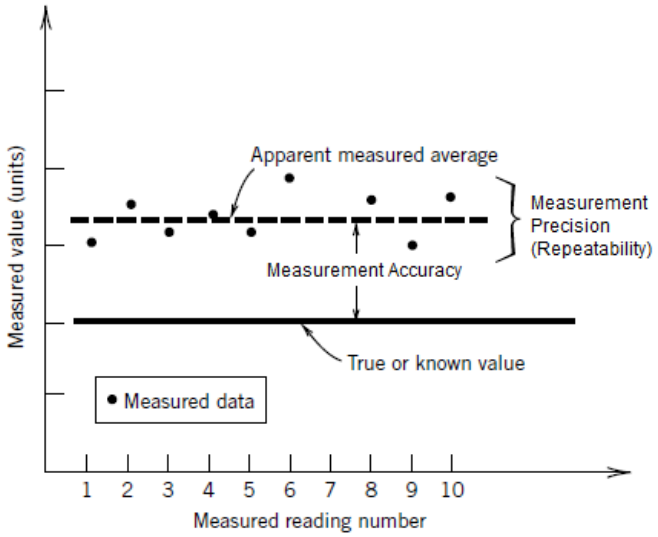

Figure 5.1: Statistics of Measured Data

The component performance values for printer components are shown below in Table 5.1.

Table 5.1: 3D Printer Component Performance Specifications

Instrument Component	**Measurement Type (units)**	**Range**	**Repeatability**	**Accuracy**
Pololu DRV8825 Stepper Motor Driver	Revolution Accuracy (degrees, ^{O})	0.05625 ^{O} to 1.8 ^{O}	5 % (0.09 ^{O})	0.05625 ^{O}
Hiwin MG12R Linear Rail/Carriage	Dimensional Accuracy (Class C, *mm*)	0.08 *mm*	100 % (0 *mm*)	0.04 *mm*
	Running Parallelism ($\mu m/m$ rail)	11 μm	100 % (0 μm)	23 μm
BrecoFlex T2.5 6 *mm* Timing Belts & Pulleys	Linear Positioning Accuracy	1 *m*	0.508 *mm*	1.04 *mm/m*
EPCOS Thermistor B57540G0104F000	Temperature (Resistive)	355 ^{O}C	2 % at 25 ^{O}C (0.5 ^{O}C)	0.25 ^{O}C

The ability of the printer to position the sliding bearing carriages and hence print-head accurately are in part determined by the precision of the constituent components of the drive train, that is, the Pololu DRV8825 motor driver, Hiwin linear railing systems, and the timing belt and pulley drives. The zero order uncertainty of a measurement or component is defined as '*the uncertainty of an instruments measurement result only with regards to its resolution*', and is given by (Figliola, R.S. & Beasley, D.E.: 2011):

$$u_O = \pm(0.5)(r) \tag{5.1}$$

μ_o	zero order uncertainty	various
r	measurement resolution	various

The instrument uncertainty is defined as the measurement accuracy of an instrument at a 95 % probability confidence level, and is a product of the components individual elemental errors:

$$u_e = \sqrt{(u_1^2 + u_2^2 + \cdots + u_n^2)} \tag{5.2}$$

$$= \frac{\sum u_c}{n} = \frac{\sum_{k=0}^{n-1}(a + kd)}{n} = \frac{1}{2n}(2a + (n-1)d)$$

a	first reading taken	various
d	difference between readings taken	various
n	total number of readings taken	integer
$\mu_{1..n}$	measurement values over range	various
μ_e	instrument error	various

Then the design-stage uncertainty, which may be used as a guide for selecting measurement equipment or componentry, is given as:

$$u_d = \sqrt{(u_o^2 + u_e^2} \tag{5.3}$$

μ_o	zero order uncertainty	various
μ_e	instrument error	various
μ_d	design-stage uncertainty	various

The overall instrument uncertainty, or estimated measurement errors, is shown in Table 5.2.

Table 5.2: 3D Printer Design Stage Uncertainty Analysis Results

Instrument Component	**Error Type**	**Zero-order Uncertainty (μ_o)**	**Instrument Uncertainty (μ_e)**	**Design-Stage Uncertainty (μ_d)**
Pololu DRV8825 Stepper Motor Driver	Revolution Accuracy	+-0.005 ^{O}	0.10125 ^{O}	0.8955 ^{O}
Hiwin MG12R Linear Rail/Carriage	Dimensional Accuracy	0.005 *mm*	0.0032 *mm*	0.0059 *mm*
	Running Parallelism	0.5x10^{-6} *mm*	2.53x10^{-10} *mm*	5x10^{-7} *mm*
BrecoFlex T2.5 6 *mm* Timing Belts & Pulleys	Locational Accuracy	0.0005 *mm*	1.04 *mm*	1.04 *mm*
EPCOS Thermistor	Temperature	0.05 $^O C$	0.3295 $^O C$	0.3333 $^O C$
Theoretical Locational Performance				**1.04 *mm***

5.2. System calibration

Practical performance testing of the additive manufacturing platform first requires that the system be calibrated, both at the sensor stage, as well as the physical system itself. Calibration by formal definition is "*Operation that, under specified conditions, in a first step, establishes a relation between the quantity values with measurement uncertainties provided by measurement standards and corresponding indications with associated measurement uncertainties (of the calibrated instrument or secondary standard) and, in a second step, uses this information to establish a relation for obtaining a measurement result from an indication*" (JCGM 200: 2008). The reason for undertaking printer calibration is so that exact, dimensionally-accurate, and smooth quality prints are obtained. Without proper calibration, numerous part defects, such as 'warping', 'elephant foot', 'sinking layers', and 'skewed prints', amongst others, are produced (F. Grieser: 2015).

The system calibration process is carried out in a methodical and specific manner as recommended by the 3D printer 'RepRap" calibration guide (RepRap Calibration: February 2016). The calibration process plan, or measurement test plan, is prescribed as:

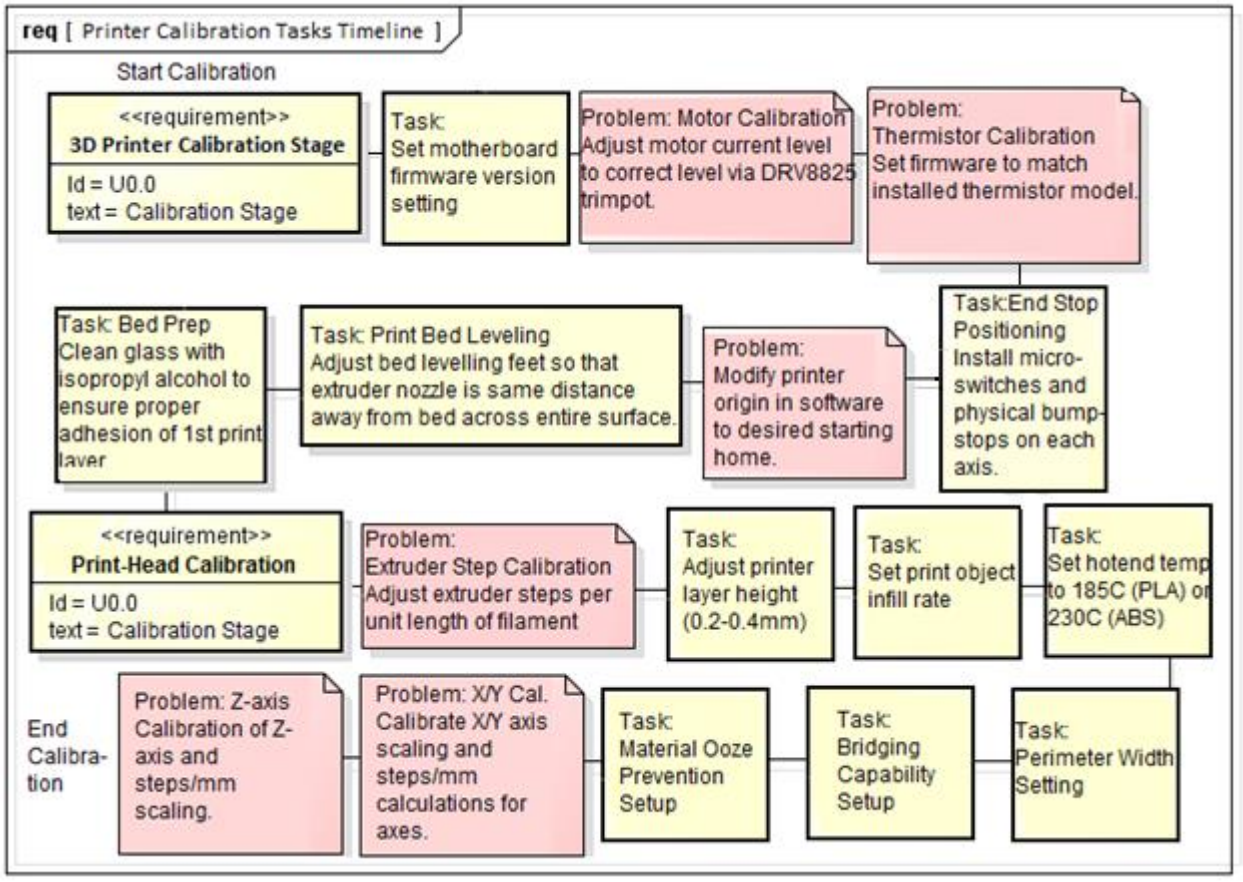

Figure 5.2: System Calibration Procedure Process Diagram

5.2.1. Motherboard and motor calibration

The first phase in calibration is to specify firmware settings relating to printer gantry velocity, material extrusion rates, acceleration rates, enabling or disabling of peripherals such as end-stops, and selection of peripheral types such as thermistors and the like. In the Arduino Marlin software, the .h files are edited for the large-scale printer, and adjusted as necessary. The full software is given in appendix E.6.

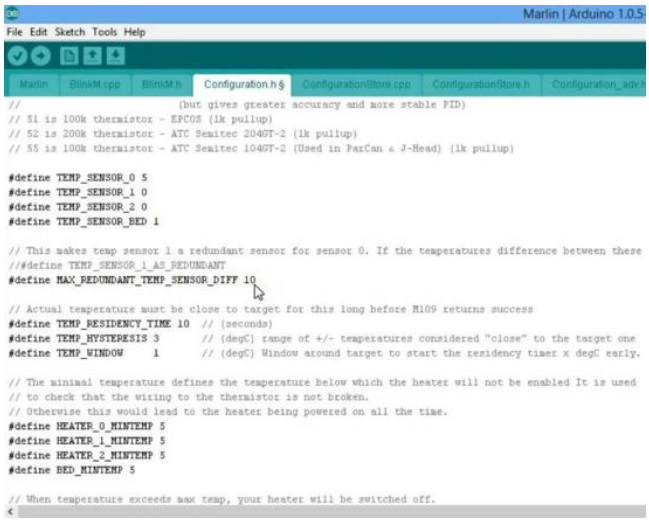

Figure 5.3: Firmware Setup in Arduino Development Environment

Thereafter, calibration for the NEMA17 48 *mm* 0.48 *N.m.* stepper motors may be performed. Adjustment of the Pololu DRV8825 is necessary since the motors produce significant noise during operation if current is over-supplied. Additionally, if the motor vibrates without turning when given a signal to move, current is under-supplied for the torque requirement of the application. Finally, if the axis moves momentarily at a high acceleration and then stops, the DRV8825 current level is over the 2.2 *A* per phase limit, causing the board to overheat and thermally protect itself by shutting down. Adjustment of motor current for each axis and the extruder is done using the linear current trim-pot ranging from 0 *V* to 1.1 *V*:

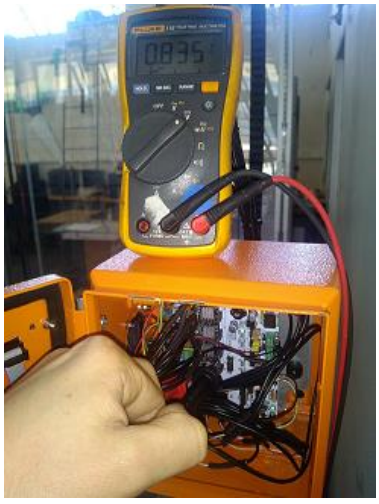

Figure 5.4: Adjusting Motor Trim-pot Current to Acceptable Level

Following motor calibration, thermistor and PID calibration is performed, whereby the heater gain, K_P, K_I, and K_D parameters are tweaked to ensure heating and stabilization of the print-head to 190 ^{O}C. Table 5.3 indicates the values that were tested for the PWM heater module to achieve satisfactory temperature stabilization of the print-head.

Table 5.3: PID Settings versus Temperature Performance

PID Setting, K,K_I,K_P,K_D	**Max Overshoot ^{O}C**	**Delay Time, *s***	**Rise Time, *s***	**Settling Time, *s***
75, 0.03, 2.04, 3.28	2	2	68	12
127.5, 0.05, 2.04, 5.00	4	1	50	12
127.5, 0.5, 2.04, 5.00	4	1	55	9
127.5, 0.05, 2.04, 50.0	1	1	61	8
191, 0.07, 2.04, 12.3	3	0.5	46	10
255, 0.07, 1.50, 50.0	2	0.5	37	7

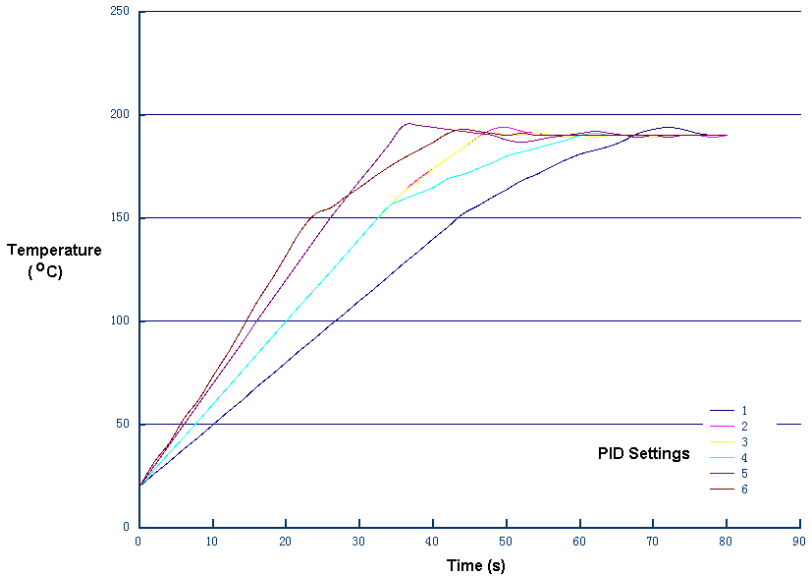

Figure 5.5: Tuning of Heater PID settings

5.2.2. End stops adjustment

Physical adjustment and setup of the 2-terminal micro-switches on each axis, that is, the 'x', 'y', and 'z' axes, is important to prevent collision of the print-head into axis endpoints, resulting in damage to the extruder, motors, gearing, and print-bed surface. Typically, a 3D printer axis is characterized by at least one physical limit switch, and the maximum feed length, or axis travel length. The end stop implemented in this design is a 2-terminal on/off switch which triggers the stepper motor drive system to stop when the axis carriage makes physical contact with this switch. The setup procedure should be duplicated for each axis, that is, performed for the two limit switches of the 'x', 'y', and 'z' axes.

Checking switch operation status

Initially, the printer 12 *V* DC supply is off, with no current available to the controller board or electrical peripherals. The print-head and carriage assembly is manually moved to the centre of the print area, with the extruder assembly being clear of the glass print-bed. 12 *V* supply is switched on and the normally open ($I_{limit\text{-}switch} = 0$) limit switch to be tested is physically contacted with the hand, closing the connection and making the output ($I_{limit\text{-}switch} = 1$). The following commands are activated in Marlin software to enable the x-axis limit switch reading:

$$\text{X\_ENABLE\_ON} = 1, \text{X\_HOME\_DIR} = 1$$

With the limit switch pushed in manually, the print-head is instructed to move away and towards the switch by 10 *mm* and check if a limit switch has been contacted by using the command "G1 X10 S1". Should the limit switches be operational and connected correctly, the axis will not move. The test is repeated with the limit switches left normally open, resulting in the axis moving when the software command is given. The test is then repeated for all switches on the 'x', 'y', and 'z' axes. Figure 5.6 demonstrates the testing of the switches.

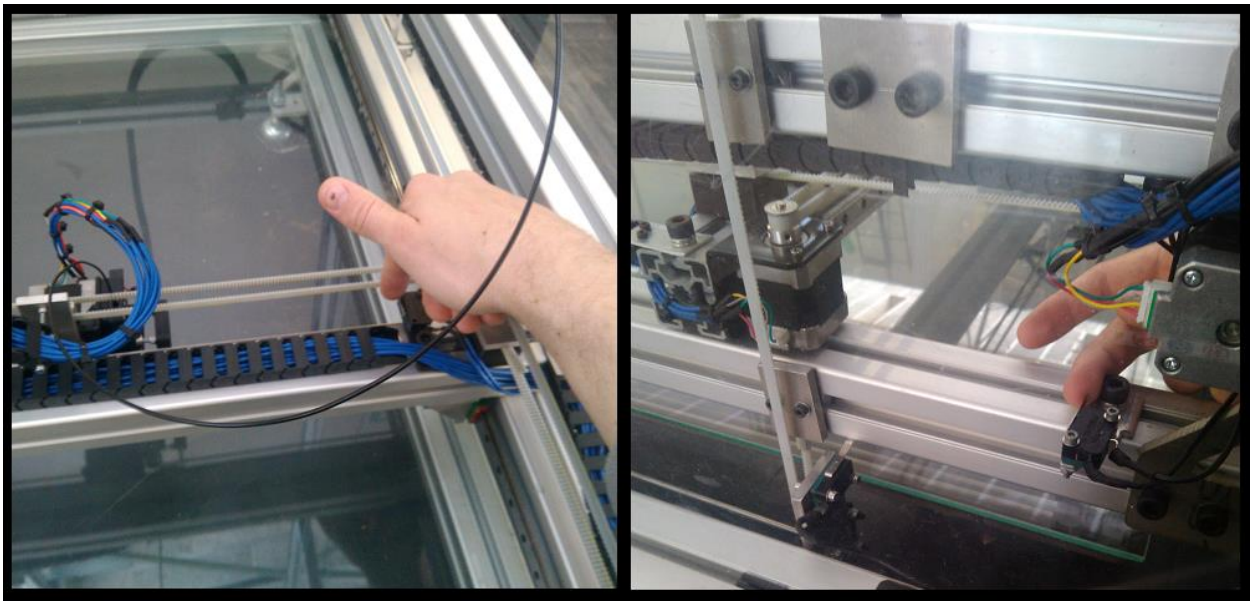

Figure 5.6: Testing of Limit Switch Operation

Determining axis boundaries

The next required axis calibration step is to ascertain the limit of x-axis travel in the direction of the selected end-stop, where the x-axis limit is the closest point to the edge of travel available before frame collision occurs. The axis move command is given such that the print-head stops just before making contact with the end-stop. At this point another incremental move command is given, producing contact between the moving gantry and the end-stop, and hence triggering the appropriate motors to stop. The gantry is commanded to move 10 *mm* away from the end-stop, and this new position now designated as the proper end-stop location, which will prevent collision of the moving gantry into the stationary frame.

5.2.3. Bed levelling and surface preparation

The 1.4 m^2 glass print bed requires levelling in order for the print-head nozzle to be located at an equal height above the bed when in various 'x' and 'y' lateral locations. The predominant motivation for print-bed levelling is so that the extruded material binds equally to the surface. Problems associated with an uneven print surface include: plastic bonding to portions of the bed, deformation or delamination of the first print layer, or collision of the print-nozzle with the bed (Reprap Calibration: 2016). The printer head assembly is first commanded via software to move to a print-bed corner. The "Bosch Rexroth VA Levelling Foot" height at the selected corner is adjusted so as to produce a 2 *mm* gap between the print nozzle exit and the glass surface. The foot height is measured using Veneer callipers, and the process repeated for each table corner, thereby levelling the surface. The process is illustrated in the Figure 5.7.

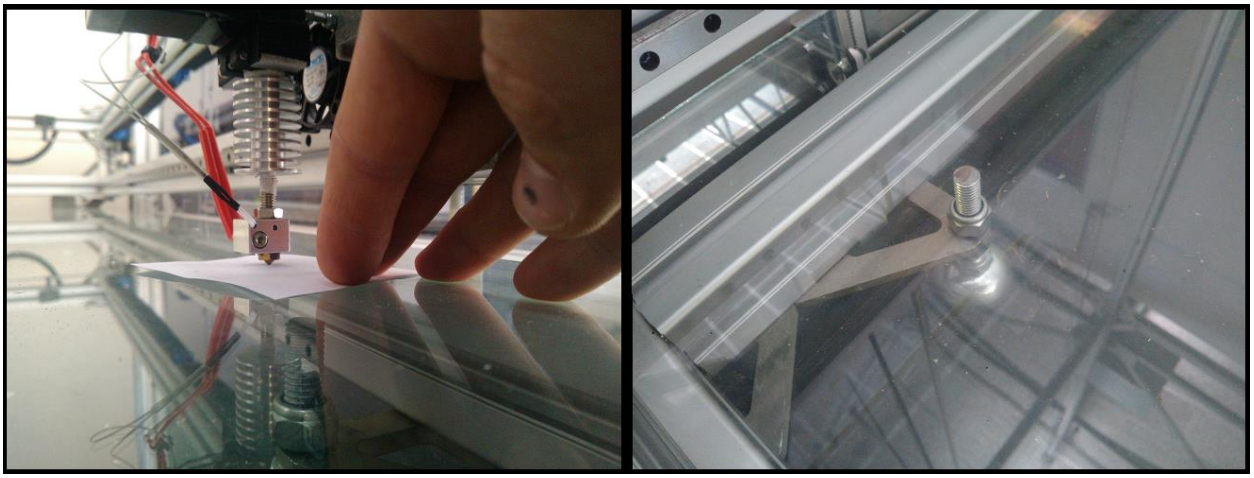

Figure 5.7: Levelling of Printer Bed via Bosch Rexroth VA Adjustable Feet

Thereafter, the glass print-surface is cleaned comprehensively with isopropyl alcohol and a non-abrasive cloth, thereby removing all oils and residue from the surface. Cleaning is performed so as to prevent poor adhesion and bubbling of the first thermoplastic layer.

5.2.4. Extruder calibration

Print-head calibration is necessary in order to produce a fluid and uniform melted thermoplastic stream from the hot-end, which exits at a constant linearized rate, is uniform in cross-sectional area, and is free from bubbles or gas particles. The software settings illustrated in Table 5.4 were found to be optimal for the printer application, after significant adjustment and fine-tuning.

Table 5.4: Extruder Software Settings

Setting Name	Setting Optimised Value	Setting Description
Extruder Steps/Distance	M92 E<new value>	To set the distance and amount of filament that is extruded per number of motor steps.
Print Layer Height	Skeinforge → Craft	To correct the layer height settings to reflect

	→ Carve <0.28 *mm*>	the printer's actual layer height.
Infill	Skeinforge → Craft	To correct the amount of filament present in
	→ Fill <1.0>	model centre – object material density setting.
Hot Temperature	PLA: 185 ^{O}C	To ensure correct plastic melt rate – varies for
	ABS: 230 ^{O}C	various plastic makes and types.
Perimeter Width	Skeinforge →	To adjust the object perimeter width ratio versus
	Craft → Carve →	print thickness.
	Edge Width/Height	(Generic Setting = 1.0)
Oozebane	Printer Settings →	To stop material oozing out of the hot-end
	Extruder → Wipe Before	nozzle during non-printing/waiting periods.
	Retract	

5.2.5. X/Y/Z axes calibration

The horizontal axes and part dimension ratios may be calibrated using the software parameters "Track Offset" and "Overall Scaling". Overall scaling is the ratio between actual measurement units in mm versus the amount of stepper motor pulses outputted for a particular part dimension being printer and is given as:

$$S_{axes} = \frac{length_{CAD\ Model}}{length_{Actual\ Part}} \tag{5.4}$$

The track offset is defined as half the width of one extruder stream of filament and assists in producing a print inside the desired perimeter of part schematic. The track offset essentially prints the perimeter layer of filament inside the desired profile as shown in Figure 5.8.

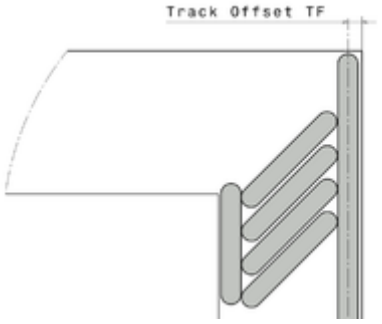

Figure 5.8: Track Offset

The distance that the extruder must move to produce a side length which is exactly to scale with the CAD model is (Hitter, M.T.: 2016):

$$M_x = (x - 2T)S \tag{5.5}$$

M_x	actual extruder movement	*mm*
x	intended dimensional length	*mm*
T	track offset	0.875 *mm*
S	scaling factor	1:1

The above derivations are used to establish the exact amount of steps required to achieve 1:1 print scaling. The z-axis part accuracy is achieved via scaling the CAD model height to that of the actual printed part. A test part, such as a cube, with designed height h_{design}, is printed and allowed to cool. The actual height h_{acutal} is measured, and the size ratio difference noted, that is:

$$part\ height\ ratio_{z-axis} = \frac{h_{design}}{h_{actual}} \tag{5.6}$$

This ratio, or difference in dimensionality is noted, and the following "STEPS_PER_MM" parameter adjusted in the config.h software file to adjust the ratio to 1:1. For a Pololu DRV8825 stepper driver with 1/32 micro-stepping, and a stepper motor with 200 steps per revolution, the steps/*mm* figure is derived as follows:

$$Feedrate = \frac{steps/rev}{circ.} = 78.35\ steps/mm \tag{5.7}$$

Where

$$steps\ per\ rev = 200 * \frac{32}{2}$$

$$circ. = \pi d = 13\pi\ mm$$

These steps conclude the fine-tuning of the system.

5.3. Measurement test plan and results

A testing plan is by definition a procedural approach to efficient experimental work for testing a system such as a machine or process. In engineering, the execution of the test plan is intended to evaluate a specific dimension of performance (Figliola, R.S., Beasley, D.E.: 2011, p.6). In the case of the additive manufacturing platform, the locational accuracy, repeatability, print time and speed, and the part dimensionality and roughness related to the adjustment of system parameters are investigated. The ultimate objective of the measurement test plan is to establish the overall precision of the printer, and later contrast the results with those obtainable by standard subtractive processes.

5.3.1. Gantry locational performance

The first experiment performed on the printer is to ascertain the accuracy of the gantry system in locating the print-head at a desired pre-programmed location. Static calibration entails a known value being input into the system under calibrated system conditions, and the system output recorded, with the values of the variables remaining constant throughout the test (Ziegler, J.G., Nichols, N.B: 1942, p.759-768). In the case of testing for the locational accuracy of a 3-axis printer an appropriate test is devised using the origin and end-stops as a probe. A tape measure and high-accuracy +-0.01 *mm* digital vernier calliper are employed to measure distance from the origin to the print-head nozzle centre point.

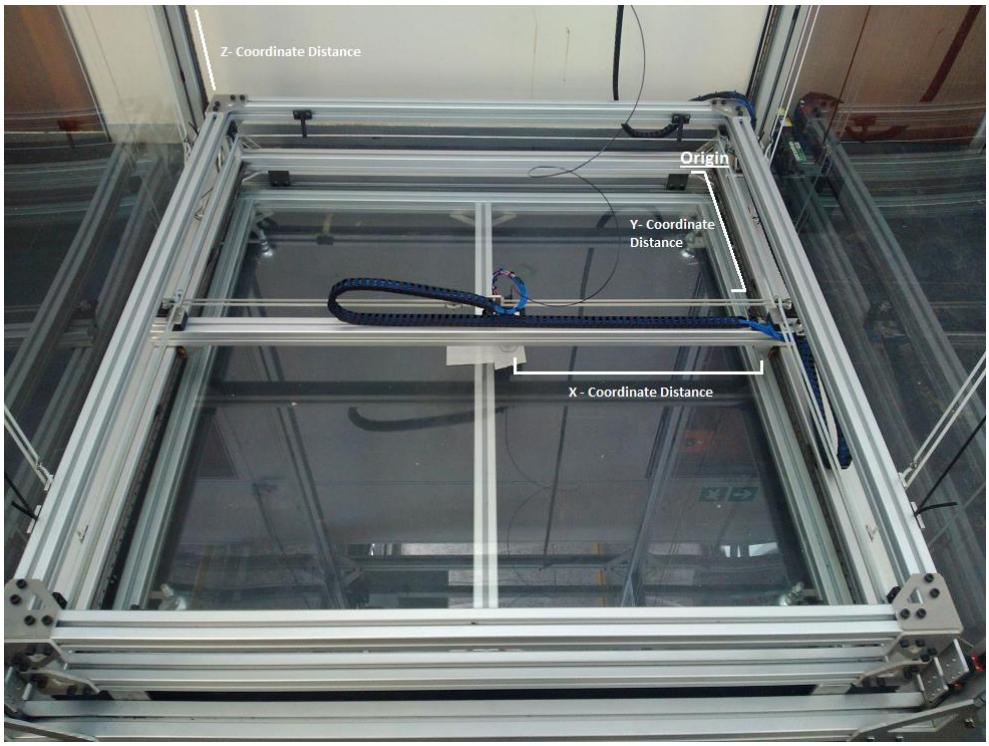

Figure 5.9: 3-Dimensional Measurement Probe Test Setup

The test begins with the nozzle being driven to the calibrated home position as defined in software, at coordinate (0, 0, 0). Thereafter, the gantry print-head is instructed via G-code to position itself at coordinate (2, 2, 2), that is, exactly 2.71 *mm* away from the probe. At this point, the distance

is noted and this value recorded. The print-head is instructed to move to coordinate location (100, 100, 100) and then directly back to the original (2, 2, 2) 'test' position. At this point the measurement is taken again, and any errors noted. This process is repeated for coordinate positions in 100 *mm* ascending increments. The results of the experiment are presented in Table 5.5.

Table 5.5: Printer Locational Error Measurement Data

Set point (*mm*)	**Test I (*mm*)**	**Test II (*mm*)**	**Test III (*mm*)**
X, Y, Z	**X, Y, Z**	**X, Y, Z**	**X, Y, Z**
100, 100, 100	0.040, 0.120, 0.050	0.020, 0.030, 0.030	0.040, 0.010, 0.100
200, 200, 200	0.090, 0.070, 0.040	0.040, 0.060, 0.090	0.060, 0.070, 0.080
300, 300, 300	0.040, 0.060, 0.090	0.080, 0.040, 0.070	0.060, 0.100, 0.090
400, 400, 400	0.030, 0.040, 0.070	0.040, 0.020, 0.030	0.100, 0.030, 0.090
500, 500, 500	0.110, 0.010, 0.060	0.060, 0.080, 0.100	0.090, 0.040, 0.080
600, 600, 600	0.030, 0.080, 0.100	0.100, 0.050, 0.130	0.030, 0.090, 0.050
700,700, 700	0.060, 0.040, 0.090	0.090, 0.070, 0.030	0.120, 0.050, 0.070
800, 800, 800	0.020, 0.090, 0.110	0.030, 0.010, 0.010	0.010, 0.090, 0.040
900, 900, 900	0.090, 0.060, 0.070	0.030, 0.040, 0.130	0.080, 0.070, 0.120
1000, 1000, 1000	0.050, 0.050, 0.140	0.090, 0.160, 0.060	0.060, 0.100, 0.040
1100, 1100, 1100	0.040, 0.010, 0.110	0.120, 0.040, 0.090	0.110, 0.070, 0.100
1200, 1200, 1200	0.020, 0.050, 0.080	0.020, 0.070, 0.080	0.030, 0.090, 0.040

Following collection of the locational errors, the pooled data which is collected so as to provide a better statistical estimate of the measured locational errors is investigated from a theoretical standpoint. The sample mean for each locational measurement is the sum of probe readings divided by the number taken:

$$\bar{x} = \frac{1}{N}\sum_{i=1}^{N} x_i \tag{5.7}$$

$\bar{x}$	measurement mean	*mm*
N	number of measurements	*i*
x_i	measurement reading	*mm*

The sample standard deviation, known as the average deviation of test readings from the mean, is:

$$s_x = \sqrt{s_x^2} = \left(\frac{1}{N-1}\sum_{i=1}^{N}(x_i - \bar{x})^2\right)^{1/2} \tag{5.8}$$

s_x	standard deviation	*mm*

It is also required to know the precision of a reading at a given probability or confidence level of 95 %:

$$\pm t_{v,P} S_x \tag{5.9}$$

$$v = N - 1 \tag{5.9.1}$$

$t_{v,P}$	coverage factor	constant
P	confidence level	%

The Chi-Squared probability distribution, which estimates reading discrepancy due to random chance, is:

$$\sqrt{\frac{v s_x^2}{\chi^2_{0.025}}} < \sigma < \sqrt{\frac{v s_x^2}{\chi^2_{0.975}}} \tag{5.10}$$

σ	random error range	*mm*
χ^2	Chi-squared constant	const.

For the printer positioning tests performed, as highlighted in Table 5.6, the statistical data is as follows:

Table 5.6: Printer Locational Error Statistical Data

Location Set Point (*mm*)	**Mean x**	**Standard Deviation, s_x**	**Coverage Factor, $t_{v,P}$**	**Chi-Square Probability, σ**
100, 100, 100	0.036, 0.058, 0.063	0.013, 0.055, 0.035	+- 0.028, 0.119, 0.076	0.101 <σ< 0.242
200, 200, 200	0.069, 0.072, 0.075	0.027, 0.005, 0.029	+- 0.058, 0.011, 0.063	0.061 <σ< 0.145
300, 300, 300	0.066, 0.072, 0.089	0.022, 0.033, 0.009	+- 0.048, 0.072, 0.019	0.062 <σ< 0.149
400, 400, 400	0.058, 0.033, 0.070	0.037, 0.010, 0.031	+- 0.081, 0.022, 0.067	0.075 <σ< 0.181
500, 500, 500	0.091, 0.050, 0.087	0.022, 0.033, 0.017	+- 0.048, 0.072, 0.037	0.066 <σ< 0.159
600, 600, 600	0.058, 0.079, 0.096	0.042, 0.021, 0.038	+- 0.092, 0.046, 0.083	0.093 <σ< 0.223
700,700, 700	0.093, 0.058, 0.070	0.026, 0.016, 0.034	+- 0.057, 0.035, 0.074	0.070 <σ< 0.167
800, 800, 800	0.024, 0.071, 0.057	0.006, 0.045, 0.049	+- 0.013, 0.098, 0.106	0.102 <σ< 0.244
900, 900, 900	0.072, 0.060, 0.113	0.030, 0.013, 0.029	+- 0.065, 0.028, 0.063	0.066 <σ< 0.159
1000, 1000, 1000	0.074, 0.109, 0.083	0.021, 0.054, 0.053	+- 0.045, 0.117, 0.115	0.120 <σ< 0.288
1100, 1100, 1100	0.091, 0.047, 0.106	0.044, 0.030, 0.009	+- 0.095, 0.065, 0.019	0.082 <σ< 0.196
1200, 1200, 1200	0.028, 0.075, 0.072	0.005, 0.023, 0.027	+- 0.011, 0.050, 0.058	0.054 <σ< 0.130
Average:	**x = 0.121 *mm***	**S_x = 0.047 *mm***	**$t_{v,P}$ = +- 0.103 *mm***	**0.079 <σ< 0.190**

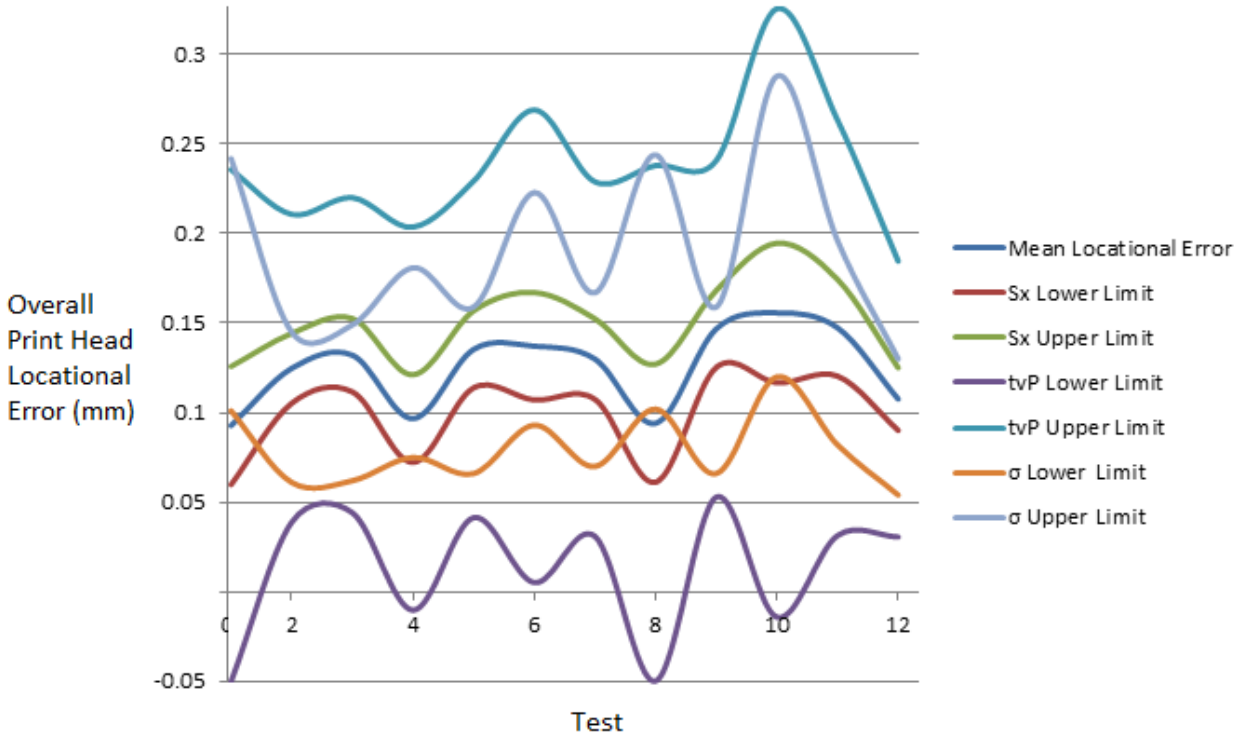

Figure 5.10: Print Head Locational Performance

The relationship between set-point value and the measurement may be compared for linearity using regression analysis. Assuming a linear relationship, the equation of an input-output regression curve is:

$$y_c = a_o + a_1 x = 0.0617424 + 1.000002448x \tag{5.11}$$

$$a_0 = \frac{\sum x_i \sum x_i y_i - \sum x_i^2 \sum y_i}{(\sum x_i)^2 - N \sum x_i^2} = 0.0617424 \tag{5.11.1}$$

$$a_1 = \frac{\sum x_i \sum y_i - N \sum x_i y_i}{(\sum x_i)^2 - N \sum x_i^2} \approx 1.00 \tag{5.11.2}$$

x_i	location set point reading	*mm*
y_i	probe location reading	*mm*
N	number of measurements	i
a_1	function gradient	-
a_o	function y-intercept	-

The ‘fit’ of the measured probe data to the expected linear output can be measured using a correlation coefficient, where a value approaching 1 denotes a very linear and accurate fit as

$$r_{xy} = \frac{N\sum_{i=1}^{N} x_i y_i - \sum_{i=1}^{N} x_i \sum_{i=1}^{N} y_i}{\sqrt{N\sum_{i=1}^{N} x_i^2 - \left(\sum_{i=1}^{N} x_i\right)^2}\sqrt{N\sum_{i=1}^{N} y_i^2 - \left(\sum_{i=1}^{N} y_i\right)^2}} = 1.000001499 \quad (5.12)$$

R_{xy}	correlation coefficient	0.00 to 1.00

Additionally, the random error uncertainty between the measured data can be approximated for the curve:

$$S_{yx} = \sqrt{\frac{\sum_{i=1}^{N}(y_i - y_{ci})^2}{N-2}} = 0.2756\,mm \quad (5.13)$$

S_{yz}	random error uncertainty	*mm*
N	number of test readings	i
y_{ci}	regression predicted reading	*mm*

$$\pm t_{11,95} S_{yx} = \pm 0.6005 \quad (5.14)$$

The regression curve for locational accuracy across a range of distance set-points from 100 *mm* to 1200 *mm* is shown in the figure below:

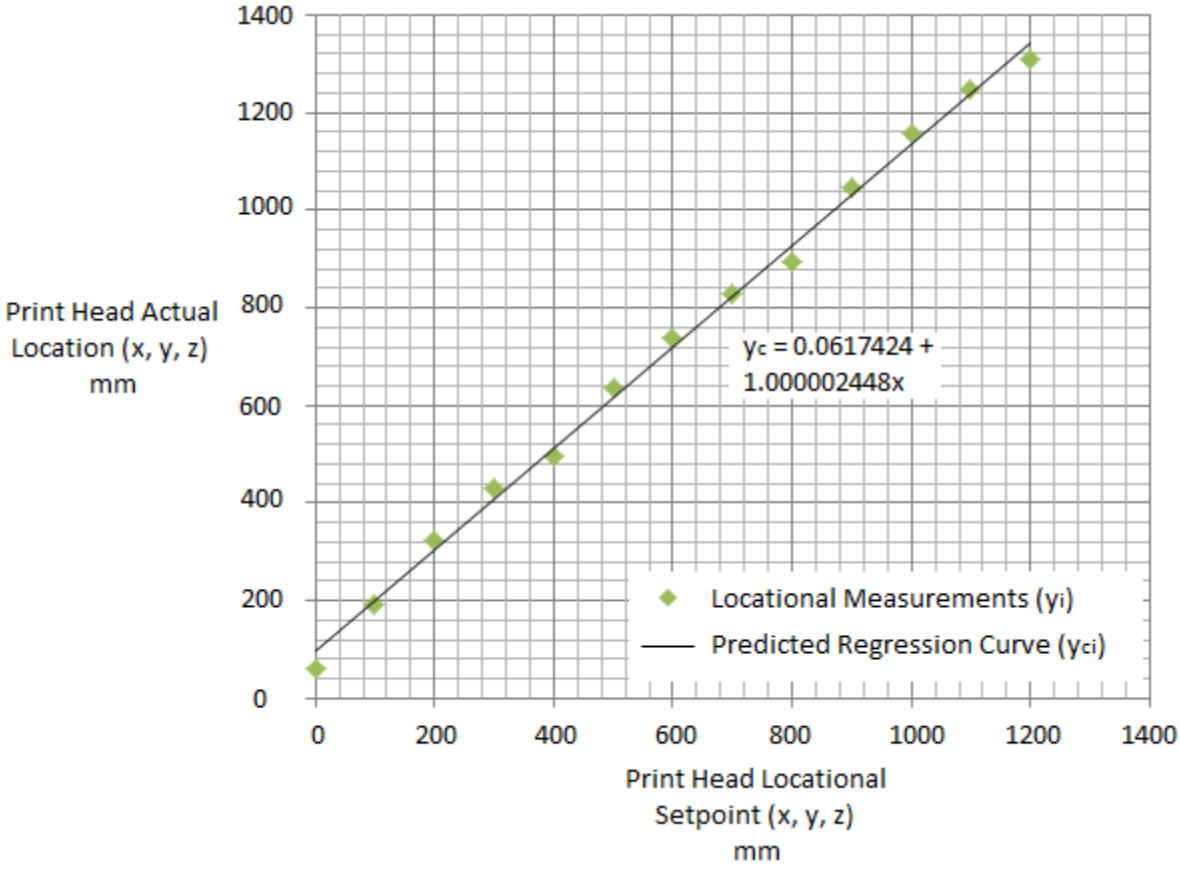

Figure 5.11: Regression Curve for Printer Locational Accuracy Test

Following plotting of the regression curve, a number of measurement errors can be computed based upon these pooled results. It is essential to calculate each individual error contributor, so as to estimate the final full-scale uncertainty of the printer's gantry system. The uncertainty of the four repeated tests due to random error is shown to be:

$$u_x = \pm \frac{t_{v,P} S_{yx}}{\sqrt{N_k}} = 0.3467\, mm \tag{5.15}$$

$$\%u_x = \frac{u_x}{r_o} * 100 = 0.028\,\% \tag{5.16}$$

$\%u_x$	random uncertainty error	%
r_o	range of measurements	*mm*
N_k	number of repeated tests	i

It is observed from the regression plots of Figure 5.11 that the relationship between the measured and measurements are not exactly linear, that is, a linear error develops which is expanded as:

$$u_{L,max} = y_i(x) - y_{ci}(x) = 0.1557\ mm \tag{5.17}$$

$$\%u_{L,max} = \frac{u_{L,max}}{r_o} * 100 = 0.013\ \%\ (0.156\ mm) \tag{5.17.1}$$

Repeatability is defined as the ability of a measurement device to produce the same output value in multiple random tests under identical conditions (Figliola, R.S., Beasley, D.E.: 2011, p.24). Repeatability errors can be found by taking note of the maximum standard deviation over the range of test measurements, that is,

$$S_{x,max} = 0.078\ mm\ \ , r_o = 1200\, mm$$

$$\%u_{Rmax} = \frac{2S_x}{r_o} * 100 = 0.013\%\ (0.156mm) \tag{5.18}$$

Finally, the overall printer locational uncertainty can be deduced by combined all the estimates thus far using the equation:

$$\%u_{overall} = (\%u_o^2 + \%u_c^2 + \%u_{nl}^2 + \%u_x^2 + \%u_{L,max}^2 + \%u_{Rmax}^2)^{0.5} \tag{5.19}$$

$$= 0.034\ \%$$

5.3.2. Part dimensionality, tolerances, and effects of parameter changes on part performance

Part dimensionality, that is, the accuracy of the printer part dimensions, was investigated since low tolerances and variability in the average part size is desired for correct plug and mould manufacturing. Engineering tolerance by definition is the allowable limits of variation in the physical dimensions of an object, space, value, or physical property (Menin, S.: 2012). Typically, in mould production, the tolerance guidelines set out by industry are grouped into three tolerance classes: normal, medium, and fine. For plastic moulding strategies such as ABS, polycarbonate, nylon, and acetyl/acrylic, the suggested tolerances for moulded parts are set out in Appendix E.5.

Parts produced with the printer are to be compared dimensionally to the guidelines given. Part tolerance is tested by designing a 10 mm^3 cube for multiple print tests. Printer parameters including gantry acceleration, gantry velocity, and heater temperature settings were independently adjusted from the minimum threshold values to maximum allowable values and separate print tests performed for each. Thereafter the dimensions of each printed part were measured using a digital micrometre, and the effects of parameter changes noted.

Table 5.7 and Figure 5.13 present the first experimental dataset relating to the effect on printed part dimensional error when gantry acceleration values are ramped up from 0.1 to 0.5 m/s^2.

Table 5.7: Printer Axes Acceleration versus Printed Part Accuracy

Test	**Printer Acceleration Setting (m/s^2)**	**Part Dimensions LxWxH (mm)**	**Total Error (mm) $(L^2+W^2+H^2)^{0.5}$**	**Tolerance Grade**
1	0.1	10.02 x 10.04 x 10.01	0.04	fine
2	0.2	10.01 x 10.09 x 10.05	0.10	fine
3	0.3	10.10 x 10.12 x 10.09	0.18	medium
4	0.4	10.08 x 10.17 x 10.13	0.23	normal
5	0.5	10.27 x 10.34 x 10.15	0.46	normal
Average:		10.09 x 10.14 x 10.08	0.196	medium

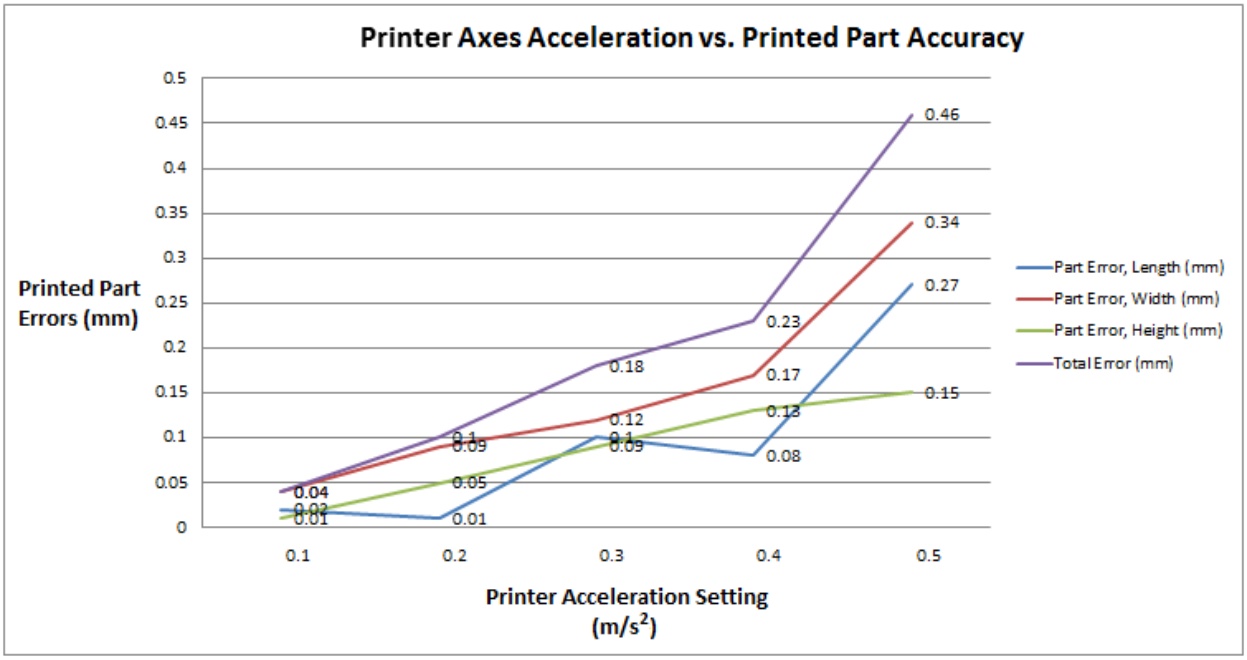

Figure 5.13: Printed Part Dimensional Errors vs. Printer Acceleration

Table 5.8 and Figure 5.14 present data relating to printer axis velocity settings versus part error variances.

Table 5.8: Printer Axes Velocity versus Printed Part Accuracy

Test	Printer Velocity Setting (*m/s*)	Part Dimensions LxWxH (*mm*)	Total Error (*mm*) $(L^2+W^2+H^2)^{0.5}$	Tolerance Grade
1	0.05	10.00 x 10.00 x 10.01	0.01	fine
2	0.10	10.01 x 10.00 x 10.01	0.02	fine
3	0.15	10.03 x 10.01 x 10.02	0.04	fine
4	0.20	10.21 x 10.15 x 10.07	0.27	normal
5	0.25	10.23 x 10.17 x 10.08	0.30	normal
Average:		10.09 x 10.06 x 10.04	0.13	fine

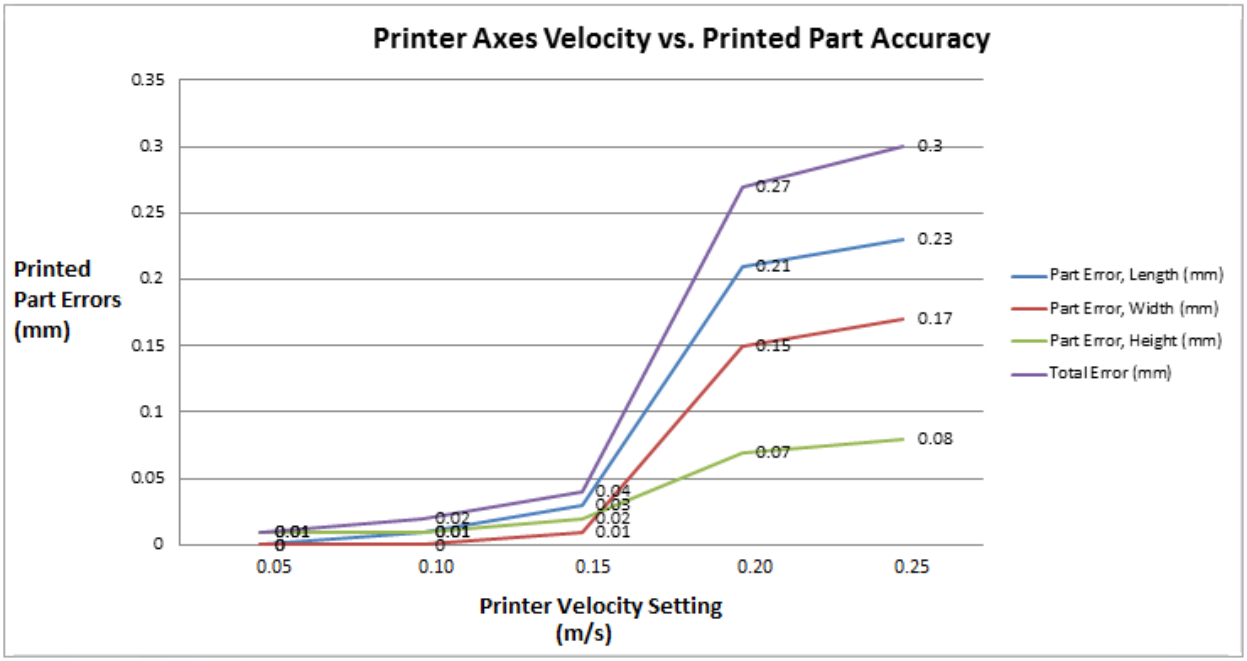

Figure 5.14: Printed Part Dimensional Errors vs. Printer Velocity Settings

Table 5.9 and Figure 5.15 presents data comparing part error versus changes in printing temperature.

Table 5.9: Extruder Heater Temperature versus Printed Part Accuracy

Test	**Heater Temperature Setting (^oC)**	**Extrusion Rate (mm^3/s)**	**Total Error (mm) $(L^2+W^2+H^2)^{0.5}$**	**Tolerance Grade**
1	180	5	0.07	fine
2	190	10	0.02	fine
3	200	15	0.06	fine
4	210	20	0.16	medium
5	220	25	0.20	medium
Average:			0.10	fine

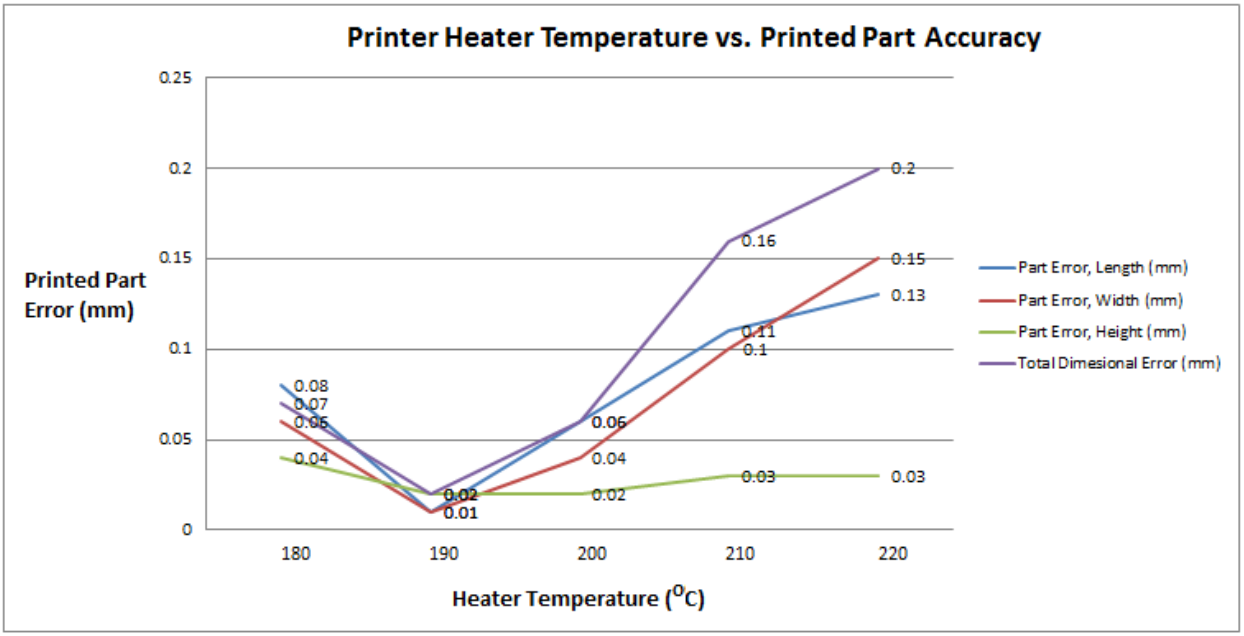

Figure 5.15: Printer Material Heater Temperature versus Printed Part Accuracy

5.4. Chapter conclusion

Chapter 5 detailed the theoretical and physical experimental setup and testing of the additive manufacturing platform with respect to print-head locational performance, part dimensionality, surface roughness, and process cost and timing. In-depth mathematical analysis was performed, and results generated which are to be used in chapter 6 as a contrast against the manufacturing alternative, subtractive CNC machining.

CHAPTER 6

Conclusions and Hypothesis Validation

This final chapter draws on and makes significance of the experimental results gathered in Chapter 5 specifically with respect to the large-scale additive manufacturing platform's printing and technical performance. The results are explained and discussed, as well as overall conclusions drawn about the machine and whether or not it fulfils the hypothesis statement, that is, if it is a suitable manufacturing platform for the production of turbine blade plugs and moulds. Thereafter further potential improvements and applications are explored, and the lessons learnt during the research process presented.

6.1. Additive manufacturing process performance evaluation

In the previous chapter, full technical performance testing of the large-scale additive manufacturing platform was performed and the results amalgamated and synthesized. Tests on the apparatus were conducted and formulated so as to achieve the research objective, that is, to ascertain if an additive manufacturing process is a suitable substitute for mould production. Experiments were compartmentalized into two main areas, namely, the statistical performance analysis of the 3-axis gantry's locational accuracy, and the effects which changes in system's parameter changes had on the quality of the printed parts produced. These results are discussed and conclusions drawn henceforth.

6.1.1. Theoretical gantry locational performance

Prior to physical testing of the 'x-', 'y-', and 'z-' axes performance, the theoretical accuracy, repeatability, precision, and machine errors were calculated using statistical analysis, as highlighted in Tables 5.1 and 5.2 respectively. Theoretical locational performance is estimated by combining and in essence averaging the component errors specified by manufacturers for each component of which the machine is built. Table 5.1 presents the manufacturer-specified range, repeatability, and accuracy of the motors, linear rail, timing belts, and drivers which make up the printer drive system. Initial inspection of Table 5.1 reveals a significant reduction in positional accuracy occurring due to belt stretch in the BrecoFlex T2.5 timing belts at 1.04 *mm/m* accuracy and 0.508 *mm* repeatability. Linear railing and stepper motor influences are less profound at 0.04 *mm* for translational positioning, 23 μm for running parallelism, and 0.05625 ^{O}, or 0.006 *mm* for motor rotational accuracy. The possible reasoning for this less-significant impact is as a result of the railing being a solid steel member as opposed to the flexible nature of timing belt's composite construction, good Class 'C' machining accuracy, and accurate 1/32 micro-stepping

achieved via the Polulu DRV8825 stepper motor driver boards. Referring to Table 5.2, component errors, in the form of theoretical Design-Stage Uncertainty, μ_d, are calculated and the an estimate of 1.04 *mm* locational error produced for the entire gantry system. This figure proposes that should the x, y, or z, axes be moved electronically to a set destination, the overall theoretical error in the print-head's new position can be estimated at 1.04 *mm*.

6.1.2. Real-life gantry locational performance

Physical testing of the printer locational performance seeks to verify the theoretical results obtained above, or to surpass the performance predication thereof. Testing, as explained in section 5.3.1, made use of a digital vernier to measure the distance from the specified origin that the print-head had travelled when given a specified jog command. The measurement tests, repeated thirty-six times, provide a good estimate of machine error within a 0.001 *mm* resolution. Referring to Table 5.5, it can be observed that for various location set-points between (100 *mm*, 100 *mm*, 100 *mm*) and (1200 *m*m, 1200 *m*m, 1200 *mm*), the locational error magnitudes do not follow a specific trend but are produced randomly, independent of the location input command. The data reveals that the errors range between 0.02 *mm* to 0.14 *mm*, with average errors being larger for the vertical axis, as opposed to the horizontal 'x' and 'y' axes. It is surmised that the reason thereof is due to the longer 5 *m* travel distance of the vertical axis, with belt stretch and oscillation of the axis occurring when changing velocity, as opposed to the sufficiently-tensioned horizontal axes timing belts and shorter, more rigid linear rail configuration. Additionally, another possible factor relating to the increased error in the z-direction may be due to friction and slight overload of the vertical stepper motors during the gantry lifting process. According to D.W. Jones, stepper motors may lose steps and locating accuracy when at the limit of their torque capacity (Jones, D.W.: 2004).

Referring to Table 5.6, which consolidates the test data and presents the mean, standard deviation, coverage factor, and Chi-Square probability distribution for the printer's locational performance, it can noted in the last row that the actual mean accuracy achieved by the machine is 0.121 *mm*, significantly better than the theoretical performance calculated via design-stage uncertainty processes as discussed in section 6.1.1. Furthermore, the standard deviation, coverage factor, and Chi-Square probability figures indicate by how much the mean locational error may vary, that is, the average performance lies within S_x = 0.047 *mm*, +-0.103 *mm*, and 0.079 *mm* < σ < 0.190 *mm* at a 95 % probability. Therefore further deduction of the Table proposes a final gantry locational accuracy within the range of 0.121 *mm* +- 0.190 *mm*. Attention needs to be brought to the graphical representation of the printer's accuracy, as shown in Figure 5.10. There appears to be no discernable correlation between printer accuracy and the print-head position, with the mean locational error being rather constant and oscillating around 0.12 *mm*. However, it may be observed that the error interval, namely the upper and lower standard deviations, increase in magnitude as the print-head is commanded to locations (900, 900, 900), (1000, 1000, 1000), and upwards. It is surmised that the 'drift' in the z-axis is as a result of excess stretch in the counterweighted belts, as the counterweight is at the bottom of the structure, increasing belt length and hence displacement. The linearity of measured data is displayed on the regression plot in Figure 5.11, highlighting a nearly perfect correlation between measured position and expected print-head position as indicated by the correlation

coefficient value of R_{xy} = 1.000001499 in equation 5.12. In Figure 5.11, print-head actual location oscillates by approximately 0.15 *mm* around the set-point, as evidenced by the green readings surrounding the y_c = 1.000002448x + 0.0617424 theoretical linear regressive plot.

The large-scale platform's performance is contrasted against currently available machine variants in Figure 6.1 with relation to price, size of parts produced, object surface resolution, and dimensional accuracy. The data gathered highlights that the large-scale printer performs well with respect to working volume and print resolution, while not sacrificing much accuracy despite its size. The reason for the low resolution and relatively good accuracy at 0.012 *mm* and 0.121 *mm* comes down to the small diameter of the printing nozzle at 0.3 *mm* and the combination of high-quality machined components, in addition to stringent assembly and calibration methods. However, due to the large printing volume of 8.112 m^3 and machine's physical enormity, invariably machine cost is high at ZAR 115'000 compared with smaller machines such as the FORMLABS FORM2 and M3D Micro printers at ZAR 55'000 and ZAR 7500 respectively. Being a fused deposition modeller, the machine compares well and improves upon the accuracy achieved by the smaller M3D fused deposition printer available commercially, but cannot achieve the part accuracy available to Stereo-lithographic printers and machined components which have accuracy ratings of 0.05 *mm* and 0.012 *mm*. The limitations are inherent to the fused deposition modelling printing process and print accuracy can only be improved up to a certain point, that is, 0.1 *mm*, without significant budget overhauls, and modification of existing motor and drive components.

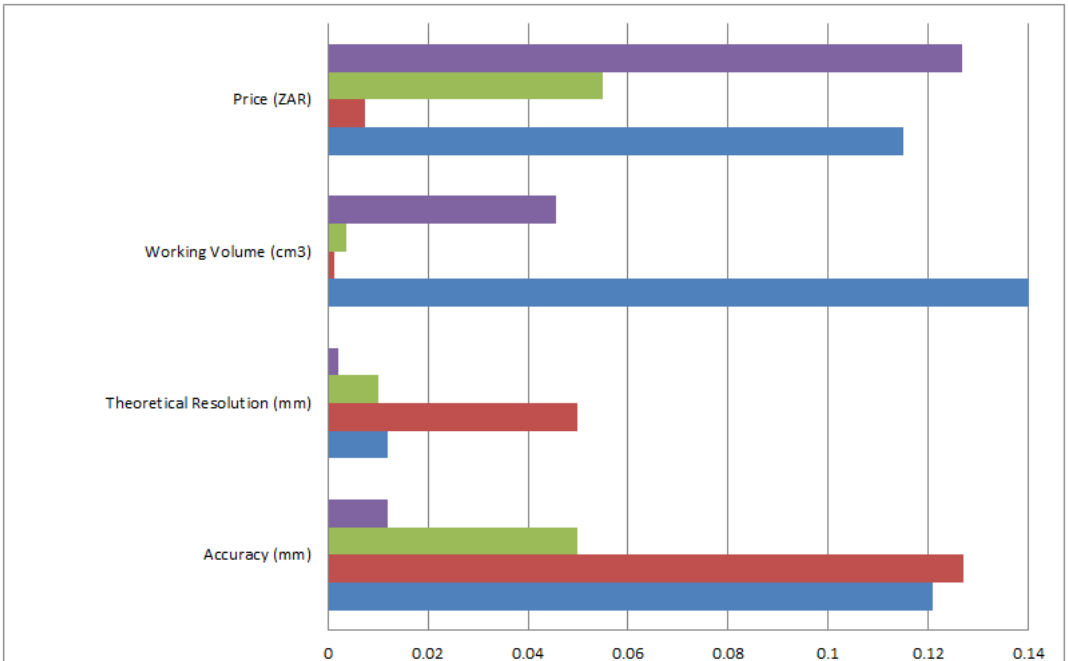

	Accuracy (mm)	Theoretical Resolution (mm)	Working Volume (m3)	Price (ZAR)
Tormach PCNC 1100 Personal CNC Mill	0.012	0.002	0.0455355	126'800
FORMLABS FORM 2 RESIN Printer	0.05	0.01	0.0036707	55'000
M3D Micro 3D Printer	0.127	0.05	0.0013929	7500
Large Scale Hybrid Printer	0.121	0.012	8.112	115'000

Figure 6.1: Comparison of Various 3-Axis Machine Locational Performance

6.1.3. Effects of parameter variation on printer performance

Velocity variation

As presented in section 5.3.2, printer performance and part reproduction accuracy was tested for various velocity, acceleration, heater temperature settings. The results thereof are presented graphically in figures 5.13 to 5.15. Referring to figure 5.13, it is observable that for low gantry velocity settings starting at 0.05 m/s, the total dimensional error of parts increases at a low rate from 0 to 0.15 *m/s*. Up until that point the total part error reading is only 0.04 *mm*. However, when velocity settings are increased over 0.15 *m/s* the total error increases substantially to 0.27 *mm*. It is theorized that this 0.15 *m/s* velocity 'cap' is due to the stepper motors losing steps at higher velocity settings, and losing positioning torque. At velocity settings above 0.15 *m/s*, the stepper motors are therefore unable to reproduce the same positioning accuracy afforded. Other factors may be the axes inertial effects, that is, the faster the print-head and associated drive-train is moving, the more time it takes for the motors to change and position the print-head, thus resulting in unanticipated positioning 'overshoot'. Finally, belt shift or backlash, and stretch of belting during operation above 0.15 *m/s* may play a role in the increased part error accumulation.

Acceleration variation

Similarly, in Figure 5.13, the printer axes acceleration settings versus printed part error follows a roughly linear trend, with errors increasing proportionally when acceleration settings are increased, from 0.04 *mm* at 0.1 m/s^2, up to 0.23 *mm* at 0.4 m/s^2. It should be noted however that increasing the acceleration beyond 0.4 m/s^2 results in a degradation of positioning accuracy further, where the graph relationship becomes almost exponential, with total part error reaching 0.46 *mm* at 0.5 m/s^2. The factors are synonymous with those experienced during the velocity tests.

Material heater temperature variation

The final parameter to be adjusted and the effects on part accuracy noted is the temperature at which the material is to be melted. PLA thermoplastic was employed for the tests due to availability, ease of printing when compared to ABS plastic, and the biodegradability of PLA. The tests are performed between the recommended melting temperature range for the material, that is, between 180 ^{O}C and 220 ^{O}C. As seen in Figure 5.15, printed part error is affected less by temperature at 0.2 *mm* maximum error when compared with velocity and acceleration variations of 0.3 *mm* and 0.46 *mm* respectively. The temperature versus error data obtained presents some interesting findings on part accuracy. When a part is produced at the minimum printing temperature 180 ^{O}C, total part dimensional error is 0.08 *mm*, and decreases to 0.02 *mm* when the printing temperature is increased to 190 ^{O}C. However, when test parts are printed at successively higher temperatures of 200, 210, and 220 ^{O}C, the part error again increases to higher values of 0.06, 0.16, and 0.20 *mm*. The reason for a larger part error at 180 ^{O}C when compared to the 190 ^{O}C setting is as a result of the material not melting quickly enough for deposition, thus causing an under-extrusion of material and therefore inaccurate part volume and density. Conversely, higher material melting temperatures cause the PLA material to bubble and bind with atmospheric gases, causing larger part volumes and thus dimensional errors and part surface defects. Thus, referring to Figure 5.15, it is surmised that the optimal printing temperature for PLA is 190 ^{O}C to eradicate material-gas cohesion, but also prevent material under-extrusion.

6.2. Research objectives achieved

In essence, the purpose of this paper and the research performed was to investigate rapid prototyping as a manufacturing method for wind turbine blade plug and mould production, and then conceptualise, design, and manufacture a machine which would perform such a task. The machine would as such, have to be performance tested to assess the suitability of said machine for the application. With regards to the research objectives which were set out in Chapter 1, all objectives were achieved, namely, a large-scale additive manufacturing platform was conceptualized, designed, manufactured, and performance tested, and fulfilled the technical metrics:

- The machine has a total print envelope of 1.2 *m* x 1.2 *m* x 5 *m*, that is, 7.2 m^3.
- The platform has the capability to print with any commercially-available filament material, and has been tested with ABS and PLA plastics.
- The design incorporates a 12 *V* DC 80 *Ah* deep cycle battery power supply with continuous recharge, allowing continuous uninterruptable printing of blade plugs.
- The print-bed, upon which the designed part is produced, is a separate assembly and is able to be moved away from the machine following print completion.
- Positioning accuracy and repeatability achieved through testing is 0.121 *mm* (Table 5.6) and 0.156 *mm* (Eq. 5.18) respectively, which just satisfies the criteria set out of 0.1 *mm* for both.
- The system achieves a 0.1 *mm* system deflection at 160 *mm/s* print-speed (Figure 5.14), which exceeds the research objectives target by 10 *mm/s*.

6.3. Fulfilment of hypothesis statement

The final research objective which requires verification of achievement is that of suitability of the large-scale manufacturing platform for the production of blade plugs with regards to machine accuracy. Conventionally, blade plugs are machined to approximate dimensions using three-axis CNC machines. Thereafter the plugs are laid over with tooling paste or laminate and are further machined to the correct dimensions. Further manual sanding allows a glass-like smooth finish to be realized (Marsh, G.: 2008). Dimensional accuracy and surface finish achieved for CNC milling is in the region of 0.025 to 0.050 *mm*, and surface roughness of 50 μm. Prior to manual polishing, the blade plugs achieve the above dimensional accuracy.

In Chapter 1, the criteria laid out for suitability via additive manufacturing were a part dimensional accuracy of 0.1 *mm* and a surface roughness measurement of 50 μm. In performance testing the locational ability of the x-y-z gantry system, it was found that the print-head was able to locate to an accuracy of 0.121 *mm* with 0.013 % uncertainty, as shown in Chapter 5, section 5.3.1. Additionally, print repeatability of 0.156 *mm* was achieved, with resolution determined by the print nozzle, in the region of approximately 0.1 *mm*. These performance attributes fall in line with those required by industry for the production of turbine blade plugs, as well as mould dimensional standards as found in Appendix E.5, thus, the additive

manufacturing technique compares admirably in accuracy and surface finish to the CNC method. Additionally, both methods require that the plug be further sanded and polished via manual methods. Therefore, the large-scale additive manufacturing platform satisfies the hypothesis statement and research objectives as laid-out, and is an acceptable manufacturing method for production of blade plugs.

6.4. Recommendations for future work

Upon further reflection following research completion, possible machine improvements were noted. The system at present contains an open-loop stepper motor control system. This system could be upgraded with an encoder closed loop feedback system to more accurately measure axis travel. Additionally, development and manufacture of the pellet-extruding print-head concept could be undertaken to exploit the financial benefits of the new technology, so as to improve the environmental-'friendliness' of the design. Finally, a host of other print materials such as carbon-fibre, ceramic-polymer, and metal-composite filaments could be tested with the printer as alternatives to PLA and ABS for production of moulds and plugs.

6.5. Chapter conclusion

The final chapter discusses the results obtained by the performance testing of the large-scale rapid prototype, and attempts to answer the hypothesis statement, and whether or not the technical performance of the machine coincides with the objectives laid out at the onset of the research. Furthermore, recommendations for future work in large-scale additive manufacturing and improvement of the machine are explored.

Bibliography

ABS. Stratasys Inc. (2007).

ABS Filament Prices. MatterHackers.com [online]. Available at <www.matterhackers.com/store/3d-printer-filament>. Accessed on [14/01/2016].

Al-Gurnawi, R. (2015). Preventing warping and improving adhesion of high temperature PLA: A practical guide. Available at <thingiverse-production-new.s3.amazonaws.com/>. Accessed on [13/01/2016].

American Wind Energy Association (2014). U.S. Wind Energy Annual Market Report (2013). Available at <www.awea.org/amr2013>. Accessed on [11/01/2016].

Augarten, S. (1983). The Most Widely Used Computer on a Chip: The TMS 1000. State of the Art: A Photographic History of the Integrated Circuit (New Haven and New York: Ticknor & Fields). ISBN 0-89919-195-9. Accessed on [12/01/2016].

Baeurle SA, Hotta A, Gusev AA (2006). "On the glassy state of multiphase and pure polymer materials". Polymer 47: 6243–6253. doi:10.1016/j.polymer.2006.05.076.

Bowyer, A., Reprap Options. Available at <http://reprap.org/wiki/RepRap_Options#Slicing_Software>. Accessed on [06/01/2016].

Marshall, B., How Stereolithography 3-D Layering Works. Howstuffworks Infospace LLC. Accessed on [14/01/2016].

Chee Kai Chua; Kah Fai Leong, Chu Sing Lim, (2003). Rapid Prototyping. World Scientific. p.124. ISBN9789812381170.

Darnell, W.H., & Mol, E.A.J. (1966), SPE Journal. p12, p20.

Deckard, C. (Oct 17, 1986) "Method and apparatus for producing parts by selective sintering", U.S. Patent 4,863,538, published September 5, 1989.

Degarmo, E. Paul; Black, J.; Kohser, Ronald A. (2003), Materials and Processes in Manufacturing (9th ed.), Wiley, p. 223, ISBN 0-471-65653-4.

Entwistle, J. (November 1, 2011) Separating Rack and Pinion Myths from Reality. Motion System Design. Retrieved from http://machinedesign.com/motorsdrives/separating-rack-and-pinion-myths-reality. Accessed on 21/04/2016.

Faludi, J. Bayley, C. Bhogal, S. Iribarne, M. (2014). Comparing Environmental Impacts of Additive Manufacturing vs.TraditionalMachining via Life-Cycle Assessment. Available at <escholarship.org/uc/item/0gv882qk>. Accessed on [11/01/2016].

Garlotta, D. (2001). A Literature Review of Polylactic Acid. Journal of Polymers and the Environment Vol.9, Issue 2.

Gibson, I., Bartolo, PJ. (2011) Stereolithography: Materials, Processes, & Applications. p.61, p.62. ISBN: 978-0-387-92903-3.

Grieser, F. (November 12, 2015) 16 Common 3D Printing Problems and Solutions. Available from <all3dp.com/common-3d-printing-problems-and-their-solutions/>. Accessed on [26/05/2016].

Grimm, Todd (2004) User's Guide to Rapid Prototyping. SME. p. 24. ISBN978-0-87263-697-2. Accessed on [06/01/2016].

Guide to Casting and Moulding Processes (2006). *Engineered Casting Solutions Magazine*. p15. Accessed on [15/01/2016].

Gutierrez-Miravete, E. (2015). Abs for 3D Printer System Acrylonitrile Butadiene Styrene Material Data Sheet. Available at <ewp.rpi.edu/hartford/~ernesto/F2014/MPT/MaterialsforStudents/Sayre/Other/>. Accessed on [13/01/2016].

Heater Settings for Polycarbonate 3D Printing. Reprap Community Forum. Available from <reprap.org/wiki/Polycarbonate>. Accessed on [13/01/2016].

Helisys, Inc., (Oct 10, 1995) Laminated Object Manufacturing Apparatus and Method. US5876550A.

Hilton, P.D., Jacobs, P.F. (2000). Rapid Tooling: Technologies and Industrial Applications. New York: Marcel Dekker.

IRENA (June 2012). Renewable Energy Technologies: Cost Analysis Series. IRENA Working Paper.Vol.1 Issue 3.

ISO 11357-2 (1999). Plastics – Differential scanning calorimetry (DSC) – Part 2: Determination of glass transition temperature.

JCGM 200:2008 International vocabulary of metrology — Basic and general concepts and associated terms (VIM)

Kellens, K., Yasa, E., Renaldi, W., Dewulf, J.P., Kruth, Duflou, J.R. (Aug 17 2011). *Energy and Resource Efficiency of SLS/SLM Processes*. Dept. of Mechanical Engineering. Leuven Engineering College.

Kohan, Melvin (1995). Nylon Plastics Handbook. Munich: Carl Hanser Verlag. p. 2.ISBN1569901899.

Kruth J.P., Wang X., Laoui T., Froyen L., (2003), Lasers and materials in selective laser sintering, Assembly Automation, Vol.23 Iss 4 p.357 - 371.

Kruth, J.P., Leu, M.C., & Nakagwa, T. (1998) Progress In Additive Manufacturing and Rapid Prototyping. Cirp Annals - Manufacturing Technology. Vol. 47, Issue 2. Pp.525-pp.540. Retrieved from <www.sciencedirect.com/science/article/pii/S0007850607632405>. Accessed on [11/01/2016].

Laoui, T., Kruth, J.P., Froyen, L. (1998), Influence of powder parameters on selective laser sintering of tungsten carbide - cobalt, Proc. 7" Europ. Conf. on Rapid Prototyping and Manuf., p.271-280.

Levasseur, M. (April 2010). 3D Printing Filaments - A Quick Guide to Choosing 3D Printing Plastics.Rotor Drone Magazine. March/April Issue. Available at <http://rotordronemag.com/wp-content/uploads/2015/07/3d-Printing_FINAL.pdf>. Accessed on [13/01/2016].

Lipson, H., Francis C. Moon, J.H., Paventi, C. (2004) "3-D Printing the History of Mechanisms." Journal of Mechanical Design J. Mech. Des. p.1029-033.

Liptak, Bela G. (2005). Instrument Engineers' Handbook: Process Control and Optimization. CRC Press. p. 2464. ISBN 978-0-8493-1081-2.

Lynch M. (Jan. 4th 1997) "Key CNC Concept #1—The Fundamentals Of CNC", Modern Machine Shop. Accessed [12/01/2016].

Martin, O; Avérous, L (2001). "Poly(lactic acid): plasticization and properties of biodegradable multiphase systems". Polymer 42 (14): 6209–6219.

Masoud, D., Mohajer, A., Behrouzifar, A., Jalali, R., Schneider, G.E. (14-26 July 2014) Evaluating The Effect Of Blade Surface Roughness In Megawatt Wind Turbine Performance Using Analytical And Numerical Approaches. 10th International Conference on Heat Transfer, Fluid Mechanics & Thermodynamics. Orlando Florida.

Menin, S. (May 10, 2012) Working with Dimensional Tolerances. Machine Design Online Magazine. Available at <machinedesign.com/materials/working-dimensional-tolerances>. Accessed on [13/06/2016].

McCracken, H. (March 4th 2013) *How an 83-Year-Old Inventor Beat the High Cost of 3D Printing. Time Magazine*. Retrieved from <techland.time.com/2013/03/04/how-an-83-year-old-inventor-beat-the-high-cost-of-3d-printing/>. Accessed [5/11/2016].

Mohanty, A.K., Misra, M., and Lawrence T. (2005) Natural Fibres, Biopolymers, and Biocomposites, volume 1. CRC Press, Boca Ralton, FL, 1st edition.

Molding & Machining Glossary (2016) Available from <www.protolabs.com/resources/glossary>Accessed on [14/01/2016].

Narayan, K. Lalit (2008). Computer Aided Design and Manufacturing. New Delhi: Prentice Hall of India. p3. ISBN812033342X

Oxford Dictionary. (2014). In: Oxford Dictionary, 1st Ed. [online] Retrieved from <oxforddictionaries.com/definition/english/mould. Accessed on [12/01/2016].

Painter, Paul C.; Coleman, Michael M. (1997). Fundamentals of polymer science : an introductory text. Lancaster, Pa.: Technomic Pub. Co. p. 1.ISBN1-56676-559-5.

Pallermo, E. (Sept 19, 2013) Fused Deposition Modelling: Most Common 3D Printing Method. Available on <www.livescience.com//39810-fused-deposition-modeling>. [06/01/2016].

Parvin, M., Williams, J. (1975). "The effect of temperature on the fracture of polycarbonate". Journal of Materials Science 10(11): 1883. Bibcode:1975JMatS..10.1883P

Peek, N. (Sept. 2010). Rapid Prototyping of Green Composites. Massachusetts Institute of Technology. p.3.

Pham, DT. Dimov, SS. (2001) Rapid Manufacturing - The Technologies and Applications of Rapid Prototyping and Rapid Tooling.Springer. ISBN-13: 978-1-4471-0703-3.

Polytetrafluoroethylene (CHEBI:53251). Available from <ebi.ac.uk>. Retrieved [04/04/16].

Reddy, J.N. (2006). *An Introduction to the Finite Element Method* (Third ed.). McGraw-Hill. ISBN 9780071267618.

REN21 (2014). Renewables 2014: Global Status Report" (PDF). p.13,17,21,25. ISBN978-3-9815934-2-6. Retrieved on [08/01/2016].

Renault, T. (1996). Selective reinforcement of photo resins with continuous fibres using 3D composite photolithography, Journal of Advanced Materials, p.8-12.

Rep-Rap Glossary. Available from <http://reprap.org/wiki/Glossary>. Accessed on [12/01/2016].

Robinson, David J. (March 1969) Dynamic Analysis of Permanent Magnet Stepping Motors. NASA Technical Note (NASA TN D-5094). Lewis Research Center.

Root, TL. (2011). Fingerprints of Global Warming on Animals & Plants [Online]. Available on <nature.com/nature/journal/v421/n6918/abs/nature01333>.Accessed on [08/01/2016].

Rutkowski, J. V.; Levin, B. C. (1986). "Acrylonitrile-butadiene-styrene copolymers (ABS): Pyrolysis and combustion products and their toxicity: a review of the literature". Fire and Materials 10 (3–4): 93.

Sachs, E. (1994). 3D Printing of Functional Parts and Tooling, Proc. IMS Int. Conf. On Rapid Product Development, Stuttgart, p.93-106.

Serini, V. (2000). Polycarbonates in Ullmann's Encyclopedia of Industrial Chemistry, Wiley-VCH, Weinheim.

Sher, D. (2015). *Cruising Through Euromold, Day 2: Seeing the Low-Cost SLS 3D Printers.* 3D Printing Industry [online]. Availalble at <3dprintingindustry.com/2015/09/24/cruising-euromold-day-2-sls-3d-printers/>. Accessed on [14/01/2016].

Smallman, R. E., R.J. Bishop. (1999). Modern Physical Metallurgy and Materials Engineering. 6th ed. Oxford: Butterworth-Heinemann.

Smitha, M., Venkataramanan, M. (March 2011). Causes and Effects of Global Warming. Indian Journal of Science and Technology.Vol.4 Issue 3. ISSN: 0974-6846.

Södergård, A., Stolt, M. (February 2002). Properties of Lactic Acid Based Polymers and Their Correlation with Composition. Progress in Polymer Science 27 (6): p.1123–1163.

Speight, J.G., Lange, N.A. (2005). McGraw-Hill, ed. Lange's Handbook of Chemistry (16 ed.). p. 2.807–2.758. ISBN0-07-143220-5.

Srinivasan, V., Bassan, J. (2012) 3D Printing and The Future Of Manufacturing. Retrieved on [06/01/2016].

Stierstorfer, J. (2006). Solar Generation - Solar Electricity for Over One Billion People and Two Million Jobs by 2020. European Photovoltaic Industry Association. Retrieved from <www.env-edu.gr>. Accessed on [08/01/2016].

Taylor, John Robert (1999). An Introduction to Error Analysis: The Study of Uncertainties in Physical Measurements. University Science Books. p. 128–129. ISBN 0-935702-75-X.

The Open University UK (2000). T838 Design and Manufacture with Polymers: Introduction to Polymers, p.9. Milton Keynes: The Open University.

Timing Belt Theory (2006). Published by Gates Mectrol, Inc. p.5-7. Retrieved from <www.gatesmectrol.com>. Accessed on [3/5/2016].

Vlachopoulos, J. (1982) Numerical Simulation of a Single-Screw Plasticating Extruder. Polymer Engineering and Science. Retrieved from <www.researchgate.net/publication/229728748>. Accessed on [20/04/2016].

Walker, D.M. (1966). Chemical Engineering Science. p21, p975.

White, D. (2004) “Reduction in Carbon Dioxide Emissions: Estimating the potential contribution from wind power.” Technical report, Renewable Energy Foundation.

Yousefian, O. & Tarbutton, J.A. (2015). Prediction of Cutting Force in 3-Axis CNC Milling Machines Based on Voxelization Framework for Digital Manufacturing. Procedia Manufacturing. Vol. 1. p.512-521. Available from <www.sme.or/namrc>. Accessed on [18/05/2016].

Zahid, M.N.O. (2014) *Controlled (CNC) Machining for Rapid Manufacturing Processes*. PhD Thesis.Loughborough University.

Appendices

A Appendix - Design Calculations

A.1. Timing belt and pulley viability derivations

It is necessary to calculate the effective forces imposed on a pulley system drive implementation, so as to assess the viability of the proposed solution.

As with all rotational systems, the pulley angular velocities can be derived from the rotational speed as:

$$\omega_{1,2} = (\pi n_{1,2})/30 \quad \text{(A1.1)}$$

$\omega_{1,2}$	pulley angular velocity	*rad.s*$^{-1}$
$n_{1,2}$	pulley rotational speed	*rev/min*

According to Gates, (Gates Mectrol Belt Theory: p.6) the '*effective tension generated at the driver pulley is the actual working force that overcomes the overall resistance to belt motion'*. Since the 3d printer drive system is representative of a power transmission drive system, the resistance to motion occurs at the driven pulley. Then the torque requirement at the driver can be derived as follows:

$$M_1 = T_e \frac{d_1}{2} = \frac{M_2}{\eta} . \frac{d_1}{d_2} = \frac{P_2 d_1}{\omega_2 \eta d_2} = \frac{P_2}{\omega_1 \eta} \quad \text{(A1.3)}$$

M_1	driving pulley torque	*N.m.*
M_2	torque at driven pulley	*N.m.*
$\omega_{1,2}$	pulley angular velocities	*rad.s*$^{-1}$
$d_{1,2}$	pulley pitch diameters	*m*
P_2	driven pulley power requirement	*W*
η	belt efficiency	0.94→0.96

The load to be transported, in this case the print-head, is attached to a linear slider assembly, which is moved via the timing belt. The load is accelerated via the timing belt and sets up inertial and tensile forces in the belt. The effective tension in the belt, as mentioned earlier, is shown to be:

$$T_e = F_a + F_f + F_w + F_{ab} + F_{ai} \quad \text{(A1.4)}$$

F_a	slider acceleration force	N
F_f	slider bearing frictional force	N
F_w	slider weight component	N
F_{ab}	belt inertial acceleration force	N
F_{ai}	idler pulley inertial force	N

The separate force components of equation A1.4 are given as:

$$F_a = m_s a \quad \text{(A.1.4.1)}$$

m_s	slider mass	kg
a	slider block linear acceleration	$m.s^{-2}$

$$F_f = \mu_r m_s g cos\beta + F_{fi} \quad \text{(A1.4.2)}$$

μ_r	slider dynamic frictional coefficient	*const.*
g	gravitational acceleration constant	9.81 m/s^2
F_{fi}	bearing/grease/preload friction	N
β	slider incline angle	^{o}

$$F_w = \mu_r m_s g \quad \text{(A1.4.3)}$$

$$F_{ab} = \frac{w_b L b a}{g} \quad \text{(A1.4.4)}$$

L	belt length	m
b	belt width	m

w_b	belt specific weight	kg/m^3

$$F_{ai} = \frac{m_i a}{2}.(1+\frac{d_b^2}{d^2}) \quad \text{(A1.4.5)}$$

m_i	idler pulley mass	kg
d	idler pulley diameter	m
d_b	idler bore diameter	m

As a timing belt rotates around two appropriately-sized pulleys under load, a differential in tension is produced on the "entering" and "leaving" sides of the belt. The relationship is denoted as effective tension, which is shown to be:

$$T_e = T_1 - T_2 \quad \text{(A.1.5)}$$

T_1	belt tight side tension	N
T_2	belt slack side tension	N

The system driving torque, *M*, for a single belt-pulley combination with diameter *d* can be expressed as:

$$M = T_e \frac{d}{2} \quad \text{(A1.6)}$$

T_e	effective belt tension	N
d	pulley pitch diameter	m

A.2. Timing belt viability calculation

Generically, a 16 tooth T2.5 16 mm diameter timing pulley and 6mm wide T2.5 timing belt are selected for each axis of motion, with NEMA17 48 *mm* 0.471 *N.m.* stepper motors driving the system. The maximum power available is derived from the stepper motor as:

$$P_2 = I_{stepper} V = (1.8\,A)(12\,V)$$

$$= 21.6\,W$$

Additionally, maximum bearing slide speed attainable for 3d printers at 300 *mm/s* linear speed is:

$$\omega_{1,2} = 37.5\ rad/s$$

Employing equation A1.3, the driver torque requirement is:

$$M_1 = \frac{P_2}{\omega_1 \eta} = \frac{21.6\ W}{(37.5\ s^{-1})(0.95)} = 0.606\ N.m.$$

Selecting a Hiwin MG12R short carriage with mass m_s = 0.034 *kg* and print-head system with mass 10 *kg* and acceleration a = 1 *m/s*^{2} results in:

$$F_a = m_s a = (10\ kg)(\frac{1\ m}{s^2}) = 10\ N$$

The bearing slide operates on a flat plane at $\beta = 0^O$ with frictional coefficient μ_r = 0.01 and small grease friction F_{fi} resulting in a carriage frictional force of:

$$F_f = \mu_r m_s g cos\beta + F_{fi}$$

$$= (0.01)(10\ kg)(9.81)(cos0) + 0.5\ N$$

$$= 1.481\ N$$

$$F_w = \mu_r m_s g = (0.01)(10\ kg)(9.81)$$

$$= 0.981\ N$$

The belt inertial acceleration force for T2.5 6 *mm* belting with a specific weight w_b = 0.009 *kg/m*, per meter is:

$$F_{ab} = \frac{w_b L b a}{g}$$

$$= \frac{(0.009\ kg.m^{-1})(1\ m)(0.006\ m)(1\ m.s^{-1})}{9.81}$$

$$= 5.504\ x\ 10^{-6}\ N$$

The inertial force required to produce movement in a 16T T2.5 idler pulley with mass m_i = 0.005 *kg* is:

$$F_{ai} = \frac{m_i a}{2}.(1 + \frac{d_b^2}{d^2})$$

$$= \frac{(0.0050\ kg)(1\ m.s^{-1})}{2}.(1+\frac{(0.0050\ m)^2}{(0.0150\ m)^2})$$

$$= 0.002\dot{7}\ N$$

Finally, the effective belt tension is calculated as:

$$T_e = F_a + F_f + F_w + F_{ab} + F_{ai}$$

$$= 10\ N + 1.4810\ N + 0.9810\ N + (5.504\ x\ 10^{-6}\ N) + 0.0027\ N$$

$$= 12.4647\ N$$

Effectively, T_1 should equal T_2 if adequate preloading or tensioning is applied prior to use. Lastly, the required pulley torque for a 15 *mm* T2.5 pulley can be calculated as:

$$M = T_e\frac{d}{2}$$

$$= (12.4647\ N)(\frac{0.0150\ m}{2})$$

$$= 0.09348\ N.m.$$

Since the stepper motors produce a maximum torque of 0.471 *N.m.*, the design factor is:

$$n = \frac{T_{motor}}{M} = \frac{0.4710\ N.m.}{0.0934\ N.m.} = 5.0400$$

Leading to the conclusion that a timing belt and pulley drive system is a viable solution.

A.3. Rack and pinion drive viability derivations

Viability of rack and pinion systems are investigated from a mechanical standpoint, specifically relating to the forces, stresses, and power requirements needed for the 3d printer application. The system should be able to accelerate a 10 *kg* load up to 300 *mm/s* in the 'x' and 'y' linear directions with an acceleration of 1 m/s^2. Initially the following system parameters are assumed for the printer gantry. Formulas and values for the tangential forces experienced between meshing gear teeth are as follows:

Pinion subassembly acceleration:

$$a = \frac{v}{t_b} \tag{A3.1}$$

Actual Tangential Meshing Force:

$$F_u = \frac{mg\mu + ma}{1000} \quad \text{(A3.2)}$$

Maximum Theoretical Tangential Design Load:

$$F_{u\,perm} = \frac{F_{uTab}}{K_A S_B f_n L_{KHB}} \quad \text{(A3.3)}$$

Strength Design Factor:

$$n = \frac{F_{u\,zul,per}}{F_u} \quad \text{(A3.4)}$$

Motor Torque Requirement:

$$T_{req.} = F_u r_{pinion} \quad \text{(A3.5)}$$

Motor Design Factor:

$$n_m = \frac{T_m}{T_{req.}} \quad \text{(A3.6)}$$

m	Mass to be moved	*kg*
v	Speed	*m/s*
t_b	Acceleration time	*s*
g	Gravitational acceleration constant	m/s^2
μ	Dynamic frictional coefficient	*const.*
K_A	Load factor	*const.*
f_n	Life-Time factor	*const.*
S_B	Safety coefficient	*const.*
L_{KHB}	Linear Load Distribution Factor	*const.*

Tooth strength calculation

The pinion acceleration along the rack can be defined as:

$$a = \frac{v}{t_b} = \frac{0.3\ m.s^{-1}}{0.3\ s} = 1\ m.s^{-2}$$

Then the tangential force experienced on the meshing teeth is found to be:

$$F_u = \frac{mg\mu + ma}{1000} = \frac{(10\ kg)(9.81)(0.1) + (10\ kg)(1\ m.s^{-2})}{1000} = 0.01981\ kN$$

Selecting a generic module 3 C45 hardened indium rack with 16MnCr5 20 tooth pinion, the maximum allowable tangential force is:

$$F_{u\ zul,per.} = \frac{F_{uTab}}{K_A S_B f_n L_{KHB}} = \frac{11.5\ kN}{(1.5)(1.2)(1.05)(1.5)} = 4.05\ kN$$

Finally the safety factor for the system is:

$$n = \frac{F_{u\ zul,per}}{F_u} = \frac{4.05\ kN}{0.01981\ kN} = 204.44$$

Therefore, due to the large safety factor, the teeth will not deform or shear under load.

Motor power calculation

It is also necessary to assess the load-carrying capacity of motors when paired to a rack and pinion drive. Assuming implementation of a NEMA17 48 *mm* stepper motor and 20 *mm* diameter pinion:

$$T_m = 0.471\ N.m.$$

The minimum system torque requirement may be derived from the tangential force, F_u, produced as:

$$T_{req.} = F_u r_{pinion} = (19.81\ \text{N})(0.01\ \text{m}) = 0.1981\ N.m.$$

The torque design factor is given as:

$$n_m = \frac{T_m}{T_{req.}} = \frac{0.471\ N.m.}{0.1981\ N.m.} = 2.377$$

The low design factor achieved requires prohibits timeous acceleration and change of direction of the system, which is not advantageous.

A.4. Power screw drive viability derivations

Square threaded power screws are employed for moving the gantry in the z direction. The design of a lightweight gantry crossbeam is governed by the strength of the stepper motors employed. A square-threaded lead-screw, with mean diameter d_m, lead angle λ, helix angle ψ, and pitch p, is under the load of

the gantry crossbeam, with compressive downward force F. Initially, mean diameter d_m, lead angle λ, helix angle ψ, and pitch p, are specified by selecting a lead-screw and stepper motor combination with the following specifications:

Motor	NEMA-17, 60 *mm* Depth
Resolution	200 *Steps/Rev*
Rated Current	1.5 *A* @ 4 *V*
Holding Torque	T_R = *0.65 N.m.*
Shaft Diameter	d_m = *5 mm*
Lead-screw Pitch	*Tr8x8 (P2)*
Lead-screw Lead	*l = 8 mm*
Lead-screw Diameter	*d = 8 mm*
Lead-screw Pitch	*p* = 2 *mm*

According to Shigley (p.408: 2008) for a steel nut being driven on the steel lead-screw with oil lubrication employed, the frictional coefficient is estimated as:

$$f = 0.13$$

Knowing the above motor and lead-screw specifications, the force rating of the motor-screw subassembly may be determined, that is, the amount of weight that the two stepper motors are able to lift. Knowing the total lifting torque available is:

$$T_R = 0.65\ N.m.$$

Since the Acme thread profile is employed on the lead-screws specified, the Acme thread angle α is:

$$2\alpha = 29^{O}$$

$$\alpha = 14.5^{O}$$

$$\sec(\alpha) = \frac{1}{\cos(\alpha)} = \frac{1}{\cos(14.5^{O})} = 1.033 \qquad \text{(A4.1)}$$

α ACME thread angle O

The formula used to calculate required lifting torque can be rearranged to obtain the lifting force of the subassembly:

$$T_R = \frac{F d_m}{2}\left(\frac{l+\pi f d_m}{\pi d_m - f l}\right) \quad \text{(A4.2)}$$

T_R	lead-screw lifting torque	*N.m.*
F	lead-screw lifting force	*N*
d_m	lead-screw mean diameter	*m*
l	lead-screw lead	*m*
f	screw-nut frictional coefficient	*const.*

Rearranging the above yields:

$$F_{lifting} = \frac{2T_R}{d_m}\left(\frac{\pi d_m - f l sec\alpha}{l + f d_m sec\alpha}\right) \quad \text{(A4.2.1)}$$

$$= \frac{2(0.65\,N.m.)}{0.008\,m}\left(\frac{(3.14)(0.008\,m) - (0.13)(0.008\,m)(1.033)}{0.008m + (0.13)(0.008)(1.033)}\right)$$

$$= 376.35\,N$$

$$\approx 38.36\,kg$$

Therefore, with a specified design factor of n_d = 3 and employing two motors, the x-axis crossbeam subassembly should be designed with a maximum weight less than:

$$w_{gantry} < \frac{2F_{lifting}}{n^d} \quad \text{(A4.3)}$$

$$< \frac{2(38.36\,kg)}{3}$$

$$w_{gantry} < 25.57\,kg$$

Self-locking lead-screw determination

Self-locking of a lead-screw is achieved whenever the thread's friction coefficient is equal to or greater than the tan of the lead angle, namely:

$$\pi f d_m > 1 \quad \text{(A4.4)}$$

$$f > \tan(\lambda) \quad \text{(A4.4.1)}$$

$$0.13 > \tan(6^{O})$$

$$0.13 > 0.105$$

f	lead-screw frictional coefficient	*const.*
d_m	lead-screw mean diameter	*m*
λ	lead-screw lead angle	*O*

Therefore the lead-screw is self-locking, which is a desirable result.

Lead-screw efficiency

Lead-screw efficiency is simply the ratio of torque to raise the load with frictional losses versus those without. The lifting torque T_O without frictional losses is:

$$T_O = \frac{Fl}{2\pi} \tag{A4.5}$$

$$= \frac{(376.35\ N)(0.008\ m)}{2(3.14)}$$

$$= 0.47918\ N.m.$$

Lifting force T_R with friction, as mentioned previously is:

$$T_R = 0.65\ N.m.$$

Then the lead-screw efficiency E is:

$$E = \frac{T_O}{T_R} = \frac{0.47918\ N.m.}{0.65\ N.m.} \tag{A4.6}$$

$$= 0.7372$$

$$= 73.72\ \%$$

Stress analysis of lead-screws

It is necessary to investigate the effect of the designed gantry load on the lead-screws, so as to ascertain if any bending or deformation occurs structurally. Firstly, the maximum nominal torsional shear stress of the screw body, τ, can be approximated as:

$$\tau = \frac{16T}{\pi d^3} \tag{A4.7}$$

$$= \frac{16(0.65\,N.m.)}{(3.14)(0.005\,m^3)}$$

$$= 26.49\,MPa$$

τ	torsional shear stress	MPa
T	applied torque	$N.m.$
d	lead-screw diameter	m
S_y	yield strength	MPa
S_{sy}	shear yield strength	MPa
F	applied force	N
A	surface area	m^2
p	lead-screw pitch	m
n_t	number of engaged threads	i
V	shear force	F
M	moment at cross-section	$N.m.$
I	moment of inertia	m^4
c	cross-section width	m

The approximate yield strength of high carbon steel used to manufacture Acme lead-screws is 450 MPa, and by definition, the shear yield strength is a percentage of the tensile yield strength:

$$S_{sy} = 0.57S_y \tag{A4.8}$$

$$= (0.57)(450\,MPa)$$

$$= 265.5\,MPa$$

Since, $\tau < S_{sy}$ the lead-screws will not shear during operation. The axial stress, that is, the normal stress acting longitudinally, is approximated as:

$$\sigma = \frac{F}{A} = \frac{4F}{\pi d^2} \tag{A4.9}$$

$$= \frac{(4)(376.35\,N)}{(3.14)(0.005\,m)^2}$$

$$= 19.17\ MPa$$

Which is substantially less than $S_y = 450\ MPa$.

The maximum bearing stress, where n_t are the number of engaged threads, is experienced at the bottom thread of the collar-screw interface, and is shown to be:

$$\sigma_b = \frac{Mc}{I} = \frac{6F}{\pi d_r n_t p} \tag{A4.10}$$

$$= \frac{6(376.35\ N)}{(3.14)(0.005\ m)(1)(0.002\ m)}$$

$$= 71.78\ MPa$$

Additionally, the transverse shear stress at on the lowest thread is:

$$T = \frac{3V}{A} = \frac{3F}{\pi d n_t p} \tag{A4.11}$$

$$= \frac{3(376.35\ N)}{(3.14)(0.005\ m)(1)(0.002\ m)}$$

$$= 35.94\ MPa$$

Since all stress approximations fall well below the material's failure strength parameters, the lead-screws are suitable for use in the intended application.

A.5. Stepper motor transfer function derivation

This derivation attempts to model the operation of a permanent-phase stepper motor when the motor completes one step, that is, 1/16th of a revolution, with both phases being energized. It is assumed that the applied torque at the start of operation is zero (Robinson, D.J: 1969, p.20). The initial conditions are:

$$[\frac{d\theta}{dt}]_0 = [\frac{d^2\theta}{dt^2}]_0 = 0$$

$$I_{1,0} = I_{2,0} = I$$

The motor torque values at the t = 0 operating point are:

$$K_T I_{2,0} cos\theta_0 - K_T I_{1,0} sin\theta_0 = T_{L,0} \tag{A5.1}$$

When $T_{L,0} = 0$, $\theta_0 = 45^{O}$, then the linearized equations of friction are: (A5.2)

$$-K_T I[sin\theta_0 + cos\theta_0]\Delta\theta(t) + K_T cos\,\theta_0 \Delta I_2(t) - K_T sin\theta_0 \Delta I_1(t)$$
$$= \frac{J}{N_{RT}}\Delta\left[\frac{d^2\theta(t)}{dt^2}\right] + \frac{D}{N_{RT}}\Delta\left[\frac{d\theta(t)}{dt}\right] + \Delta T_L(t)$$

$$\Delta E_1(t) = R\Delta I_1(t) + L\Delta\left[\frac{dI_1(t)}{dt}\right] + \frac{K_v}{N_{RT}} sin\theta_0 \Delta[\frac{d\theta(t)}{dt}] \quad \text{(A5.3)}$$

$$\Delta E_2(t) = R\Delta I_2(t) + L\Delta\left[\frac{dI_2(t)}{dt}\right] + \frac{K_v}{N_{RT}} cos\theta_0 \Delta[\frac{d\theta(t)}{dt}] \quad \text{(A5.4)}$$

Taking the Laplace transforms of equations A5.2 to 5.4 yields:

$$\Delta\theta(s) = \frac{K_T cos\theta_0 \Delta I_2(s) - K_T sin\theta_0 \Delta I_1(s) - T_L(s)}{\frac{JS^2}{N_{RT}} + \frac{Ds}{N_{RT}} + K_T I[sin\theta_0 + cos\theta_0]} \quad \text{(A5.5)}$$

$$\Delta I_1(s) = \frac{\Delta E_1(s) + \frac{E_{1,0}}{s} - \frac{K_v}{N_{RT}} sin\theta_0 s\Delta\theta(s)}{R + Ls} \quad \text{(A5.6)}$$

$$\Delta I_2(s) = \frac{\Delta E_2(s) + \frac{E_{2,0}}{s} - \frac{K_v}{N_{RT}} cos\theta_0 s\Delta\theta(s)}{R + Ls} \quad \text{(A5.7)}$$

Substituting equations A5.6 and A5.7 into A5.5, the resulting transfer function for a bipolar permanent magnet stepper motor is:

$$\theta(s) = \frac{(\frac{-1}{J})\Delta T_L(s)(N_{RT})}{s^2 + \frac{D}{Js} + \frac{\sqrt{2K_T I N_{RT}}}{J}} \quad \text{(A5.8)}$$

A.6. Thermistor transfer function derivation

Thermistors of the NTC variety operate by varying resistance as temperature changes. The resistance at temperature T is given by:

$$R(t) = R_o e^{\left(\frac{B}{T(t) - T_O}\right)} \quad \text{(A6.1)}$$

T_O	reference temperature	^OC
T	current temperature	^OC
R	resistance reading at current temperature	Ω
R_O	nominal resistance at reference temperature	Ω
B	characteristic temperature constant	*const.*

With the thermal behaviour being approximated by:

$$Q = K_d t_c \frac{dT}{dt} \tag{A6.2}$$

Q	port heat flow	*J/s*
K_d	dissipation factor	*const.*
T_c	thermal time constant	*const.*
dT/dt	temperature rate change	*const.*

Taking the Laplace transform of equation and re-arranging A5.9:

$$L\{R(t)\} = L\left\{R_o e^{\left(\frac{B}{T(t)-T_O}\right)}\right\}$$

$$R(s) = R_O \int_0^\infty e^{\left(\frac{B}{T(t)-T_O}\right)} e^{-st} dt$$

$$R(s) = R_O \int_0^\infty e^{\left(\frac{B}{T(t)-T_O}\right)-st} dt$$

$$R(s) = R_o \left[-\frac{1}{s} e^{\left(\frac{B}{T(s)-To}-st\right)}\right] |_0^\infty$$

$$R(s) = -\frac{R_o}{s}\left[\frac{1}{s-\frac{B}{T(s)-T_o}}\right] \tag{A6.3}$$

A.7. Filament extrusion theory

All FDM filament extruders follow the same basic operation procedure, with physical modelling of the system being quite uniform among the various extruder configurations. Initially, a current value is sent to the extruder stepper motor via a motor driver breakout board with a nominal voltage and power rating. Therefore the stepper motor power characteristics are expressed as:

$$P_{motor} = VI_{supplied} \tag{A.7.1}$$

$$T_{motor,rated}\ (Manufacturer\ Specified)$$

P_{motor}	=	motor output power	*W*
V	=	rated dc terminal voltage	*V*
$I_{supplied}$	=	supplied current from driver board	*A*

The rotation of the motor shaft with angular velocity ω rad.s^{-1} produces a linear movement of filament down into the heated section of the extruder. The linear velocity of filament, also known as the feed-rate, can be expressed as a function of the stepper motor speed as:

$$Feedrate_{Filament} = \frac{2\pi n_{motor}}{60} * r_{drive-gear} \quad \text{(A7.2)}$$

$Feedrate_{filament}$	=	filament linear speed	*mm/s*
n_{motor}	=	current motor shaft speed	*rev/min*
$r_{drive\text{-}gear}$	=	knurled extruder gear radius	*mm*

Additionally, it is known that the force required to push 1.75 *mm* thermoplastic filament through a hot-end heated to 190 ^{O}C is given by manufacturers, then the required stepper motor torque required to extrude various filaments is obtained via:

$$T_{motor,required} = F_{extrusion} r_{drive-gear} \quad \text{(A7.3)}$$

$T_{motor,required}$	=	motor torque required for extruding	*N.m.*
$F_{extrusion}$	=	material extrusion force (pre-specified)	*N*
$r_{drive\text{-}gear}$	=	knurled extruder gear radius	*mm*

A.8. Pellet extrusion theory

Operation and system parameters of common single-screw pellet extruders can be approximated quite accurately using work previously performed by Auger and Vlachopoulos (E.E. Agur & J. Vlachopoulos: 1982, p.1084-1085). Each section of the pellet extruder, namely, the feed hopper, solids-conveying, melting, melt-conveying, die, and die exit regions are to be modelled using the following derivations.

Feed hopper

Cylindrical plastic pellets flow into the auger drive inlet via the feed hopper due to gravitational action. According to D.M. Walker (1966, p.21), the base pressure distribution in the feed hopper, assuming stress equilibrium amongst pellets, is given by the following expressions for vertical hopper sections:

$$p = p_o e^{\left(-\frac{4BDH}{W}\right)} + \frac{\rho_{bulk} g W}{4BD^*}\left[1 - e^{\left(-\frac{4BDH}{W}\right)}\right] \quad \text{(A8.1)}$$

Where

$$B = \frac{sin\delta sin\kappa_0}{1-sin\delta cos\kappa_o} \quad \text{(A8.1.1)}$$

$$\kappa_0 = \beta_w + sin^{-1}\left(\frac{sin\beta_w}{sin\delta}\right), sin^{-1} > \frac{\pi}{2} \quad \text{(A8.1.2)}$$

$$\beta_w = tan^{-1}(f'_w) \quad \text{(A8.1.3)}$$

f'_w	wall static friction coefficient	*const.*
p	pressure at hopper base	N/m^2
p_o	pressure at height H in section	N/m^2
W	hopper width	m
ρ_{bulk}	average pellet density	kg/m^3
g	gravitational acceleration	$kg.m/s^2$
D^*	distribution factor	*const.*
δ	effective friction angle	*o*
α	hopper wall angle	*o*

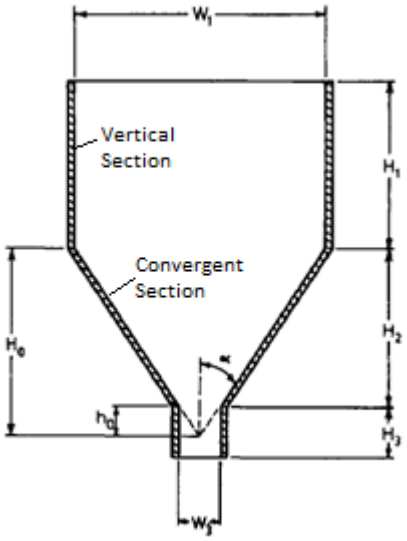

Figure A8.1: Geometry of Feed Hopper

However, for convergent hopper profiles, as highlighted above in Figure 3.4, the pressure distribution is:

$$p = (\frac{h_o}{H_o})^{\psi} p_o + \frac{p_{bulk} g h_o}{\psi - 1} + [1 - \left(\frac{h_o}{H_o}\right)^{\psi - 1}] \quad \text{(A8.2)}$$

Where

$$\psi = \frac{2B'D^*}{tan\alpha} \quad \text{(A8.2.1)}$$

$$B' = \frac{sin\delta \sin(2\alpha + \kappa_o)}{1 - sin\delta \cos(2\alpha + \kappa_o)} \quad \text{(A8.2.2)}$$

$$\kappa_o = \beta_w + sin^{-1}\left(\frac{sin\beta_w}{sin\delta}\right), sin^{-1} < \frac{\pi}{2} \quad \text{(A8.2.3)}$$

$$\beta_w = tan^{-1} f'_w \quad \text{(A8.2.4)}$$

Solids conveying zone

The solids conveying zone in a screw-type extruder contains the drive motors, auger bit, and cylindrical hollow piping section as indicated in Figure 3.3 above. According to Darnell and Mol, (SPE J.: April 1956) the flow of plastic in this region is "*due to the frictional flow of the barrel and screw surfaces on the solid polymer granules*". Assuming that the transported materials are isothermal [8], and travel as a solid mass with inter-particular pressure varying only in the longitudinal direction towards the extruder end, the pressure along the extruder length can be expressed as:

$$p = p_o e^{-\lambda z b} \tag{A8.3}$$

Where

$$\lambda = \frac{A_1 K - B_1}{A_2 K - B_2} \tag{A8.3.1}$$

$$A_1 = f_b W_b sin\varphi + 2H f_s sin\Theta_b + W_s f_s sin\Theta_b \tag{A8.3.2}$$

$$A_2 = H W_a sin\Theta_a \tag{A8.3.3}$$

$$B_1 = f_b W_b cos\varphi - 2H f_s \left(\frac{D_a}{D_b}\right) sin\Theta_b cotan\Theta_a \tag{A8.3.4}$$

$$- W_s f_s \left(\frac{D_s}{D_b}\right) sin\Theta_b cotan\Theta_s$$

$$B_2 = H W_a \left(\frac{D_a}{D_b}\right) cos\,\Theta_a \tag{A8.3.5}$$

$$K = \left(\frac{D_a}{D_b}\right)\left(\frac{sin\Theta_a + f_s cos\Theta_a}{cos\Theta_a - f_s sin\Theta_a}\right) \tag{A8.3.6}$$

p_O	feed hopper base pressure	N/m^2
z_b	down-channel distance	m
f_b	dynamic frictional coefficient barrel	-
f_s	dynamic frictional coefficient screw	-
H	screw channel depth	m
W_b, W_s	channel widths, screw ends	m
Θ_b, Θ_s	helix angles, screw ends	^{O}
D_b, D_s	barrel/screw diameters	m
W_a, D_a, θ_a	average channel parameters	$m, m, ^O$

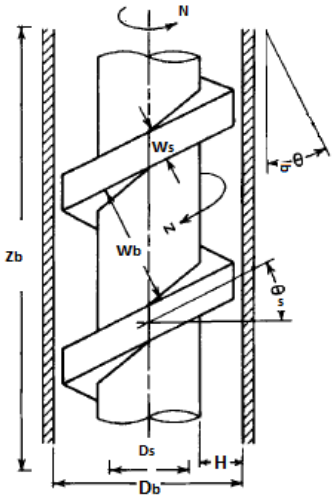

Figure A8.2: Geometry of Extruder Screw

Melting zone and extruder head

Following on experimental work performed by Tadmor and Klein, (Engineering Principles of Plasticating Extrusion: 1970) expressions have been developed to explain the physical melting and transportation of thermoplastics within the heated barrel section of screw-drive extruders. Material states exist whereby solid and melted phases exist together, fully melted closer to the extruder head, with solid pellets existing close to the screw center. It should be noted that melting also occurs and forms a liquid film at the heated barrel's surface, as illustrated in Figure A8.3.

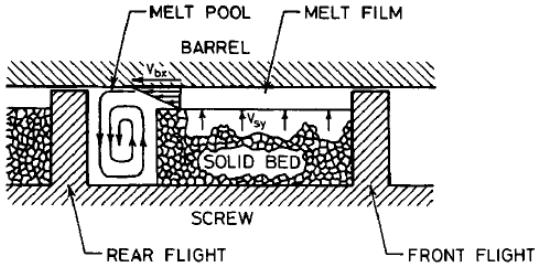

Figure A8.3: Plastic Melt Action within Heated Barrel

The rate of melting of plastic pellets where $(dT/dy)_{y=0}$ is the temperature gradient between solid and melted particles, can be approximated by:

$$\omega = \Phi\left(\frac{dT}{dy}\right)_{y=0} X \qquad \text{(A8.4)}$$

Where,

$$\Phi = \frac{k_m}{Cp_s(T_{melt}-T_{sol}) + \lambda + Cp_m(T_{bulk}-T_{melt})} \qquad \text{(A8.4.1)}$$

Mass-flow rate of melted plastic can also be calculated as:

$$\frac{Q}{W} = \int_0^H v_z \, dy \qquad \text{(A8.4.2)}$$

X	width of solid bed	m
v_{bx}	cross-channel component of barrel velocity	m/s
T_{bulk}	temperature of melt film	K
T_{melt}	melting temperature of polymer	K
T_{sol}	temperature of solid pellet bed	K

ρ_m	melted material density	g/m^3
Cp_m, Cp_s	specific heat of polymer melt/solid	J/g
K_m	melt thermal conductivity	$W/m.K$
λ	polymer heat of fusion	J/g
Q/W	mass flowrate	kg/s
v_z	down-channel velocity of material	m/s

A.9. CNC cutting tool force derivations

In this appendix, the cutting forces induced on a CNC cutting tool are derived. According to Yousefian and Tarbutton, the radial, tangential, and axial cutting forces acting on the cutting zone of the routing bit, are defined as:

$$F_{tc,rc,ac} = Voxel\ Size \text{ x } ([K_{tc,rc,ac} \text{ x } \sum_{i=1}^{n} C_{th}(\theta_i)\delta_i] + K_{te,re,ae} \quad \text{(A9.1)}$$

The Boolean condition for δ_i is:

$$\delta_i = \begin{cases} 1;\ when\ ith\ cutting\ voxel\ is\ in\ cutting\ zone \\ 0;\ when\ ith\ cutting\ voxel\ not\ in\ cutting\ zone \end{cases} \quad \text{(A9.2)}$$

The un-routed thickness of material which is about to be cut is:

$$C_{th}(\theta_i) = f_t \sin(\theta_i)\sin(\kappa) \quad \text{(A9.3)}$$

And the voxel size is equal to $1/4^{th}$ the circumference of the cutting tool cross-section. The equation can be further developed as:

$$\begin{bmatrix} F_t \\ F_r \\ F_a \end{bmatrix} = [3\ x\ 3\ Transformation\ Matrix] \begin{bmatrix} F_X \\ F_Y \\ F_Z \end{bmatrix}$$

$$\begin{bmatrix} F_t \\ F_r \\ F_a \end{bmatrix} = \begin{bmatrix} \cos(\theta) & \sin(\theta)\sin(\kappa) & \sin(\theta)\cos(\kappa) \\ \sin(\theta) & \cos(\theta)\sin(\kappa) & \cos(\theta)\cos(\kappa) \\ 0 & \cos(\kappa) & \sin(\kappa) \end{bmatrix} \begin{bmatrix} F_X \\ F_Y \\ F_Z \end{bmatrix} \quad \text{(A9.4)}$$

Where $F_{x,y,z}$ are the dynamometer-measured tool forces, θ is the cutting voxel angle, and κ is the axial immersion angle. Calculating the forces for equation A9.4 yields the results shown in Table 4.14 (O Yousefian, J.A. Tarbutton: 2015).

A.10. Stepper motor load carrying capacity calculations

Two NEMA17 60 *mm* stepper motors are selected to drive the vertical "z-axis". It is required to determine the amount of weight that can be lifted by a timing belt-pulley drive configuration, so as to appropriately size design the "z-axis" gantry subassembly. Driver pinions are specified as:

$$GT2\ 16T\ ALU.Timing\ Pulley$$

$$d_{pinion} = 9.68\ mm$$

$$r_{pinion} = \frac{d_{pinion}}{2} = \frac{9.68\ mm}{2} = 4.84\ mm = 0.00484\ m \tag{A10.1}$$

d_{pinion}	timing pulley pitch diameter	m
r_{pinion}	timing pulley pitch radius	m
T_{motor}	motor torque	$N.m.$
F	force	N
W_{hold}	holding weight	kg

The NEMA17 stepper motor has a maximum holding torque of:

$$T_{motor} = 0.65\ N.m.$$

Then maximum force output at the pulley teeth-belt interface is calculated as:

$$F = \frac{T_{motor}}{r_{pinion}} \tag{A10.2}$$

$$= \frac{0.65\ N.m.}{0.00484\ m}$$

$$= 134.2975\ N$$

Therefore for a dual motor setup, the theoretical holding force is:

$$F_{hold} = 2F \tag{A10.3}$$
$$= (2)(134.2975\,N)$$
$$= 268.60\,N$$

The theoretical holding weight is then:

$$W_{hold} = \frac{F_{hold}}{g} \tag{A10.4}$$
$$= \frac{268.60\,N}{9.81\,m.s^{-2}}$$
$$= 27.38\,kg$$

The gantry has an approximate weight of $M_{gantry} \approx 12\,kg$, then the safety factor for the stepper motors is:

$$n = \frac{W_{hold}}{m_{gantry}} \tag{A10.5}$$
$$= \frac{27.38\,kg}{12\,kg}$$
$$\approx 2.28$$

A.11. Design-stage uncertainty calculations for printer componentry

The following calculations follow on from the explanation as given in Section 5.2. For the Pololu DRV8825 stepper motor driver, the zero order uncertainty is:

$$u_O = \pm(0.5)(resolution) \tag{5.1}$$
$$= \pm(0.5)(0.01^O)$$
$$= \pm 0.005^O$$

The instrument error for a specific motor step is:

$$u_c = AR \tag{5.2.1}$$
$$= (0.05625^O)(1.8^O)$$
$$= 0.10125^O$$

A	Instrument Accuracy	O
R	Instrument Range	O

Over the driver's operating range of 0 to 360 ^{O}, the average instrument error per revolution is:

$$u_e = \frac{\sum u_c}{n} \tag{5.2.2}$$

$$= \frac{\sum_{k=0}^{n-1}(a+kd)}{n} = \frac{1}{2}(2a+(n-1)d)/n$$

$$= \frac{1}{2}(2(0^o)+(200-1)(1.8^o))/200$$

$$= 0.8955^{\,o}$$

a	first reading taken	various
d	difference between readings taken	various
n	total number of readings taken	integer

Then finally, the design stage uncertainty for the Pololu DRV8825 motor driver is:

$$u_d = \sqrt{(u_o^2 + u_e^2} \tag{5.3}$$

$$= \sqrt{(0.005^2 + 0.8955^2}$$

$$= 0.8955^{\,o}$$

Similarly, for the Hiwin MG12R linear guides and carriages, the design stage uncertainty for dimensional accuracy is:

$$u_o = (0.5)(0.01mm) = 0.005\ mm$$

$$u_c = (0.04)(0.08\ mm) = 0.0032\ mm$$

$$u_d = \sqrt{0.005^2 + 0.0032^2} = 0.0059\ mm$$

Design stage uncertainty for running parallelism of the rails is:

$$u_o = (0.5)(1\ x\ 10^{-6}\ mm) = 0.5\ x\ 10^{-6}\ mm$$

$$u_c = (23\ x\ 10^{-6}\ mm)(11\ x\ 10^{-6}\ mm) = 2.53\ x\ 10^{-10}\ mm$$

$$u_d = \sqrt{(0.5x10^{-6})^2 + (2.53x10^{-10})^2} = 5\ x\ 10^{-7} mm$$

Design stage uncertainty for the BrecoFlex T2.5 timing belt and pulley drivetrain is:

$$u_o = (0.5)(0.001\,mm) = 0.0005\,mm$$

$$u_c = (1.04\,mm.m^{-1})(1\,m) = 1.04\,mm$$

$$u_d = \sqrt{0.0005^2 + 1.04^2} = 1.04\,mm$$

Similarly, for the EPCOS 100K NTC thermistor:

$$u_o = (0.5)(0.1\,^oC) = 0.05\,^oC$$

$$u_c = (0.25)(355\,^oC) = 88.75\,^oC$$

$$u_e = \frac{\frac{1}{2}\left(2(-55\,^o) + (355-1)(1^o)\right)}{355} = 0.3295\,^oC$$

$$u_d = \sqrt{0.05^2 + 0.3295^2} = 0.3333\,^oC$$

A.12. Statistical calculations for printer locational accuracy

Statistical analysis is expanded upon from section 5.3. The mean is calculated by finding the average location from the four tests performed:

$$\bar{x} = \frac{1}{N}\sum_{i=1}^{N} x_i \tag{5.7}$$

$$\overline{x_{100,100,100}} = \frac{1}{3}[\,0.047\,mm + 0.021\,mm\, + 0.040\,mm\,] = 0.036\,mm$$

The calculation is repeated for location tests up to 1200 *mm*. Similarly the pooled standard deviation is:

$$s_x = \sqrt{s_x^2} = \left(\frac{1}{N-1}\sum_{i=1}^{N}(x_i - \bar{x})^2\right)^{1/2} \tag{5.8}$$

$$s_{x,100,100,100} = \left(\frac{1}{3-1}[(\,0.047 - 0.036\,)^2 + (0.021 - 0.036\,)^2 + (0.040 - \,0.036)^2]\right)^{1/2}$$
$$= 0.013\,mm$$

Confidence interval at 95 % probability:

$$v = N - 1 = 12 - 1 = 11$$

$$\pm t_{v,P} S_x = \pm t_{3,95} S_x = \pm(2.179)(\,0.013\,mm) = \pm 0.029\,mm \tag{5.9}$$

The Chi-Squared probability distribution:

$$\sqrt{\frac{vs_x^2}{\chi^2_{0.025}}} < \sigma < \sqrt{\frac{vs_x^2}{\chi^2_{0.975}}} \tag{5.10}$$

$$\sqrt{\frac{(11)(0.029)^2}{21.5}} < \sigma < \sqrt{\frac{(11)(0.029)^2}{3.82}}$$

$$0.020\ mm\ < \sigma < 0.049\ mm$$

Regression curve:

$$y_c = a_o + a_1 x = 0.0617424 + 1.000002448x \tag{5.11}$$

Where

$$\sum x_1 = 100 + 200 + 300 + \cdots + 1100 + 1200 = 7800$$

$$\sum x_1 y_1 = (100)(100.036) + (200)(200.069) + \cdots + (1200)(1200.028) = 6500497.5$$

$$\sum y_1 = 100.036 + 200.069 + \cdots + 1100.091 + 1200.028 = 7800.76$$

$$a_0 = \frac{\sum x_i \sum x_i y_i - \sum x_i^2 \sum y_i}{(\sum x_i)^2 - N\sum x_i^2} = \frac{(7800)(6500497.5) - (6500000)(7800.76)}{(7800\ x\ 7800) - (12)(6500000)} = 0.0617424 \tag{5.11.1}$$

$$a_1 = \frac{\sum x_i \sum y_i - N\sum x_i y_i}{(\sum x_i)^2 - N\sum x_i^2} = \frac{(7800)(7800.76) - (12)(6500497.5)}{(7800x7800) - (12)(60840000)} = 1.000002448 \tag{5.11.2}$$

Correlation coefficient:

$$r_{xy} = \frac{N\sum_{i=1}^{N} x_i y_i - \sum_{i=1}^{N} x_i \sum_{i=1}^{N} y_i}{\sqrt{N\sum_{i=1}^{N} x_i^2 - \left(\sum_{i=1}^{N} x_i\right)^2}\sqrt{N\sum_{i=1}^{N} y_i^2 - \left(\sum_{i=1}^{N} y_i\right)^2}} = \tag{5.12}$$

$$= \frac{(12)(6500497.5) - (7800)(7800.76)}{\sqrt{(12)(7800^2) - (7800^2)}\sqrt{(12)(6500995.054) - (7800.76)}} = 1.000001499$$

Additionally, the random error uncertainty between the measured data can be approximated for the curve:

$$S_{yx} = \sqrt{\frac{\sum_{i=1}^{N}(y_i - y_{ci})^2}{12-2}} = \sqrt{\frac{0.5776}{4-2}} = 0.2756 \tag{5.13}$$

$$\sum_{i=1}^{N}(y_i - y_{ci})^2 = 0.036^2 + 0.069^2 + 0.066^2 + 0.058^2 + \cdots + 0.091^2 + 0.028^2 = 0.76^2$$

The t-estimator establishes the random uncertainty of the regression analysis for a 95 % confidence level:

$$\pm t_{11,95} S_{yx} = \pm(2.179)(0.2756) = 0.6005 \quad (5.14)$$

The uncertainty of the four repeated tests due to random error is shown to be:

$$u_x = \pm \frac{t_{v,P} S_{yx}}{\sqrt{N_k}} = \frac{(0.6005)}{\sqrt{3}} = 0.3467\ mm \quad (5.15)$$

$$\%u_x = \frac{u_x}{r_o} * 100 = \frac{0.3467\ mm}{1200\ mm} * 100 = 0.028\ \% \quad (5.16)$$

Linearity uncertainity:

$$u_{L,max} = y_i(x) - y_{ci}(x) = 0.1557\ mm \quad (5.17)$$

$$\%u_{L,max} = \frac{u_{L,max}}{r_o} * 100 = \frac{0.1557\ mm}{1200\ mm} * 100 = 0.013\ \% \quad (5.17.1)$$

Repeatability uncertainty error:

$$S_{x,max} = 0.078\ mm \quad , r_o = 1200\ mm$$

$$\%u_{Rmax} = \frac{2S_x}{r_o} * 100 = \frac{(2)(0.078\ mm)}{1200 mm} * 100 = 0.013\ \% \quad (5.18)$$

Overall printer locational uncertainity:

$$\%u_{overall} = (\%u_o^2 + \%u_c^2 + \%u_{nl}^2 + \%u_x^2 + \%u_{L,max}^2 + \%u_{Rmax}^2) \quad (5.19)$$

$$(0.0059\ mm^2 + (2.5x10^{-13}) + (1.04\ mm)^2 + (0.3467)^2 + (0.1557)^2 + (0.078)^2$$

$$= 0.034\ \%$$

B Appendix - Rumba Controller Board Connection Diagram

The GeeeTech Rumba integrated control board has been exclusively developed as the control unit for 3D printing, routing, laser cutting, and other Computer Numerical Control applications. The board can be controlled via G-code written to an SD memory card, which is placed in the GeeeTech LCD2004 Extension Screen, or via USB online programming on a personal computer. Hardware and software is interfaced via Arduino Marlin cross-compiling firmware and Repertier Host 3D CAD scaling software. Additionally, the system contains the following hardware peripherals as shown in Figure A.1:

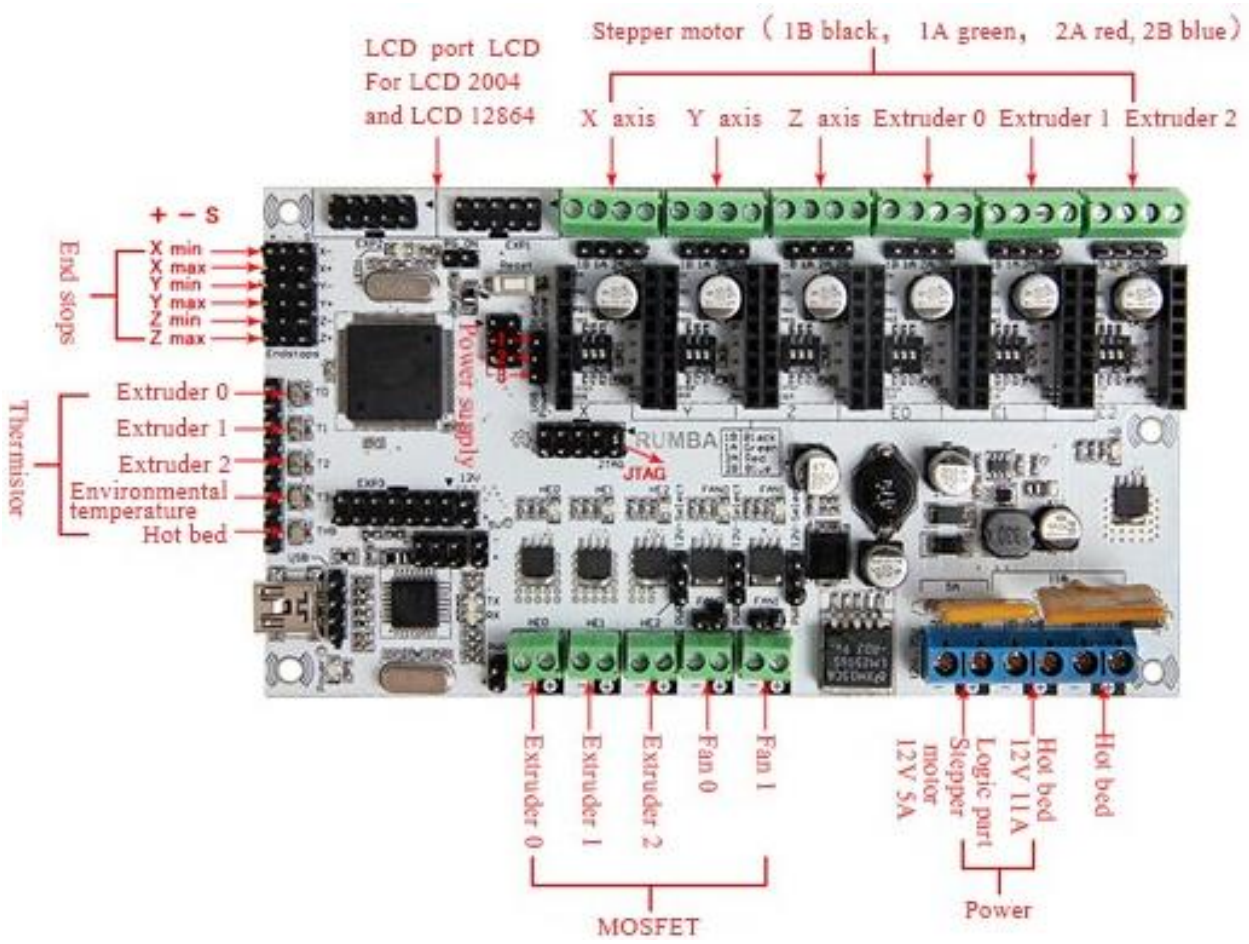

Figure B.1: GeeeTech Rumba 3D Printer Controller Board Electrical Layout

C Appendix - Pololu DRV8825 Driver Connection Diagram

The Pololu DRV8825 stepper motor driver is a micro-stepping bipolar stepper motor driver featuring variable current-limiting, incorporates over-temp and over-amperage protection, and six micro-step resolutions up to 1/32th of a step. The product interfaces with a controller motherboard and is able to drive a stepper motor up to 2.2 *A* at 2.5 *V* to 5.25 *V*.

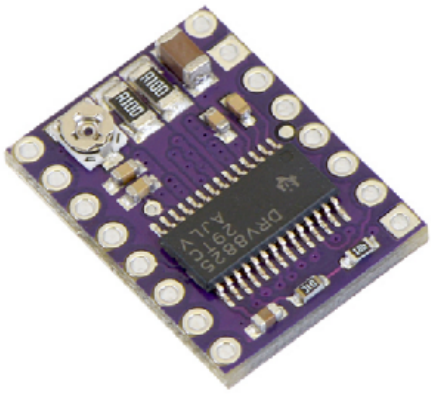

Minimum operating voltage:	8.2 V
Maximum operating voltage:	45 V
Continuous current per phase:	1.5 A[2]
Maximum current per phase:	2.2 A[3]
Minimum logic voltage:	2.5 V[4]
Maximum logic voltage:	5.25 V[4]
Microstep resolutions:	full, 1/2, 1/4, 1/8, 1/16, and 1/32
Reverse voltage protection?:	N
Bulk packaged:	N
Header pins soldered:	N[5]

Figure C.1: Pololu DRV8825 Stepper Motor Driver Shield

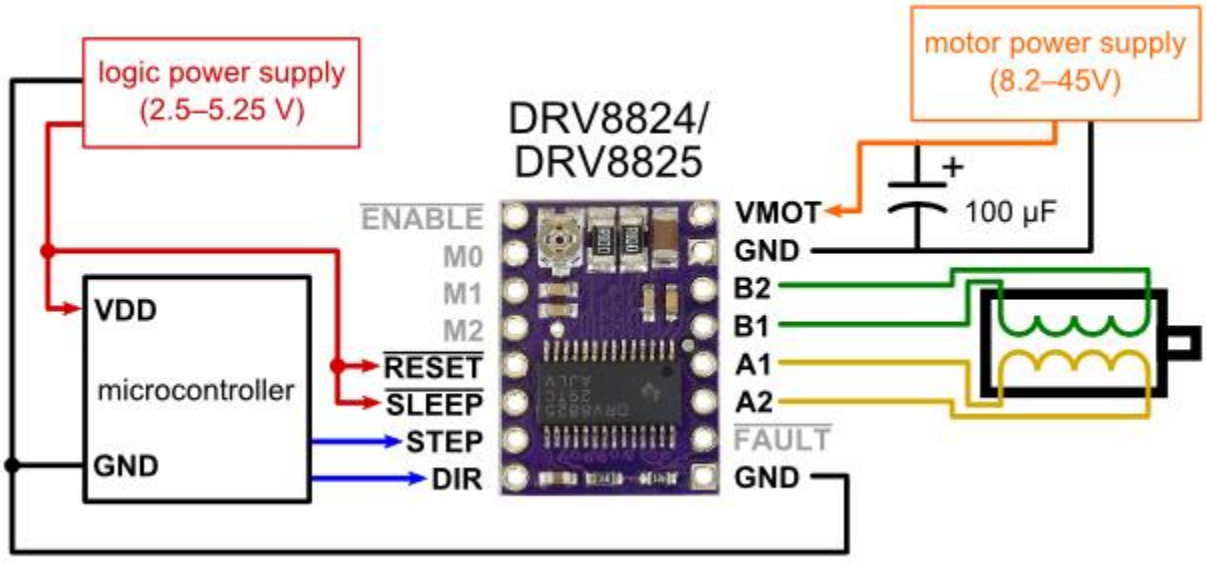

Figure C.2: Pololu DRV8825 Connection Diagram

D Appendix - Pololu Bipolar Stepper Motor Detail

Stepper motors are generically employed in situations where accurate position control and monitoring is required. There is no feedback loop with stepper motor control, therefore the 3D printer drive control system is deemed 'open-loop'. The Pololu bipolar dc stepper motor dimensional and electrical specifications are shown henceforth: (Pololu.com: 2016)

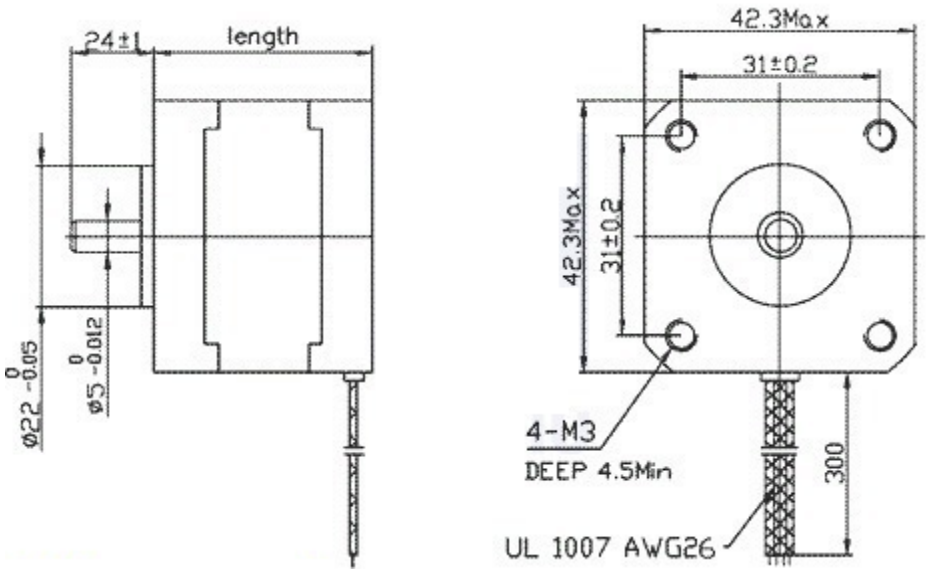

Figure D.1: Pololu NEMA 17-48mm/4.8 Bipolar Stepper Motor Dimensions

The electrical specifications are as follows: (Pololu.com: 2016)

- Size: 42.3 *mm* square × 48 *mm*, not including the shaft (NEMA 17)
- Weight: 350 *g*
- Shaft diameter: 5 *mm* "D"
- Steps per revolution: 200
- Current rating: 1.2 *A* per coil
- Voltage rating: 4 *V*
- Resistance: 3.3 *Ω* per coil
- Holding torque: 3.2 *kg-cm*
- Inductance: 2.8 *mH* per coil
- Lead length: 30 *cm*
- Output shaft supported by two ball bearings

E Appendix - Conceptual Costing Analysis

E.1. Horizontal multi-zoned filament 3D printer

Table E.1: Horizontal Multi-Zoned 3D Printer Cost Breakdown

Component	Quantity	Supplier	Subtotal
Frame			
Bosch Rexroth ALU.	5200 *mm* x 2	Tectra Automation	ZAR 6623.28
60 x 60L Profile	2000 *mm* x 2		
Aluminium Tooling	400 mm^2 x 8	Eurosteel	ZAR 1112.64
Plate 6 mm	200 mm^2 x 8		ZAR 556.32
	200 *mm* x 50 *mm* x 8		ZAR 417.15
	500 *mm* x 100 *mm* x 10		ZAR 712.50
Steel Caster Wheels	x4	Steel Pipes/Fittings	ZAR 356.00
T-Nut M8 10 *mm*			
Plain Glass 5 *mm*	2 m x 1 m x 5	PG Glass	ZAR 3600.00
X,Y,Z Axes			
Hiwin MG12R	26 *m*	Netram Technologies	ZAR 33800.00
Linear Rail			
Hiwin MG12 Carriage	x25	Netram Technologies	ZAR 4625.00
Nema17 Stepper w/	x10	Netram Technologies	ZAR 10849.50
460 *mm* Leadscrew			
Leadscrew Nut TR8x8P2	x20	Netram Technologies	ZAR 4499.00
SKF 10 *mm* x 3 *mm*	1 *m* x 20	CNCDirect SA	ZAR 14022.00
Ballscrew Rod			
NEMA17 Steel	x50	Netram Technologies	ZAR 5950.00
L – Bracket			

Drag Chain 20 x 10 *mm*	22 *m*	Hobbytronics	ZAR 3476.00
BR Series 5-5 Coupling	15x	Netram Technologies	ZAR 1035.00
NEMA-17 Bracket Steel	18x	Netram Technologies	ZAR 2142.00
SKF 6195-2Z 5 *mm* BB	25x	MCL Engineering	ZAR 500.00
NEMA17 Motors 48 *mm*	25x	Netram Technologies	ZAR 6625
Filament Extruder (5x)			
J Head Hot End Mk8	5x	3D Print Store SA	ZAR 595.00
NEMA17 48 *mm* Motor	5x	3D Print Store SA	ZAR 321.00
Cold End DIY Extruder	5x	3D Print Store SA	ZAR 345.00
NEMA17 L-Bracket	5x	3D Print Store SA	ZAR 119.00

Grand Total: ZAR 129’476.68

E.2. Vertical pellet-based 3D printer

Table E.2: Vertical Pellet-Based 3D Printer Cost Breakdown

Component	**Quantity**	**Supplier**	**Subtotal**
Frame			
Aluminium Square Extrusions (50.8 mm^2)	6 *m* x 2	Eurosteel	ZAR 1458.28
Stainless Steel Round Bar 5 *mm*	6 *m* x 1	Eurosteel	ZAR 71.82
Alu. Tooling Plate 6 *mm*	200 mm^2 x 24	Eurosteel	
	100 mm^2 x 44		
	150 x 50 *mm* x 3		
	400 x 200 *mm* x 6		
	100 x 200 *mm* x 4		
	80 x 50 *mm* x 28		ZAR 3211.50
Alu. Angle Iron 25.4 mm^2	3 *m*	Eurosteel	ZAR 41.04

Unglazed Glass 5 *mm*	1400 mm^2 x 1	PG Glass	ZAR 703.84
Bosch Rexroth Mounting Rim Profile 10 *mm*	2000 *mm* x 1	Tectra Automation	ZAR 96.51
Bosch Rexroth 45/45 Lift-Off Hinge	6x		ZAR 1364.44
Bosch Rexroth D44 M12 Levelling Foot	8x		ZAR 1569.82
Bosch Rexroth 10 *mm* Double Ball Latch	2x		ZAR 1503.34
10 *mm* M4 T-Nut	50x		ZAR 418.38
10 *mm* M8 T-Nut	390x		ZAR 3666.69
Bosch Rexroth 60 x 60L Profile Alu.	5.6 *m* x 7		ZAR 20134.77
Bosch Rexroth 45 x 45L Profile Alu.	5.6 *m* x 8		ZAR 11567.44
Polycarbonate Sheet 2 *mm*	2590 x 1530 *mm* x 4 2390 x 670 *mm* x 4	Maizey Plastics CC	ZAR 13567.67

X,Y,Z Axes

Hiwin MGN12R Carriage	7x	Netram Technologies	ZAR 1294.65
Hiwin MGN12 Linear Rail	24.7 *m*	Netram Technologies	ZAR 33053.65
Timing Belt T2.5 6 *mm*	50 *m* Reel	3D Print Store CC	ZAR 2750.00
Timing Pulley T2.5 16T	14x	3D Print store	ZAR 796.00
Drag Chain 20x10 *mm*	10 *m*	Hobbytronics	ZAR 1580.00
BR Series 5-5 Coupling	3x	Netram Technologies	ZAR 207.00
NEMA-17 Bracket Steel	18x	Netram Technologies	ZAR 2142.00
SKF 6195-2Z 5 *mm* BB	14x	MCL Engineering	ZAR 280.00

Pellet Extruder (1x)

12 *V* DC Cooling Fan	1x	Netram Technologies	ZAR 39.95
12 *V* 40*W* Reprap Cartridge Heater	2x	Netram Technologies	ZAR 139.90
Thermistor NTC 100K	2x	Netram Technologies	ZAR 59.90
GT2 Pulley 40T	1x	Netram Technologies	ZAR 69.95
GT2 Pulley 16T	1x	Netram Technologies	ZAR 49.95
MK8 0.4 *mm* /3 *mm* Nozzle	1x	Netram Technologies	ZAR 109.95
NEMA17 1.5 *A* 60 *mm*	1x	Netram Technologies	ZAR 339.95

Grand Total: ZAR 109’514.11

E.3. Horizontal hybrid FDM-CNC 3D printer

Table E.3: Horizontal Hybrid FDM-CNC 3D Printer Cost Breakdown

Component	**Quantity**	**Supplier**	**Subtotal**
Frame			
Bosch Rexroth ALU. 60x60L Profile	5200 *mm* x 4 2000 *mm* x 2	Tectra Automation	ZAR 14381.97
Bosch Rexroth ALU. 45x45L Profile	2000 *mm* x 2		ZAR 1445.93
Aluminium Tooling Plate 6 *mm*	400 mm^2 x 8	Eurosteel	ZAR 1112.64
	200 mm^2 x 8		ZAR 556.32
	500 *mm* x 100 *mm* x 2		ZAR 150.00
Steel Caster Wheels T-Nut M8 10 *mm*	x8	Steel Pipes/Fittings	ZAR 712.00
Plain Glass 5 *mm*	2 *m* x 1 *m* x 5	PG Glass	ZAR 3600.00

X,Y,Z Axes

Hiwin MGN12R Carriage	7x	Netram Technologies	ZAR 1294.65
Hiwin MGN12 Linear Rail	15.5 *m*	Netram Technologies	ZAR 19500.00
Drag Chain 20x10 *mm*	8 *m*	Hobbytronics	ZAR 1264.00
Mod 1.5 Rack	13 *m*	CNC Direct	ZAR 5409.30
Steel Anodised			
Mod 1.5 Pinion 16T	3x	CNC Direct	ZAR 335.16
NEMA17 48 *mm* Stepper	6x	Netram Technologies	ZAR 1590.00
Nema17 Stepper w/	1x	Netram Technologies	ZAR 1084.95
460 *mm* Leadscrew			
Leadscrew Nut TR8x8P2	1x	Netram Technologies	ZAR 224.95

Hybrid CNC-FDM Tool Head

J Head Hot End Mk8	5x	3D Print Store SA	ZAR 595.00
Cold End DIY Extruder	5x	3D Print Store SA	ZAR 345.00
NEMA17 L-Bracket	5x	3D Print Store SA	ZAR 119.00
CNC Spindle 1.0 *kW*-ER20	1x	CNC Direct SA	ZAR 16017.00
CNC Chuck 3 Tooth SC	1x	CNC Direct SA	ZAR 10500.00
Tungsten Carbide Bit	1x	CNC Direct SA	ZAR 1500.00
Mechanical Subassembly	1x	In-house Manuf.	ZAR 2000.00

Grand Total: ZAR 91474.95

E.4. Electronics and fastener costs – common to all concepts

Table E.4: Electronics and Fastener 3D Printer Cost Breakdown

Electronics

NEMA17 48 *mm*	4x	3D Print Store CC	ZAR 1156.00
Microswitch 2 Terminal	6x	Hobbytronics PE	ZAR 155.70
Geetech Rumba Control	1x	Netram Technologies	ZAR 1350.00
DRV8825 Driver Board	6x	Netram Technologies	ZAR 420.00
Rittal E-Box 150x120	1x	Rubicon PE	ZAR 1466.92
12 *V* Battery 70 *Ah* DC	1x	Dixon Batteries PE	ZAR 849.99
12 *V* Smart6 Charger	1x	Dixon Batteries PE	ZAR 963.30
SD Card MMC	1x	Game	ZAR 89.00
LCD2004 Kit	1x	Netram Technologies	ZAR 374.95
12 *V* Cooling Fan	2x	Netram Technologies	ZAR 119.85

Fasteners

M8x20 Capscrew	390x	Ibayi Bolt & Nut CC	ZAR 243.36
M8 Washer Med.	390x	Ibayi Bolt & Nut CC	ZAR 17.12
M4x20 Capscrew	50x	Ibayi Bolt & Nut CC	ZAR 17.04
M4 Washer Med.	50x	Ibayi Bolt & Nut CC	ZAR 0.64
M4 Nyloc Nut	20x	Ibayi Bolt & Nut CC	ZAR 1.84

Grand Total: ZAR 7225.72

E.5. Tolerance guide for polymer moulds

Table E.5: Suggested Industrial Tolerance Ratings for Polymer-Based Molding Strategies

Drawing Code	Part Dimension	ABS	Polycarbonate	Nylon	Acetal/Acrylic
	mm	mm	mm	mm	mm
Side Length	<25.4	0.127	0.101	0.101	0.139
Concentricity	Any	0.228	0.127	0.254	0.254
Flatness	<76.2	0.381	0.127	0.254	0.381
Side Wall	Any	0.076	0.076	0.127	0.1143
Bottom Wall	Any	0.101	0.076	0.101	0.089

F Appendix – Printer Source Code In Arduino IDE 1.6.9

Marlin - Configuration.h | Arduino 1.6.9

File Edit Sketch Tools Help

Marlin | Conditionals.h | Configuration.h § | Configuration_adv.h | M100_Free_Mem_Chk.cpp | Marlin.h | MarlinSerial.cpp

```
#ifndef CONFIGURATION_H
#define CONFIGURATION_H
#include "boards.h"
#include "macros.h"
#include <U8glib.h>
#if ENABLED(USE_AUTOMATIC_VERSIONING)
  #include "_Version.h"
#else
  #include "Version.h"
#endif
#define STRING_CONFIG_H_AUTHOR "(TB Momsen)" // Who made the changes.
#define SHOW_BOOTSCREEN
#define STRING_SPLASH_LINE1 SHORT_BUILD_VERSION // will be shown during bootup in line 1
#define SERIAL_PORT 0
#define BAUDRATE 250000
#ifndef MOTHERBOARD
  #define MOTHERBOARD 80
#endif
#define CUSTOM_MACHINE_NAME "NMMU AM Printer"
#define EXTRUDERS 1
#define POWER_SUPPLY 1
#define TEMP_SENSOR_0 1
#define TEMP_SENSOR_1 0
#define TEMP_SENSOR_2 0
#define TEMP_SENSOR_3 0
#define TEMP_SENSOR_BED 0
#define MAX_REDUNDANT_TEMP_SENSOR_DIFF 10
#define TEMP_RESIDENCY_TIME 10  // (seconds)
#define TEMP_HYSTERESIS 3       // (degC) range of +/- temperatures considered "close" to the target one
#define TEMP_WINDOW     1       // (degC) Window around target to start the residency timer x degC early.
#define TEMP_BED_RESIDENCY_TIME 10  // (seconds)
#define TEMP_BED_HYSTERESIS 3       // (degC) range of +/- temperatures considered "close" to the target one
#define TEMP_BED_WINDOW     1       // (degC) Window around target to start the residency timer x degC early.
#define HEATER_0_MINTEMP 5
#define HEATER_1_MINTEMP 5
#define HEATER_2_MINTEMP 5
#define HEATER_3_MINTEMP 5
#define BED_MINTEMP 5
#define HEATER_0_MAXTEMP 230
#define HEATER_1_MAXTEMP 230
#define HEATER_2_MAXTEMP 230
#define HEATER_3_MAXTEMP 230
#define BED_MAXTEMP 130
#define EXTRUDER_WATTS (12.0*12.0/6.7) // P=U^2/R
#define BED_WATTS (12.0*12.0/1.1)      // P=U^2/R
#define PIDTEMP
```

Figure F.1.: Printer Operation Source Code – Arduino 1.6.9.

Marlin - Configuration.h | Arduino 1.6.9

File Edit Sketch Tools Help

Marlin | Conditionals.h | Configuration.h § | Configuration_adv.h | M100_Free_Mem_Chk.cpp | Marlin.h | MarlinSerial.cpp

```
#define BANG_MAX 127 // limits current to nozzle while in bang-bang mode; 255=full current
#define PID_MAX BANG_MAX // limits current to nozzle while PID is active (see PID_FUNCTIONAL_RANGE below); 255
#if ENABLED(PIDTEMP)
#define PID_AUTOTUNE_MENU // Add PID Autotune to the LCD "Temperature" menu to run M303 and apply the result.
#define PID_DEBUG // Sends debug data to the serial port.
#define PID_FUNCTIONAL_RANGE 20 // If the temperature difference between the target temperature and the actual
                                // is more than PID_FUNCTIONAL_RANGE then the PID will be shut off and the h
#define PID_INTEGRAL_DRIVE_MAX PID_MAX  //limit for the integral term
#define K1 0.95 //smoothing factor within the PID
#define  DEFAULT_Kp 2.04
#define  DEFAULT_Ki 0.08
#define  DEFAULT_Kd 50.00
#endif // PIDTEMP
#define MAX_BED_POWER 255 // limits duty cycle to bed; 255=full current
#if ENABLED(PIDTEMPBED)
  #define PID_BED_INTEGRAL_DRIVE_MAX MAX_BED_POWER //limit for the integral term
 #endif // PIDTEMPBED
#define PREVENT_DANGEROUS_EXTRUDE
#define EXTRUDE_MINTEMP 170
#define USE_XMIN_PLUG
#define USE_YMIN_PLUG
#define USE_ZMIN_PLUG
#define USE_XMAX_PLUG
#define ENDSTOPPULLUPS // Comment this out (using // at the start of the line) to disable the endstop pullup r
const bool X_MIN_ENDSTOP_INVERTING = true; // set to true to invert the logic of the endstop.
const bool Y_MIN_ENDSTOP_INVERTING = true; // set to true to invert the logic of the endstop.
const bool Z_MIN_ENDSTOP_INVERTING = true; // set to true to invert the logic of the endstop.
const bool X_MAX_ENDSTOP_INVERTING = false; // set to true to invert the logic of the endstop.
const bool Y_MAX_ENDSTOP_INVERTING = false; // set to true to invert the logic of the endstop.
const bool Z_MAX_ENDSTOP_INVERTING = false; // set to true to invert the logic of the endstop.
const bool Z_MIN_PROBE_ENDSTOP_INVERTING = false; // set to true to invert the logic of the endstop.
#define Z_MIN_PROBE_USES_Z_MIN_ENDSTOP_PIN
#define X_ENABLE_ON 0
#define Y_ENABLE_ON 0
#define Z_ENABLE_ON 0
#define E_ENABLE_ON 0 // For all extruders
#define DISABLE_X false
#define DISABLE_Y false
#define DISABLE_Z false
#define DISABLE_E false // For all extruders
#define DISABLE_INACTIVE_EXTRUDER true //disable only inactive extruders and keep active extruder enabled
#define INVERT_X_DIR true
#define INVERT_Y_DIR false
#define INVERT_Z_DIR false
#define INVERT_E0_DIR false
#define INVERT_E1_DIR false
#define INVERT_E2_DIR false
#define INVERT_E3_DIR false
```

Figure F.2.: Printer Operation Source Code – Arduino 1.6.9.

Marlin - Configuration.h | Arduino 1.6.9

File Edit Sketch Tools Help

Marlin | Conditionals.h | Configuration.h § | Configuration_adv.h | M100_Free_Mem_Chk.cpp | Marlin.h | MarlinSerial.cpp

```
#define max_software_endstops true  // If true, axis won't move to coordinates greater than the defined length:
#define X_MIN_POS 0
#define Y_MIN_POS 0
#define Z_MIN_POS 0
#define X_MAX_POS 1080
#define Y_MAX_POS 1120
#define Z_MAX_POS 4000
#define MANUAL_HOME_POSITIONS  // If defined, MANUAL_*_HOME_POS below will be used
#if ENABLED(MANUAL_HOME_POSITIONS)
  #define MANUAL_X_HOME_POS 4
  #define MANUAL_Y_HOME_POS 4
  #define MANUAL_Z_HOME_POS 4
  //#define MANUAL_Z_HOME_POS 402 // For delta: Distance between nozzle and print surface after homing.
#endif
#define Z_SAFE_HOMING
#if ENABLED(Z_SAFE_HOMING)
  #define Z_SAFE_HOMING_X_POINT ((X_MIN_POS + X_MAX_POS) / 2)    // X point for Z homing when homing all axis
  #define Z_SAFE_HOMING_Y_POINT ((Y_MIN_POS + Y_MAX_POS) / 2)    // Y point for Z homing when homing all axis
#endif
#define HOMING_FEEDRATE {60*45, 60*45, 1*45, 0}  // set the homing speeds (mm/min)
#define DEFAULT_AXIS_STEPS_PER_UNIT   {160,160,160,160}  // default steps per unit for Ultimaker  (400steps/re
#define DEFAULT_MAX_FEEDRATE          {100, 100, 3, 100}    // (mm/sec)
#define DEFAULT_MAX_ACCELERATION      {1000,1000,25,1000}    // X, Y, Z, E maximum start speed for accelerated
#define DEFAULT_ACCELERATION          500    // X, Y, Z and E acceleration in mm/s^2 for printing moves
#define DEFAULT_RETRACT_ACCELERATION  500    // E acceleration in mm/s^2 for retracts
#define DEFAULT_TRAVEL_ACCELERATION   500    // X, Y, Z acceleration in mm/s^2 for travel (non printing) moves
#define DEFAULT_XYJERK                10.0    // (mm/sec)
#define DEFAULT_ZJERK                 0.2     // (mm/sec)
#define DEFAULT_EJERK                 5.0    // (mm/sec)
#define CUSTOM_M_CODES
#define EEPROM_SETTINGS
#define PLA_PREHEAT_HOTEND_TEMP 190
#define PLA_PREHEAT_HPB_TEMP 70
#define PLA_PREHEAT_FAN_SPEED 255   // Insert Value between 0 and 255
#define ABS_PREHEAT_HOTEND_TEMP 240
#define ABS_PREHEAT_HPB_TEMP 110
#define ABS_PREHEAT_FAN_SPEED 255   // Insert Value between 0 and 255
#define LANGUAGE_INCLUDE GENERATE_LANGUAGE_INCLUDE(en)
#define DISPLAY_CHARSET_HD44780_JAPAN        // this is the most common hardware
#define DOGLCD      // Full graphics display
#define SDSUPPORT
#define LCD_FEEDBACK_FREQUENCY_DURATION_MS 50
#define LCD_FEEDBACK_FREQUENCY_HZ 500
#define REPRAP_DISCOUNT_FULL_GRAPHIC_SMART_CONTROLLER
#define SOFT_PWM_SCALE 0
#include "Configuration_adv.h"
```

Figure F.3.: Printer Operation Source Code – Arduino 1.6.9.

Marlin - Configuration_adv.h | Arduino 1.6.9

File Edit Sketch Tools Help

Marlin | Conditionals.h | Configuration.h § | Configuration_adv.h § | M100_Free_Mem_Chk.cpp | Marlin.h | MarlinSerial.cpp

```
#ifndef CONFIGURATION_ADV_H
#define CONFIGURATION_ADV_H
#include "Conditionals.h"
#if DISABLED(PIDTEMPBED)
  #define BED_CHECK_INTERVAL 5000 // ms between checks in bang-bang control
  #if ENABLED(BED_LIMIT_SWITCHING)
    #define BED_HYSTERESIS 2 // Only disable heating if T>target+BED_HYSTERESIS and enable heating if T>target-
  #endif
#endif
#if ENABLED(THERMAL_PROTECTION_HOTENDS)
  #define THERMAL_PROTECTION_PERIOD 40        // Seconds
  #define THERMAL_PROTECTION_HYSTERESIS 4     // Degrees Celsius
  #define WATCH_TEMP_PERIOD 20                // Seconds
  #define WATCH_TEMP_INCREASE 2               // Degrees Celsius
#endif
#if ENABLED(THERMAL_PROTECTION_BED)
  #define THERMAL_PROTECTION_BED_PERIOD 20    // Seconds
  #define THERMAL_PROTECTION_BED_HYSTERESIS 2 // Degrees Celsius
#endif
#if ENABLED(PIDTEMP)
  // this adds an experimental additional term to the heating power, proportional to the extrusion speed.
  // if Kc is chosen well, the additional required power due to increased melting should be compensated.
  #define PID_ADD_EXTRUSION_RATE
  #if ENABLED(PID_ADD_EXTRUSION_RATE)
    #define DEFAULT_Kc (100) //heating power=Kc*(e_speed)
    #define LPQ_MAX_LEN 50
  #endif
#endif
#define AUTOTEMP
#if ENABLED(AUTOTEMP)
  #define AUTOTEMP_OLDWEIGHT 0.98
#endif
#define EXTRUDER_RUNOUT_MINTEMP 190
#define EXTRUDER_RUNOUT_SECONDS 30.
#define EXTRUDER_RUNOUT_ESTEPS 14. //mm filament
#define EXTRUDER_RUNOUT_SPEED 1500.  //extrusion speed
#define EXTRUDER_RUNOUT_EXTRUDE 100
#define TEMP_SENSOR_AD595_OFFSET 0.0
#define TEMP_SENSOR_AD595_GAIN   1.0
#define CONTROLLERFAN_PIN -1 //Pin used for the fan to cool controller (-1 to disable)
#define CONTROLLERFAN_SECS 60 //How many seconds, after all motors were disabled, the fan should run
#define CONTROLLERFAN_SPEED 255  // == full speed
#define FAN_KICKSTART_TIME 100
#define FAN_MIN_PWM 255
#define EXTRUDER_0_AUTO_FAN_PIN 8
#define EXTRUDER_1_AUTO_FAN_PIN 8
```

Figure F.4.: Printer Operation Source Code – Arduino 1.6.9


```
#define EXTRUDER_3_AUTO_FAN_PIN 8
#define EXTRUDER_AUTO_FAN_TEMPERATURE 10
#define EXTRUDER_AUTO_FAN_SPEED   255  // == full speed
#define ENDSTOPS_ONLY_FOR_HOMING // If defined the endstops will only be used for homing
#define Z_DUAL_STEPPER_DRIVERS
#if ENABLED(Z_DUAL_STEPPER_DRIVERS)
  #define Z_DUAL_ENDSTOPS
  #if ENABLED(Z_DUAL_ENDSTOPS)
    #define Z2_USE_ENDSTOP _XMAX_
  #endif
#endif // Z_DUAL_STEPPER_DRIVERS
#define X_HOME_BUMP_MM 5
#define Y_HOME_BUMP_MM 5
#define Z_HOME_BUMP_MM 2
#define HOMING_BUMP_DIVISOR {2, 2, 4}  // Re-Bump Speed Divisor (Divides the Homing Feedrate)
#define AXIS_RELATIVE_MODES {false, false, false, false}
#define INVERT_X_STEP_PIN false
#define INVERT_Y_STEP_PIN false
#define INVERT_Z_STEP_PIN false
#define INVERT_E_STEP_PIN false
#define DEFAULT_STEPPER_DEACTIVE_TIME 120
#define DISABLE_INACTIVE_X true
#define DISABLE_INACTIVE_Y true
#define DISABLE_INACTIVE_Z true  // set to false if the nozzle will fall down on your printed part when print h
#define DISABLE_INACTIVE_E true
#define DEFAULT_MINIMUMFEEDRATE       0.0     // minimum feedrate
#define DEFAULT_MINTRAVELFEEDRATE     0.0
#define DEFAULT_MINSEGMENTTIME        20000
#define SLOWDOWN
#define MINIMUM_PLANNER_SPEED 0.05// (mm/sec)
#define MICROSTEP_MODES {16,16,16,16,16} // [1,2,4,8,16]
#define DIGIPOT_MOTOR_CURRENT {135,135,135,135,135} // Values 0-255 (RAMBO 135 = ~0.75A, 185 = ~1A)
#define DIGIPOT_I2C_NUM_CHANNELS 8
#define DIGIPOT_I2C_MOTOR_CURRENTS {1.0, 1.0, 1.0, 1.0, 1.0, 1.0, 1.0, 1.0}
#define ENCODER_RATE_MULTIPLIER         // If defined, certain menu edit operations automatically multiply the
#define ENCODER_10X_STEPS_PER_SEC 75    // If the encoder steps per sec exceeds this value, multiply steps move
#define ENCODER_100X_STEPS_PER_SEC 160  // If the encoder steps per sec exceeds this value, multiply steps move
#define CHDK_DELAY 50 //How long in ms the pin should stay HIGH before going LOW again
#if ENABLED(SDSUPPORT)
  #define SD_DETECT_INVERTED
  #define SD_FINISHED_STEPPERRELEASE true  //if sd support and the file is finished: disable steppers?
  #define SD_FINISHED_RELEASECOMMAND "M84 X Y Z E" // You might want to keep the z enabled so your bed stays in
  #define SDCARD_RATHERRECENTFIRST  //reverse file order of sd card menu display. Its sorted practically after
  #if ENABLED(LCD_PROGRESS_BAR)
    #define PROGRESS_BAR_BAR_TIME 2000
    #define PROGRESS_BAR_MSG_TIME 3000
    #define PROGRESS_MSG_EXPIRE   0
```

Figure F.5.: Printer Operation Source Code – Arduino 1.6.

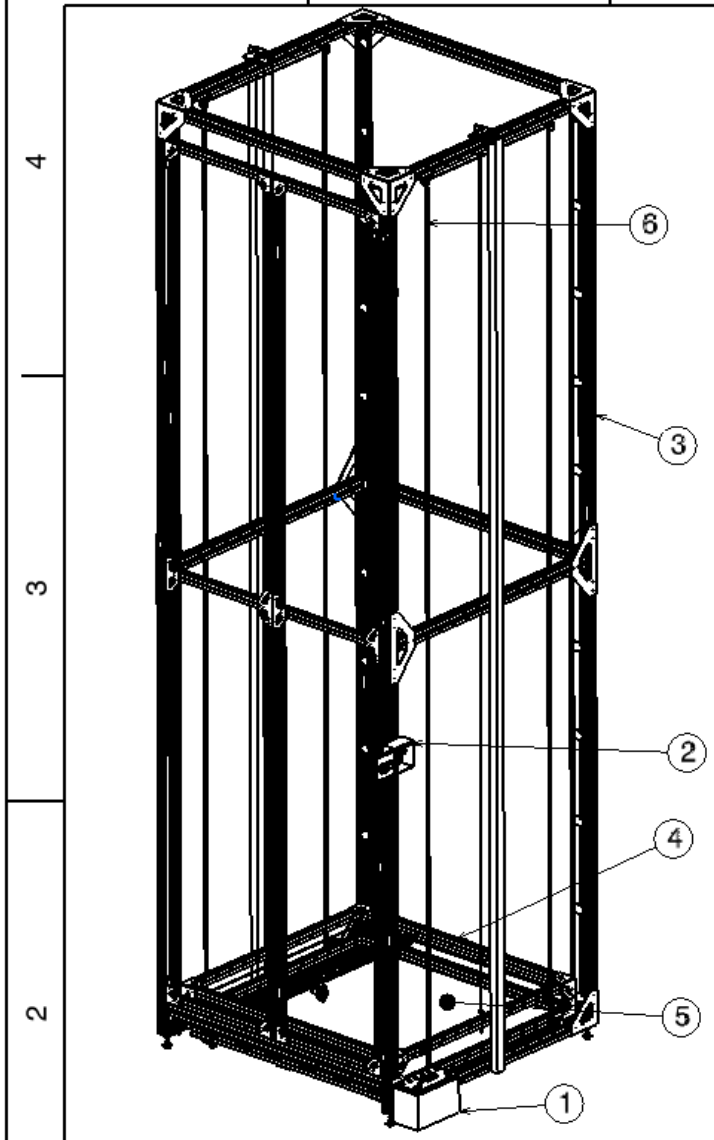

System	Description
1	12V DC System Power Supply
2	Control Box
3	Outer Frame
4	Gantry System
5	Print Bed
6	Belt Drive System

Isometric view
Scale: 1:30

DESIGNED BY: T.B. Momsen
DATE: 4/28/2016
CHECKED BY: T.B. Momsen
DATE: 4/28/2016
SIZE: A4
SCALE: 1:30
WEIGHT [kg]: 250
DRAWING NUMBER: 31
SHEET: 1/1

3D Printer Assembly - Systems View

3D Printer Project

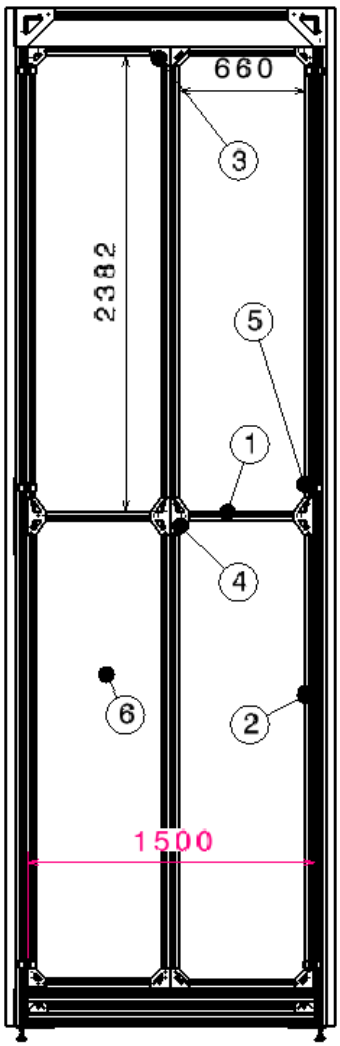

Front view
Scale: 1:30

Double Door Assembly
Bill of Materials

Item	Dimensions	Qty.
BR 45x45L ALU. Profile (1)	0.66m	6
BR 45x45L ALU. Profile (2)	4.9m	4
Gusset Plate (3)	0.1mx0.1m	8
Gusset Plate (4)	0.2mx0.1m	4
BR 45/45 Lift-Off Hinge (5)	45x60mm	6
Polycarbonate Sheeting (6)	2.39mx0.69mx2mm	4

DESIGNED BY: T.B. Momsen	Outer Frame: Front View Detail
DATE: 4/28/2016	
CHECKED BY: T.B. Momsen	
DATE: 4/28/2016	
SIZE A4	3D Printer Project
SCALE 1:1 / WEIGHT (kg): 276.53	DRAWING NUMBER 30 / SHEET 1/1

This drawing is our property; it can't be reproduced or communicated without our written agreement.

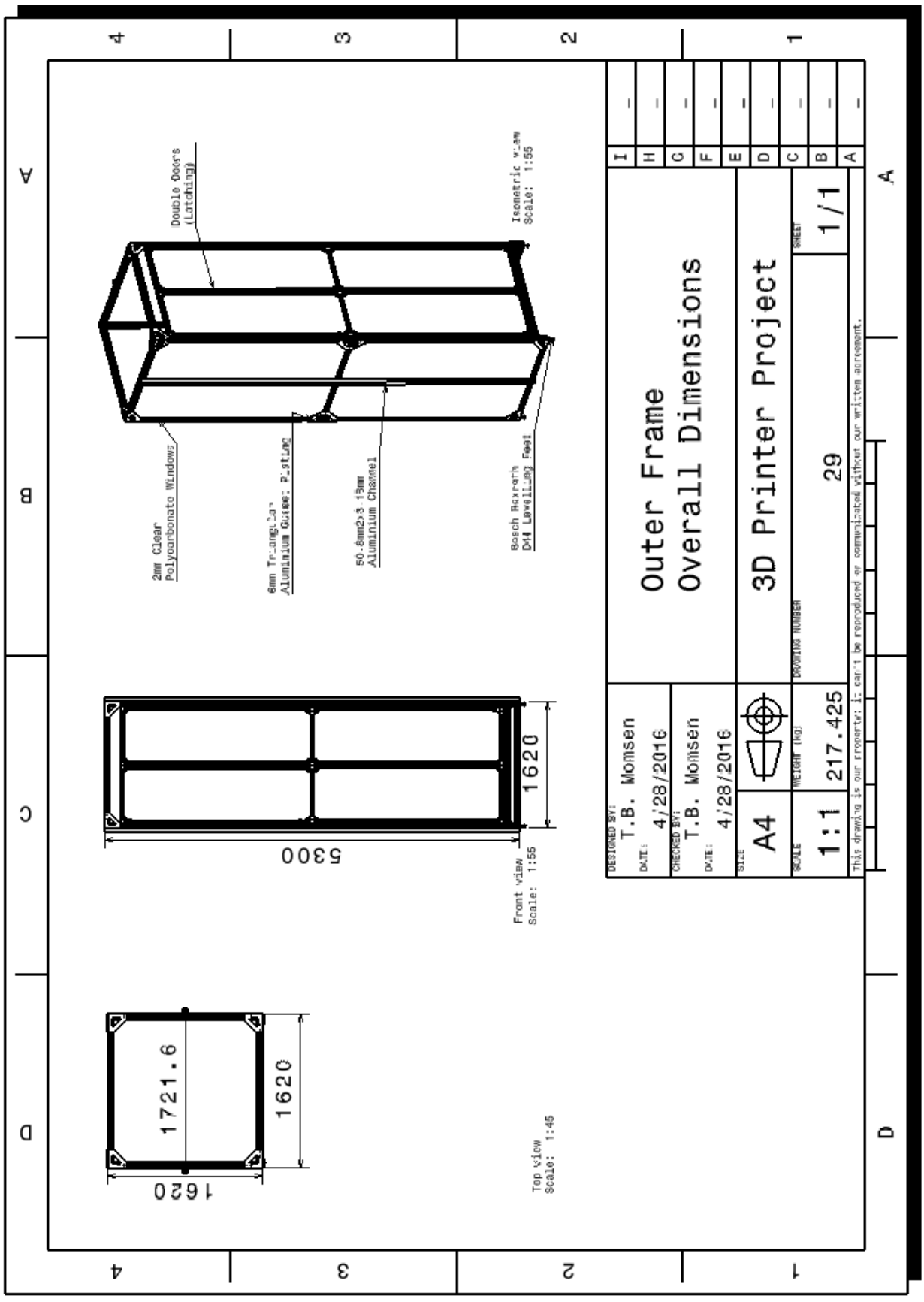
Outer Frame
Overall Dimensions
3D Printer Project
T.B. Momsen
4/28/2016
A4
1:1
217.425
29
1/1
Isometric view
Scale: 1:55
Front view
Scale: 1:55
Top view
Scale: 1:45
5300
1620
1721.6
1620
Double Doors (Latching)
2mm Clear Polycarbonate Windows
6mm Triangular Aluminum Guides: Flatland
50.8mm2x3.18mm Aluminum Channel
Bosch Rexroth D44 Leveling Feet

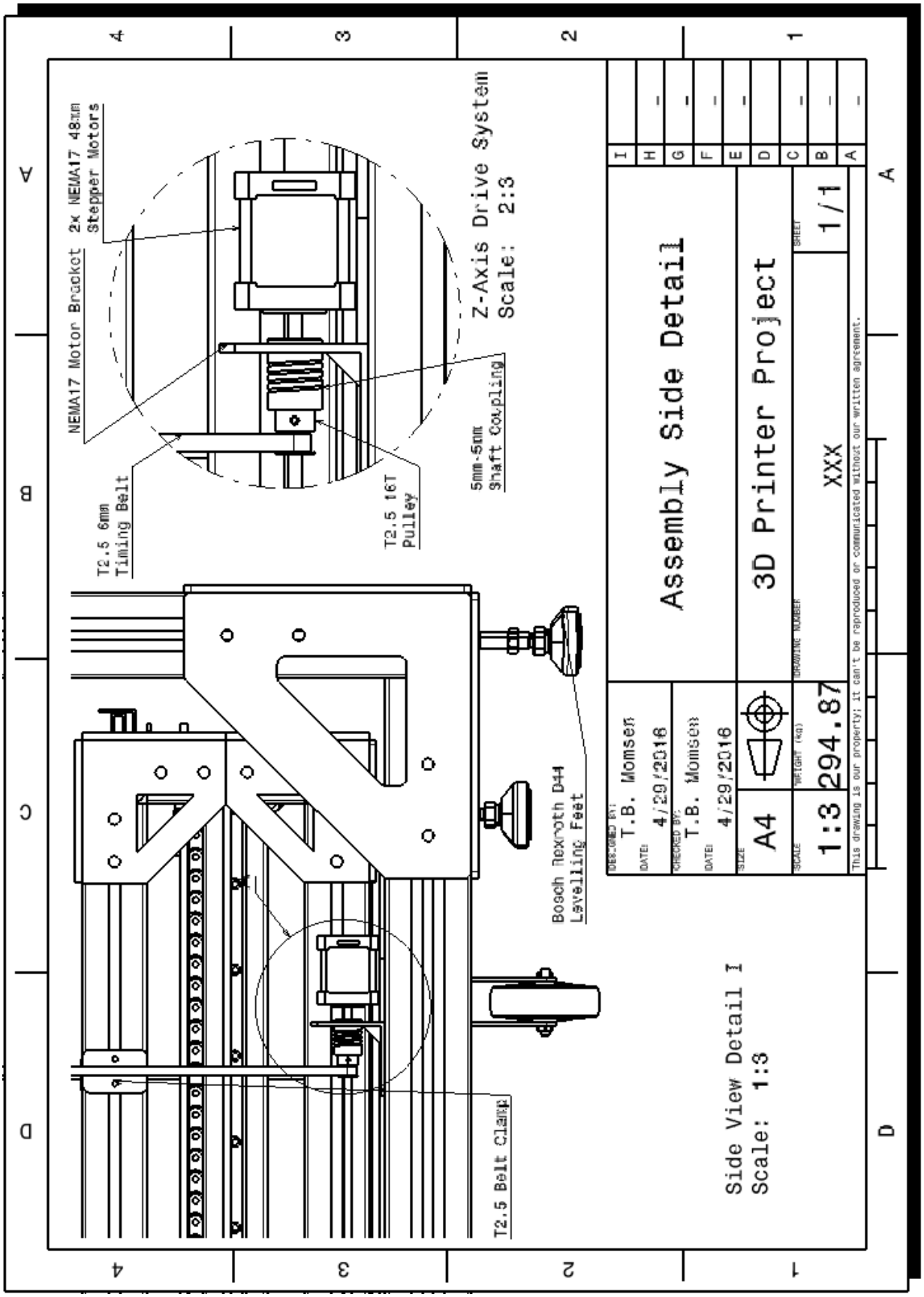
Assembly Side Detail
3D Printer Project
XXX
T.B. Momsen
4/29/2016
A4
1:3
294.87
1/1
Z-Axis Drive System
Scale: 2:3
NEMA17 Motor Bracket
2x NEMA17 48mm
Stepper Motors
T2.5 6mm
Timing Belt
T2.5 16T
Pulley
5mm-5mm
Shaft Coupling
Bosch Rexroth D44
Levelling Feet
T2.5 Belt Clamp
Side View Detail I
Scale: 1:3

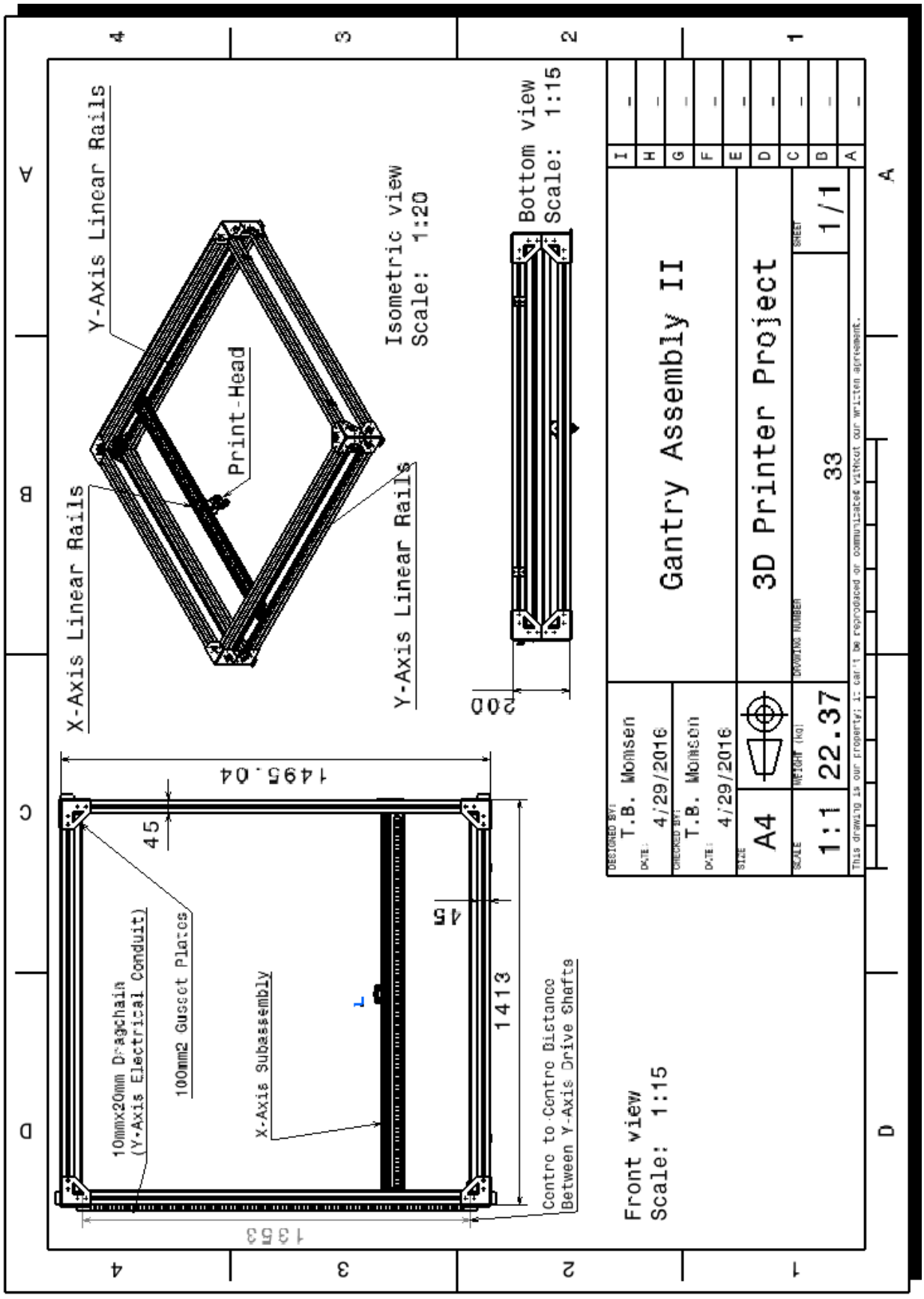
Gantry Assembly II
3D Printer Project
T.B. Monsen
4/29/2016
A4
1:1
22.37
33
1/1
Front view
Scale: 1:15
Isometric view
Scale: 1:20
Bottom view
Scale: 1:15
X-Axis Linear Rails
Y-Axis Linear Rails
Print-Head
10mmx20mm Dragchain
(Y-Axis Electrical Conduit)
100mm2 Gusset Plates
X-Axis Subassembly
Centre to Centre Distance
Between Y-Axis Drive Shafts
1495.04
1413
1553
45
200

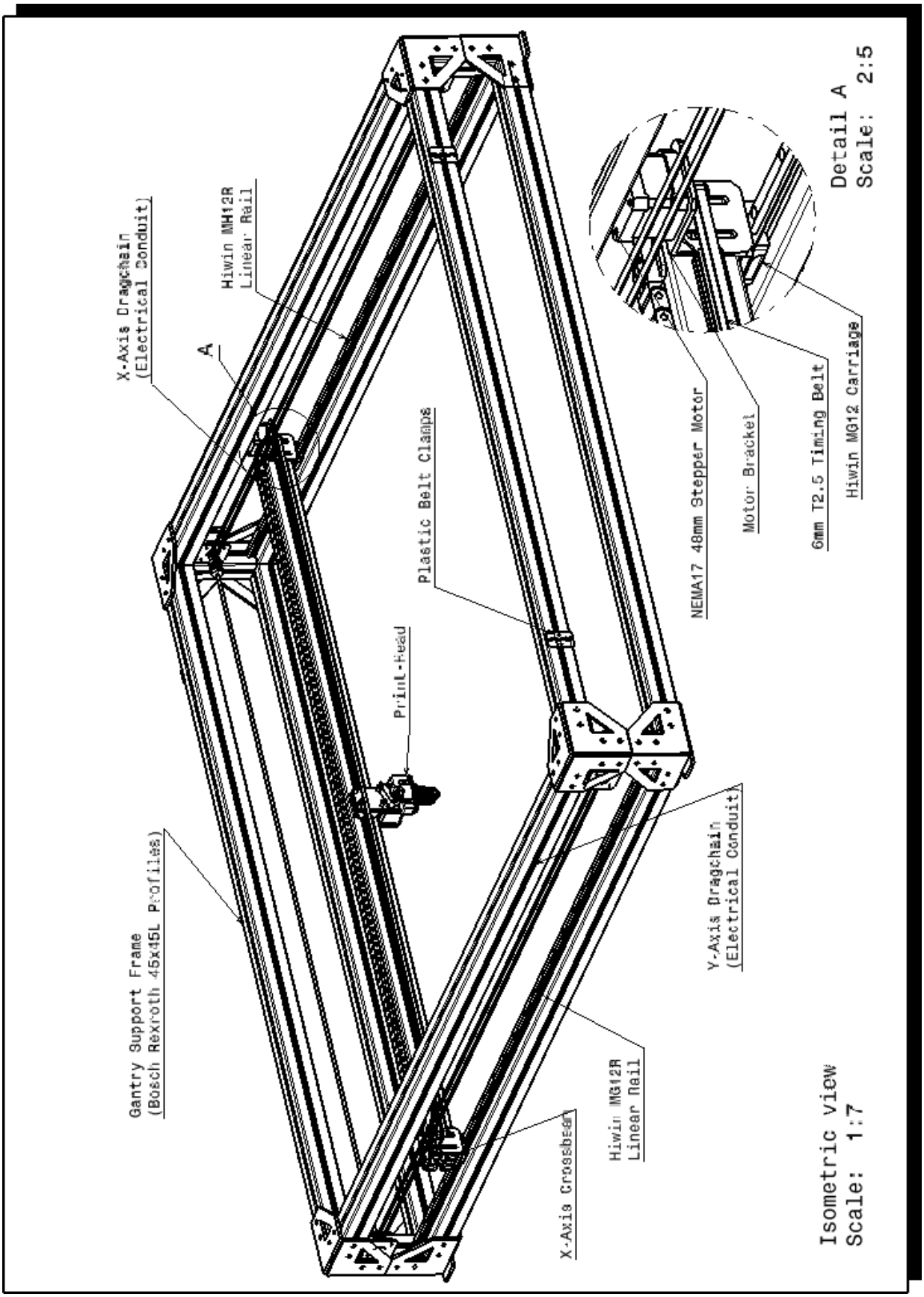
X-Axis Dragchain
(Electrical Conduit)
Hiwin MH12R
Linear Rail
A
Plastic Belt Clamps
Print-Head
Gantry Support Frame
(Bosch Rexroth 45x45L Profiles)
X-Axis Crossbeam
Hiwin MG12R
Linear Rail
Y-Axis Dragchain
(Electrical Conduit)
NEMA17 48mm Stepper Motor
Motor Bracket
6mm T2.5 Timing Belt
Hiwin MG12 Carriage
Detail A
Scale: 2:5
Isometric view
Scale: 1:7

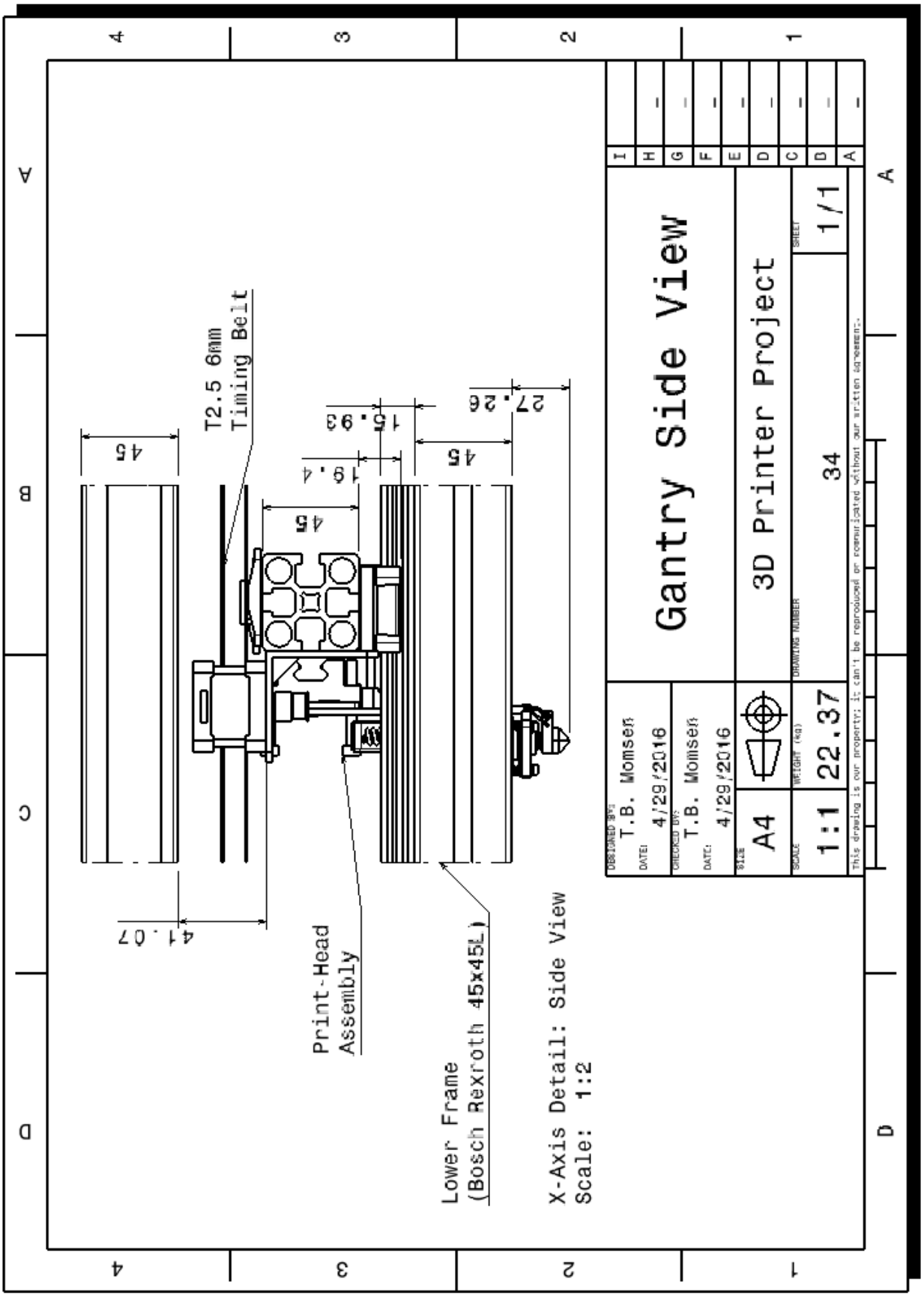
Gantry Side View
3D Printer Project
34
1/1
T.B. Momsen
4/29/2016
A4
1:1
22.37
T2.5 6mm
Timing Belt
45
19.4
15.93
27.26
41.07
Print-Head
Assembly
Lower Frame
(Bosch Rexroth 45x45L)
X-Axis Detail: Side View
Scale: 1:2

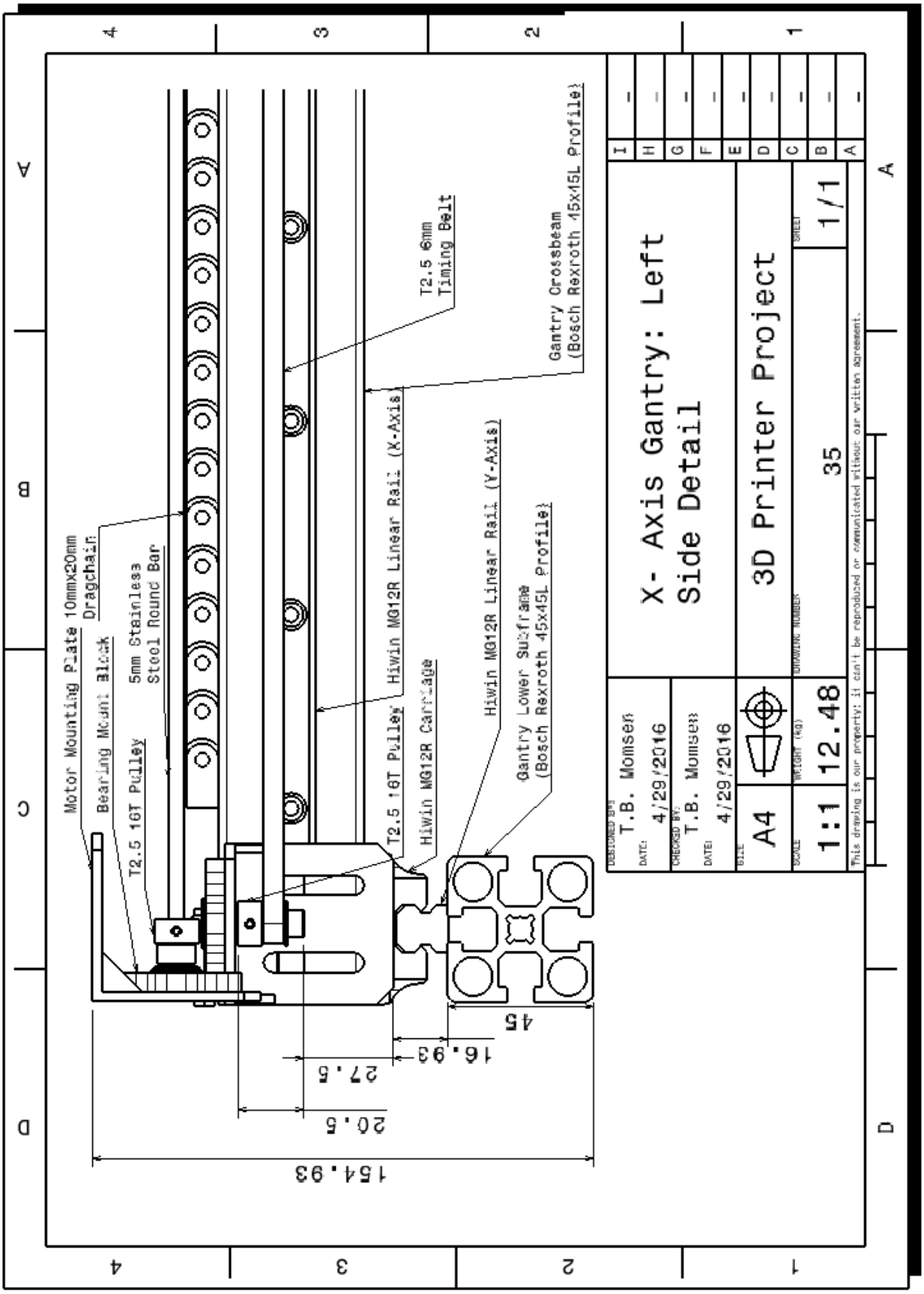
Motor Mounting Plate 10mmx20mm
Bearing Mount Block
T2.5 16T Pulley
5mm Stainless Steel Round Bar
Dragchain
T2.5 6mm Timing Belt
Gantry Crossbeam (Bosch Rexroth 45x45L Profile)
Hiwin MG12R Linear Rail (X-Axis)
Hiwin MG12R Linear Rail (Y-Axis)
Hiwin MG12R Carriage
T2.5 16T Pulley
Gantry Lower Subframe (Bosch Rexroth 45x45L Profile)
154.93
20.5
27.5
16.93
45
X- Axis Gantry: Left Side Detail
3D Printer Project
T.B. Momsen
4/29/2016
A4
1:1
12.48
35
1/1
This drawing is our property; it can't be reproduced or communicated without our written agreement.

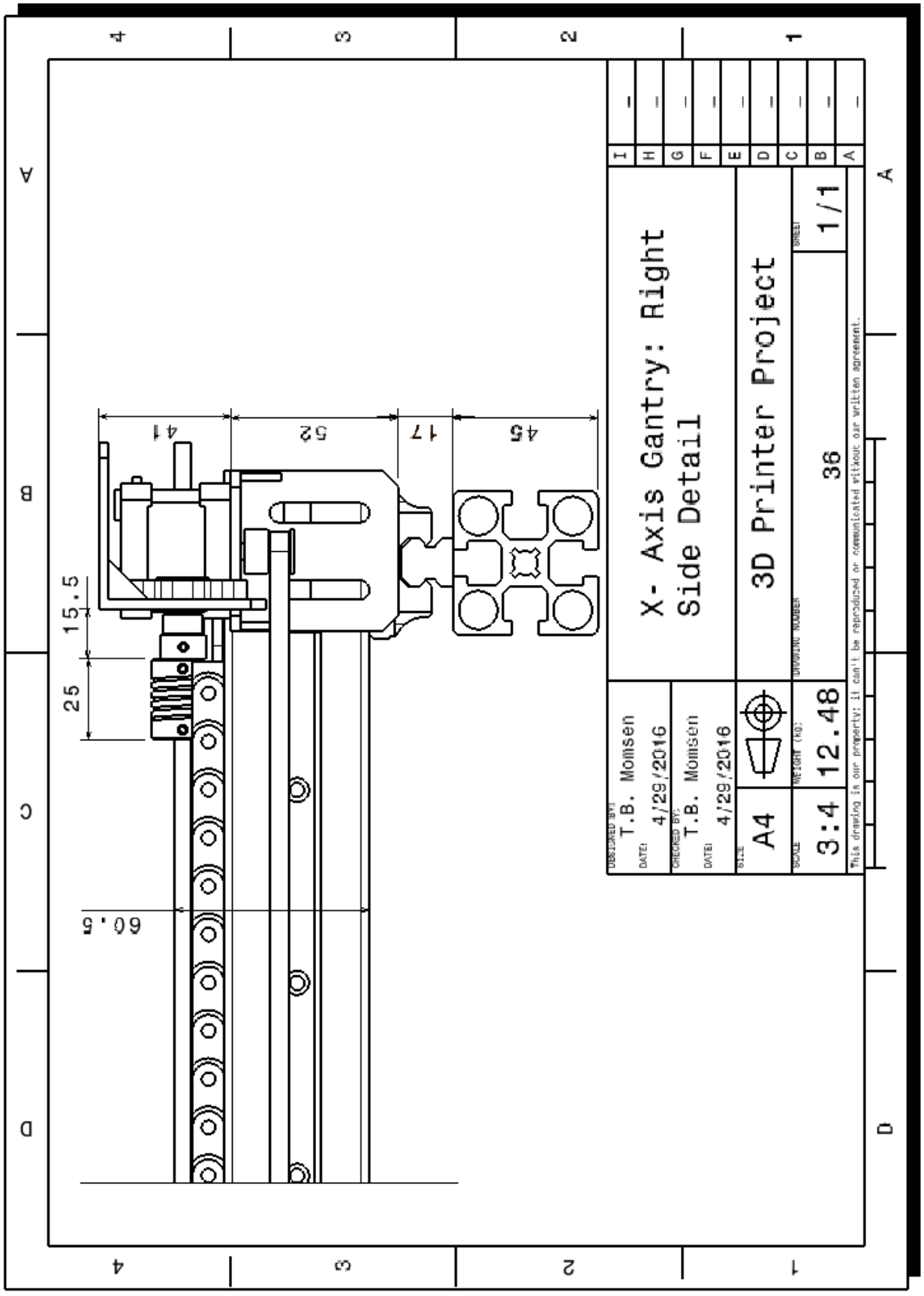
X- Axis Gantry: Right
Side Detail
3D Printer Project
36
1/1
A4
3:4
12.48
T.B. Monsen
4/29/2016
T.B. Monsen
4/29/2016
This drawing is our property; it can't be reproduced or communicated without our written agreement.
41
52
17
45
15.5
25
60.5

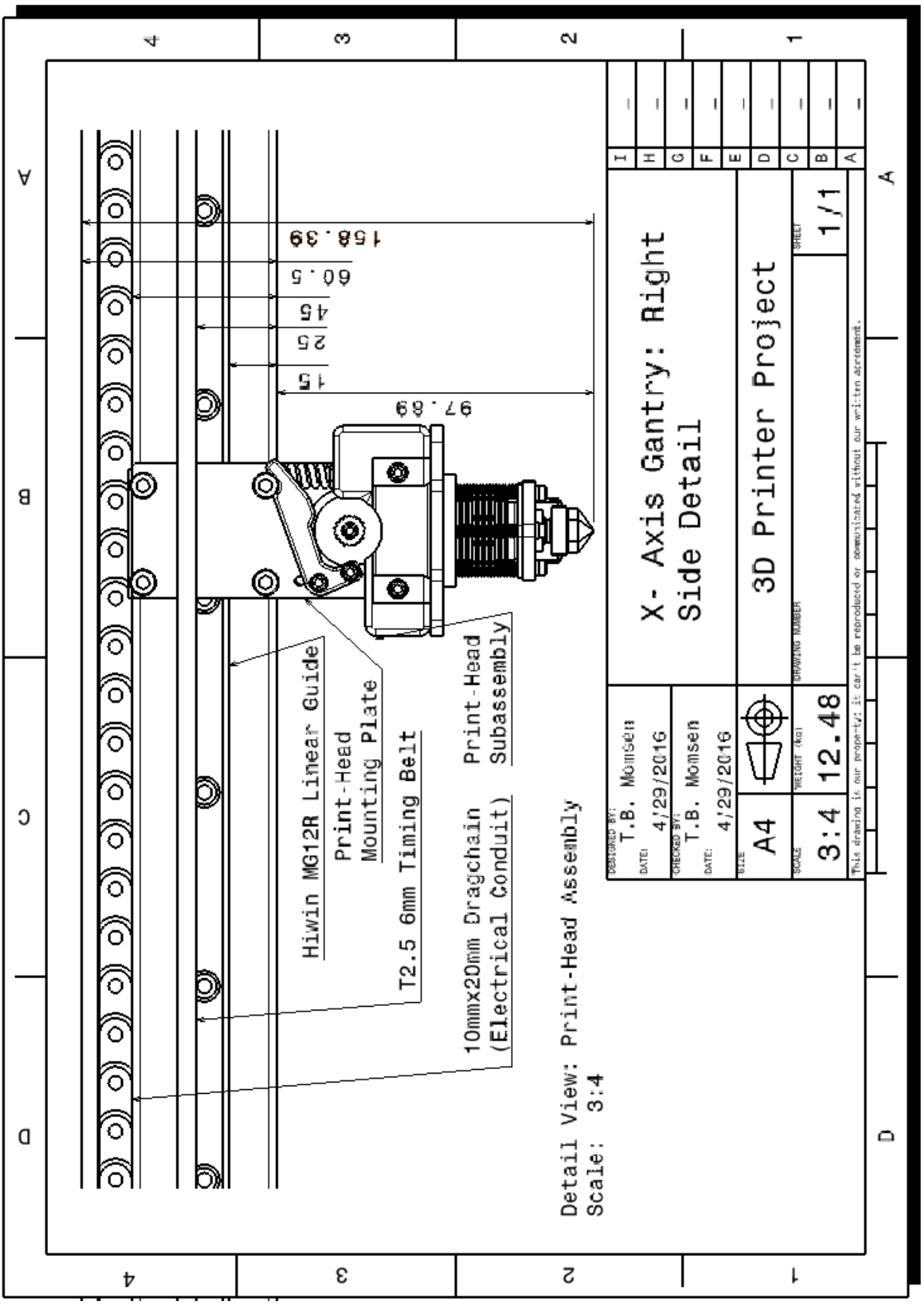
Hiwin MG12R Linear Guide
Print-Head Mounting Plate
T2.5 6mm Timing Belt
10mmx20mm Dragchain (Electrical Conduit)
Print-Head Subassembly
Detail View: Print-Head Assembly
Scale: 3:4
158.39
60.5
45
25
15
97.69
X- Axis Gantry: Right Side Detail
3D Printer Project
DESIGNED BY: T.B. Momsen
DATE: 4/29/2016
CHECKED BY: T.B. Momsen
DATE: 4/29/2016
SIZE A4
SCALE 3:4
WEIGHT (lbs) 12.48
DRAWING NUMBER
SHEET 1/1
This drawing is our property; it can't be reproduced or communicated without our written agreement.

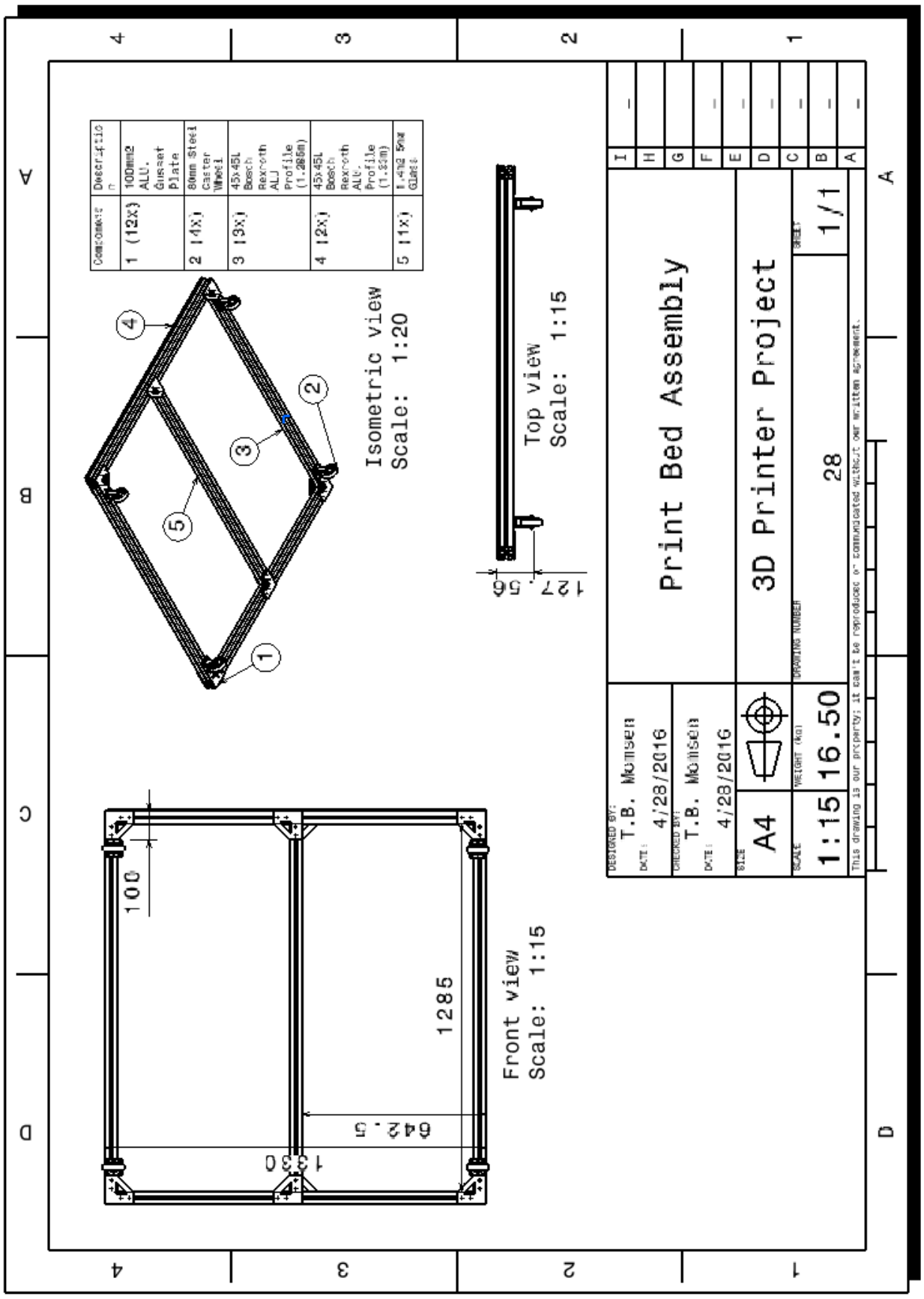
Print Bed Assembly
3D Printer Project
28
1/1
A4
1:15
16.50
T.B. Mønsen
4/28/2016
Isometric view
Scale: 1:20
Top view
Scale: 1:15
Front view
Scale: 1:15
100
1285
1330
642.5
127.56
1 (12x) 100mm2 ALU. Gusset Plate
2 (4x) 80mm Steel Caster Wheel
3 (3x) 45x45L Bosch Rexroth ALU Profile (1.285m)
4 (2x) 45x45L Bosch Rexroth ALU. Profile (1.33m)
5 (1x) T-slot Nut Guide
This drawing is our property; it can't be reproduced or communicated without our written agreement.

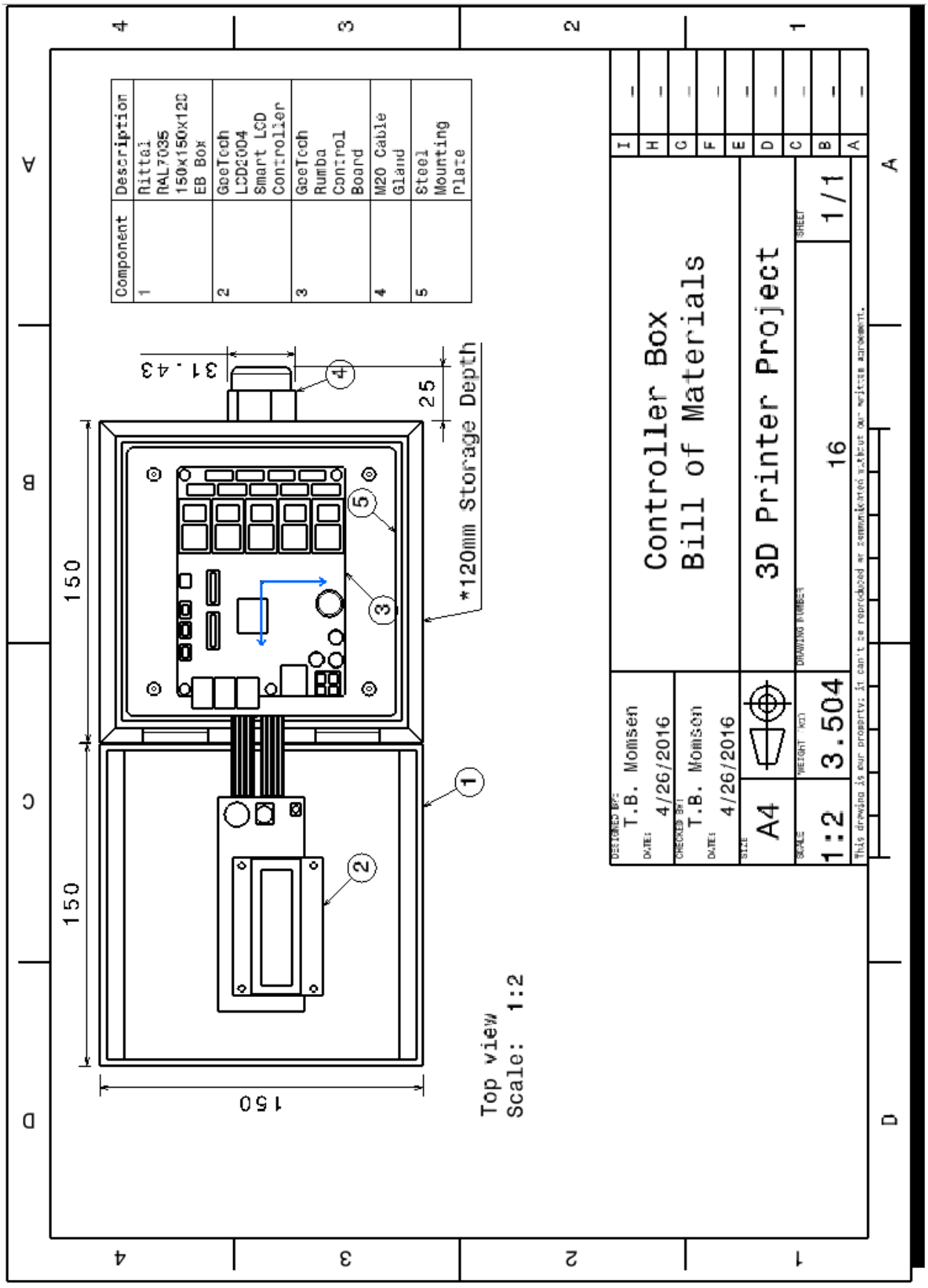
Controller Box
Bill of Materials
3D Printer Project
T.B. Monsen
4/26/2016
A4
1:2
3.504
16
1/1
Component
Description
1
Rittal RAL7035 150x150x120 EB Box
2
GeeTech LCD2004 Smart LCD Controller
3
GeeTech Rumba Control Board
4
M20 Cable Gland
5
Steel Mounting Plate
31.43
25
*120mm Storage Depth
150
150
150
Top view
Scale: 1:2

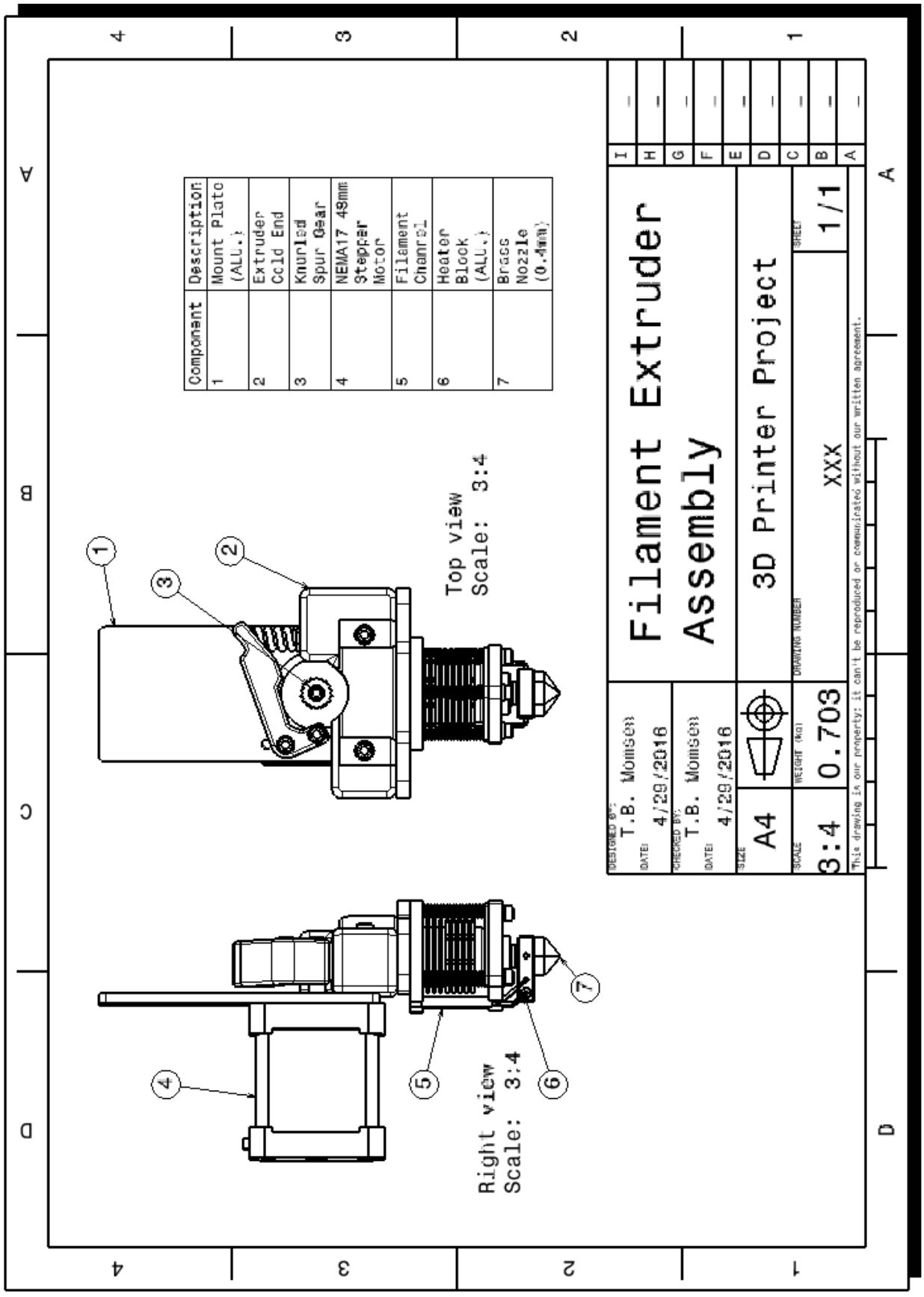
Filament Extruder Assembly
3D Printer Project
XXX
T.B. Momsen
4/29/2016
A4
0.703
1/1
3:4
Component
Description
1
Mount Plate (ALL)
2
Extruder Cold End
3
Knurled Spur Gear
4
NEMA17 48mm Stepper Motor
5
Filament Channel
6
Heater Block (ALL)
7
Brass Nozzle (0.4mm)
Top view
Scale: 3:4
Right view
Scale: 3:4

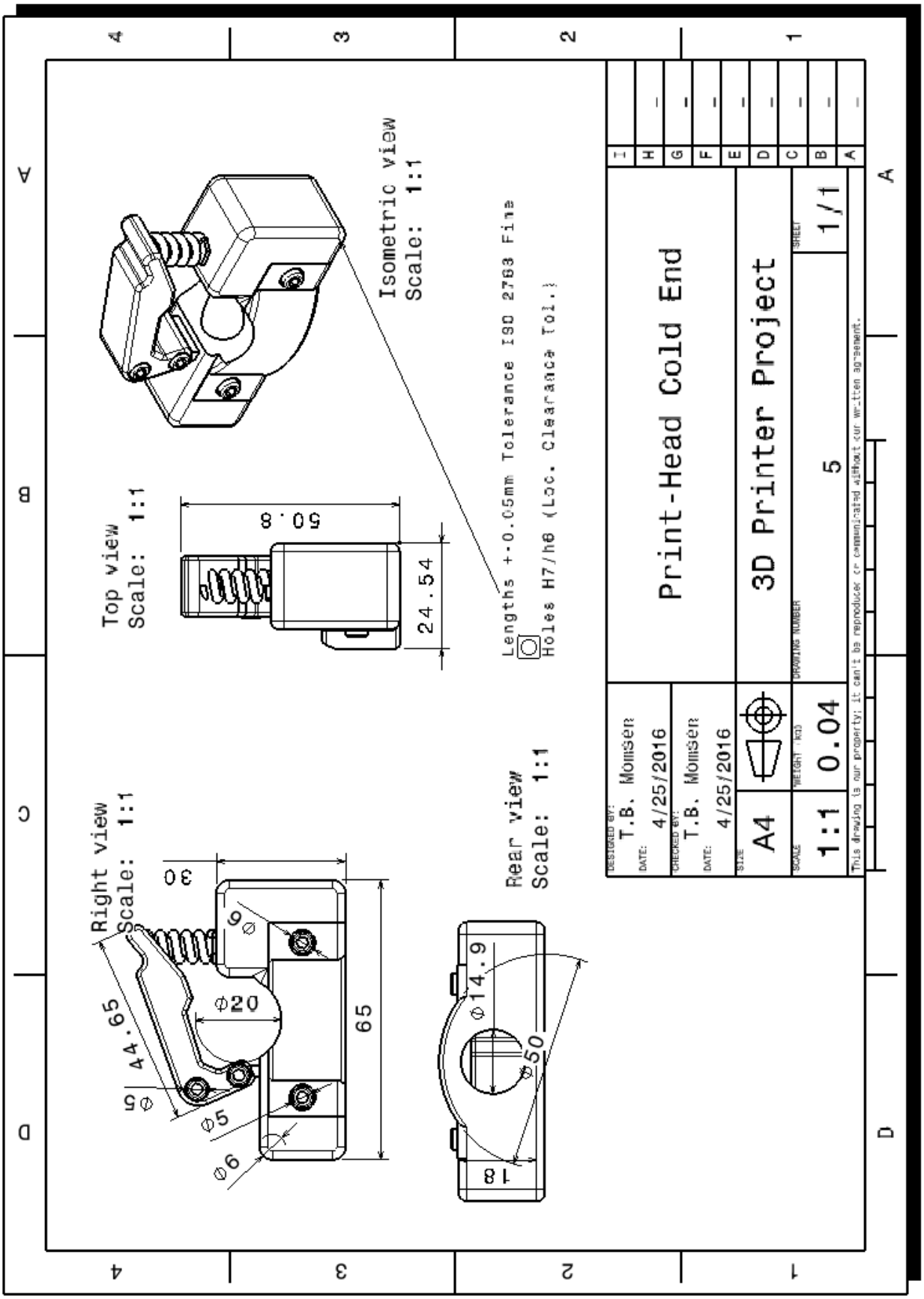
Isometric view
Scale: 1:1
Top view
Scale: 1:1
50.8
24.54
Lengths +-0.05mm Tolerance ISO 2768 Fine
Holes H7/h6 (Loc. Clearance Tol.)
Right view
Scale: 1:1
30
Φ9
44.65
Φ5
Φ20
65
Φ5
Φ6
Rear view
Scale: 1:1
Φ14.9
Φ50
18
Print-Head Cold End
3D Printer Project
DESIGNED BY: T.B. Monsen
DATE: 4/25/2016
CHECKED BY: T.B. Monsen
DATE: 4/25/2016
SIZE A4
SCALE 1:1
WEIGHT (KG) 0.04
DRAWING NUMBER 5
SHEET 1/1
This drawing is our property; it can't be reproduced or communicated without our written agreement.

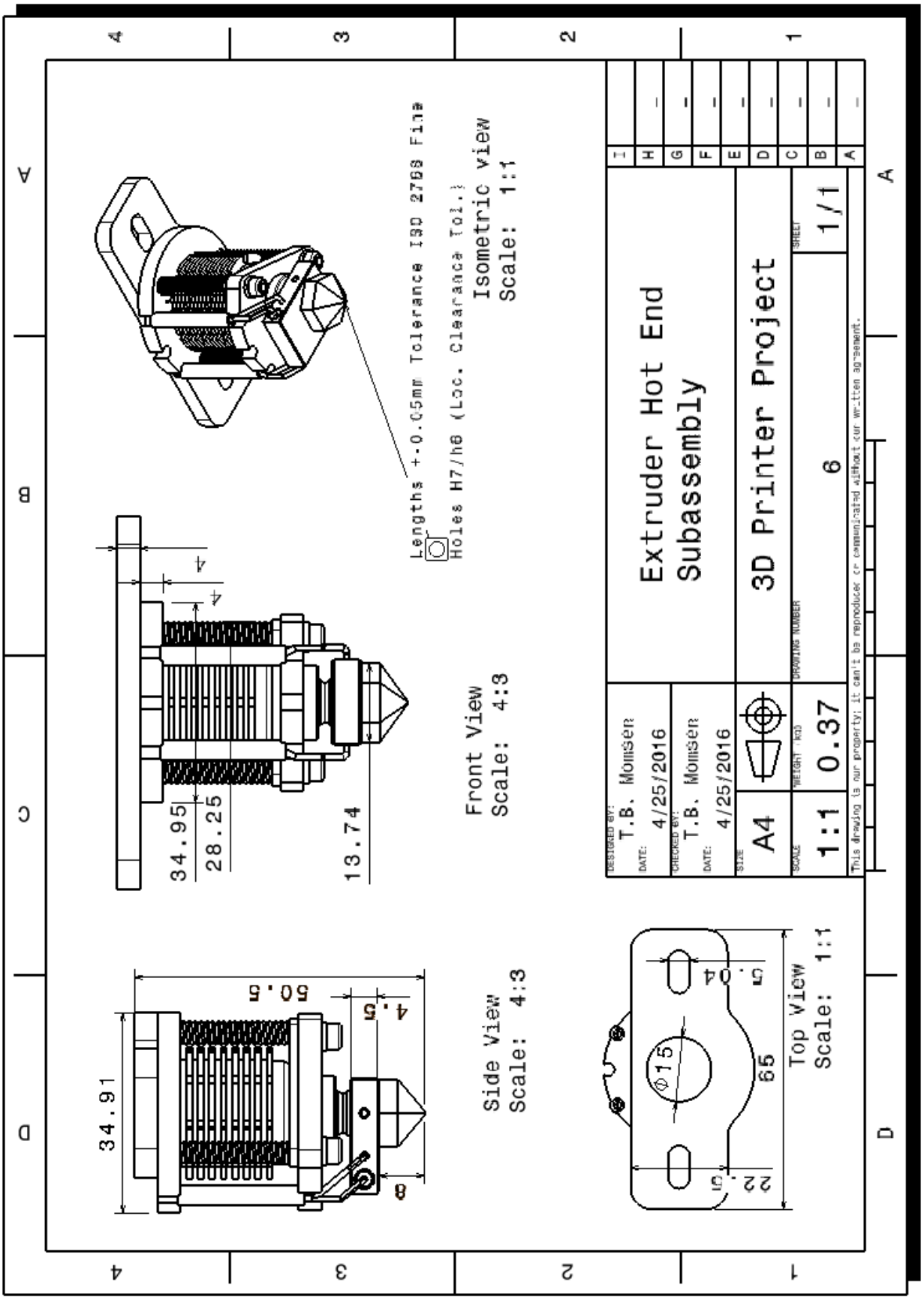
Extruder Hot End
Subassembly
3D Printer Project
DESIGNED BY: T.B. Monsen
DATE: 4/25/2016
CHECKER BY: T.B. Monsen
DATE: 4/25/2016
SIZE A4
SCALE 1:1
WEIGHT (kg) 0.37
DRAWING NUMBER 6
SHEET 1/1
This drawing is our property; it can't be reproduced or communicated without our written agreement.
Lengths +-0.05mm Tolerance ISO 2768 Fine
Holes H7/h6 (Loc. Clearance Tol.)
Isometric view
Scale: 1:1
Front View
Scale: 4:3
34.95
28.25
13.74
4
4
Side View
Scale: 4:3
34.91
50.5
4.5
8
Top View
Scale: 1:1
65
Φ15
22.5
10.04
5

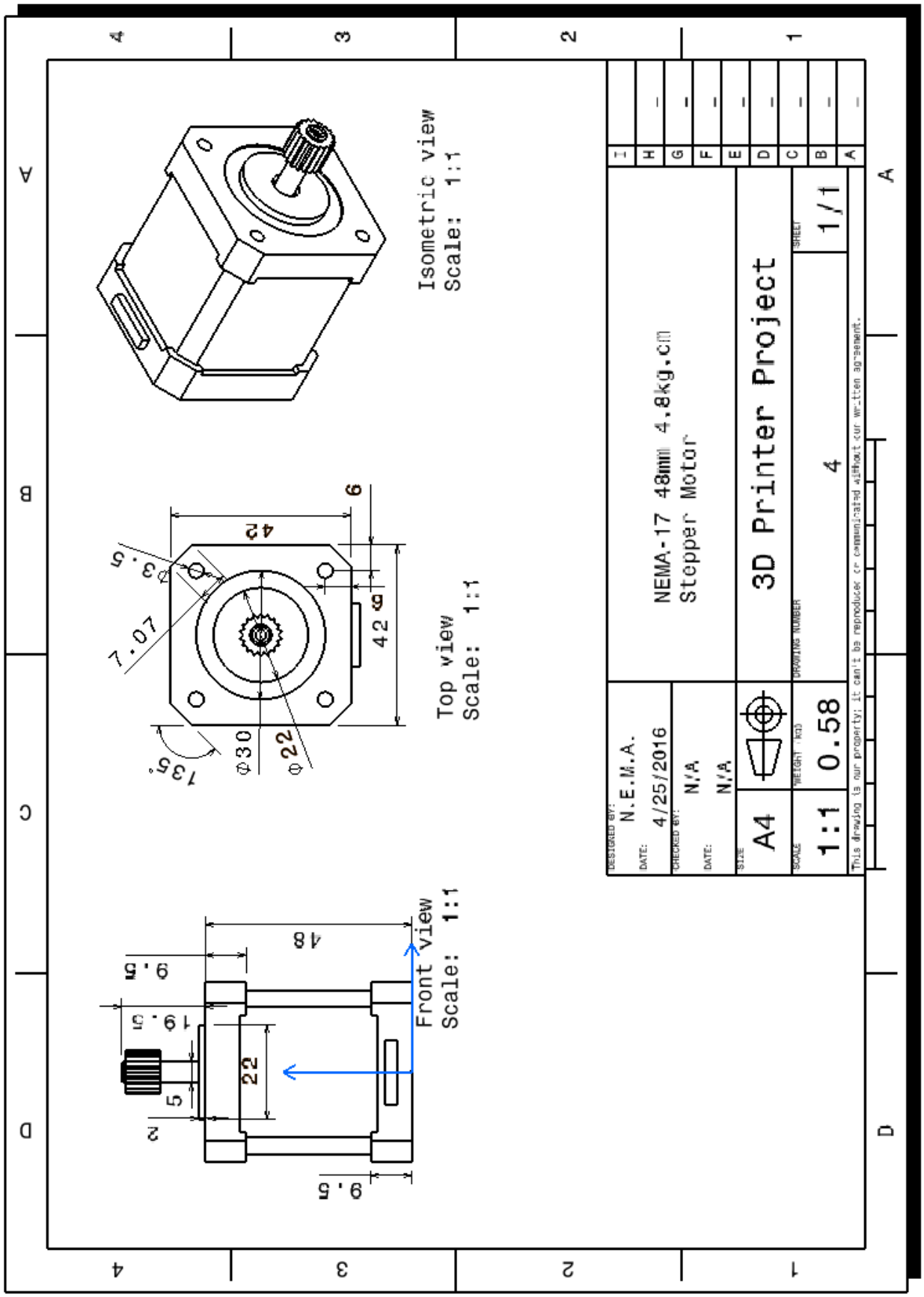
Isometric view
Scale: 1:1
Top view
Scale: 1:1
Front view
Scale: 1:1
NEMA-17 48mm 4.8kg.cm
Stepper Motor
3D Printer Project
DESIGNED BY: N.E.M.A.
DATE: 4/25/2016
CHECKED BY: N/A
DATE: N/A
SIZE A4
SCALE 1:1
WEIGHT (KG) 0.58
DRAWING NUMBER 4
SHEET 1/1
This drawing is our property; it can't be reproduced or communicated without our written agreement.

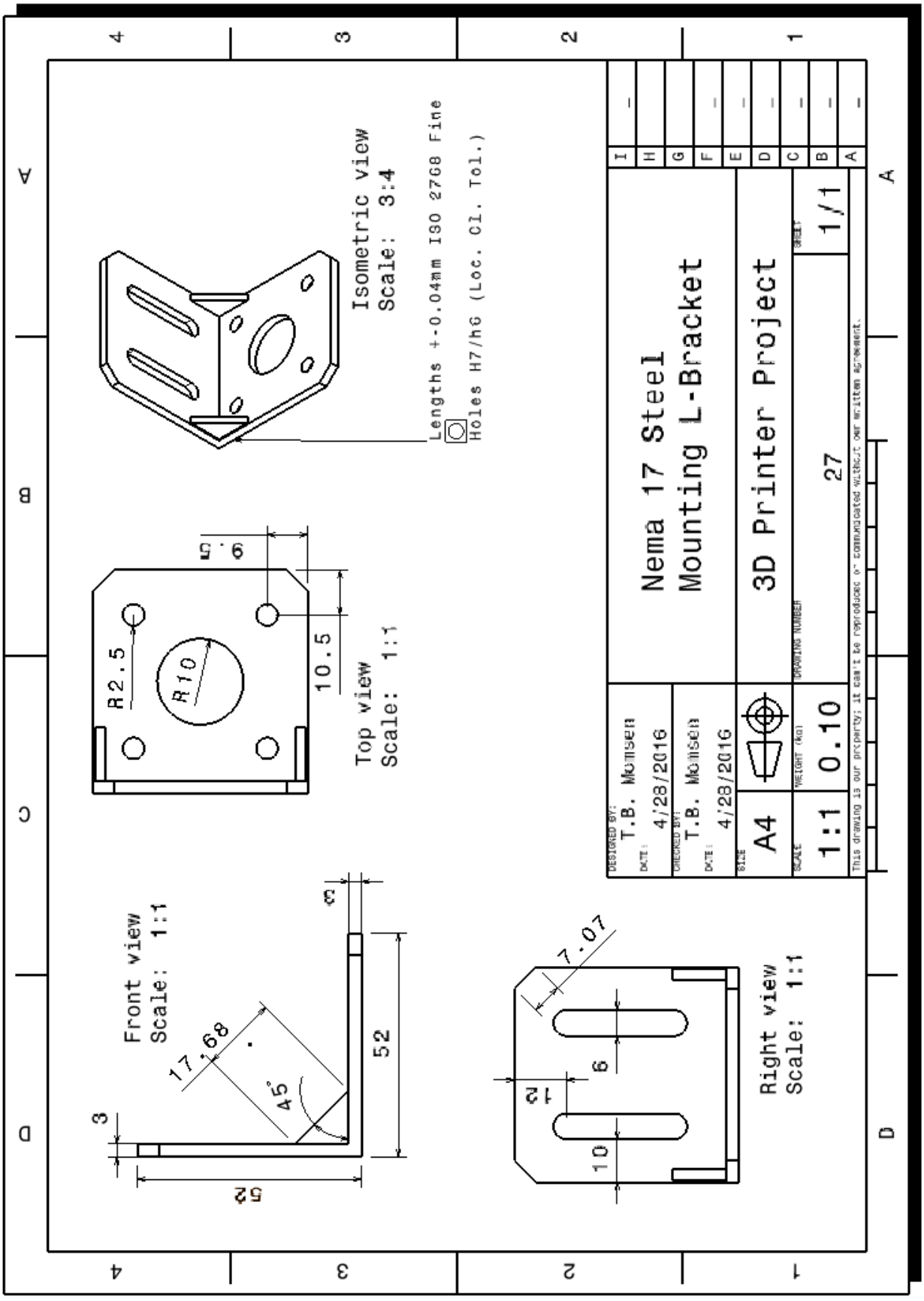
Nema 17 Steel
Mounting L-Bracket
3D Printer Project
27
1/1
A4
1:1
0.10
T.B. Monsen
4/28/2016
Isometric view
Scale: 3:4
Lengths +-0.04mm ISO 2768 Fine
Holes H7/hG (Loc. Cl. Tol.)
Top view
Scale: 1:1
R2.5
R10
10.5
9.5
Front view
Scale: 1:1
17.68
45°
52
3
Right view
Scale: 1:1
7.07
6
10

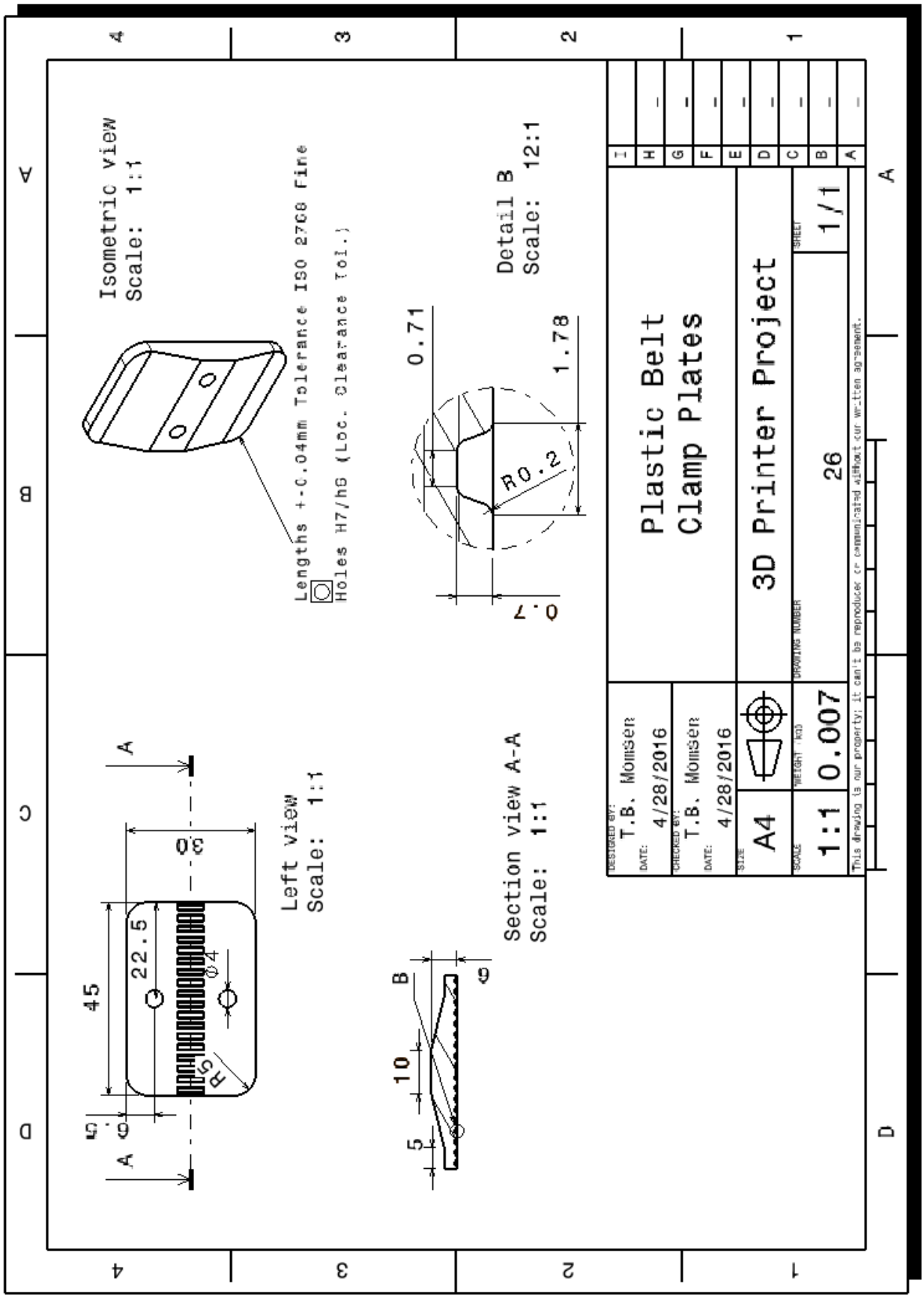
Isometric view
Scale: 1:1
Lengths +-0.04mm Tolerance ISO 2768 Fine
Holes H7/h6 (Loc. Clearance Tol.)
Detail B
Scale: 12:1
0.71
1.78
R0.2
0.7
Left view
Scale: 1:1
Section view A-A
Scale: 1:1
45
22.5
30
Ø4
R5
10
5
B
A
Plastic Belt
Clamp Plates
3D Printer Project
26
A4
1:1
0.007
1/1
T.B. Monsen
4/28/2016
This drawing is our property; it can't be reproduced or communicated without our written agreement.

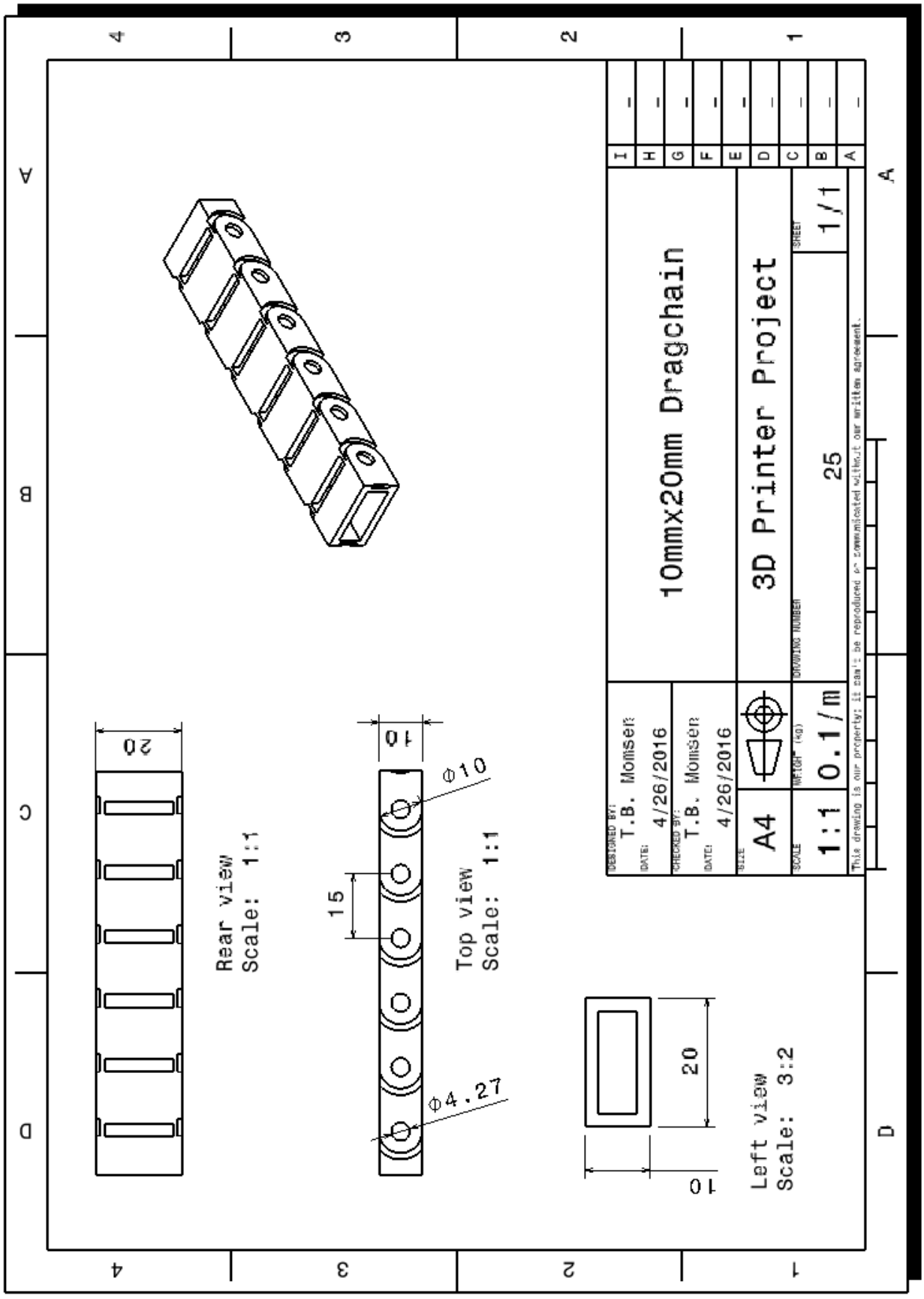
10mmx20mm Dragchain
3D Printer Project
T.B. Monsen
4/26/2016
A4
1:1
0.1/m
25
1/1
Rear view
Scale: 1:1
Top view
Scale: 1:1
Left view
Scale: 3:2
20
10
15
Φ10
Φ4.27

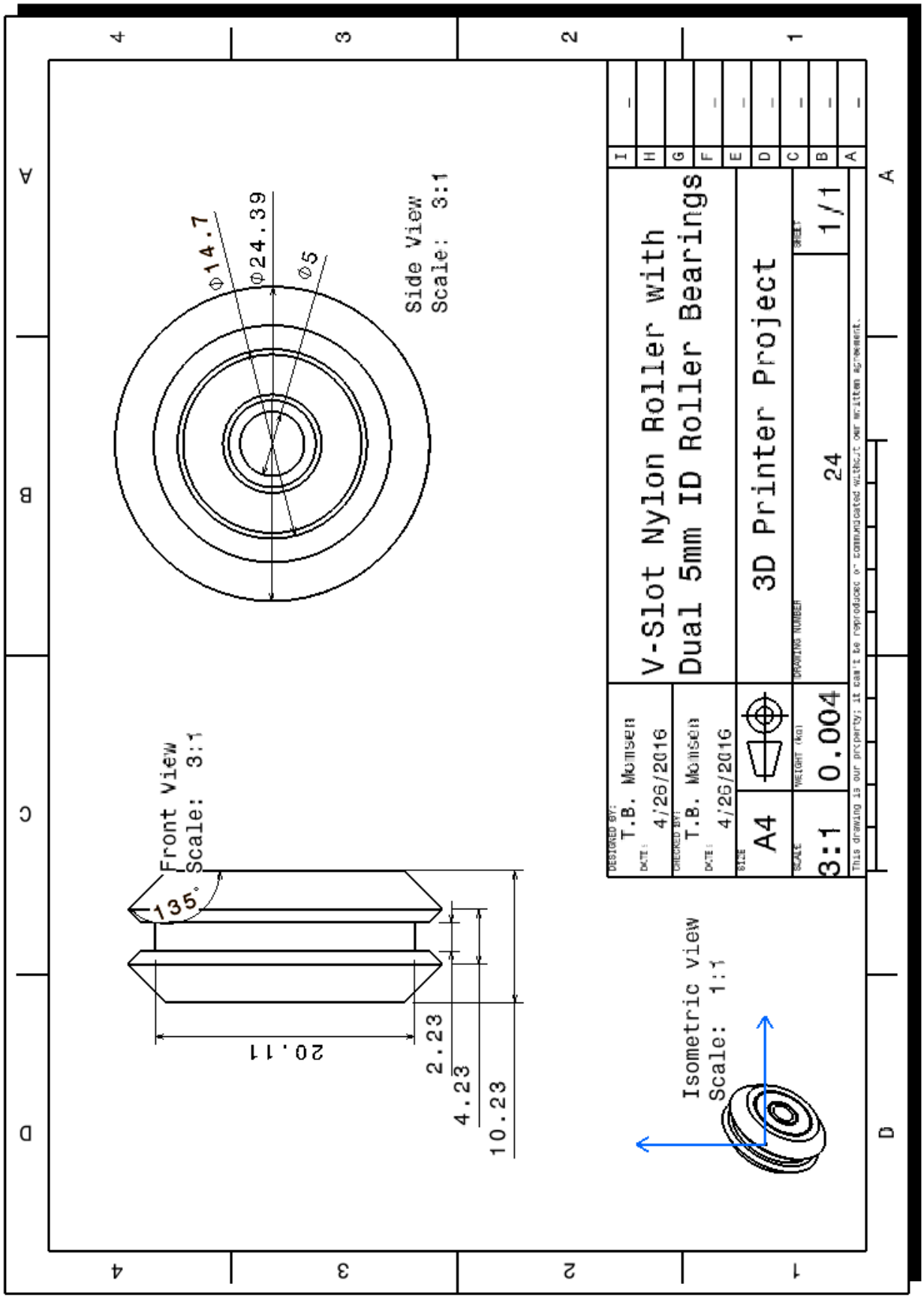
Side View
Scale: 3:1
Φ14.7
Φ24.39
Φ5
Front View
Scale: 3:1
135°
20.11
2.23
4.23
10.23
Isometric view
Scale: 1:1
V-Slot Nylon Roller with
Dual 5mm ID Roller Bearings
3D Printer Project
24
1/1
A4
0.004
3:1
T.B. Mousseau
4/26/2016
This drawing is our property; it can't be reproduced or communicated without our written agreement.

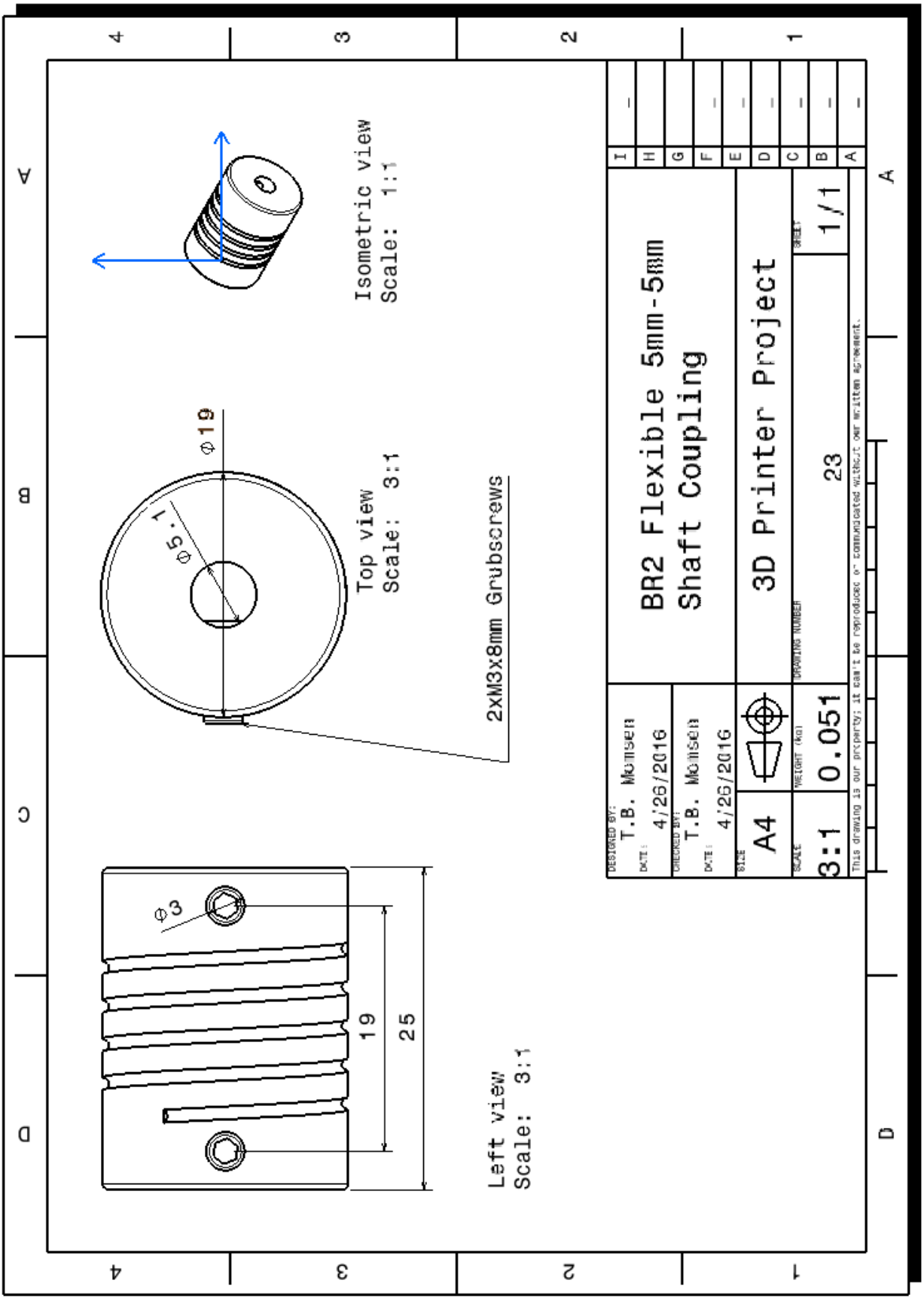
Isometric view
Scale: 1:1
Top view
Scale: 3:1
2xM3x8mm Grubscrews
Left view
Scale: 3:1
BR2 Flexible 5mm-5mm
Shaft Coupling
3D Printer Project
DESIGNED BY: T.B. Monsen
DATE: 4/26/2016
CHECKED BY: T.B. Monsen
DATE: 4/26/2016
SIZE A4
WEIGHT (Kg) 0.051
DRAWING NUMBER 23
SHEET 1/1
SCALE 3:1
This drawing is our property; it can't be reproduced or communicated without our written agreement.

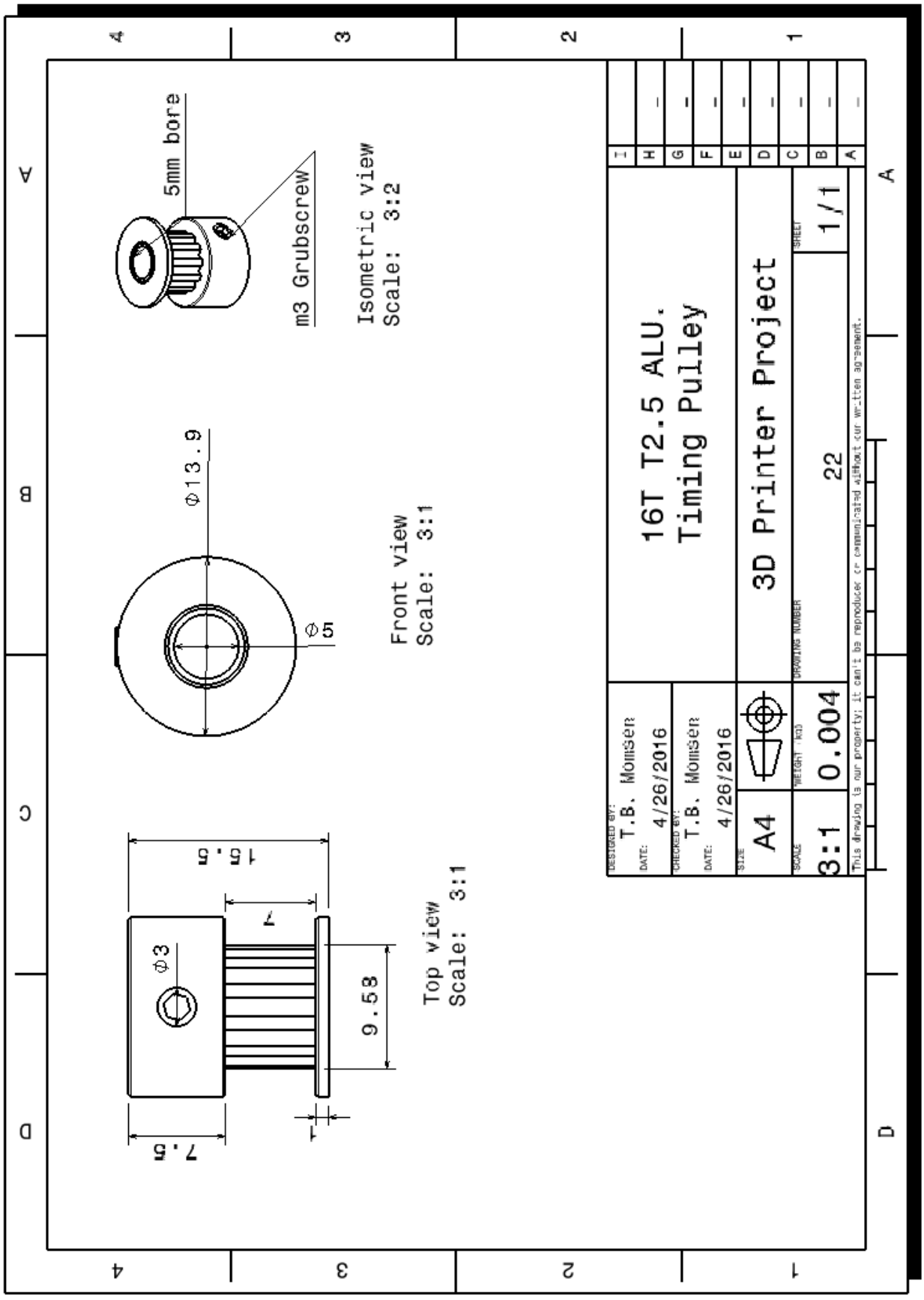
5mm bore
m3 Grubscrew
Isometric view
Scale: 3:2
Φ13.9
Φ5
Front view
Scale: 3:1
15.5
7
Φ3
9.58
7.5
Top view
Scale: 3:1
16T T2.5 ALU.
Timing Pulley
3D Printer Project
22
A4
3:1
0.004
1/1
T.B. Monsen
4/26/2016
This drawing is our property; it can't be reproduced or communicated without our written agreement.

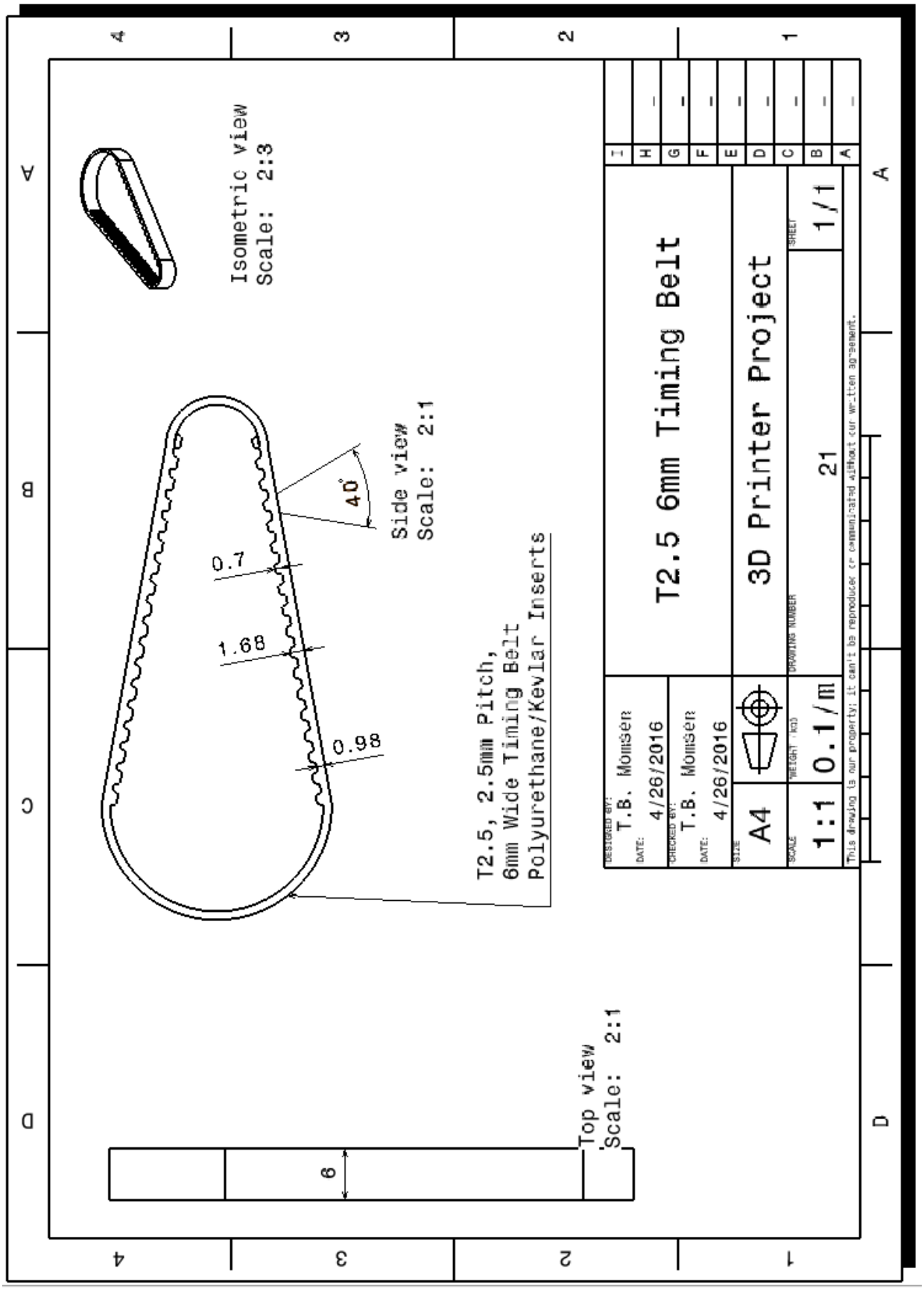
Isometric view
Scale: 2:3
Side view
Scale: 2:1
40°
0.7
1.68
0.98
T2.5, 2.5mm Pitch,
6mm Wide Timing Belt
Polyurethane/Kevlar Inserts
Top view
Scale: 2:1
6
T2.5 6mm Timing Belt
3D Printer Project
DESIGNED BY: T.B. Monsen
DATE: 4/26/2016
CHECKED BY: T.B. Monsen
DATE: 4/26/2016
SIZE A4
SCALE 1:1
WEIGHT (KG) 0.1/m
DRAWING NUMBER 21
SHEET 1/1
This drawing is our property; it can't be reproduced or communicated without our written agreement.

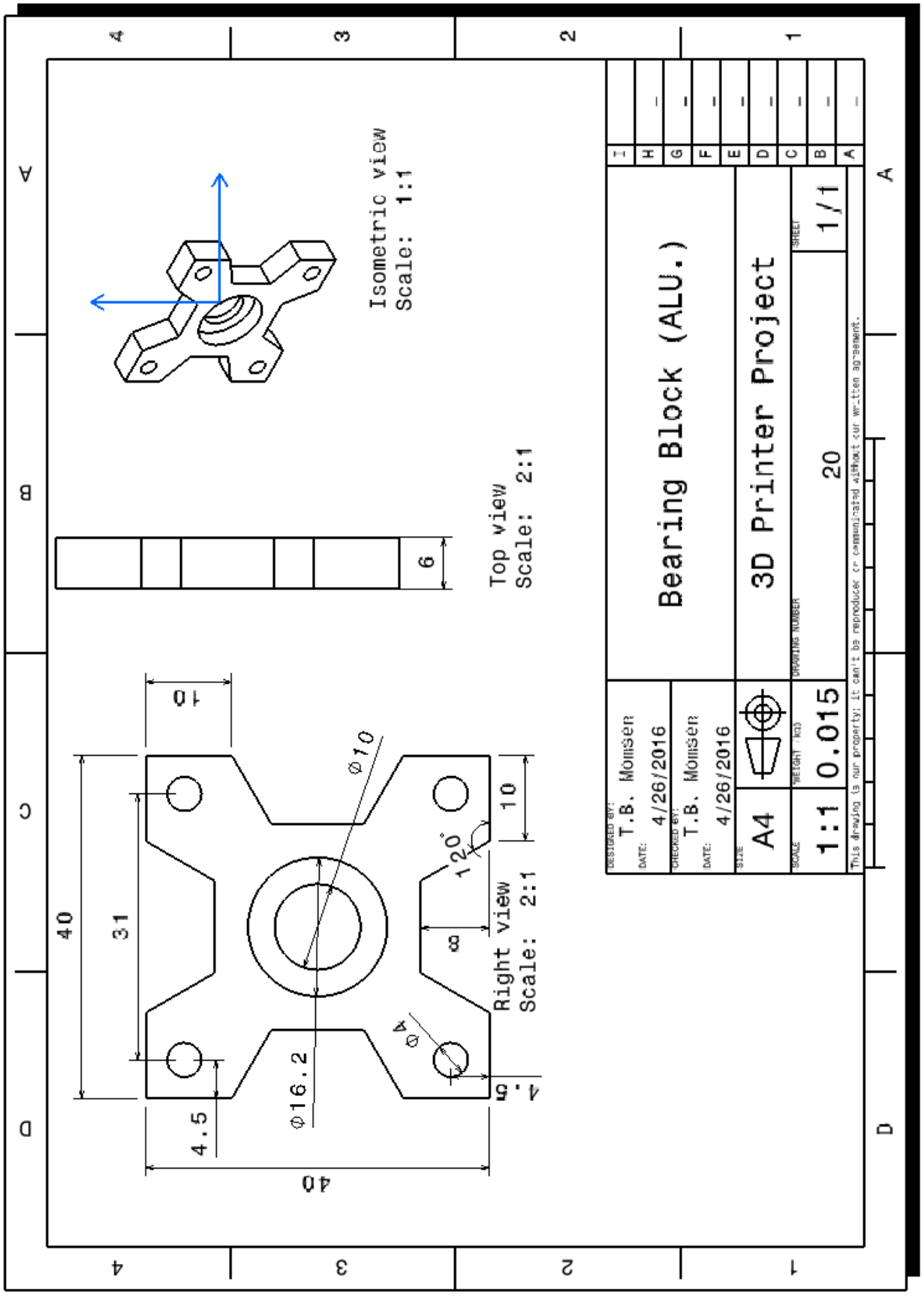
Isometric view
Scale: 1:1
Top view
Scale: 2:1
Right view
Scale: 2:1
Bearing Block (ALU.)
3D Printer Project
T.B. Mollsén
4/26/2016
A4
1:1
0.015
20
1/1
40
31
10
4.5
Ø16.2
Ø10
Ø4
120°
8
6
This drawing is our property; it can't be reproduced or communicated without our written agreement.

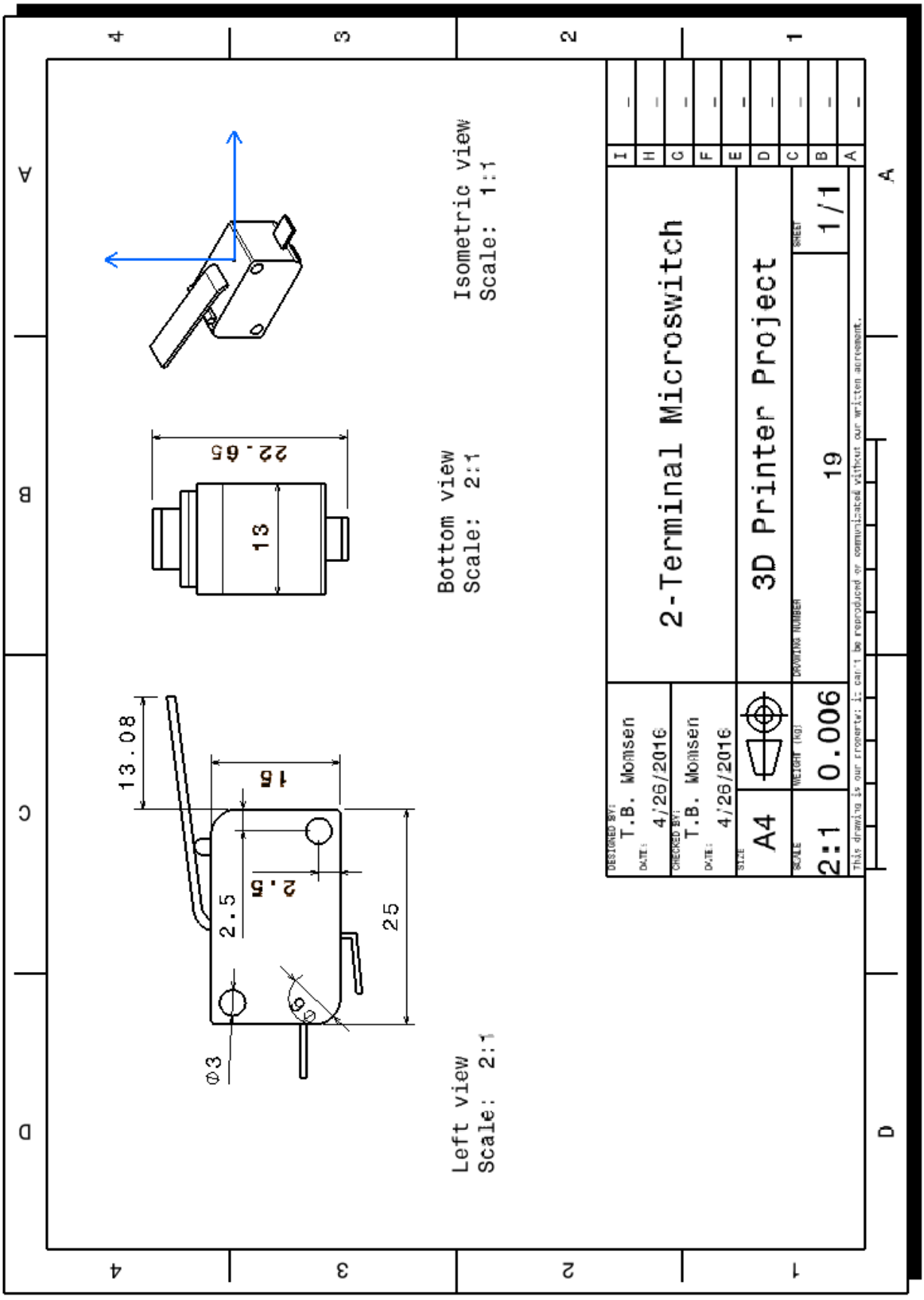
Isometric view
Scale: 1:1
Bottom view
Scale: 2:1
Left view
Scale: 2:1
22.65
13
13.08
15
2.5
2.5
25
Ø3
2-Terminal Microswitch
3D Printer Project
DESIGNED BY: T.B. Mollsen
DATE: 4/26/2016
CHECKED BY: T.B. Mollsen
DATE: 4/26/2016
SIZE A4
SCALE 2:1
WEIGHT (KG) 0.006
DRAWING NUMBER 19
SHEET 1/1
This drawing is our property; it can't be reproduced or communicated without our written agreement.

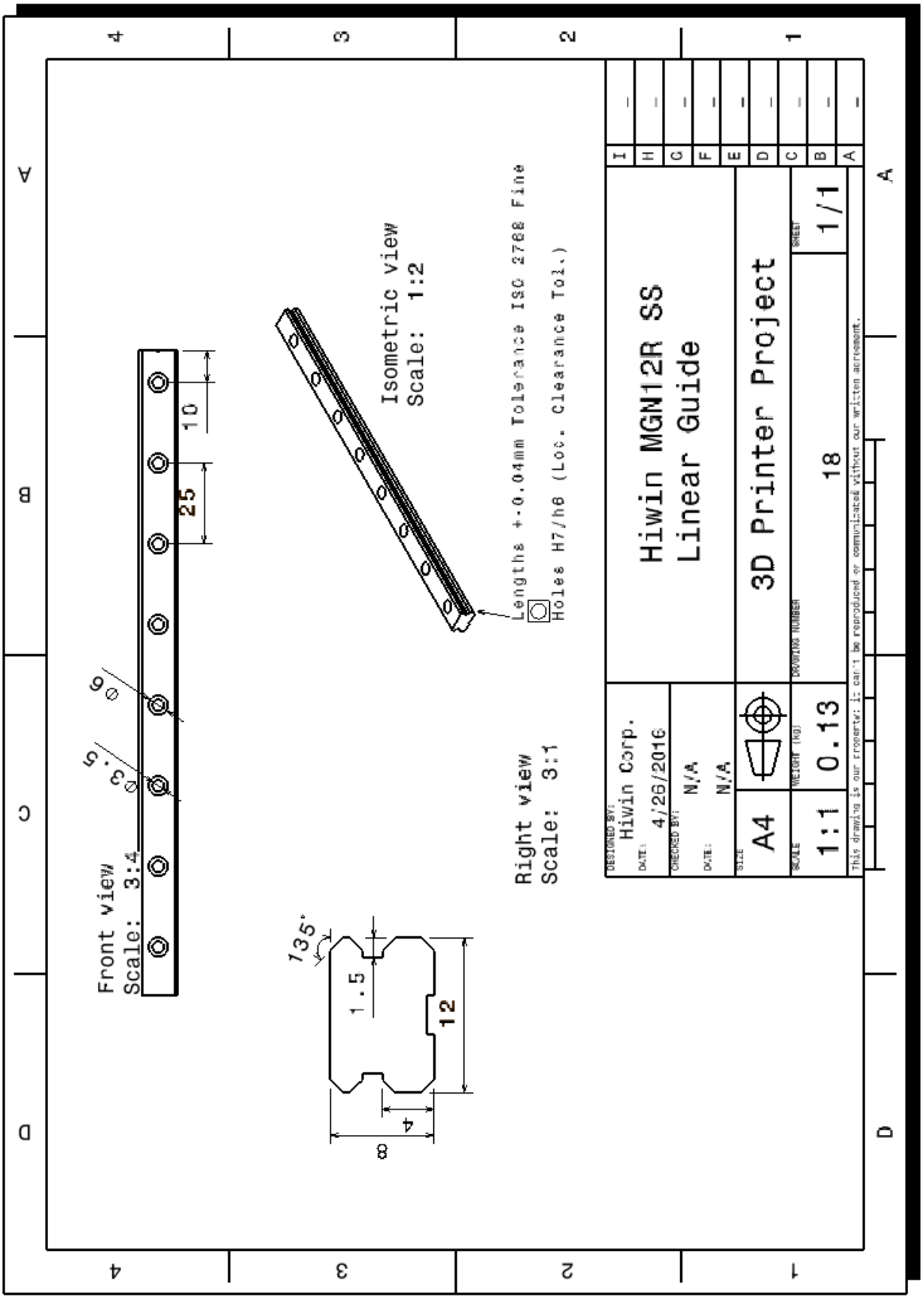
Front view
Scale: 3:4
25
10
Isometric view
Scale: 1:2
Lengths +-0.04mm Tolerance ISO 2768 Fine
Holes H7/h8 (Loc. Clearance Tol.)
Right view
Scale: 3:1
135°
1.5
12
4
8
Hiwin MGN12R SS
Linear Guide
3D Printer Project
DESIGNED BY: Hiwin Corp.
DATE: 4/26/2016
CHECKED BY: N/A
DATE: N/A
SIZE A4
WEIGHT (kg) 0.13
SCALE 1:1
DRAWING NUMBER 18
SHEET 1/1
This drawing is our property; it can't be reproduced or communicated without our written agreement.

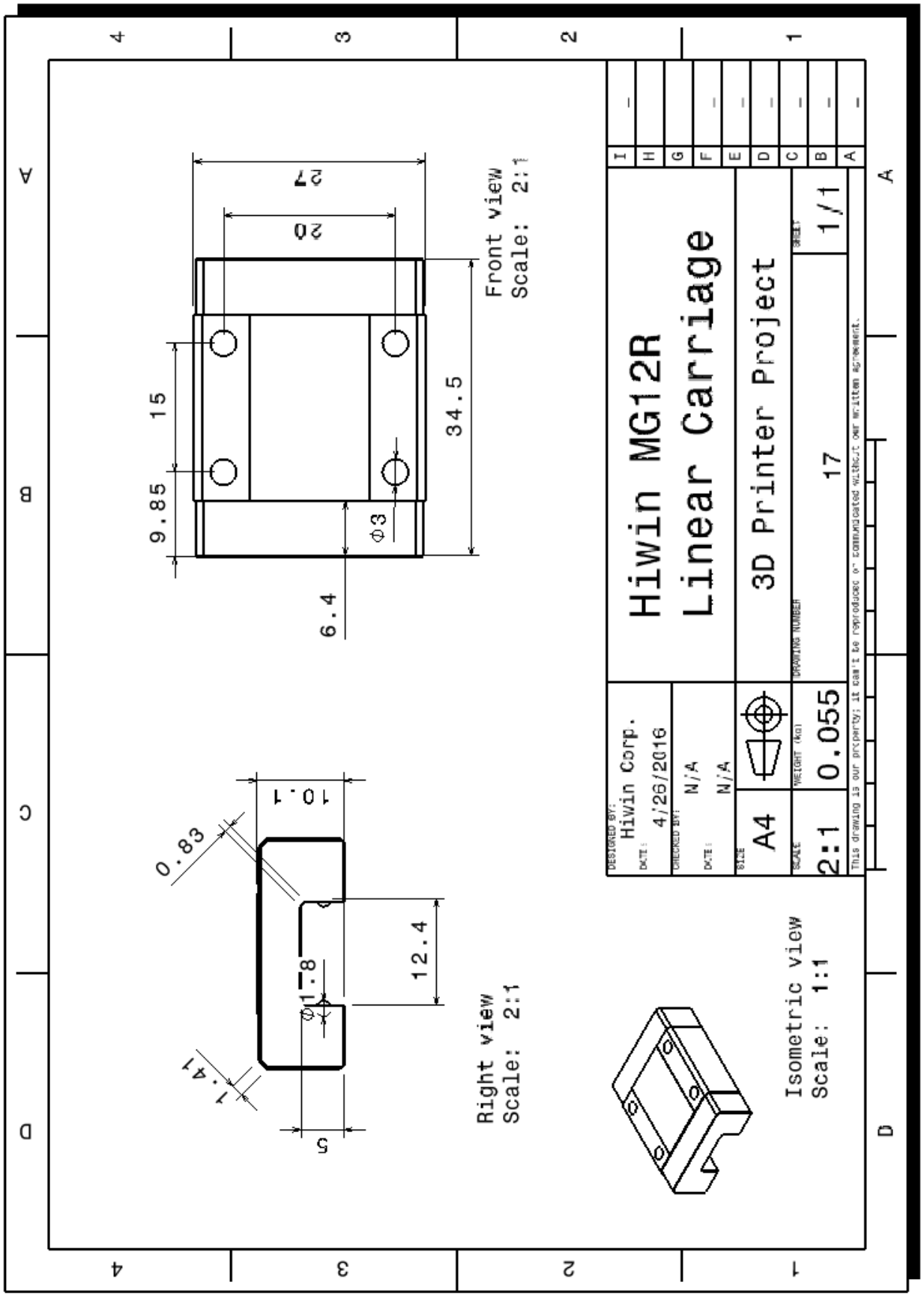
Hiwin MG12R
Linear Carriage
3D Printer Project
DESIGNED BY: Hiwin Corp.
DATE: 4/26/2016
CHECKED BY: N/A
DATE: N/A
SIZE A4
SCALE 2:1
WEIGHT (Kg) 0.055
DRAWING NUMBER 17
SHEET 1/1
This drawing is our property; it can't be reproduced or communicated without our written agreement.
Front view
Scale: 2:1
27
20
15
9.85
34.5
Φ3
6.4
Right view
Scale: 2:1
10.1
0.83
12.4
Φ1.8
1.47
5
Isometric view
Scale: 1:1

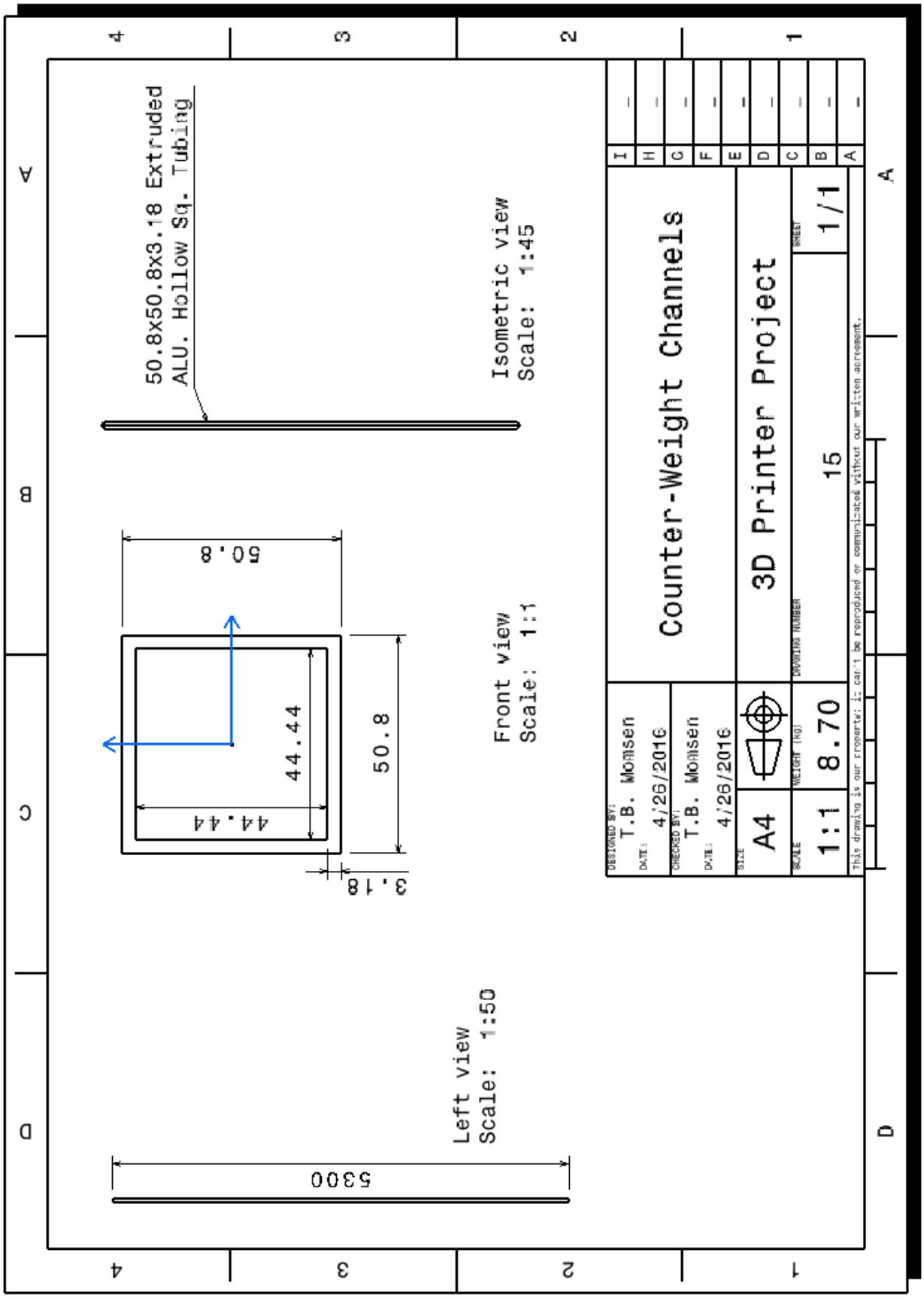
50.8x50.8x3.18 Extruded
ALU. Hollow Sq. Tubing
Isometric view
Scale: 1:45
Front view
Scale: 1:1
50.8
44.44
44.44
50.8
3.18
Left view
Scale: 1:50
5300
Counter-Weight Channels
3D Printer Project
15
1/1
A4
1:1
8.70
T.B. Monsen
4/26/2016
T.B. Monsen
4/26/2016

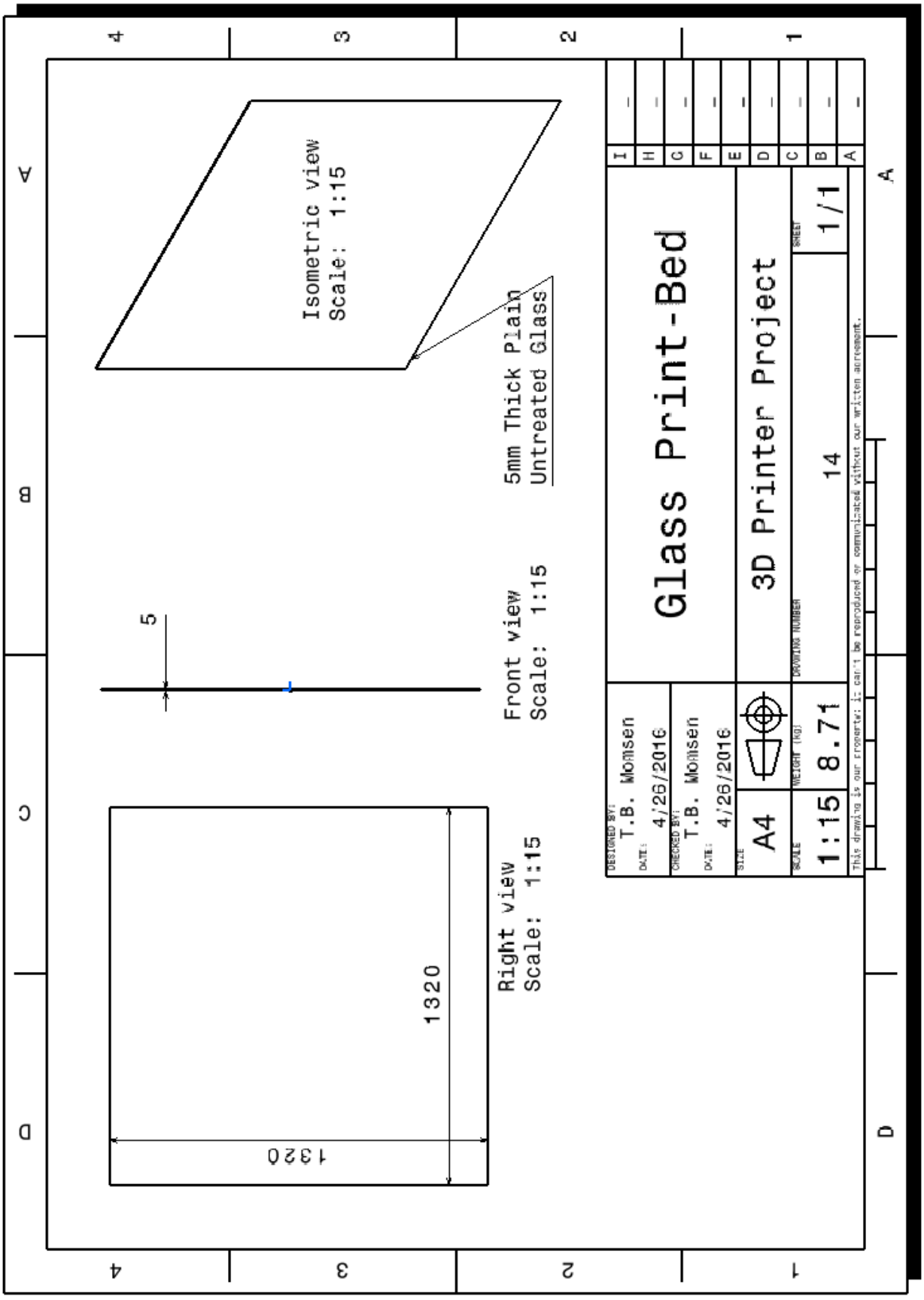
Isometric view
Scale: 1:15
5mm Thick Plain
Untreated Glass
Front view
Scale: 1:15
5
Right view
Scale: 1:15
1320
1320
Glass Print-Bed
3D Printer Project
14
1/1
A4
1:15
8.71
T.B. Monsen
4/26/2016
T.B. Monsen
4/26/2016
This drawing is our property; it can't be reproduced or communicated without our written agreement.

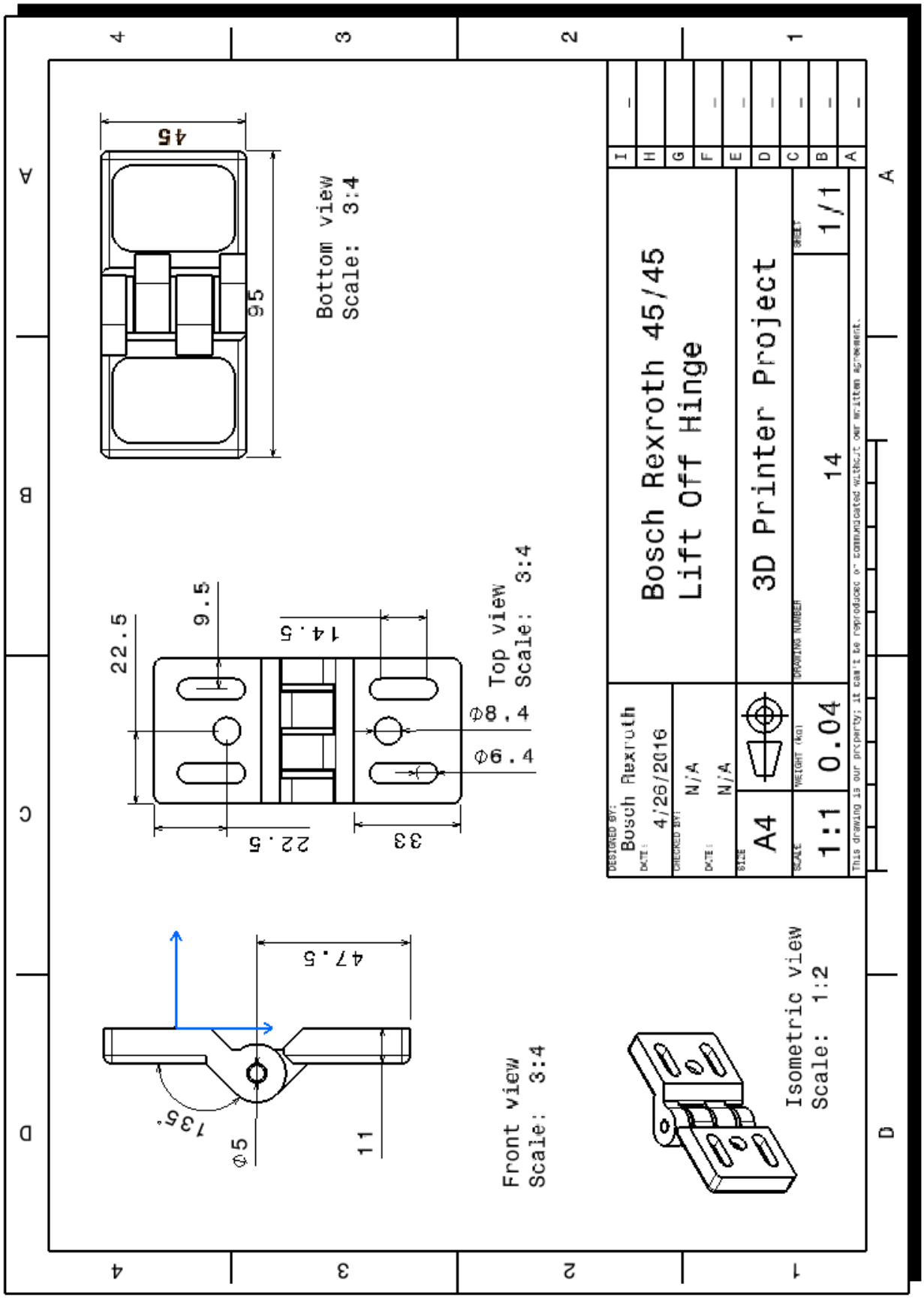
Bosch Rexroth 45/45
Lift Off Hinge
3D Printer Project
14
1/1
A4
1:1
0.04
4/26/2016
N/A
Bosch Rexroth
This drawing is our property; it can't be reproduced or communicated without our written agreement.
Bottom view
Scale: 3:4
Top view
Scale: 3:4
Front view
Scale: 3:4
Isometric view
Scale: 1:2
45
95
22.5
9.5
14.5
22.5
33
Φ8.4
Φ6.4
47.5
11
Φ5
135°

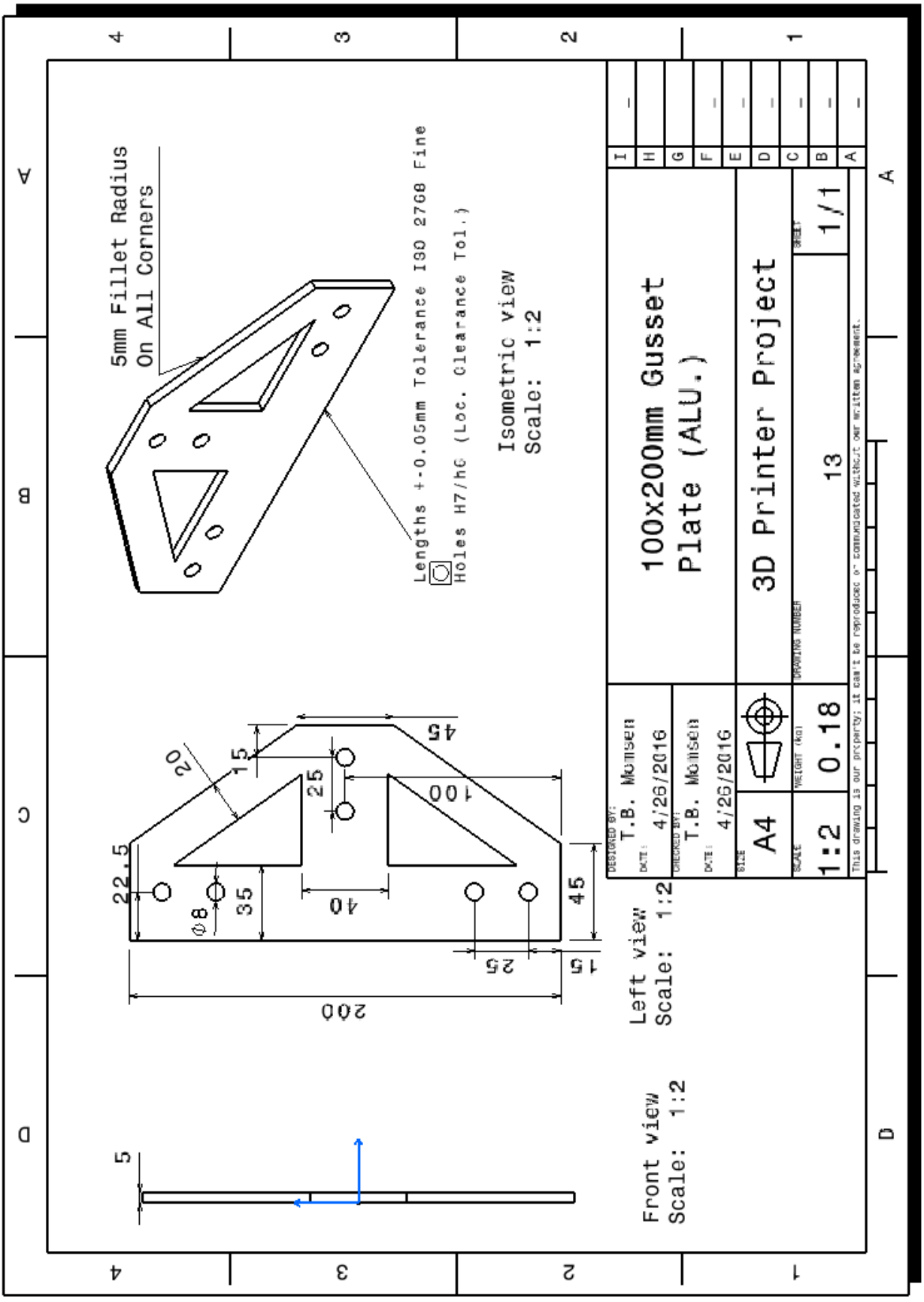
5mm Fillet Radius
On All Corners
Lengths +-0.05mm Tolerance ISO 2768 Fine
Holes H7/h6 (Loc. Clearance Tol.)
Isometric view
Scale: 1:2
100x200mm Gusset
Plate (ALU.)
3D Printer Project
13
1/1
T.B. Mousen
4/26/2016
A4
1:2
0.18
Left view
Scale: 1:2
Front view
Scale: 1:2
200
100
45
40
35
25
22.5
20
15
5
Ø8

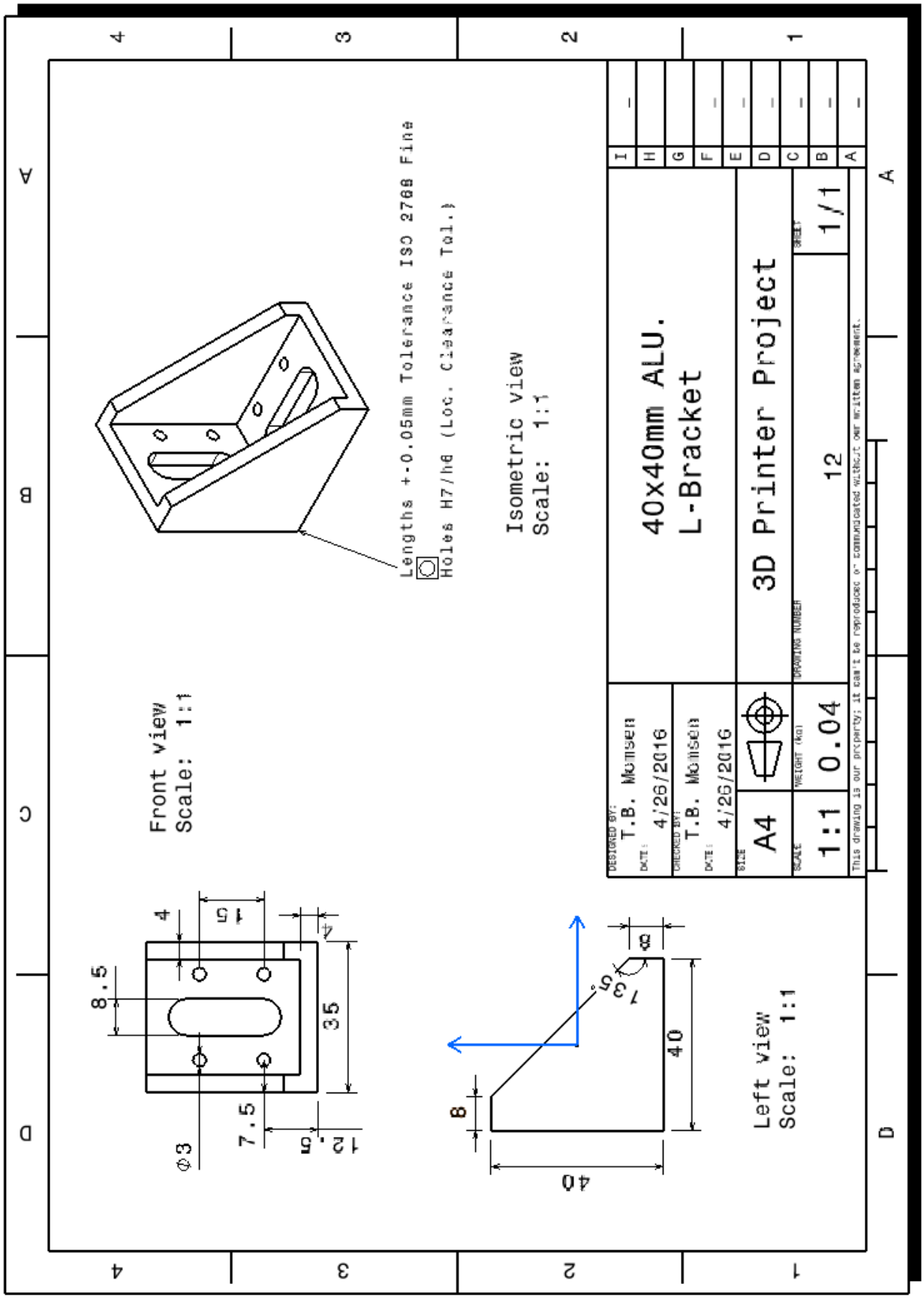
Lengths +-0.05mm Tolerance ISO 2768 Fine
Holes H7/h6 (Loc. Clearance Tol.)
Isometric view
Scale: 1:1
Front view
Scale: 1:1
Left view
Scale: 1:1
40x40mm ALU.
L-Bracket
3D Printer Project
DESIGNED BY: T.B. Mönsen
DATE: 4/26/2016
CHECKED BY: T.B. Mönsen
DATE: 4/26/2016
SIZE A4
SCALE 1:1
WEIGHT (kg) 0.04
DRAWING NUMBER 12
SHEET 1/1
This drawing is our property; it can't be reproduced or communicated without our written agreement.

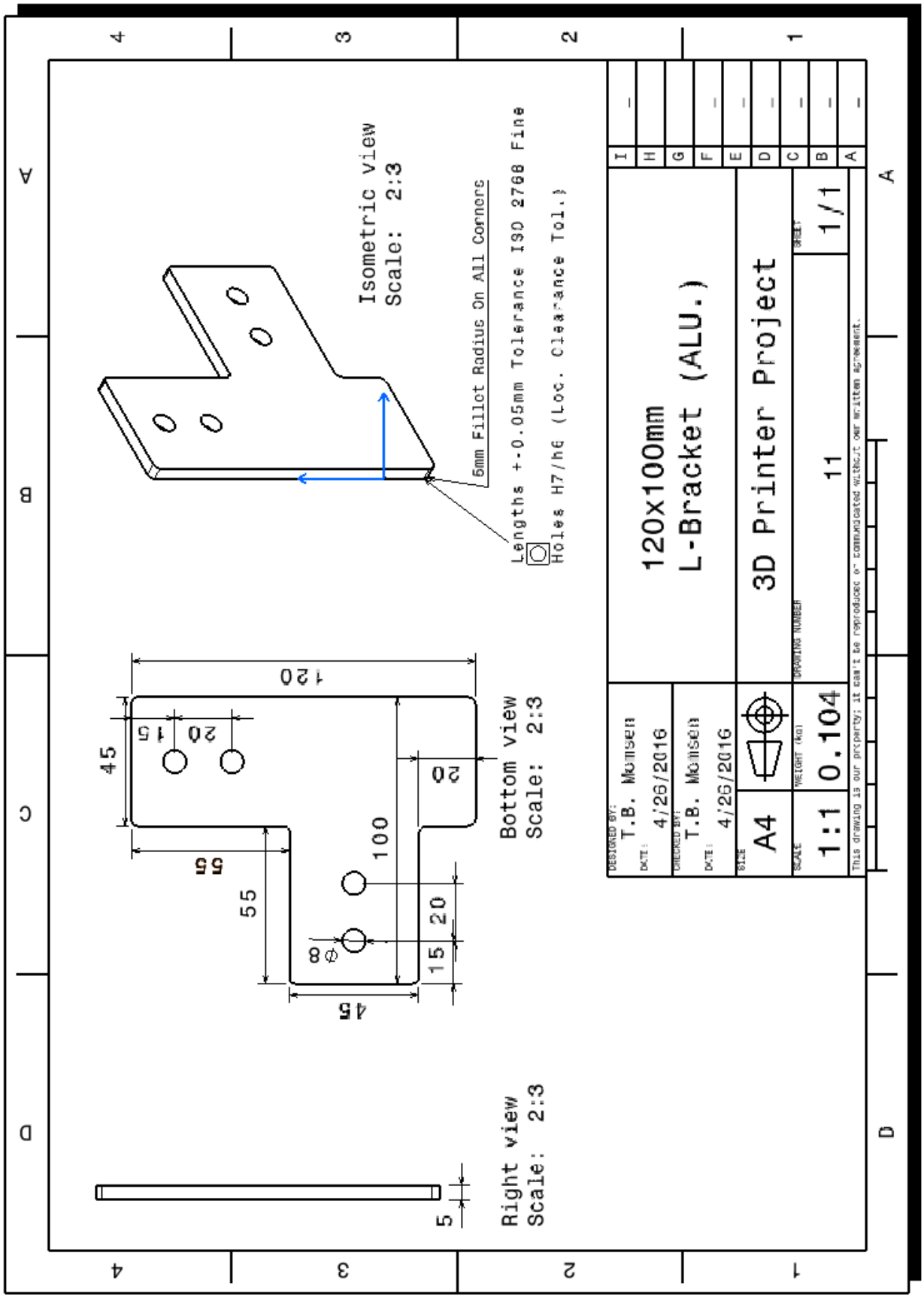
Isometric view
Scale: 2:3
5mm Fillet Radius On All Corners
Lengths +-0.05mm Tolerance ISO 2768 Fine
Holes H7/h6 (Loc. Clearance Tol.)
120x100mm
L-Bracket (ALU.)
3D Printer Project
DESIGNED BY: T.B. Mollsen
DATE: 4/26/2016
CHECKED BY: T.B. Mollsen
DATE: 4/26/2016
SIZE A4
SCALE 1:1
WEIGHT (Kg) 0.104
DRAWING NUMBER 11
SHEET 1/1
This drawing is our property; it can't be reproduced or communicated without our written agreement.
Bottom view
Scale: 2:3
120
45
15
20
55
100
20
8Φ
45
Right view
Scale: 2:3
5

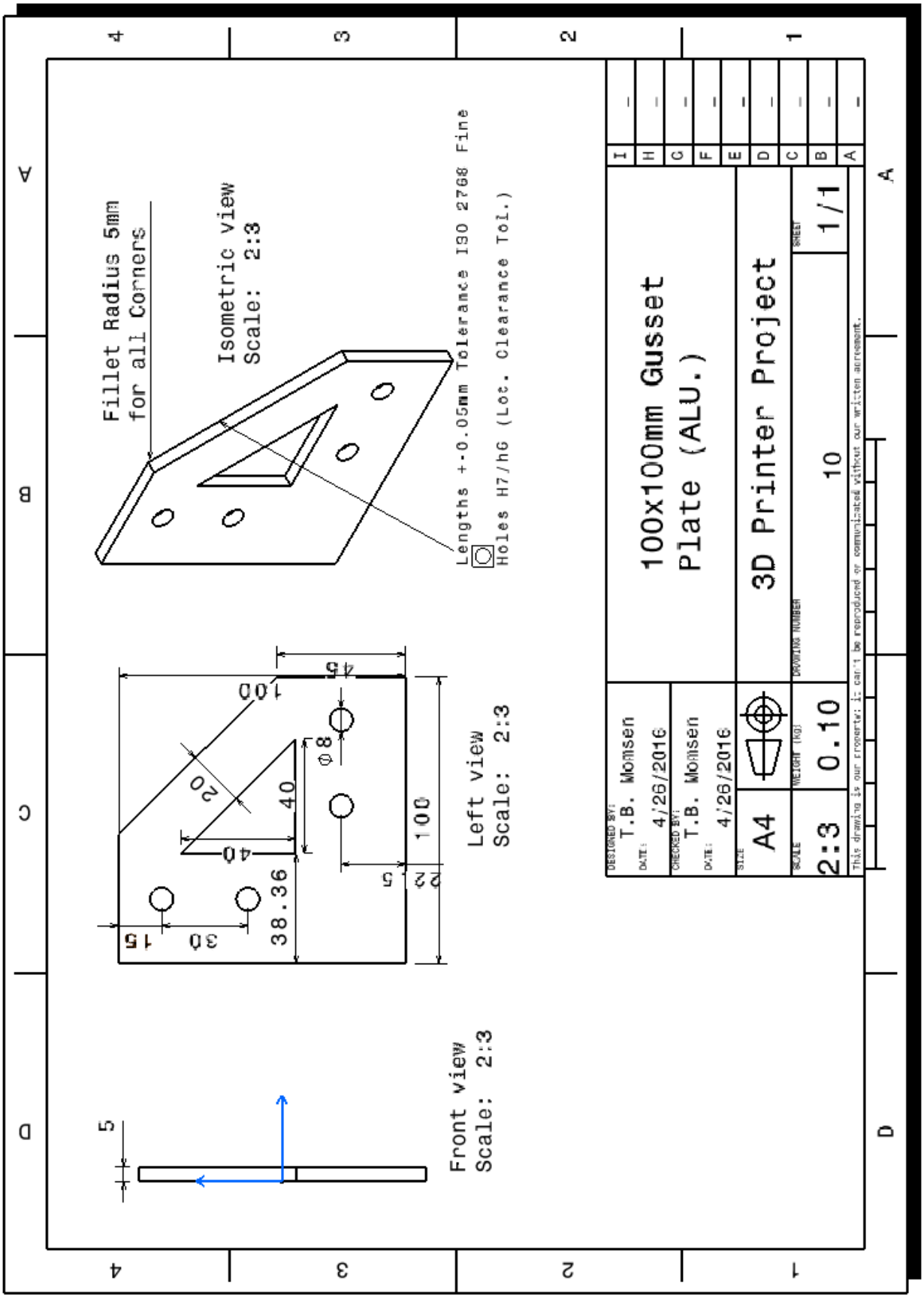
Fillet Radius 5mm
for all Corners
Isometric view
Scale: 2:3
Lengths +-0.05mm Tolerance ISO 2768 Fine
Holes H7/h6 (Loc. Clearance Tol.)
Left view
Scale: 2:3
Front view
Scale: 2:3
100x100mm Gusset
Plate (ALU.)
3D Printer Project
DESIGNED BY: T.B. Momsen
DATE: 4/26/2016
CHECKED BY: T.B. Momsen
DATE: 4/26/2016
SIZE A4
WEIGHT (KG) 0.10
SCALE 2:3
DRAWING NUMBER 10
SHEET 1/1
This drawing is our property; it can't be reproduced or communicated without our written agreement.

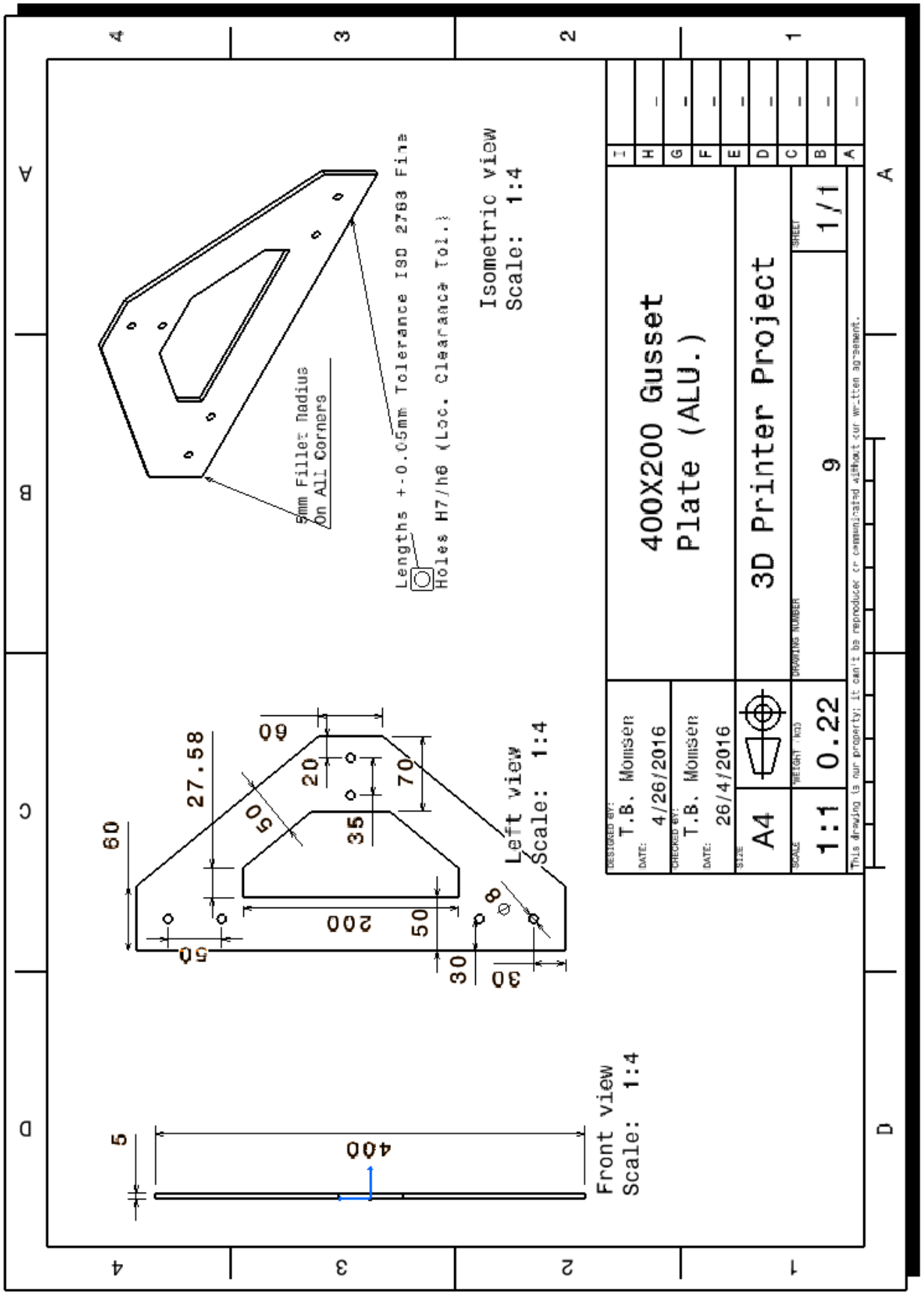
400X200 Gusset Plate (ALU.)
3D Printer Project
T.B. Monsen
4/26/2016
A4
1:1
0.22
9
1/1
Isometric view
Scale: 1:4
Lengths +-0.05mm Tolerance ISO 2768 Fine
Holes H7/h6 (Loc. Clearance Fit)
5mm Fillet Radius On All Corners
Left view
Scale: 1:4
Front view
Scale: 1:4
This drawing is our property; it can't be reproduced or communicated without our written agreement.

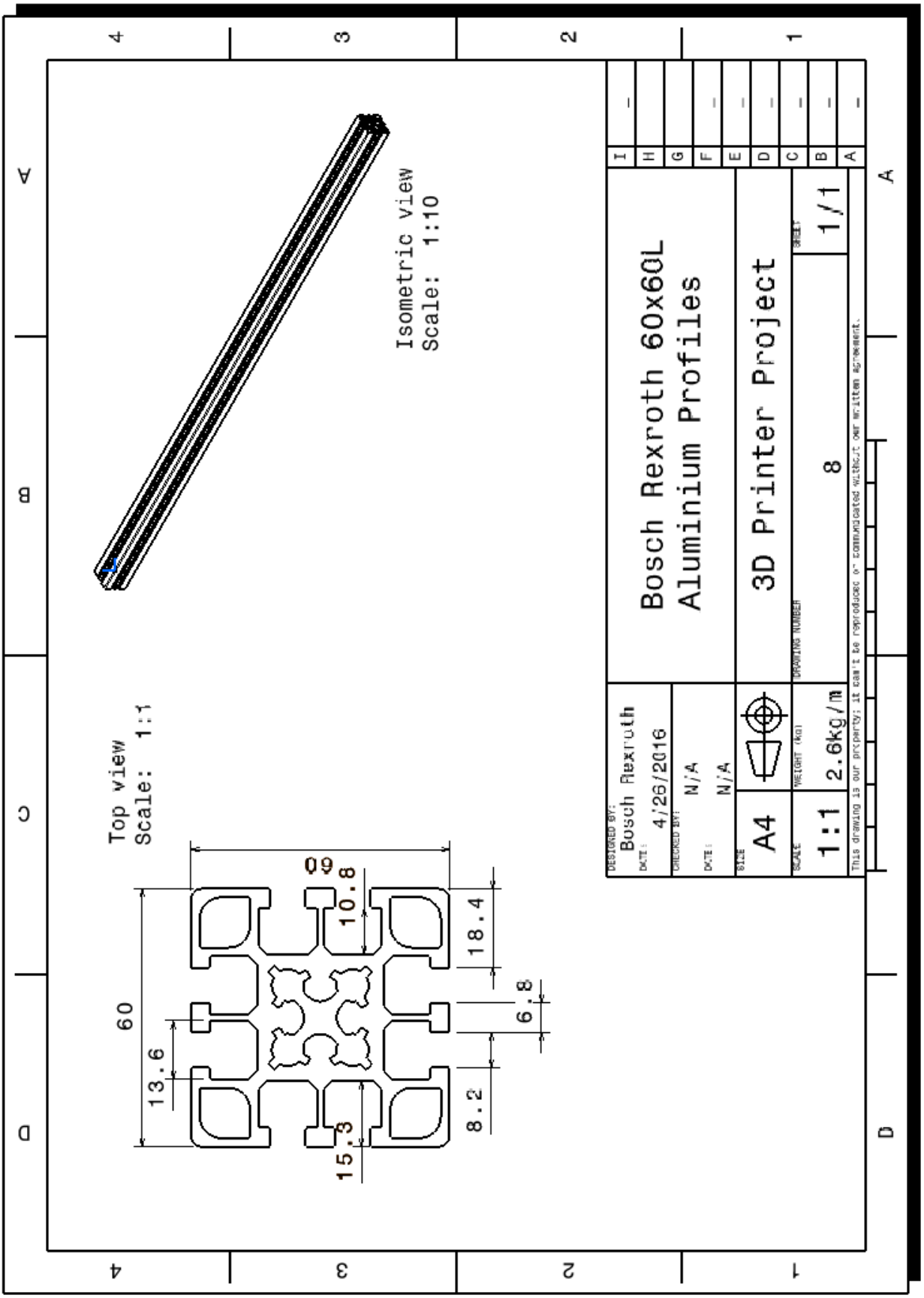
Isometric view
Scale: 1:10
Top view
Scale: 1:1
60
13.6
15.3
8.2
6.8
18.4
10.8
09
Bosch Rexroth 60x60L
Aluminium Profiles
3D Printer Project
DESIGNED BY:
Bosch Rexroth
DATE:
4/26/2016
CHECKED BY:
N/A
DATE:
N/A
SIZE
A4
SCALE
1:1
WEIGHT (Kg)
2.6kg/m
DRAWING NUMBER
8
SHEET
1/1
This drawing is our property; it can't be reproduced or communicated without our written agreement.

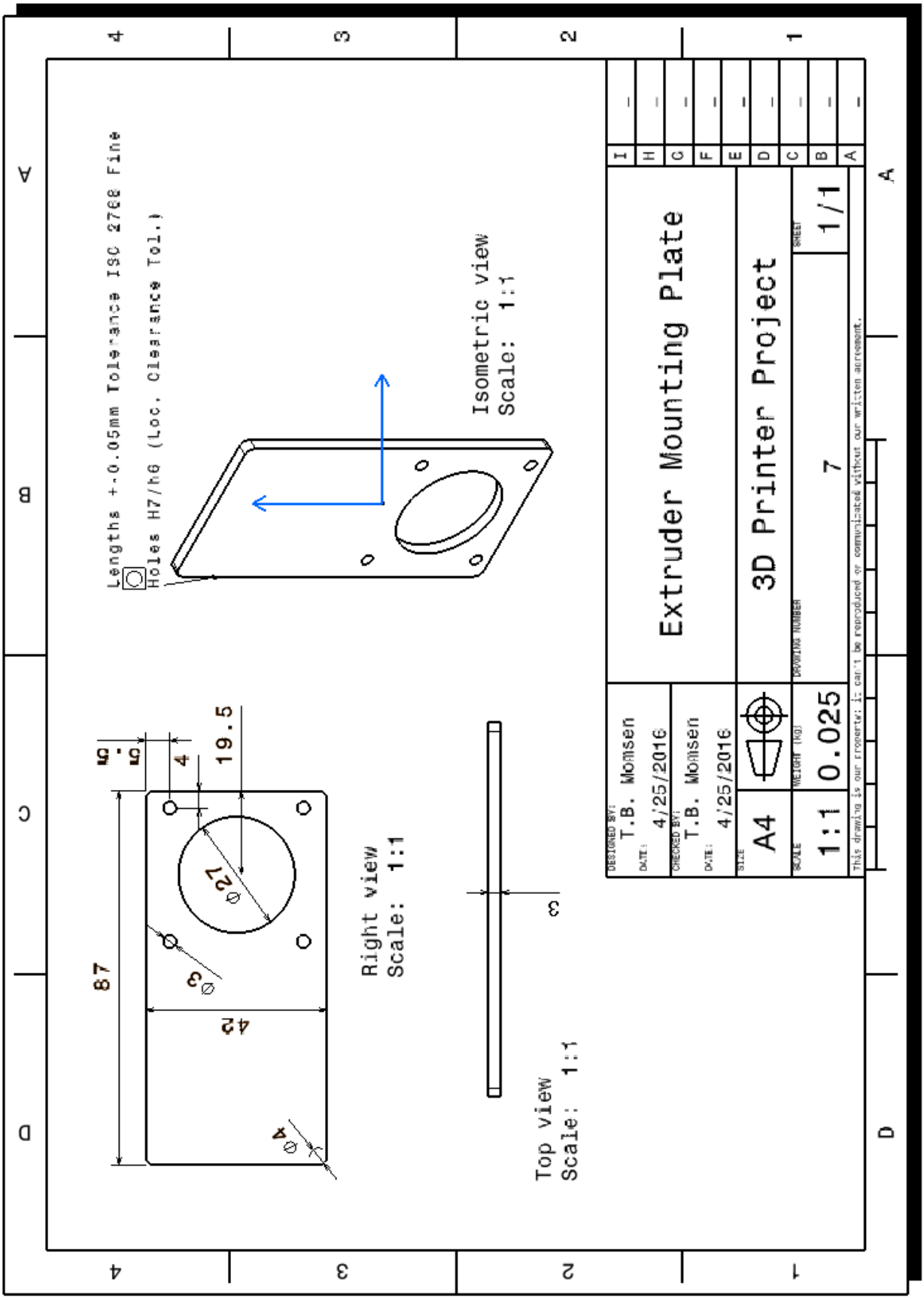
Lengths +-0.05mm Tolerance ISO 2768 Fine
Holes H7/h6 (Loc. Clearance Tol.)
Isometric view
Scale: 1:1
Extruder Mounting Plate
3D Printer Project
DESIGNED BY: T.B. Momsen
DATE: 4/25/2016
CHECKED BY: T.B. Momsen
DATE: 4/25/2016
SIZE A4
WEIGHT (kg) 0.025
SCALE 1:1
DRAWING NUMBER 7
SHEET 1/1
This drawing is our property; it can't be reproduced or communicated without our written agreement.
Right view
Scale: 1:1
Top view
Scale: 1:1
87
42
19.5
4
5
3
22
4

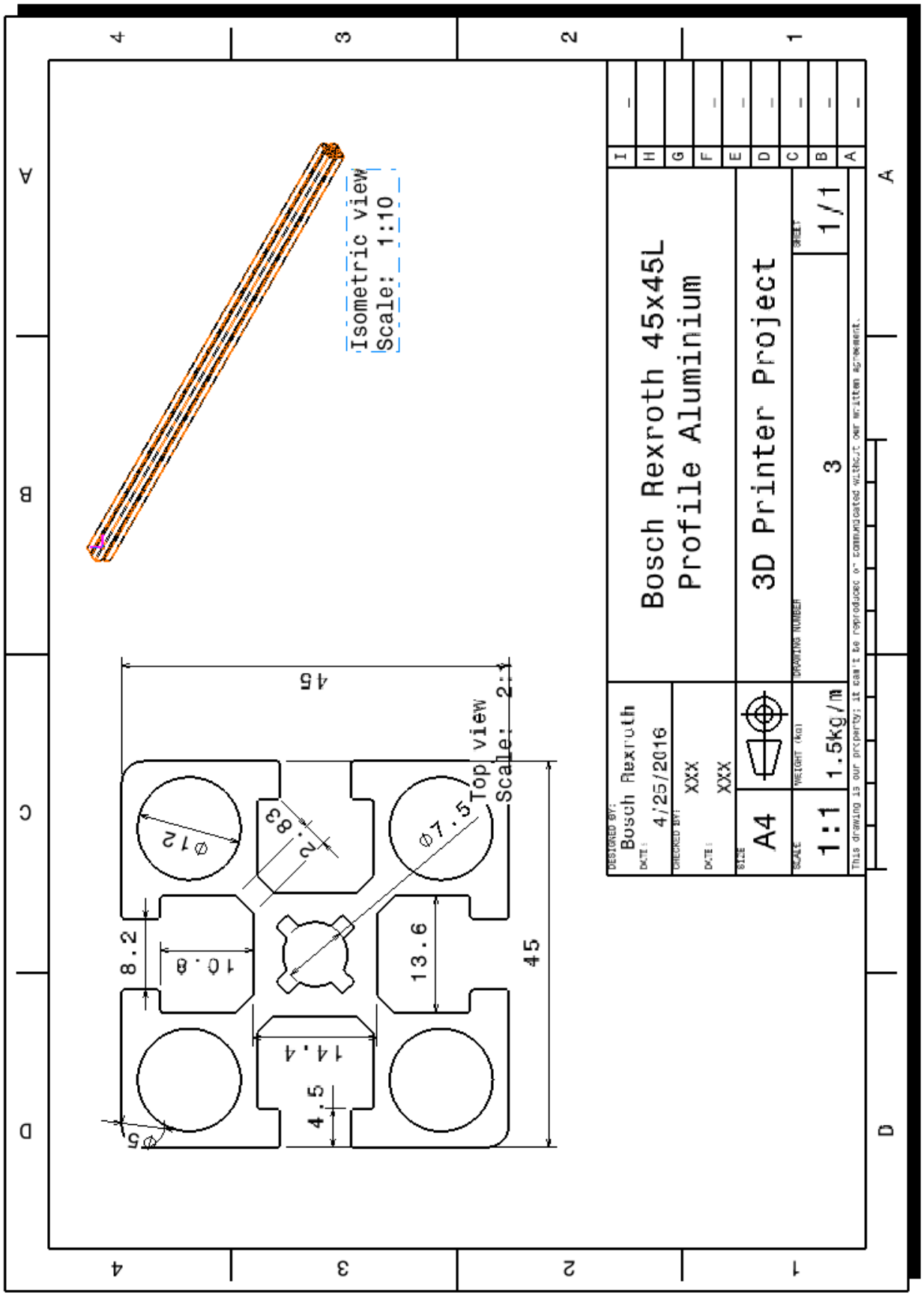
Isometric view
Scale: 1:10
Top view
Scale: 2:1
45
Ø12
8.3
Ø7.5
8.2
10.8
13.6
45
14.4
4.5
Ø5
Bosch Rexroth 45x45L
Profile Aluminium
3D Printer Project
DESIGNED BY:
Bosch Rexroth
DATE:
4/25/2016
CHECKED BY:
XXX
DATE:
XXX
SIZE
A4
SCALE
1:1
WEIGHT (Kg)
1.5kg/m
DRAWING NUMBER
3
SHEET
1/1
This drawing is our property; it can't be reproduced or communicated without our written agreement.

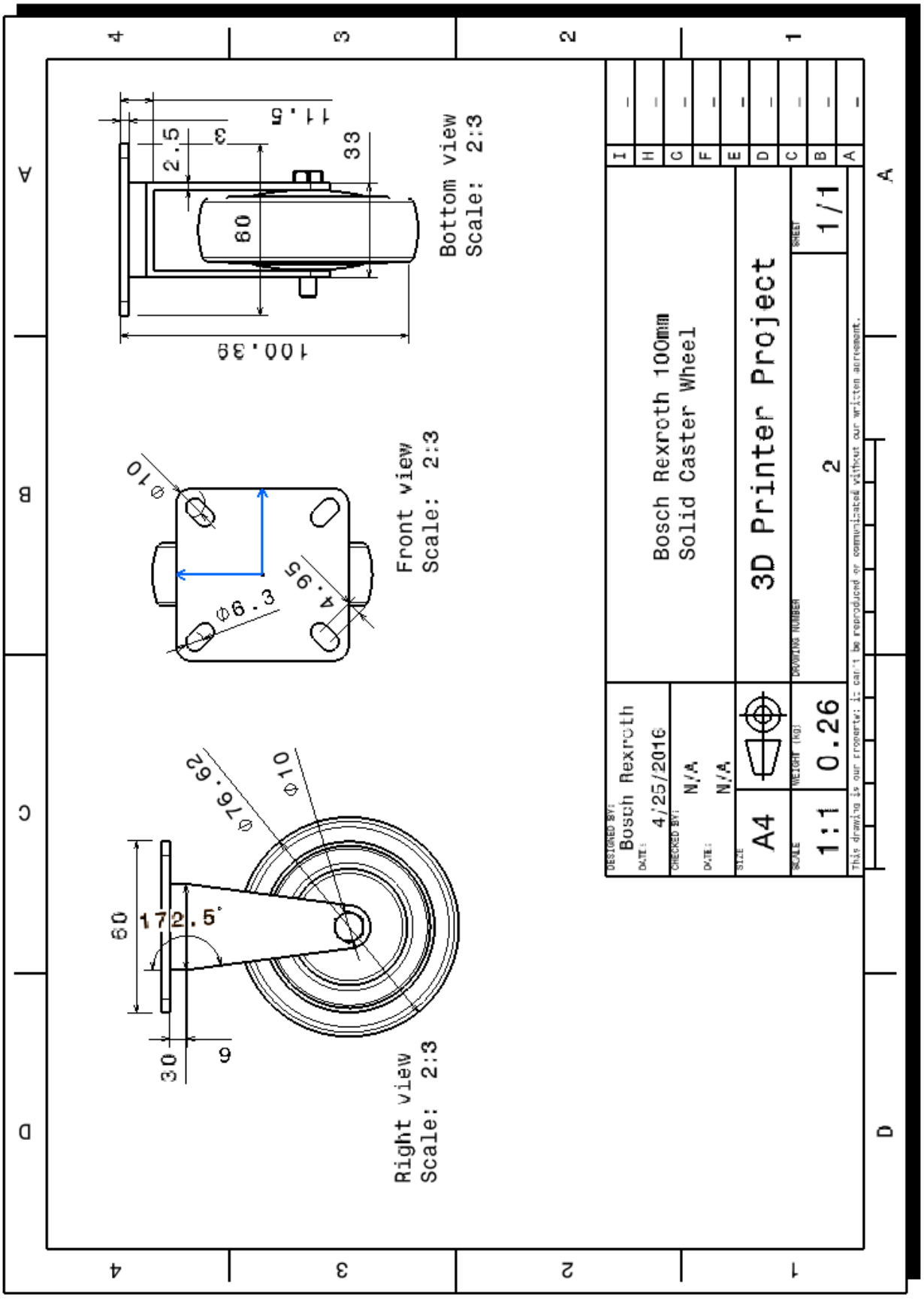
Bottom view
Scale: 2:3
Front view
Scale: 2:3
Right view
Scale: 2:3
Bosch Rexroth 100mm
Solid Caster Wheel
3D Printer Project
A4
1:1
0.26
1/1
Bosch Rexroth
4/25/2016
N/A
N/A

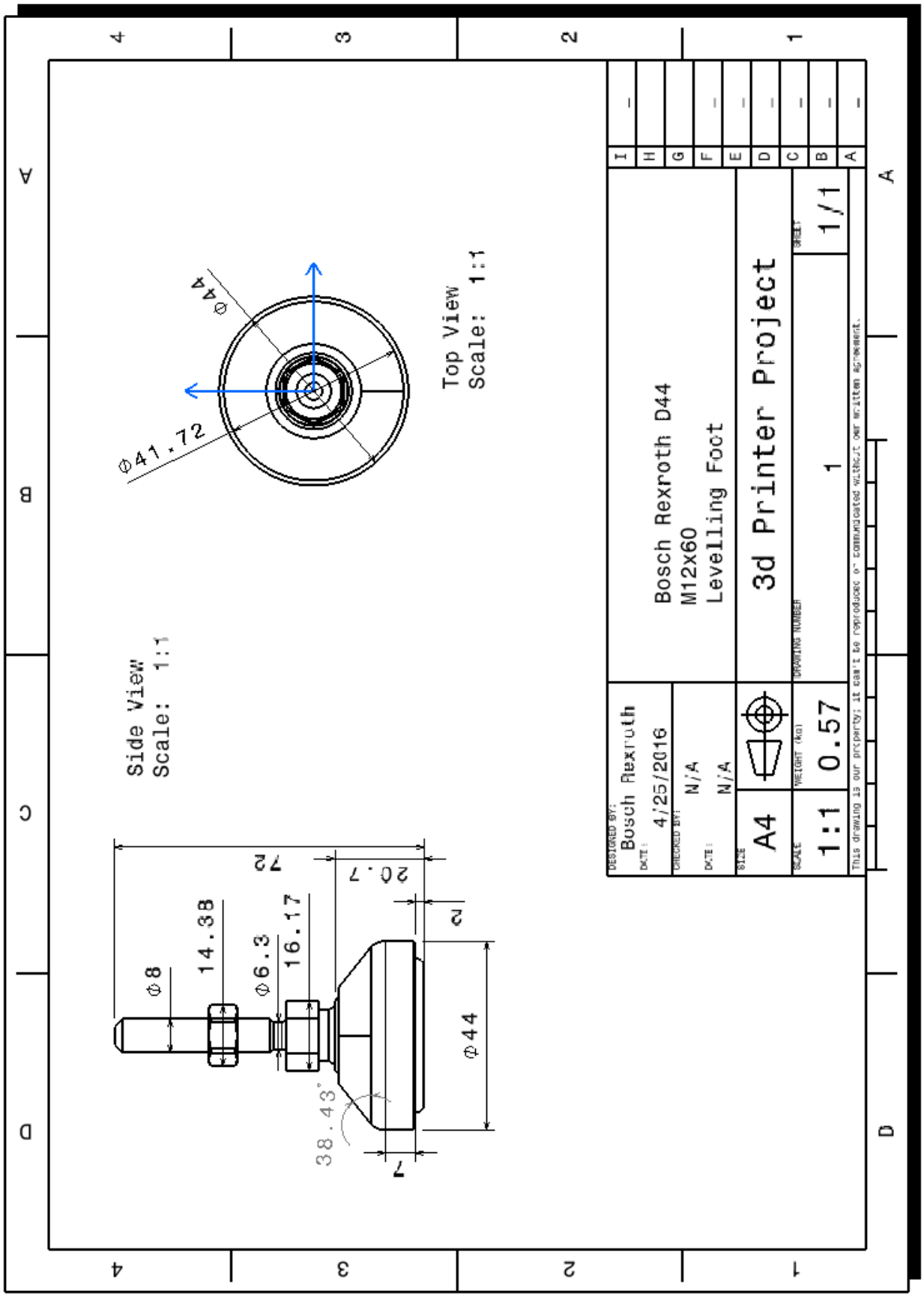
Top View
Scale: 1:1
Ø41.72
Side View
Scale: 1:1
27
20.7
2
Ø8
14.38
Ø6.3
16.17
Ø44
38.43°
7
Bosch Rexroth D44
M12x60
Levelling Foot
3d Printer Project
DESIGNED BY:
Bosch Rexroth
DATE:
4/25/2016
CHECKED BY:
N/A
DATE:
N/A
SIZE
A4
WEIGHT (Kg)
0.57
SCALE
1:1
DRAWING NUMBER
1
SHEET
1/1
This drawing is our property; it can't be reproduced or communicated without our written agreement.